THE UNIVERSITY of EDINBURGH

This thesis has been submitted in fulfilment of the requirements for a postgraduate degree (e.g. PhD, MPhil, DClinPsychol) at the University of Edinburgh. Please note the following terms and conditions of use:

- This work is protected by copyright and other intellectual property rights, which are retained by the thesis author, unless otherwise stated.
- A copy can be downloaded for personal non-commercial research or study, without prior permission or charge.
- This thesis cannot be reproduced or quoted extensively from without first obtaining permission in writing from the author.
- The content must not be changed in any way or sold commercially in any format or medium without the formal permission of the author.
- When referring to this work, full bibliographic details including the author, title, awarding institution and date of the thesis must be given.

Mesoscopic discrete element modelling of cohesive powders for bulk handling applications

by

Subhash Chandra Thakur

A dissertation submitted in partial fulfilment
for the degree of *Doctor of Philosophy*

in the

School of Engineering

The University of Edinburgh

2014

Declaration of Authorship

This thesis entitled, “Mesoscopic discrete element modelling of cohesive powders for bulk handling application” is submitted to the University of Edinburgh for the degree of Doctor of Philosophy. The research work described and reported in this thesis has been completed solely by Subhash Chandra Thakur under the supervision of Prof. Jin Y. Ooi, Dr. Jin Sun and Dr. Hossein Ahmadian. I confirm that:

- Where I have consulted the published work of others, this is always clearly attributed.
- Where I have quoted from the work of others, the source is given.
- I have acknowledged all main sources of help.
- Where the thesis is based on work done by myself jointly with others, I have

made clear exactly what was done by others and what I have contributed myself. This applies in the area of the contact model development and implementation where work has been carried out jointly with J.P. Morrissey. Also the experiments on rotary drum reported in chapter 3 were carried out by Mateusz Wojitkowski and it is included for comparison.

Publications based on this thesis:

- Thakur, S.C., Ahmadian, H., Sun, J., Ooi, J.Y. (2014). An experimental and numerical study on packing, compression, and shear behaviour of detergent powders. *Particuology, Volume 12, Pages 2-12.*
- Thakur, S.C., Morrissey, J.P., Sun, J., Chen, J-F., Ooi, J.Y. (2014). Micromechanical analysis of cohesive granular materials using discrete element model with an adhesive elastoplastic contact model. *Accepted in Granular matter.*
- Thakur, S.C., Ooi, J.Y., Ahmadian, H. (2014). Scaling of discrete element model parameter in uniaxial test simulation. *Submitted to Chemical Engineering Science.*
- Thakur, S.C., Ooi, J., Ahmadian, H. (2013). *Scaling of discrete element model parameter in uniaxial test simulation.* The 6th International conference on discrete element methods, Golden, Colorado, USA.
- Thakur, S.C., Ooi, J.Y., Imole, O.I., Wojtkowski, M.B., Magnanimo, V., Ahmadian, H., Montes, E.C., and Ramiaoli, M., (2013). *Characterisation of cohesive powders for bulk handling and DEM modelling*, in: Bischoff, M., Onate, Owen, D.R.J., Ramm, E. and Wriggers, P. (Ed.), III International

Conference on Particle-Based Methods-Fundamentals and Applications. Sttutgart, Germany

- Thakur, S.C., Sun, J., Ooi, J.Y., Ahmadian, H. (2012). *An experimental and numerical study on packing, compression, and shear behaviour of detergent powders.* International conference on Conveying and Handling of Particulate Solids (CHOPS). Friedrichshafen, Germany.
- Thakur, S.C., Morrissey, J.P., Sun, J., Chen, J-F., Ooi, J.Y. (2012). *DEM modelling of cohesive bulk materials.* International conference on Conveying and Handling of Particulate Solids (CHOPS). Friedrichshafen, Germany.
- Thakur, S.C., Morrissey, J.P., Sun, J., Chen, J-F., Ooi, J.Y. (2011). *A DEM study of cohesive particulate solids: plasticity and stress-history dependency.* International conference on Particulate System Analysis organized by Royal Society of Chemistry. Edinburgh, Scotland, UK.
- Morrissey, J.P., Thakur, S.C., Sun, J., Chen, J-F., Ooi, J.Y. (2011). *Modelling Cohesive-Frictional Particulate solids for Bulk Handling Applications.* II International Conference on Particle-based Methods – Fundamentals and Applications. Barcelona, Spain.
- Morrissey, J.P., Thakur, S.C., Sun, J., Chen, J-F., Ooi, J.Y. (2011).*Particle Scale Modelling of Frictional Cohesive Granular Materials.* EDEM conference. Edinburgh, Scotland, UK.

The following reports have been produced:

- Thakur, S.C., and Imole, O.I. (2011). *A literature review on cohesive solids.* PARDEM WP2 state-of-the art report.
- Thakur, S.C., and Ooi, J.Y., Ahmadian, H. (2013). Scaling of discrete element model parameters in uniaxial test simulation. *Submitted to Newcastle Innovation Centre, Procter and Gamble, Newcastle, UK.*

Signed:

Dated:

UNIVERSITY OF EDINBURGH

Abstract

Institute for Infrastructure and Engineering

School of Engineering

Doctor of Philosophy

by

Subhash Chandra Thakur

Many powders and particulate solids are stored and handled in large quantities across various industries. These solids often encounter handling and storage difficulties that are caused by the material cohesion. The cohesive strength of a bulk material is a function of its past consolidation stress. For example, high material cohesive strength as a result from high storage stresses in a silo can cause ratholing problems during discharge. Therefore, it is essential to consider the stress-history dependence when evaluating such handling behaviour.

In recent years the Discrete Element Method (DEM) has been used extensively to study the complex behaviour of granular materials. Whilst extensive DEM studies have been performed on cohesionless solids, much less work exists on modelling of cohesive solids. The commonly used DEM models to model adhesion such as the JKR, DMT and linear cohesion models have been shown to have difficulty in predicting the stress-history dependent behaviour for cohesive solids. DEM modelling of cohesive solid at individual particle level is very challenging. To apply the model at single particle level accurately would require one to determine the model parameters at particle level and consider the enormous complexity of interfacial interaction. Additionally it is computationally prohibitive to model each and every individual particle and cohesion arising from several different phenomena. In this study an adhesive elasto-plastic contact model for the mesoscopic discrete element method (DEM) with three dimensional non-spherical particles is proposed with the aim of achieving quantitative predictions of cohesive powder flowability. Simulations have been performed for uniaxial consolidation followed by unconfined compression to failure using this model. Additionally, the scaling laws necessary to produce scale independent predictions for cohesionless and cohesive solids was also investigated. The influence of DEM input parameters and model implementation have been explored to study the effect of particle (meso-scale) properties on the bulk behaviour in uniaxial test simulation.

The DEM model calibration was achieved using the Edinburgh Powder Tester (EPT) – an extended uniaxial tester to measure flowability of bulk solids. The EPT produced highly repeatable flowability measurements and was shown to be a good

candidate for DEM model calibration. The implemented contact model has been shown to be capable of predicting the experimental flow function (unconfined compressive strength versus the prior consolidation stress) for a limestone powder which has been selected as a reference solid in the Europe wide PARDEM research network. Contact plasticity in the model is shown to affect the flowability significantly and is thus essential for producing satisfactory computations of the behaviour of a cohesive granular material. The model predicted a linear relationship between a normalized unconfined compressive strength and the product of coordination number and solid fraction. Significantly, it has been found that contribution of adhesive force to the limiting friction has a significant effect on bulk unconfined strength. Failure to include the adhesive contribution in the calculation of the frictional resistance may lead to under-prediction of unconfined strength and incorrect failure mode. The results provide new insights and propose a micromechanical based measure for characterising the strength and flowability of cohesive granular materials.

Scaling of DEM input parameters in a 3D simulation of the loading regimes in a uniaxial test indicated that whilst both normal and tangential contact stiffness (loading, unloading, and load dependent) scales linearly with radius of the particle, the adhesive forces scales with the square of the radius of the particles. This is a first step towards a mesoscopic representation of a cohesive powder that is phenomenological based to produce the key bulk characteristics of a granular solid and the results indicate that it has potential to gain considerable computational advantage for large scale DEM simulations. The contact model parameters explored include particle contact normal loading stiffness, tangential stiffness, and contact friction coefficient. The DEM model implementation parameters included numerical time step, strain rate, and boundary condition. Many useful observations have been made with significant implications for the relative importance of the DEM input parameters. Finally the calibration procedure was applied to a spray dried detergent powder and the simulation results are compared to whole spectrum of loading regime in a uniaxial experiment. The experimental and simulation results were found to be in reasonable agreement for the flow function and compression behaviour.

Table of Contents

Declaration of Authorship ..... **i**

Abstract ..... **iv**

Table of Contents ..... **vii**

List of Figures ..... **xii**

List of Tables ..... **xx**

Acknowledgements ..... **xxiii**

1 Introduction **1**

1.1 General background 1

1.2 Objectives and scope of this thesis 3

1.3 Organization of the thesis 4

2 Literature review **6**

2.1 Introduction 6

2.2 Numerical modelling of particulate solids 7

2.2.1 Continuum vs discrete approach 7

2.2.2 Discrete element method (DEM) 8

2.3 An overview of DEM 11

2.3.1 Formulation 11

2.3.1 Determination of computational time step 12

2.3.2 Particle shape 13

2.3.3 Scaling 15

2.4 Contact force model 16

2.4.1 Non adhesive elastic contact models 17

2.4.1.1 Linear spring contact model 17

2.4.1.2 Hertz-Mindlin contact model 20
2.5 Modelling of adhesion 22
2.5.1 Normal force contact models 22
2.5.1.1 Elastic model with adhesion 22
2.5.1.2 Perfectly plastic and elastic-plastic model with adhesion 23
2.5.1.3 Elasto plastic model with load dependent adhesion 24
2.5.2 Limiting tangential force 31
2.5.2.1 Tangential force contact models 31
2.6 Attractive forces causing adhesion 37
2.6.1 van der Waals force 37
2.6.2 Liquid bridge force 38
2.6.3 Electrostatic forces 39
2.6.4 Magnetic forces 40
2.6.5 Solid bridge forces 40
2.6.6 Other forces 41
2.6.7 Comparison between adhesive forces 41
2.6.8 Measurement of adhesion 45
2.7 Particle adhesion to bulk cohesion 46
2.8 Measurement of cohesive behaviour of bulk solids 50
2.8.1 Direct shear testers 52
2.9 Choosing a tester 56
2.9.1 Uniaxial tester 57
2.9.2 FT4 rheometer 58
2.9.3 Rotating drum test 59
2.10 Summary 60
3 Characterisation of test solids 62

3.1 Introduction 62
3.2 Materials and methods 63
3.2.1 Physical characterisation of test solids 63
3.3 Flow properties measurement 66
3.3.1 Edinburgh Powder Tester 66
3.3.1.1 Effect of filling method 70
3.3.1.2 Effect of powder sample aspect ratio 72
3.4 FT4 rheometer 75
3.5 Rotating drum test 76
3.6 Results and discussions 77
3.6.1 Repeatability 77
3.6.2 Flow function from FT4 and EPT 78
3.6.3 Angle of surface and angle of stability from rotary drum test 83
3.7 Summary 87
4 Micromechanical study of cohesive granular material 89
4.1 Introduction 89
4.2 DEM modelling of uniaxial test 90
4.3 Proposed contact model 92
4.4 Modelling strategy 98
4.5 Numerical simulation set-up 100
4.6 Numerical repeatability and prediction of flowability 104
4.7 Micromechanical analyses of porosity, plasticity and cohesion 108
4.8 Interaction between adhesion parameters 115
4.9 Summary 124
5 Numerical upscaling in uniaxial test simulation 126
5.1 Introduction 126

5.2 Scaling approach 127
5.2.1 Scaling relations for cohesionless system 127
5.2.2 Scaling relations for cohesive system 129
5.3 Simulation set-up 131
5.4 Simulation results 134
5.4.1 Cohesionless system 134
5.4.2 Cohesive system 137
5.4.2.1 Constant adhesion 137
5.4.2.2 Load dependent adhesion 141
5.5 Summary 144
6 Influence of DEM input parameters and model implementation 146
6.1 Introduction 146
6.2 Experimental behaviour of cohesive powder under compression and shear 147
6.3 DEM input parameters 149
6.3.1 Particle contact loading (plastic) stiffness 149
6.3.2 Particle tangential stiffness 152
6.3.3 Inter-particle friction coefficient 155
6.4 DEM model implementation 160
6.4.1 Numerical time-step 160
6.4.2 Strain rate 162
6.4.3 Boundary friction 167
6.4.3.1 Particle to cylinder wall friction 167
6.4.3.2 Particle to platen friction 170
6.5 Summary 174
7 Example application to detergent powders 176

7.1 Introduction 176

7.2 Materials 177

7.3 Measurement of powder physical properties 177

7.4 Measurement of powder mechanical properties 180

7.5 Results and discussion 182

7.5.1 Experimental results 182

7.5.1.1 Packing 182

7.5.2 Confined compression and decompression 186

7.5.3 Unconfined compression and flow function 188

7.6 DEM simulation 191

7.6.1 Model implementation 191

7.6.2 Simulation results 194

7.7 Summary 195

8 Conclusions and recommendations for future research 198

8.1 Characterization of test solids 198

8.2 Micromechanical study of cohesive powder 199

8.3 Scaling of DEM model parameter 199

8.4 Parametric study 200

8.5 Comparison of experiments and DEM simulation for detergent powder . 201

8.6 Recommendation for future research 201

References 204

List of Figures

Figure 2.1 Number of publications related to discrete element method in past 25 years obtained from the Web of Science using following keywords:..... 9

Figure 2.2 Number (>50) of publications related to DEM in past 25 years obtained from web of science 10

Figure 2.3 Calculation cycle in DEM (after Itasca (2003)) 11

Figure 2.4 Schematic of normal force displacement response of linear spring dashpot model..... 17

Figure 2.5 Scehmatic of normal force displacement response of Hertz Mindlin contact model 20

Figure 2.6 Particle normal and tangential contact forces..... 32

Figure 2.7 Liquid bridge between two spheres of equal radius 39

Figure 2.8 Adhesion forces between stiff particle and smooth surface for different size particles (After Tomas (2004)) 42

Figure 2.9 Adhesion forces between stiff particle and smooth surface for different separation distance (After Tomas (2004))..... 42

Figure 2.10 Influence of size of asperity on van der Waals force (After Schulze, 2007) 44

Figure 2.11 Effect of asperity on liquid bridge and electrostatic force (After Schulze, 2007) 44

Figure 2.12 SEM image of 60 micron limestone powder showing asperities 45

Figure 2.13 SEM image of detergent powder showing asperities 45

Figure 2.14 Schematic illustration of normal force-separation curve obtained in Air by AFM (Jones, 2003a)..... 46

Figure 2.15 Static angle of repose..... 51

Figure 2.16 shear testers (Schwedes, 2003))..... 52

Figure 2.17 Measurement of unconfined yield strength 53

Figure 2.18 Jenike shear tester (Bell, 2001)..... 54

Figure 2.19 Peschl torsional shear tester (Bell, 2001) 55

Figure 2.20 Schluze ring shear tester (Schulze, 2007)..... 56

Figure 2.21 Stages in uniaxial test: a) Confined consolidation b) removal of load and confinement c) unconfined shearing 57

Figure 2.22 Edinburgh Powder Tester 58

Figure 2.23 FT4 Rheometer 59

Figure 3.1 SEM images of industrial solids 64

Figure 3.2 Stress strain response during confined compression- Limestone A 67

Figure 3.3 Bulk density and stress response during confined compression -Limestone A 67

Figure 3.4 Porosity and stress response during confined compression- Limestone A 68

Figure 3.5 Unconfined stress strain response at different consolidation stress- Limestone A 69

Figure 3.6 Flow function- Limestone A..... 70

Figure 3.7 Direct filling by spoon 71

Figure 3.8 Filling by passing the powder through sieve 71

Figure 3.9 Effect of fill method on compressibility- Limestone A..... 72

Figure 3.10 Schematic of pin in and pin out conditions in EPT 73

Figure 3.11 Limestone A (d_{50}=4.7 μm)..... 74

Figure 3.12 Limestone B (d_{50}=31.3 μm)..... 74

Figure 3.13 Detergent A (d_{50}=334 μm)..... 74

Figure 3.14 Detergent B (d_{50}=311 μm)..... 74

Figure 3.15 Cocoa A (d_{50}= 8.7 μm) 74

Figure 3.16 Cocoa B (d_{50}= 24.3 μm) 74

Figure 3.17 Angle of surface and angle of stability 77

Figure 3.18 Flow function obtained by FT4 80

Figure 3.19 Flow function obtained by EPT 80

Figure 3.20 Time between events using rotating drum experiments 83

Figure 3.21 Angle of stability measurements using rotating drum test 84

Figure 4.1 Normal contact force-displacement function for the nonlinear contact model 93

Figure 4.2 Normal contact force-displacement function for the linear contact model 94

Figure 4.3 Scanning electron microscopic (SEM) image of ESKAL 500 101

Figure 4.4 Paired particle of aspect ratio of 1.5 used in DEM 101

Figure 4.5 DEM simulation of uniaxial test: a) loading, b) unloading, and c) unconfined compression 103

Figure 4.6 Confined compression - axial stress (σ_a) vs axial strain (ε_a) for three random simulations and a large size simulation 105

Figure 4.7 Unconfined compression- axial stress (σ_a) vs axial strain (ε_a) for three random simulations and a large size simulation 105

Figure 4.8 Predicted unconfined axial stress (σ_a)-strain (ε_a) relationship. 107

Figure 4.9 Predicted vs. test flow function for a limestone powder. 107

Figure 4.10 (a) Linear elasto-plastic contact model with constant contact adhesion (b) Typical bulk stress strain response during confined compression 108

Figure 4.11 Effect of particle contact plasticity on flow function (f_0=-0.002 N, K_{adh}=0 kN/m) 110

Figure 4.12 Bulk plasticity ($\varepsilon_p/\varepsilon$) as a function of particle plasticity 111

Figure 4.13 Confined compression- axial stress (σ_a) vs. axial strain (ε_a) with λ_p = 0 112

Figure 4.14 Confined compression- porosity (η) vs. axial strain (ε_a) with λ_p = 0.99 113

Figure 4.15 Unconfined strength (σ_u) as a function of consolidated porosity (η_c) at different contact plasticity 114

Figure 4.16 Normalised unconfined strength ($\sigma_a d^2/f_0$, $\sigma_u d^2/f_0$) versus coordination number (Z_i, Z): f_0=-0.002N unless stated explicitly 115

Figure 4.17 - Variation of porosity (η_f) at end of filling with k_{adh} and f_0: k_1 = 1 and k_2 = 10 kN/m 117

Figure 4.18 Inter-particle force ratio vs fill porosity 118

Figure 4.19 Consolidated porosity (η_c) as a function of consolidation stress (σ_1): k_1 = 1 and k_2 = 10 kN/m 119

Figure 4.20 Predicted flow function for different k_{adh} and f_0 with k_1 = 1 and k_2 = 10 kN/m 120

Figure 4.21 Mohr circle for uniaxial tension and compression 121

Figure 4.22 Normalised unconfined compressive force ($\sigma_u d^2/f_{atp}$) as a function of coordination number (Z) and consolidated porosity (η_c) 122

Figure 4.23 Unconfined stress strain behaviour as a function of limiting friction (case I: f_0=-0.002 N, k_2=10 and K_{adh}=0.1 kN/m, case II: f_0=-0.007 N, k_2=*10 and* k_{adh} =0 kN/m) 123

Figure 5.1 Simulation set-up 132

Figure 5.2 Different cases of simulated contact model 133

Figure 5.3 Confined compression: Axial strain vs axial stress 135

Figure 5.4 Confined compression: Axial stress vs. porosity 135

Figure 5.5 Porosity variation plotted against the height 136

Figure 5.6 Evolution of coordination number 137

Figure 5.7 Confined compression: Axial stress vs strain 138

Figure 5.8 Confined compression: Porosity vs axial stress..... 139

Figure 5.9 Unconfined compression: Axial stress vs strain..... 140

Figure 5.10 Reduction in computational time with scaling 141

Figure 5.11 Confined compression: Axial stress vs strain..... 142

Figure 5.12 Confined compression: Porosity vs axial stress 143

Figure 5.13 Unconfined compression: Axial stress vs axial strain 144

Figure 6.1 Typical stress–strain behaviour during confined loading-unloading, obtained from EPT 148

Figure 6.2 Typical porosity–stress behaviour during confined loading-unloading, obtained from EPT 148

Figure 6.3 Typical stress-strain behaviour during unconfined compression to failure obtained from EPT 148

Figure 6.4 Typical flow function obtained from EPT..... 148

Figure 6.5 Effect of contact loading stiffness (k_1) on porosity stress behaviour during confined compression..... 150

Figure 6.6 Effect of loading stiffness on unconfined stress strain behaviour 151

Figure 6.7 Effect of consolidated porosity (@100kPa) on unconfined strength for varying contact loading stiffnesses 151

Figure 6.8 Effect of tangential stiffness on porosity stress behaviour 152

Figure 6.9 Effect of tangential stiffness on unconfined stress strain 153

Figure 6.10 Effect of tangential stiffness on unconfined stress strain (same porosity) 154

Figure 6.11 Effect of tangential stiffness on evolution of coordination number during unconfined compression..... 155

Figure 6.12 Effect of inter-particle friction coefficient on stress porosity relationship 156

Figure 6.13 Effect of inter-particle friction coefficient on fill and consolidated porosity 157

Figure 6.14 Effect of inter-particle friction coefficient on unconfined yield strength 158

Figure 6.15 Effect of inter-particle friction coefficient on unconfined stress strain behaviour 159

Figure 6.16 Effect of inter-particle friction coefficient on unconfined stress strain (same porosity) 160

Figure 6.17 Effect of time step on confined stress strain behaviour 161

Figure 6.18 Effect of time step on unconfined stress strain behaviour 162

Figure 6.19 Effect of strain rate on porosity stress behaviour during confined compression 163

Figure 6.20 Effect of strain rate ($1\ s^{-1}$ - $5\ s^{-1}$) on porosity stress behaviour during confined compression 164

Figure 6.21 Effect of strain rate on unconfined strength at two consolidation stresses ($k_2=10^5$ N/m, $k_{adh}=0$ N/m) 165

Figure 6.22 Effect of strain rate on unconfined strength at two levels of contact plasticity 166

Figure 6.23 Effect of strain rate on unconfined stress strain behaviour (Maximum inertial number range ($2.3*10^{-5}$-$7.1*10^{-4}$)) 167

Figure 6.24 The geometry and loading in uniaxial test with various parameters defined 168

Figure 6.25 Effect of particle to cylinder wall friction on stress porosity relationship 169

Figure 6.26 Effect of particle to cylinder wall friction on stress porosity relationship 169

Figure 6.27 Effect of particle to wall friction on unconfined strength 170

Figure 6.28 Effect of end platen friction on porosity stress relationship (frictionless cylinder walls) 171

Figure 6.29 Effect of end platen friction on porosity stress relationship (cylinder wall friction=0.5) 172

Figure 6.30 Effect of end platen friction on unconfined strength 173

Figure 6.31 Effect of lateral constraint due to end platen friction 173

Figure 7.1 Particle size distribution of the spray dried detergent powders 179

Figure 7.2 SEM photographs of different size Sample A: (a) passing through 250 µm, (b) between 250–500 µm, and (c) retained on 500 µm 180

Figure 7.3 SEM photographs of different size Sample B: (a) passing through 250 µm, (b) between 250–500 µm, and (c) retained on 500 µm 180

Figure 7.4 (a) Edinburgh Powder Tester, (b) compression, (c) unconfined sample, and (d) crushed sample 181

Figure 7.5 Confined stress strain behaviour for full size range Sample A and Sample B 187

Figure 7.6 Confined porosity-stress behaviour of full size range Sample A and Sample B 187

Figure 7.7 Confined stress-strain behaviour of different sieve cut fractions of Sample A and Sample B. 188

Figure 7.8 Confined porosity-stress behaviour of different sieve cut fractions of Sample A and Sample B. 188

Figure 7.9 Unconfined stress strain of Sample A 189

Figure 7.10 Unconfined stress-strain of Sample B 189

Figure 7.11 . Flow functions for uncut Sample B and Sample A 190

Figure 7.12 Flow functions for different size fractions of Sample B and Sample A. 190

Figure 7.13 Snapshots of uniaxial test simulations: (1) filling, (2) confined consolidation, and (3) unconfined compression..... 193

Figure 7.14 Confined stress-strain behaviour (simulation vs experiments)..... 194

Figure 7.15 Change in porosity vs stress behaviour (simulation vs experiments)... 194

Figure 7.16 Unconfined stress-strain behaviour (simulation vs experiments)..... 195

Figure 7.17 Flow function behaviour (simulation vs experiments) 195

List of Tables

Table 2.1 Summary of normal force contact models with adhesion 25

Table 2.2 Summary of tangential force models 35

Table 3.1 Physical properties of powders 65

Table 3.2 Powder flow properties produced 78

Table 3.3 Powder flow properties produced by EPT for Limestone A (μ±Sn) 78

3.4 Ranking of powders flowability using FT4 and EPTEPT 81

Table 3.5 Measurement of flow properties using rotary drum, FT4 and EPT experiments 85

Table 3.6 Measurement of flow properties using rotary drum, FT4 and EPT 85

Table 4.1 Simulation parameters..... 102

Table 5.1 DEM input parameters 133

Table 7.1 Distribution of moisture content (%) across different size fractions (n=3) 178

Table 7.2 Initial sample porosity (%) measurements for Sample A and Sample B powders 184

Table 7.3 Breakdown of bulk porosity (%) for the SDD powder sample (250–500 μm) 186

Table 7.4 Simulation parameters..... 192

Abbreviation

C_u	coefficient of uniformity, (–)	Zi	Instantaneous coordination number
D_{60}	diameter of particle at 60% passing, (m)	σ_u	unconfined yield strength (kPa)
D_{10}	diameter of particle at 10% passing, (m)	σ_a	axial stress (kPa)
d_{avg}	average particle diameter (m)	σ_t	bulk tensile strength (kPa)
e	co-efficient of restitution	σ_1	axial consolidation stress (kPa)
F_{at}	average adhesive strength at contact (N)	ρ	particle density (kg/m^3)
f_0	constant adhesive strength at first contact (N)	ρ_s	skeletal density or particle density, (kg/m^3)
f_t	contact tangential force (N)	ρ_b	bulk density, (kg/m^3)
f_{ct}	coulomb limiting tangential force (N)	ε	total bulk deformation
f_{nd}	normal damping force (N)	ε_a	bulk axial strain
f_i^c	contact force (N)	ε_p	total plastic deformation
f_{atp}	average tensile force at the peak (N)	β_n	normal dashpot co-efficient
f_{td}	tangential damping force (N)	β_t	tangential dashpot coefficient
f_{hys}	hysteretic spring force (N)	ϕ	angle of friction (°)
f_{ts}	tangential spring force (N)	$\triangle f_{ts}$	incremental tangential force (N)
$f_{ts(n-1)}$	tangential spring force at previous time step (N)	δ	total normal overlap (m)
g	gravitational constant (m/s^2)	δ_{max}	maximum normal overlap (m)
I_i	moment of inertia (m^4)	δ_p	plastic overlap (m)
k_1	loading stiffness parameter (kN/m)	η	sample bulk porosity
k_2	unloading/reloading stiffness parameter (kN/m)	η_c	consolidated bulk porosity
k_{adh}	adhesive stiffness parameter (kN/m)	η_f	fill porosity
k_t	tangential stiffness (kN/m)	η_{inter}	inter particle porosity, (–)
l_i^c	Vector from centre of particle to the contact point	η_{intra}	intra particle porosity,(–)
m^*	equivalent mass of the particles (kg)	η_p	particle porosity, (–)
N	number of particles	μ	co-efficient of friction
n	non-linear index parameter	μ_r	coefficient of rolling friction
P	Pressure (kPa)	τ_i	total applied torque (N m)
R_i	distance from the contact point to the particle centre of mass, (m)	w	moisture content, (%)

$\boldsymbol{u}$	unit normal vector	ω_i	unit angular velocity vector (radian/s)
$\boldsymbol{v}_{\mathbf{t}}$	relative tangential velocity (m/s)	Φ	angle of shearing resistance, (°)
v_{n}	magnitude of relative normal velocity (m/s)	λ_p	Contact plasticity
v_{pores}	specific volume of mercury penetrating the particle pores, (L/kg)	λ_b	Bulk plasticity
Z	coordination number at peak	$\dot{\gamma}$	shear rate

Acknowledgements

I would like to express my deepest gratitude to my supervisor, Prof. Jin Y. Ooi, for the continuous support during my PhD study and research, for his excellent supervision, patience, and immense knowledge. I could not have been imagined a better supervisor for my PhD study.

I am extremely grateful to Dr. Jin Sun for his excellent supervision, guidance, and inspiration during my early days of PhD. I am also thankful to Dr. Hossein Ahmadian for his supervision, motivation, and support during my stay at Procter and Gamble Technical Centres Ltd, Newcastle. I would like to thank Prof. Jian-Fei Chen and Dr. Luis Martin de Juan for many useful discussions. I am thankful to Dr. Zhijun Zhong for all his assistance in the laboratory set up. I would like to thank Dr. J.P. Morrissey for his many help and expertise in DEM and coding. I would also like to express my sincere thanks to Zayeed Alam for his support and encouragement.

I am also very grateful for the studentship provided by the European Community under the Marie Curie Initial Training Network for the PARDEM Project. I would like to extend my gratitude to my colleagues in PARDEM Project including Prashant, Pratap, and Reza for many useful discussions and wonderful time; it was indeed a great pleasure working with all of you.

Last but not least I would like to thank my family and friends for their unconditional support and endless love.

Dedication

I would like to dedicate this thesis to my parents and to my brother, who have supported and encouraged me to achieve success in my higher education.

Chapter 1

Introduction

1.1 *General background*

Many powders and particulate solids are stored and handled in large quantities in various industries such as pharmaceutical, food, and chemical industries: they constitute over 75% of material feedstock in industry (Nedderman, 2005). One of the common issues experienced by many of these materials is the flow difficulty arising from material cohesion. Poor flow affects storage, transfer, production, packing, compaction, fluidisation, distribution, and end use of the product in a negative manner, resulting in, for example, arching and ratholing in silo storage, segregation in blending, inaccurate dosage in filling, all of which ultimately lead to economic losses.

The flowability of cohesive solids is often measured using the flow function introduced by Jenike (1964), which describes the unconfined strength as a function of the consolidation stress. The flow function of a cohesive solid is an important material property for appropriate, efficient, and economic design of bulk handling equipment. Apart from the more traditional direct shear tests such as the Jenike circular cell (1964) and the Carr and Walker (1968) or Schulze annular ring cell Schulze (1994), indirect uniaxial shear tests are often used to evaluate the flowability for a cohesive material (Bell et al., 2007; Enstad and Ose, 2003; Freeman and Fu, 2011; Parrella et al., 2008; Röck et al., 2006; Williams et al., 1971; Zhong et al., 2005). The flow function of a cohesive solid shows the manifestation of the unconfined yield strength that arises from the historical consolidation stress and therefore the cohesive strength is stress-history dependent. Such stress-history

dependent cohesive behaviour must be captured if a numerical model is to successfully simulate the cohesive powder flow.

In recent years the Discrete Element Modelling (DEM) has been used extensively to study the complex behaviour of granular material. Whilst a lot of DEM studies have been performed on cohesionless solids, much less work exists on modelling of cohesive solids. The interaction between particles in DEM is governed by contact model. A number of contact models (Brilliantov et al., 2007; Derjaguin et al., 1975; Gilabert et al., 2007; Johnson et al., 1971; Luding, 2008; Molerus, 1975; Thornton and Ning, 1998; Tomas, 2003; Walton and Johnson, 2010) have been proposed for modelling cohesive powders. However, the common adhesion models including JKR (Johnson et al., 1971), DMT (Derjaguin et al., 1975), Maugis (1992), and Matuttis and Schinner (2001), which are elastic contact models, may not be able to capture sufficiently the stress history dependent behaviour shown in experiments of cohesive powders.

To apply the model at the single particle level requires the model parameters to be determined at the true particle-particle interaction level. This would require one to consider the enormous complexity of interfacial interaction including the influence of surface topology and chemistry and properties of the interstitial media. Whilst many studies have been reported on these measurements using microscopic measurement techniques such as Atomic Force Microscopy (AFM), nano-indentation Friction Force Microscopy (FFM), the measurements tend to be on either highly idealised particle (such as specially manufactured perfect sphere) or suffer from enormous scatter and uncertainty with regard to the accuracy of the measurement (Heim et al., 2005; Tykhoniuk et al., 2007). Additionally, it is prohibitive to model each and every individual particle and cohesion arising from several different phenomena including van der Waals, capillary bridge and electrostatic forces separately, even in a very small system of fine powders. For example, a uniaxial test simulation of a cylindrical sample of 40 mm diameter and 80 mm in height with 4.7

μm sized limestone powder containing >10^{12} particles may take in the order of 60 years if this was to be simulated with a 4 core, 64-bit computer.

1.2 *Objectives and scope of this thesis*

This study focuses on an intermediate scale between the micro- and macro-scales, aiming to produce a phenomenological contact model that can reproduce the bulk cohesive strength, stress history dependency, and other behaviour evidenced in experiments. The study aims to provide micromechanical based measure to characterise strength and flowability of cohesive materials. The study also aims to evaluate Edinburgh Powder Tester as a tool for DEM model calibration for industrial practice. The study attempts to evaluate predictive capability of the DEM contact model to simulate the behaviour of selected powder under quasi-static and slow shearing regime. Additionally the study aims to establish scaling laws that would permit a mesoscopic representation of a cohesive powder using much larger DEM particles. The additional study on scaling of DEM model parameter was motivated by increased interest relating to use of DEM at industrial scale. The study also aims to explore the effect of selected DEM model parameters on the full spectrum of cohesive behaviour from filling of a space (fill porosity) to loading under confined compression, and finally unconfined loading to failure.

The key tasks for the research are to:

1. develop and implement an appropriate contact model for cohesive solids
2. conduct material characterisation tests that will provide the material data necessary to calibrate the DEM model.
3. conduct DEM simulations and compare with experiments.
4. establish micromechanical based measure to characterise strength and flowability of cohesive materials

5. establish/evaluate appropriate scaling laws in quasi-static and slow shearing regime to enable DEM simulation at industrial scale.
6. study the influence of DEM input parameters and model implementation.

1.3 *Organization of the thesis*

The thesis is divided into eight chapters. A brief overview of each chapter is outlined below.

Chapter 1 presents the general background, objectives and scope of this study. The organization of the thesis is summarised.

Chapter 2 reviews the literature directly related to this study. Amongst other things, a brief introduction of numerical modelling in particulate solids, overview of DEM, contact models in DEM, forces causing adhesion, laboratory experiments for flow properties measurement is provided. Several issues that are important for this study and for achieving satisfactory predictions are also discussed. These include adhesive elasto plastic contact model, computational time step, particle shape, and scaling to produce scale independent response.

Chapter 3 presents evaluation of Edinburgh Powder Tester (EPT) for characterisation of flow properties of 6 industrial cohesive powders and the results are compared with commercial test methods including FT4 rheometer and Rotating drum.

Chapter 4 describes the development of a mesoscopic phenomenological discrete element method (DEM) model coupled with a calibration methodology for quantitative prediction of powder flow behaviour. The DEM predictions are compared with the experimental results and the effects of various DEM parameters on filled porosity, compressibility and unconfined strength are explored.

Chapter 5 describes the scaling of discrete element model parameters in simulation describing the loading regimes in a uniaxial test that would permit a mesoscopic representation of a cohesive powder using much larger DEM particles.

Chapter 6 investigates the influence of DEM model parameters and model implementation to study the sensitivity of particle properties on bulk behaviour in uniaxial test simulation. Amongst other things the influence of particle contact normal loading stiffness, tangential stiffness, particle contact friction coefficient, numerical time step, strain rate, and boundary condition on the whole spectrum of loading regime from filling, compression to unconfined shearing uniaxial test simulation is investigated.

Chapter 7 presents a study of packing, compression, and caking behaviour of spray dried detergent powders using experiments, and an attempt to model the full spectrum of the loading regimes from compression to shear failure using DEM.

In chapter 8, general conclusions from this thesis are drawn and recommendations are made for future research.

Chapter 2

Literature review

2.1 *Introduction*

Particulate solids constitute 75% of material in feedstock industries. Majority of the powder handled in the industries can be cohesive and they pose significant flow problems during different processes including mixing, transfer, feeding, storage, packing, and compaction. The problems involving cohesive particles are complex in nature and the success of the numerical and experimental approach will depend on accurate characterisation and modelling of its physical behaviour. While several particle level and bulk experiments are used to characterise the cohesive behaviour of powders, many issues remain for numerical modelling of cohesive powders.

The objective of this chapter is to present a literature review of the work that is directly related to the work discussed in this thesis. This review consists of an introduction two different approaches of numerical modelling: Continuum and discrete approach. An overview of Discrete Element Modelling (DEM) is provided and the issues related to numerical time step, shape of the particles, and scaling of DEM model parameters are discussed. The DEM contact model which describes the interaction between particles is reviewed. In the next section forces giving rise to bulk cohesion is presented and the link between particle adhesion and bulk cohesion is reviewed. Finally, a review on testers used to characterise cohesive and flow properties of powder is presented.

2.2 *Numerical modelling of particulate solids*

2.2.1 Continuum vs discrete approach

The large and complex nature of particulate solids has resulted in the increasing use of numerical methods to simulate bulk material behaviour. With the rapid improvement in computational resources, there has been an increase in the use of numerical methods and it is surpassing expensive physical prototypes. There are two conventional approaches to simulate complex behaviour of bulk material; Finite Element Method (FEM) and Discrete Particle Method (DPM). FEM is a continuum method and in this method bulk material is generally considered as a continuous medium. FEM uses a discretisation method to solve continuum problem. It has been useful in modelling of static bulk material applications with relatively small deformation. One example is silo and hopper design by Jenike (1964). However, problems can arise in the application of FEM to applications with relatively larger deformations because of remeshing difficulties (D'Addetta, 2004). Additionally, bulk materials are discrete in nature and strain localization phenomena including cracks and shear bands occur, and in such a case the material cannot be considered as a continuous medium. Most continuum models based on continuum damage mechanics cannot account for the discrete nature of material failure in a natural way and need some extension (Kuhl, 2000).

Due to difficulties in the FEM to simulate discrete events including strain localisation phenomena, mixing of different materials, and segregation DPM is gaining popularity in bulk materials modelling (Coetzee and Els, 2009). In DPM, solid is replaced by a discontinuous particle composite. There are several discrete particle methods available with the soft contact Discrete Element Method (DEM) developed by Cundall and Strack (1979) is being the most popular. In DEM the motion of each particle can be tracked continuously over a range of length and time scales providing comprehensive information on bulk material behaviour. Unlike FEM, DEM allows the modelling of dynamic, quasi-static and static zones within a bulk material system and phenomena like strain localisation, segregation, and mixing

can be successfully studied. Another numerical approach to model bulk material is combined DEM/FEM method. In the combined DEM/FEM (Munjiza et al., 1995), each particle is described as a deformable continuous body as in FEM while the particle movement and interactions are considered as in DEM.

Both DEM and DEM/FEM require high computational power as opposed to pure continuum methods. Yet, with increasing computational power and ongoing progress in computational speed-up (Mio et al., 2009) DEM, developed by Cundall and Strack (1979), has increasingly been used to model many problems involving discrete phenomena including powder packing (Yen and Chaki, 1992), compaction (Sheng et al., 2004), powder flow (Moreno-atanasio et al., 2005), rotating drum (Walton and Johnson, 2010), mixing (Chaudhuri et al., 2006), hopper flow (Ketterhagen et al., 2009), fluidized bed (Xu, 1997), pneumatic conveying (Sakai and Koshizuka, 2009) and so on. A detailed report on the application of DEM can be found in the paper by Zhu et al. (2008). The DEM simulations of the aforementioned phenomena have given many significant insights into the microscopic details at particle level and useful information to understand complex behaviour exhibited by granular material. In the following section brief description of DEM is presented.

2.2.2 Discrete element method (DEM)

The discrete element method (DEM) was first developed by Cundall and Strack, (1979) as a tool for analysing quasi-static problems related to densely packed granular materials. In recent years, DEM has become increasingly popular. A survey of the literature related to DEM shows the increasing popularity of DEM over past 25 years, as shown in Figure 2.1.

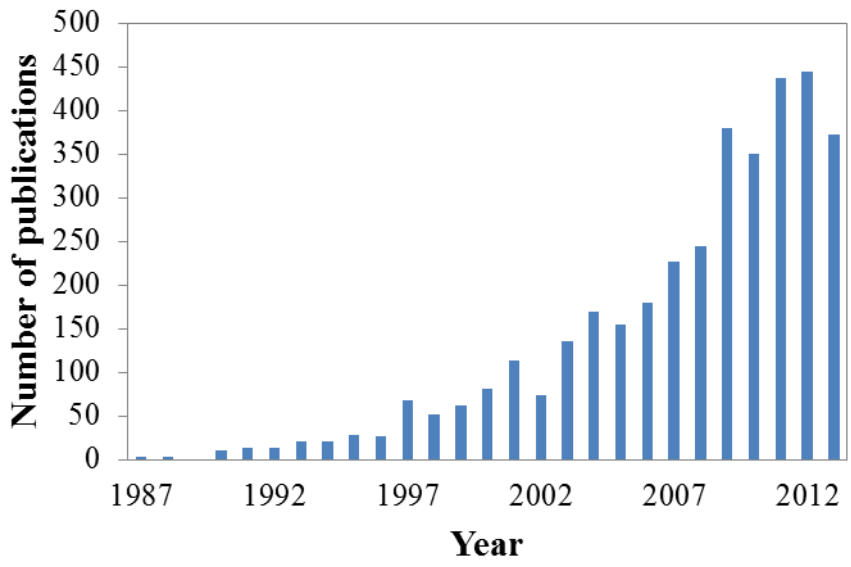

Figure 2.1 Number of publications related to discrete element method in past 25 years obtained from the Web of Science using following keywords:
(discrete element method/model, distinct element method/model, discrete particle method/model, discrete particle simulation, granular dynamics simulation)

Although DEM was first developed in the field of rock mechanics, it has increasingly been used in several other research areas. As shown in Figure 2.2, DEM has been used in areas involving bulk granular material including engineering, material science, physics, geology, mineralogy, and agriculture and more.

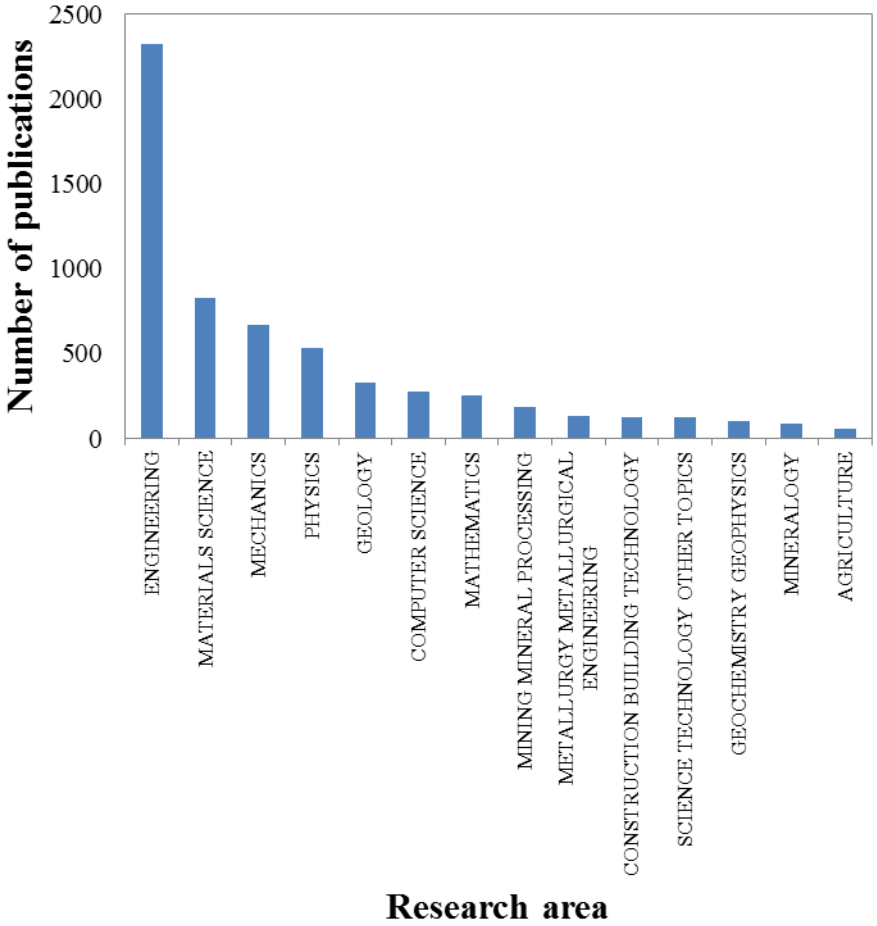

Figure 2.2 Number (>50) of publications related to DEM in past 25 years obtained from web of science

Numerical calculation in the discrete element method employs two main equations in calculation cycle: 1- Newton's equations of translational and rotational motion for each particle, and 2- the forces and torques which are calculated based on contact constitutive laws. Figure 2.3 shows a simplified calculation cycle in DEM. The particles are modelled as rigid bodies interacting at soft contacts. An overlap is allowed at particle contact, however, this overlap is not real but it allows modelling the deformation at the particle contact in an indirect way. The numerical time step should be chosen such that any disturbance during a single time step only affects the immediate neighbouring particles to ensure stability of the whole system.

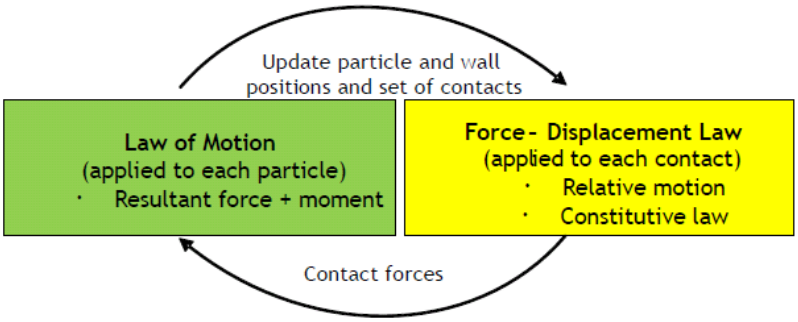

Figure 2.3 Calculation cycle in DEM (after Itasca (2003))

In this thesis the DEM work was performed using commercial software EDEM by DEM Solutions Ltd. (2010).

2.3 *An overview of DEM*

2.3.1 Formulation

Particle-Particle interactions are modelled using the soft contact approach where rigid particles are allowed to overlap each other at the contact point with very small overlaps, typically less than 1% of the particle diameter at each time step. The contact force is calculated according to the contact model as a function of the overlap.

The changes in positions and velocities of the particles due to the contact and gravitational forces are calculated from the integration of Newton's motion equations. For particle *i* the translational motion equation is

$$m_i \frac{d^2}{dt^2} \boldsymbol{x}_i = \boldsymbol{f}_i + m_i \boldsymbol{g} \tag{2.1}$$

where m_i is the mass of the particle, t is time, $\boldsymbol{x_i}$ is its position, $\boldsymbol{f_i}$ is the summation of all forces acting on the particle ($\boldsymbol{f_i} = \sum_c \boldsymbol{f_i^c}$), and $\boldsymbol{g}$ is acceleration due to gravity. The rotational motion equation for particle i is given by equation **(2.2)**:

$$I_i \frac{d}{dt}\boldsymbol{\omega_i} = \boldsymbol{T}_i \tag{2.2}$$

where I_i is the moment of inertia for particle i, $\boldsymbol{\omega_i}$ is its angular velocity and $\boldsymbol{T_i}$ is the total torque acting on it, which is defined by equation **(2.3)**, where $\boldsymbol{l_i^c}$ is the vector from the centre of particle i to the contact point and $\boldsymbol{f_i^c}$ is the contact force.

$$\boldsymbol{T_i} = \sum_{i=1}^{Nc} \boldsymbol{l_i^c} \times \boldsymbol{f_i^c} \tag{2.3}$$

2.3.1 Determination of computational time step

The time-step in DEM simulation is time increment between two consecutive iterations. A sufficiently small integration time step is required to ensure the stability of simulation by having a sufficient number of time steps within each collision. In a granular system assembly, force transmission between individual particles is through the Rayleigh wave that travels around the surface of elastic bodies. The DEM time step should be chosen such that the time step for calculating particle information should be less than the time required for a Rayleigh wave to transverse the minimum size particle in the assembly. The Rayleigh wave velocity *(V_r)* for the force transmission is given by equation **(2.4)**

$$V_r = \chi . \sqrt{\frac{G}{\rho_s}} \tag{2.4}$$

where G is the shear modulus, ρ_s is the solid density of particle, and χ is a parameter related to poisson's ratio *(υ)* (Thornton and Randall, 1988) by equation **(2.5)**

$$\chi = 0.1631\upsilon + 0.8766 \tag{2.5}$$

If the particles in the granular assemblies have same properties, the critical time step *(T_c)* can be given by equation **(2.6)**

$$Tc = \frac{\pi . r_{\min} \sqrt{\frac{\rho_s}{G}}}{01631\upsilon + 0.8766} \quad \textbf{(2.6)}$$

where r_{min} =minimum size of particle in the granular assembly.

Particle Flow Code (PFC) by Itasca (2003) presented a simple method to calculate critical time step using equation **(2.7):**

$$T_c = \sqrt{m / k_{\max}} \quad \textbf{(2.7)}$$

where m is mass of particle and k_{max} is maximum contact stiffness in the granular assembly. In DEM simulations the actual time step is normally chosen by multiplying the critical time step by a factor of safety. A study by O'Sullivan and Bray (2004) has shown that the critical time step is a function of packing configuration and number of contacts per particle. They suggest that a critical time step of less than $0.221\sqrt{m/k}_{\max}$ should be chosen for an assembly of particle for three dimensional cases if rotation is allowed. According to Itasca (2003), a time step of 80% of critical time-step should be chosen for general simulations, and 25% for rapidly changing simulation for Hertz-Mindlin contact model. EDEM (DEM Solutions, 2010) suggests a time step of 20% of Rayleigh time step (given by equation (2.6) for densely packed assembly and 40% for loose system.

2.3.2 Particle shape

The great majority of DEM studies in the literature were conducted using either 2D disks or 3D spheres. Spherical particles are preferred because they facilitate the contact detection and calculation of inter-particle forces, however, spherical particles are more prone to rolling within a granular assembly than non-spherical particles due to lack of interlocking. Real particles are rarely spherical and it has been shown that particle shape significantly affects powder packing, compressibility, and flow (Deng and Davé, 2013; Johanson, 2009; Kaerger et al., 2004; Wu and Cocks, 2006; Zou and

Yu, 1996). In general, the more aspherical the particle, the more difficult it is to pack, compress, and flow. A number of numerical and experimental studies (Aoki and Suzuki, 1971; Chong et al., 1979; Li et al., 2004; Roberts and Beddow, 1968) have also shown that particle shape affects the flowability of the powder. Recent DEM studies (Chung and Ooi, 2008; Härtl and Ooi, 2008; Zhou and Ooi, 2009) have shown that particle interlocking arising from geometric interaction contributes significantly to the bulk granular friction, so it is important to introduce a degree of non-sphericity in particle shape to capture the behaviour of real solids which are very rarely spherical.

Rolling friction is often used in order to simulate the effect of particle shape. Wensrich and Katterfeld (2012) used an approach of incorporating the effect of particle shape through the inclusion of rolling friction for spherical particles. They ran a series of simulations of angle of repose tests with paired particles and idealized spherical particles with rolling friction. They found some similarity; however, there was a significant discrepancy quantitatively. The reason for this discrepancy was attributed to the fact that particle shape may also resist rotation as well as causing rotation. However, rolling friction always opposes the rolling. Another issue with simulating shape of particles using rolling friction is the effect of particle shape on co-ordination number (CN). The coordination number can be defined as the average number of inter-particle contacts in the assemblies of particles. Different assemblies with different shape of particles can have significantly different CN at the same porosity. Additionally in densely packed system, the dilation related to interlocking cannot be simulated using spherical particles with rolling friction. It has been reported that spherical particles cannot represent the “real” solids regardless of the angle of inter-particle friction (Cleary, 2010). The spherical particles fails to capture interlocking related dilation, voidage distribution, and material shear strength arising from interlocking (Cleary, 2010). Therefore, it is important to introduce an appropriate degree of non-sphericity in particle shape to capture the behaviour of real solids which are very rarely spherical.

There have been several methods for representing non-spherical particles including single particle approach and clustered-particle approach (Höhner et al., 2011). In single particle approach, the particle is a single particle of complicated geometry including ellipsoid (Ng and Lin, 1997; Ting et al., 1995), polyhedron (Cundall, 1988), superquadratic (Cleary and Sawley, 2002). Ellipsoidal particles have smaller tendency to rotate and provide a smooth surface, however, ellipsoidal and other shaped particle are computationally intensive. The detailed description about different shape descriptors can be found in work by (Hogue, 1998; Latham and Munjiza, 2004). In the clustered-particle approach, any shape of surface can be fitted by overlapping spheres (Favier and Fard, 1999). The overlapping spheres do not interact with each other. In this method, contact detection and force calculation is spherical particles based and computationally efficient. However, the smooth surface of real particles may not be represented by limited number of overlapping spheres. Markauskas et al., (2009) found that the clustered-sphere approach is adequate to model real smooth and rough elliptical particles. Because of its simplicity this method is becoming popular and has been used by several researchers (for example say, Chung and Ooi, 2006; Härtl and Ooi, 2008; Kodam et al., 2009; Kruggel-Emden et al., 2008; Thakur et al., 2013) after it was purposed by Favier and Fard, (1999), Jensen et al.(1999), and Vu-Quoc et al.(2000). The clustered-sphere method is implemented in two major commercial DEM packages: PFC 3D by Itasca and in EDEM by DEM solutions.

2.3.3 Scaling

One of the issues with DEM modelling of fine particles for practical applications is the challenge of modelling very small particles due to the lack of computational power. Even the smallest industrial processes involve interaction of trillions of particles, and it becomes impractical and computationally impossible to account for every individual real particle.

There can be several possible solutions (Mio et al., 2009) for the speed-up of DEM simulation, such as optimization of the hardware and the software, including improving DEM algorithm, parallel computing, and simplifying the calculation process. Common ways to simplify the calculation process include using a lower spring stiffness, using mono-sized particles, using a cut-off distance for long range forces (Mio et al., 2009). Another possibility can be the use of higher particle density in quasi-static simulation (Sheng et al., 2004) known as density scaling. Poschel et al. (2001) proposed a general approach to scale down the experiments to laboratory size. They found that the dynamics of the granular system changed if all sizes were scaled by a constant factor, but leaving the material properties the same. They suggested scaling material properties including elastic constant, dissipative constant and time when geometric size is scaled. By keeping geometric similarity by scaling all lengths by a scaling factor would require the same number of particles with smaller size in the system and ultimately may lead to no reduction in computational time. This was also highlighted by Feng et al.(2007). Such an approach is more suitable for problems in geo-mechanics where the original physical problem is scaled down to a laboratory model to get the same results. Another possible solution is to use larger size elements (particles) to reduce the number of particles whilst keeping the original system size the same, however, this would violate geometric similarity and may introduce some error in the bulk response Feng et al.(2007). The major issue in this kind of approach is to adjust DEM model parameters such that DEM simulation result exhibits the same dynamic and static properties as the experimental granular material.

2.4 *Contact force model*

The total forces between particles can arise both from non-adhesive forces (e.g. body forces or gravitational force) and adhesive forces. The adhesive forces may originate from a number of sources including liquid bridge force, van der Waals force,

electrostatic force, magnetic force, solid bridge force and other forces. These forces are described in detail in section 2.6.

The force interaction between particles in DEM is modelled using contact models. A number of contact models have been used to model elastic, elastic-adhesive, perfectly plastic, elasto-plastic, elasto-plastic-adhesive behaviour of particles. Following is the brief review of the contact models used in DEM.

2.4.1 Non adhesive elastic contact models

2.4.1.1 Linear spring contact model

The linear spring contact model proposed by Cundall and Strack (1979) is probably the most used contact model in DEM. In this contact model, a parallel linear spring-dashpot models the interaction in normal direction and a parallel linear spring-dashpot in series with a slider models the interaction in tangential direction. The spring accounts for the elastic contribution to the response while the dashpot accounts for the energy dissipation. The total force (F) is sum of the forces in normal (f_n) and tangential (f_t) direction.

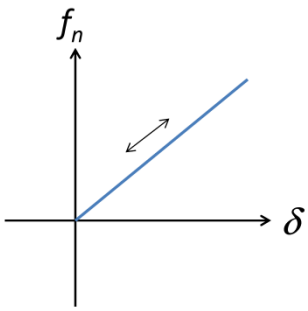

Figure 2.4 Schematic of normal force displacement response of linear spring dashpot model

The total contact normal force, f_n, is the sum of the spring force, f_{ns}, and the normal damping force, f_{nd}:

$$f_n = (f_{ns} + f_{nd})\boldsymbol{u} \tag{2.8}$$

where, $\boldsymbol{u}$ is the unit normal vector pointing from the contact point to the particle centre. The force-overlap relationship for normal contact, $f_{ns,}$ is mathematically expressed by:

$$f_{ns} = k_n \delta_n \tag{2.9}$$

The normal contact stiffness (k_n) is given by following relationship (Maw et al., 1976):

$$k_n = \frac{16}{15} R^{*\frac{1}{2}} E^* \left(\frac{15 m^* V^2}{16 E^* R^{*\frac{1}{2}}} \right)^{\frac{1}{5}} \tag{2.10}$$

where R* is the equivalent radius, E* is the equivalent Young's modulus, m^* is the equivalent mass,and V is a typical impact velocity.

$$\frac{1}{R^*} = \frac{1}{R_i} + \frac{1}{R_j} \tag{2.11}$$

$$\frac{1}{E^*} = \frac{(1-\upsilon_i)^2}{E_i} + \frac{(1-\upsilon_j)^2}{E_j} \tag{2.12}$$

$$\frac{1}{m^*} = \frac{1}{m_i} + \frac{1}{m_j} \tag{2.13}$$

The normal damping force, $f_{nd,}$ is given by:

$$f_{nd} = \beta_n v_{relative,n} \tag{2.14}$$

where $v_{relative,n}$ is the magnitude of the relative normal velocity, and β_n is the normal dashpot coefficient described below.

Similarly, the contact tangential force, $\boldsymbol{f_t}$, is given by the sum of tangential spring force, $\boldsymbol{f_{ts}}$, and tangential damping force, $\boldsymbol{f_{td}}$., as given by:

$$\boldsymbol{f}_t = (\boldsymbol{f}_{ts} + \boldsymbol{f}_{td}) \tag{2.15}$$

The tangential spring force is expressed in incremental terms:

$$\boldsymbol{f}_{ts} = \boldsymbol{f}_{ts(n-1)} + \boldsymbol{\Delta f}_{ts} \tag{2.16}$$

where $\boldsymbol{f_{ts(n-1)}}$is the tangential spring force at the previous time step, and $\boldsymbol{\Delta f_{ts}}$ is the increment of the tangential force and is given by:

$$\boldsymbol{\Delta f}_{ts} = k_t \boldsymbol{\delta}_t \tag{2.17}$$

where k_t is the tangential stiffness, and δ_t is the increment of the tangential displacement. The relationship between k_t and k_n is given by Mindlin (1949)

$$k_t = k_n \frac{2(1-\upsilon)}{(2-\upsilon)} \tag{2.18}$$

The tangential damping force is product of tangential dashpot coefficient, β_t, and the relative tangential velocity, $\boldsymbol{v_{relativ,t}}$, as given by:

$$f_{td} = \beta_t \boldsymbol{v}_{relative,t} \tag{2.19}$$

The limiting tangential friction force is calculated using the Coulombic friction criterion:

$$f_{ct} \leq \mu . f_{ns} \tag{2.20}$$

The relationship between damping coefficient and coefficient of restitution e is expressed as:

$$\beta_{n,t} = \sqrt{\frac{4m^* k_{n,t}}{1+\left(\frac{\pi}{\ln e}\right)^2}} \tag{2.21}$$

where $\beta_{n,t}$ is damping coefficient in normal and tangential direction, and the coefficient of restitution e defined in the simulation as an input parameter.

2.4.1.2 Hertz-Mindlin contact model

The Hertz-Mindlin contact model is a nonlinear elastic contact model as shown schematically in Figure 2.5. The contact model is used in this study to model interaction between particle and wall.

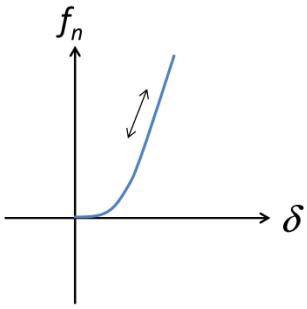

Figure 2.5 Schematic of normal force displacement response of Hertz Mindlin contact model

In this contact model, the normal force is based on the Hertz contact theory (Hertz, 1881) and gives a nonlinear elastic relationship between normal contact force and normal displacement. The total contact normal force, f_n, is the sum of the spring force, f_{ns}, and the normal damping force, f_{nd}:

$$f_n = (f_{ns} + f_{nd})\boldsymbol{u} \tag{2.22}$$

where, $\boldsymbol{u}$ is the unit normal vector pointing from the contact point to the particle centre. The force-overlap relationship for normal contact, $f_{ns,}$ is mathematically expressed by:

$$f_{ns} = \frac{4}{3} E^* \sqrt{R^*} \delta_n^{3/2} \tag{2.23}$$

The normal damping force can be expressed as:

$$f_{nd} = 2\sqrt{\frac{5}{6}} \beta_d \sqrt{m^* . k_n}\, v_{relative,n} \tag{2.24}$$

where $v_{relative,n}$ is the relative normal velocity, and β_d is a damping constant given below, k_n is the normal contact stiffness and given by:

$$k_n = 2E^* \sqrt{R^* \delta_n} \tag{2.25}$$

The contact tangential force, $\boldsymbol{f_t}$, is given by the sum of tangential spring force, $\boldsymbol{f_{ts}}$, and tangential damping force, $\boldsymbol{f_{td}}$., as given by:

$$\boldsymbol{f_t} = (\boldsymbol{f_{ts}} + \boldsymbol{f_{td}}). \tag{2.26}$$

The tangential spring force is expressed in incremental terms:

$$\boldsymbol{f_{ts}} = \boldsymbol{f_{ts(n-1)}} + \boldsymbol{\Delta f_{ts}}, \tag{2.27}$$

where $\boldsymbol{f_{ts(n-1)}}$is the tangential spring force at the previous time step, and $\boldsymbol{\Delta f_{ts}}$ is the increment of the tangential force and is given by:

$$\boldsymbol{\Delta f_{ts}} = -k_t \boldsymbol{\delta_t}, \tag{2.28}$$

where k_t is the tangential stiffness, and $\boldsymbol{\delta_t}$ is the increment of the tangential displacement.

$$k_t = 8G^* \sqrt{R^* \delta_n} \tag{2.29}$$

The damping force is given by following relationship:

$$f_{td} = 2\sqrt{\frac{5}{6}} \beta_d \sqrt{m^* . k_t}\ v_{relative,t} \tag{2.30}$$

The coefficient of restitution, e is related to the damping constant by:

$$\beta_d = \frac{\ln(e\ )}{\sqrt{\ln^2(e) + \pi^2}} \tag{2.31}$$

The limiting tangential friction force is calculated using the Coulombic friction criterion:

$$f_{ct} \leq \mu . f_{ns} \tag{2.32}$$

The equations given in this section are only provided for completeness and are based on the Manual of the commercial software EDEM, and work of Chung (2006).

2.5 *Modelling of adhesion*

2.5.1 Normal force contact models

The production of cohesive powders in industries is rapidly increasing and the powders often cause various bulk handling problems. The problems involving cohesive particles are complex in nature and the success of the numerical and theoretical analyses will depend on correctness of the contact model. In this section a review of contact models which include the effect of adhesion is presented. A more comprehensive study on the details of contact models can be found in Tomas (2004).

2.5.1.1 Elastic model with adhesion

Johnson et al. (1971) extended the Hertzian contact model and included the effect of attractive forces (adhesion) between two attractive bodies. The theory calculates the increase in contact area resulting from mutual attraction between the attracting bodies. According to the JKR theory, the adhesive force is related to surface-energy interactions (van der Waals interactions) between two spheres in contact and is proportional to surface energy and the radius of curvature at the contact (see Table 2.1). The theory assumes that the two particles in contact only feel an attractive force across the contact region while the surface areas outside the actual contact area are force free. Another elastic contact model that considers long range attractive forces was proposed by DMT (Derjaguin et al., 1975). Tabor (1977) showed that JKR and DMT theories are the extreme limits of a single theory and can be related to Tabor parameter. The JKR theory applies to large and soft surfaces whereas the DMT theory applies to small and stiff surfaces. Maugis (1992) showed that it is not physically consistent to have tensile stresses in the area of contact and no adhesion forces outside as in JKR model and vice versa no tensile stresses in the area of contact and adhesion forces outside as in DMT model. To avoid this inconsistency, Maugis proposed a Maugis-Dugdale model, which allows an analytical solution to be

solved. Maugis' (1992) contact model is probably the most accurate approach for elastic solids and can be applied to any materials with low and high adhesion. Maugis (1992) showed that the transition from JKR to DMT models can be related to Maugis parameter (equivalent to Tabor parameter) and JKR and DMT models are extreme cases of Maugis-Dugdale (1992) contact model. Another elastic contact model was porposed by Matuttis and Schinner (2001). In the contact model, a linear relationship between cohesive force and the contact length is assumed. The cohesion force is simply added to the Hertz-Mindlin contact model. The commercial code EDEM(DEM Solutions, 2010) has implemented this contact model.

None of the elastic contact models discussed above account for increasing adhesion because of elastic flattening of contact. Dahneke (1972) found that elastic flattening of contact contributes significantly to adhesive force and proposed a model that can account for increasing van der Walls force with increasing elastic flattening of contact. However Molerus (1975) argued that Dahneke's assumption of purely elastic contact cannot be applied to cohesive powders consolidated by external forces. If the external load applied on cohesive powder is removed, the elastic repulsion should return the system to its original state prior the application of load, and the magnitude of cohesive force would not depend on previously applied load. This is in sharp contrast with experimental results on cohesive powders.

2.5.1.2 Perfectly plastic and elastic-plastic model with adhesion

Molerus (1975) was first to purpose a purely plastic contact model that can capture plastic deformation dependent cohesive strength. To account for both elastic and plastic behaviour of a cohesive material Schubert et al. (1976) proposed a linearly elastic-purely plastic model. In this contact model, the initial loading response is non-linear elastic until the yield point is reached and linear plastic after the yield.

2.5.1.3 Elasto plastic model with load dependent adhesion

Walton and Braun (1986) were probably the first to introduce an elasto-plastic bilinear spring model, based on an approximation of finite element analysis (FEA) results, to account for the plasticity at the contact for cohesionless solids. The first contact model with elasto-plastic deformation and adhesion was introduced by Thornton and Ning (1998). For cohesive solids, the plastic deformation in the contact region causes a larger effective radius of the deformed contact region upon unloading, resulting in a larger pull-off force. They modelled such behaviour using a modified JKR curve with a larger contact radius.

A more elaborate and detailed contact model accounting for load, time and rate dependent visco-elastic, plastic, visco-plastic, adhesion and dissipative behaviour was proposed by Tomas (2001). In the contact model initial loading response is Hertzian which switches to linear elasto-plastic loading after yielding. Contact unloading is elastic and follows Hertzian contact. The contact model also takes account of hysteretic behaviour during the unloading/reloading cycle. A linear adhesion limit accounts for increasing adhesion with increasing plastic deformation. However this model is computationally intensive. By ignoring the initial non-linear portion before yielding on the basis that fine particles show a negligible range of Hertz-like behaviour (Tomas, 2000), Tykhoniuk et al., (2007) showed that simpler piece-wise linear models such as the ones proposed in (Luding et al., 2003) produced similar results at a smaller computational cost. Luding (2008) further improved the piece-wise linear model by recognizing the loading history dependent nature of the unloading/reloading stiffness by making the unloading/reloading stiffness a function of the previously experienced maximum overlap. This has introduced an element of nonlinearity in unloading/reloading path. Walton and Johnson (2009) also proposed a contact model similar to Tomas and Luding’s model but separated the rate of increase of the pull-off force from the slope of the tensile force-displacement unloading curve, which requires an additional parameter in comparison to Luding’s model to describe the adhesive behaviour.

While JKR and DMT contact models are widely accepted contact models for an elastic sphere with adhesion, a number of elastic contact models including JKR (Johnson et al., 1971), DMT ((Derjaguin et al., 1975), Maugis (1992), and Matuttis and Schinner (2001) may not be able to capture the stress history dependent behaviour shown in experiments of cohesive powders (Bell et al., 2007; Enstad and Ose, 2003; Freeman and Fu, 2011; Parrella et al., 2008; Röck et al., 2006; Williams et al., 1971). Since the contact area between two fine particles is very small, even moderate forces (in the order of 1 nN) can cause plastic deformation at the contact (Tomas, 2007) which can give rise to a stress history dependent behaviour. Therefore, it is proposed that contact plasticity has an important role in correctly simulating the stress history dependency. While the elasto plastic contact models proposed by Thornton and Ning (1998) and Tomas (2001) are the most realistic, they have complicated formulations and can be computationally intensive to implement. Table 2.1 presents a summary of adhesive contact models with their important characteristic and corresponding mathematical normal force-displacement relationship.

Table 2.1 Summary of normal force contact models with adhesion

Authors/ Year	Characteristics	Force displacement equation	Schematic of the contact model
JKR (1971)	Elastic-nonlinear, constant adhesion force, does not consider long range van der Waals, suitable for large and soft spheres	$f_{adh} = -3\pi\gamma R^*$ where, γ=surface energy R*=Equivalent radius of particle	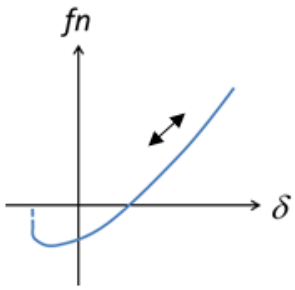
DMT (1975)	Elastic-nonliear, constant adhesion force, considers long range van der Waals, suitable for small and stiff spheres	$f_{adh} = -4\pi\gamma R^*$	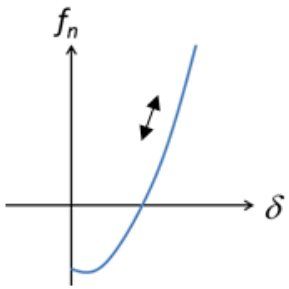

Maugis (1991)	Elastic-nonlinear, constant adhesion force, can be applied to any materials with low or high adhesion force	$f_{adh} = -2\sigma_o m^2 a^2 \left[\cos^{-1}\left(\frac{1}{m}\right) + \frac{1}{m^2}\sqrt{m^2 - 1} \right]$ $m = \frac{c}{a}$; where c= adhesive contact area, a=real contact area, σ_0=maximum force predicted by Lennard Jone's Potential	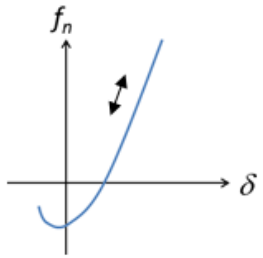
Matuttis and Schinner (2001)	Elastic-linear, adhesion force proportional to the contact area.	$f_{adh} = -kA$ where k= adhesive energy A= contact area	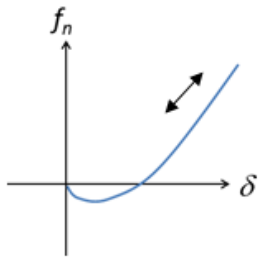
Gilabert (2007)	Linear elastic, approximation for long range van der Waals, constant adhesion force	$f_{adh} = -f_0\left(1 - \frac{\delta}{s}\right)$ for $0 \le \delta \le s$ $f_{adh} = -f_0$ for $\delta > 0$ where s= separation distance,	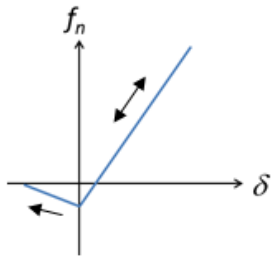

		δ=normal overlap	
Molerus (1975)	Perfectly plastic, adhesion force proportional to plastic deformation	$f_{adh} = f_0 + \frac{p_{vdw}}{p_f} F_n$ where f_0= adhesive force without any deformation, p_{vdw}= attractive van der Walls pressure given by, p_f=plastic micro yield strength of contact, F_n=normal force, $p_{vdw} = \frac{H}{6\pi a_0^3}$ H=Hamaker's constant, a_0=separation distance	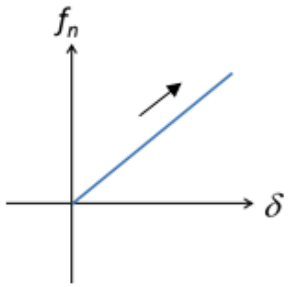
Schubert (1976)	Nonlinear elastic-purely plastic, adhesion force proportional to plastic deformation	$f_{adh} = f_0 + \frac{p_{vdw}}{p_f\left(1+\frac{2A_e}{3A_p}\right)} F_n$ where, A_e=*elastic contact area* A_p= *plastic contact area*	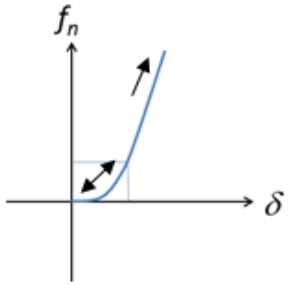

Thornton and Ning (1998)	Hertzian elastic, linear plastic, accounts for plastic flattening of contact	$fn = 4/3E^* \sqrt{R^* \delta_y^{\,3}} + \pi p_f R^* (\delta - \delta_y)$ $-\,Loading$ $fn = 4/3E^* \sqrt{R^* (\delta - \delta_p)^3} - Unloading$ where δ_y =yield overlap, δ_p=Permanent plastic deformation	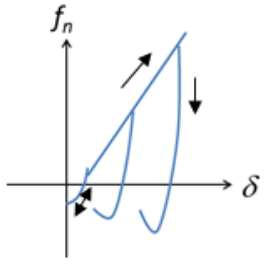
Tomas (2001)	Hertzian elastic, linear plastic, nonlinear elastic unloading, load, time and rate dependent viscoelastic, plastic, viscoplastic, adhesion	$fn = 4/3E^* \sqrt{R^* \delta^{\,3}} - elastic\,loading$ $fn = \pi R^* p_f (k_A - k_p)\delta + f_0 - elasto - plastic\,loading$ $fn = 4/3E^* \sqrt{R^* (\delta - \delta_p)^3} - \pi R^* k_p p_f \delta_p + f_0$ $-\,unloading$ $fn = -4/3E^* \sqrt{R^* (\delta_t - \delta)^3} + \pi R^* p_f (k_A - k_p)\delta_t + f_0$ $-\,reloading$ $fn = -\pi R^* p_{vdw} \delta + f_0 - adhesion\,limit$ where k_a=elastic-plastic contact area coefficient k_p=plastic repulsion coefficient, δ_t=total overlap	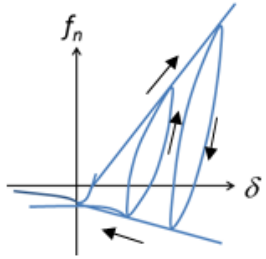

Luding (2003)	Linear elastic, linear plastic, load independent unloading stiffness, load dependent adhesion,	$f_n = \begin{cases} f_0 + k_1\delta & \text{if } k_2(\delta - \delta_p) \geq k_1\delta \\ f_0 + k_2(\delta - \delta_p) & \text{if } k_1\delta > k_2(\delta - \delta_p) > -k_{adh}\delta \\ f_0 - k_{adh}\delta & \text{if } -k_{adh}\delta \geq k_2(\delta - \delta_p) \end{cases}$	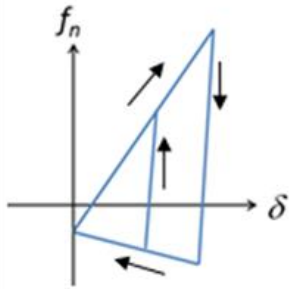
Luding (2008)	Linear elastic, linear plastic, load dependent unloading stiffness, load dependent adhesion, does not account for permanent plastic deformation	$fn = \begin{cases} f_0 + k_1\delta & \text{if } k_2(\delta - \delta_p) \geq k_1\delta \\ f_0 + k_2(\delta - \delta_p) & \text{if } k_1\delta > k_2(\delta - \delta_p) > -k_{adh}\delta \\ f_0 - k_{adh}\delta & \text{if } -k_{adh}\delta \geq k_2(\delta - \delta_p) \end{cases}$ $k_2(\delta_{max}) = \begin{cases} \hat{k}_2 & \text{if } \delta_{max} \geq \delta^*_{max} \\ k_1 + (\hat{k}_2 - k_1)\frac{\delta_{max}}{\delta^*_{max}} & \text{if } \delta_{max} < \delta^*_{max} \end{cases}$	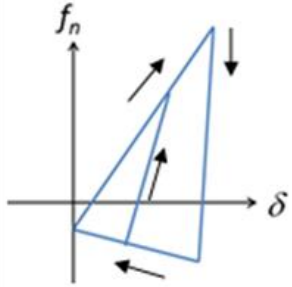
Walton and Braun (2009)	Linear elastic, linear plastic, load dependent adhesion, accounts for permanent plastic deformation, separated the rate of increase of adhesion force from tensile force-displacement	$f_{adh} = -C_n 3(or\,4)\pi\gamma R^*$ where C_n (less than 1) is a factor to account for the effects of asperity	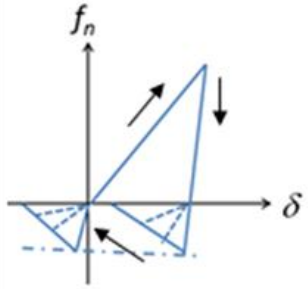

2.5.2 Limiting tangential force

The literature is rather vague about limiting tangential force models. One of the questions to be addressed in the area of tribology is whether the relationship between limiting friction and normal force is linear. A number of microscopic inter-particle friction experiments have reported the relationship between limiting friction and normal force (Berman et al., 1998; Briscoe and Kremnitzer, 1979; Ecke, 2001; Jones et al., 2004; Ruths et al., 2003; Schwarz et al., 1997; Skinner and Gane, 1972). Both nonlinear (Hertzian and JKR) and linear (Coulombic) relationships were found between the frictional and normal forces. Briscoe and Kremnitzer (1979) found a non-linear relationship at tensile loads and a linear relationship at compressive loads. They assumed a single asperity contact. In contrast, Ruths et al. (2003) found a linear dependence in a study conducted on boundary friction of two different atomic silane monolayer with low adhesion in a single asperity contact with surface forces apparatus (SFA) and frictional force microscopy (FFM). Schwarz et al. (1997) conducted a study using frictional force spectroscopy on nano-size carbon compounds with a single asperity and found that the frictional force was proportional to the 2/3 power of load similar to the theoretical model based on a Hertzian-type tip–sample contact. Friction force experiments by Jones et al. (2004) found non-linear relationship between the normal and friction forces for ballotini indicating single asperity contacts and a linear relationship for materials including alumina, limestone powder, zeolite and titania supporting multi-asperity contact.

2.5.2.1 Tangential force contact models

Surface friction between the particles contributes to tangential force. For elastic and cohesionless particles, the tangential force-displacement relationship is provided by Hooke's law. Hooke's law provides a linear elastic tangential force-displacement relation as shown in Table 2.2. Mindlin and Deresiewicz (1953) (MD) proposed a more complex tangential force model for elastic frictional contact with unload and reload hysteresis. Di Renzo and Di Maio (2005) stated that MD paper is remarkably complex and argued that contact model can be computationally intensive for the

simulation of systems with large numbers of particles. To overcome this difficulty, Cundall and Strack (1979), Walton and Braun (1986) (WB), Tsuji et al.(1992), Di Renzo and Di Maio, (2005) all proposed simplified tangential force models.

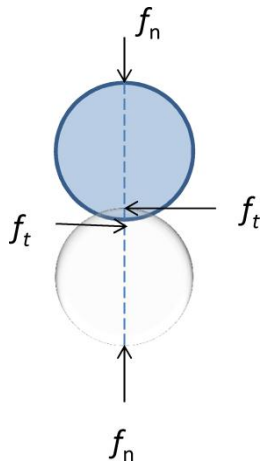

Figure 2.6 Particle normal and tangential contact forces

Cundall and Strack (1979) proposed a linear model with constant stiffness parameters. Walton and Braun (1986) suggested an incremental tangential model different for loading and unloading cases. In this contact model the tangential stiffness is not a constant and is dependent on normal force. A linear tangential spring with a stiffness coupled non-linearly to the normal displacement without adjusting any parameters was proposed by Tsuji et al.(1992). A modification of the Tsuji et al.(1992) model was proposed by Di Renzo and Di Maio (2005). Di Renzo and Di Maio (2005) found that the tangential force calculated from the MD model is a fraction (2/3) of the expected value from the Tsuji model (for high and low impact angles) and suggested scaling the tangential force by 2/3. The contact model proposed by Cundall and Strack (1979) is simple, easy to implement and computationally efficient, and it has found wide application in several areas including silo flow (Yang and Hsiau, 2001), spout-fluid bed (Zhong et al., 2006), mixing in rotary kilns (Finnie et al., 2005), and in vibrated fluidized bed (Tatemoto et al., 2005).

Although the normal force model proposed by WB was elaso-plastic, the tangential force model does not account for plastic deformation. A more realistic tangential force model accounting for both elastic-plastic deformations and interfacial friction between spherical particles was later proposed by (Vu-Quoc et al., 2001; Zhang and Vu-Quoc, 2007). This improved model is based on finite element analysis of frictional elasto-plastic spheres. None of the contact models discussed above consider the effect of adhesion on frictional resistance.

For cohesive particles, it can be expected that attractive forces would contribute to the friction limit. This was confirmed by Skinner and Gane (1972), when they conducted micro-friction experiments between soft metal stylus and a hard smooth surface of graphite or diamond in a scanning electron microscope and found that the attractive force can be considered as an additive term to the normal force in the calculation of limiting friction. The contribution of the adhesion force to the friction limit was considered by Derjaguin et al. (1975), (Luding, 2008; Savkoor and Briggs, 1977; Thornton and Yin, 1991; Tomas, 2001). Derjaguin et al. (1975) were the first to consider the contribution of constant adhesion to the friction limit calculation. Savkoor and Briggs (1977) extended JKR theory to account for the influence of adhesion on the tangential force calculation. They argued that when the tangential force reaches the critical peeling force, the contact would peel and contact area would diminish abruptly to the Hertzian area before sliding occurs. However, Thornton and Yin (1991) assumed a smooth transition from peeling to sliding, and after peeling the contact model was proposed to follow Mindlin and Deresiewicz (1953). They showed a good agreement between the results from their model and the experimental results from Briscoe and Kremnitzer (1979). Tomas (2001) proposed a model by supplementing Mindlin's (1949) no slip solution and considered the effect of elasto plastic flattening in the limiting friction calculation. In his model, the increase of adhesion due to flattening of contacts contributes to the friction limit. (Luding, 2008) used a tangential force model similar to linear spring model (Cundall and Strack, 1979), but the friction limit for the tangential force was adapted from

Tomas (2001). Table 2.2 presents summary of different tangential contact models with key characteristics.

Table 2.2 Summary of tangential force models

Authors/Year	**Characteristics**	**Schematic of the contact model**
Hooke's	Elastic, linear	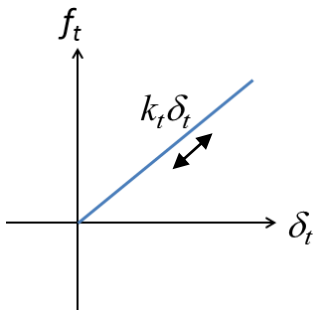
Mindlin (1949)	Elastic, nonlinear, Coulombic friction limit	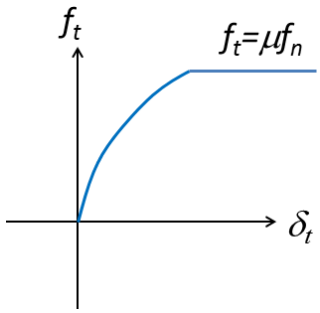
Mindlin and Deresiewicz (1953)	Elastic-nonlinear, hysteretic loading and unloading	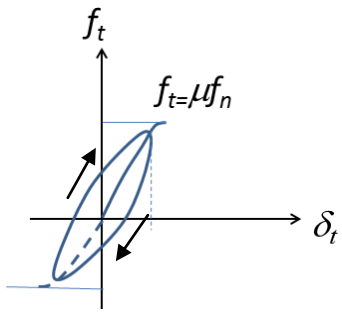
Walton and Braun (1986)	Elastic-nonlinear, hysteretic loading and unloading	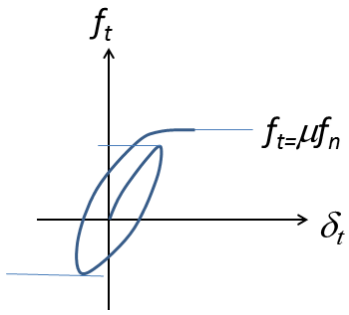

Thornton and Yin, (1991)	Elastic-nonlinear, hysteretic loading and unloading	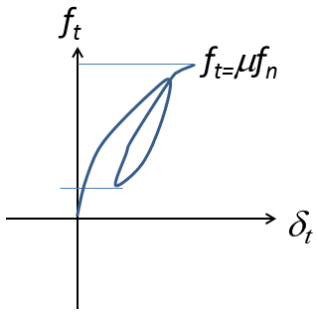
Derjaguin et al. (1975)	Elastic linear, friction limit includes effect of constant adhesion	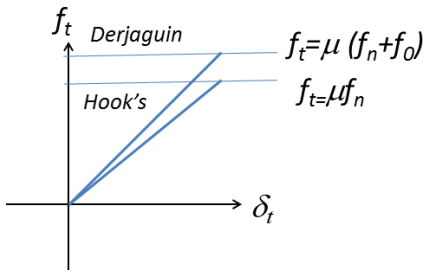
Tomas (2001)	Elastic linear, friction limit includes effect of constant and load dependent adhesion	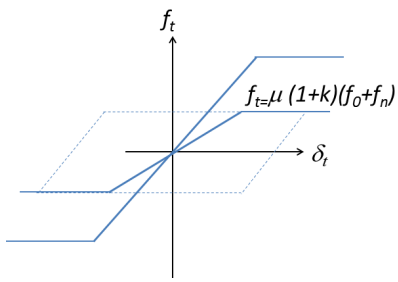
Luding (2008)	Elastic linear, friction limit includes effect of constant and load dependent adhesion	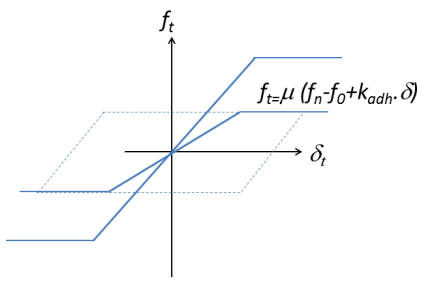

2.6 *Attractive forces causing adhesion*

At atomic level, adhesion is generally referred to attractive forces between unlike particles whereas cohesion is termed as attractive forces between like particles. However in this thesis, adhesion refers to inter-particle attractive forces at particle level whereas cohesion refers to bulk level. The bulk cohesion of powders depends on the adhesive forces between individual particles. Adhesive forces are caused by many different mechanisms. The mechanisms giving rise to adhesion is described in the following section.

2.6.1 van der Waals force

van der Waals forces include all intermolecular forces that act between electrically neutral molecules. There are three different types of van der Waals forces; Keesom, Debye, and London dispersion forces. The Keesom attraction force occurs between rotating permanent dipoles. The Debye interaction is an outcome of permanent dipoles introducing temporary dipoles in opposing molecules. Finally, the London dispersion force is an induced dipole interaction created by fluctuations of electrostatic charges. Among these forces the dispersion force is the most important contributor to van der Waals force, because it acts between all molecules or atoms, on a distance that ranges from more than 10 nm down to 2A.. Hamaker (1937) provided the interaction force between a sphere and a semi-infinite body due to London van der Waals interactions at macroscopic level. He attributed London van der Waals force as the major force causing adhesion between molecules of any substance and ignored the attractive forces arising from Keesom and Debye's interactions. According to Hamaker, van der Waals force can be calculated from equations (2.33).

$$f_0 = \frac{AR}{12s^2} \qquad \textbf{(2.33)}$$

where *A*=Hamaker's constant and s=separation between the particles. Based on a macroscopic approach proposed by Hamaker, A can be expressed as :

$$A = \pi^2 C_f \rho_a^{\ 2} \tag{2.34}$$

where C_f is a constant and ρ_a is number of atoms per unit volume of contacting bodies and is a material property. The van der Waals forces in a medium can either be positive or negative, depending on the numerical value of the Hamaker constant. A list of Hamaker's constant for inorganic solids in different media can be found in work by Bergstrm (1997).

JKR (Johnson et al., 1971) and DMT (Derjaguin et al., 1975) models also provide an expression for van der Waals force calculation based on surface energy (γ) concept.

$$f_{0\,DMT} = -2\pi\gamma R \tag{2.35}$$

$$f_{0\,JKR} = -\frac{3}{2}\pi\gamma R \tag{2.36}$$

While the JKR model is more applicable to soft and large spheres, DMT model is more suitable for small and stiff spheres. The van der Waals forces are a major source of adhesion in submicron size dry powders.

2.6.2 Liquid bridge force

When a quantity of low viscosity liquid is introduced between two particles, a stable bridge is formed in the contact zone of particles which produces a resultant attractive force between two particles. The attraction force arises from capillary pressure and from the surface tension of the liquid acting between the particles. The liquid bridge force between spheres of equal radius arising from surface tension of the liquid and difference in capillary force can be given as (Seville et al., 1997):

$$F_{ls} = 2\pi r\gamma + \Delta p r^2 \tag{2.37}$$

Where Δp = difference in pressure between atmosphere and liquid bridge, r = size of liquid bridge as shown in Figure 2.7. The presence of liquid within a particulate solid

can affect tensile strength, flow properties and agglomeration behaviour (Schubert, 1984). For detailed treatment of capillary forces and their influence on the behaviour of particulate solids, see review paper by Schubert (1984) on this subject.

.

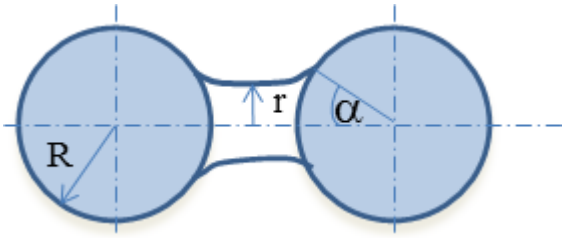

Figure 2.7 Liquid bridge between two spheres of equal radius

2.6.3 Electrostatic forces

Electrostatic forces can arise from the formation of potential difference between particles or triboelectric charging. In the case of tribolectric charging force, (F_{tel}) between point charge (Q) and its image charge (Q') can be given by classic Coulomb's law.

$$F_{tel} = \frac{-QQ'}{4\pi\varepsilon_0 l^2} \qquad \textbf{(2.38)}$$

where ε_0 is permittivity of free space, and l is distance between the charge and its image. When electrostatic adhesion is due to potential difference, ΔU between particles of different work function, the force of attraction is given by:

$$F_{vel} = \pi\varepsilon_0 \frac{R(\Delta U)^2}{l} \qquad \textbf{(2.39)}$$

Triboelectric charging is a process in which certain materials become electrically charged when they come into contact with another material through friction. Triboelectric charge transfer is the most common source of charge building up in powder handling (Matsusaka et al., 2010). Electrostatic forces are different in conductors and non-conductors (insulators).

2.6.4 Magnetic forces

Attraction force may also arise when the particles can be magnetized. Magnetic force can be given by:

$$F_m = \frac{p^2}{6\pi\mu_0 l^2} \tag{2.40}$$

where p=degree of magnetization, and μ_0=permeability of vacuum. Attraction force arising from magnetization may contribute to adhesion in very specific cases such as magnetite (Dry et al., 1988).

2.6.5 Solid bridge forces

The solid bridges between particles can arise from several mechanisms. Rumpf (1958) was the first to propose several mechanisms (crystallisation, sintering, partial melting, liquid binder solidification, and chemical reaction) of solid bridge formation and has since been studied and extended by many others.

- **Crystallisation-** When crystalline water-soluble powders are exposed to high humidity (>65%) they will partially dissolve. If the water is evaporated out of the liquid, stable solid bridges are formed. Solid bridges can be formed if the crystalline powders stored in a closed container are exposed to high humidity and temperature fluctuations. Solid bridge formation due to crystallization is a common phenomenon in bulk solids including fertilizers (Bröckel et al., 2007; Thompson, 1972), food powders, and many other chemicals.
- **Sintering-** Sintering is caused by diffusion of molecules or atoms of the material at the contact points. Sintering usually takes place at a very high temperature (70-90% of the melting temperature of the powder metal-Kalpakjian and Schmid, 2010). The sintering mechanism is used in the production of powder metals and ceramics.
- **Partial melting-** Partial melting is caused by local friction between particles giving rise to pressure induced phase change or a temperature which

ultimately leads to melting and solidification and formation of bridges. Ice crystals and snow is product of partial melting.

- **Liquid binder solidification/chemical reaction-** Solid bridges are formed as an outcome of chemical reaction between two different materials eg. the reaction between mortar and bricks. The binder liquid solidifies and does not evaporate as in the case of recrystallisation. An example is solidification of asphalt.
- **Glass transition-** Glass transition temperature can be defined as the temperature at which an amorphous substance changes from the glassy to rubbery stage. The glass transition temperature in solids can be reached either by increasing temperature or by increasing amount of water content or both. Water acts as a plasticizer in amorphous solids and decreases the glass transition temperature. Above the glass transition, the viscosity decreases and at sufficiently low viscosity material starts sticking at the contact. The glass transition is one of the sources of cohesion and cakiness in many food powders including coffee, milk, sugar, and beverage powders and has been studied extensively (Fitzpatrick et al., 2007; Foster et al., 2006; Okasanen, C.A. and Zografi, 1990; Palzer, 2005).

2.6.6 Other forces

Adhesion may also arise from mechanical interlocking. For example interlocking of chain branches as in proteins, interlocking of contacts by overlaps of surface roughness, and interlocking of hook-like bonds (Tomas, 2004).

2.6.7 Comparison between adhesive forces

Disregarding the solid bridge forces, the effect of particle size on adhesive forces is shown in Figure 2.8 (for ideal conditions). At small separation distances, the force due to liquid bridge is the largest, followed by van der Waals force. For a dry system, van der Waals force dominates for particle size smaller than 100 μm. In a

wet system, van der Waals force drops significantly due to reduction in the Hamaker constant in water.

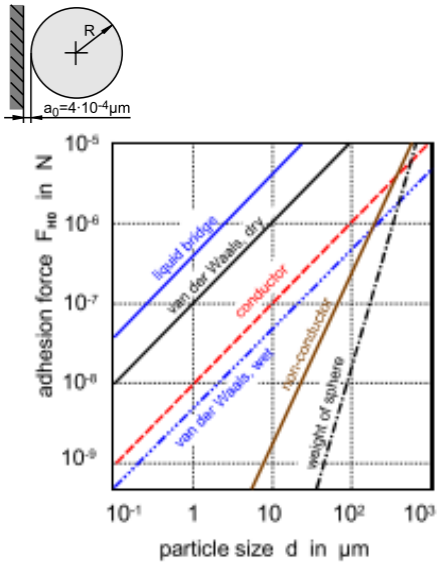

Figure 2.8 Adhesion forces between stiff particle and smooth surface for different size particles (After Tomas (2004))

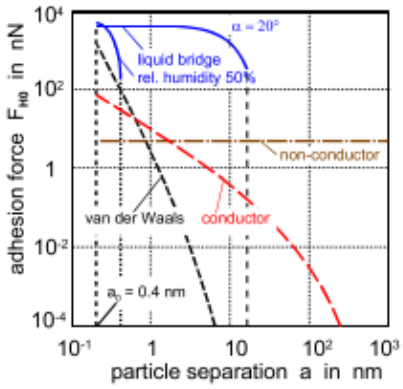

Figure 2.9 Adhesion forces between stiff particle and smooth surface for different separation distance (After Tomas (2004))

The electrostatic forces are smaller. The weight force becomes dominant after a certain particle size (~100 µm). This is the reason fine particles (<100um) stick to each other and form a very loose porosity, however coarse particles roll and slide due to the larger gravitational force and achieve a denser porosity.

It can be observed from sections 2.6.1-2.6.3 that van der Waals, electrostatic (conductor), and liquid bridge forces are dependent on the distance between interacting bodies. Figure 2.9 (Tomas, 2004) shows the effect of separation distance on inter particle adhesion force. The adhesive forces between particle and wall are calculated as a function of separation distance. It can be seen that van der Waals forces are very large at small distances but decreases with increasing distance. This shows that the van der Waals force has large influence on particles in contact. The electrostatic force due to insulator (non-conductor) is constant; however the force due to insulator has long range nature as van der Waals force. The liquid bridge force

is hardly influenced by separation distance until the separation occurs rupturing the bond. The above mechanism shows that when the particles are in contact with each other, bulk cohesion is governed mostly by liquid bridge and van der Waals force, where liquid bridge will only be formed in presence of low viscosity liquid. Thus, for fine and dry bulk solids, van der Waals forces are dominant. Electrostatic forces can be neglected in many applications, because their effect is small compared to other inter-particle forces at small distances.

The van der Waals interaction between perfectly spherical and smooth spheres is well understood, however, real powders are neither smooth nor perfectly spherical. Even so called “perfect” micro-spheres with sphericity of 0.99 were observed to have many asperities (Massimilla and Donsi, 1976). In the case of particles with asperities, the contact between the particles occurs through asperities. It is generally assumed that the size of the asperities dominates the adhesive force between powders. In calculating the van der Waals forces for an asperity to plane contact, when the radius of the particle in equation (2.33) is replaced by radius of asperity the van der Waals force drops significantly (Seville et al., 1997). When the surface of the particle is rough, the van der Waals force should include the attractions between primary particles, and between particle and asperity. For a spherical particle with a hemispherical asperity of constant size and plane contact, Forsyth and Rhodes (2000) showed that the van der Walls force due to asperity only always underestimates the force and the van der Walls force due to asperity and particle always overestimates the force. They suggested that the particular situation being considered should determine which of these is a more desirable error. For example, if one wanted to make sure that powder stored in a hopper will flow freely when the hopper is opened, it is much better to overestimate the force considering the worst case scenario.

The effect of size of asperity on van der Waals force has been investigated for particle and plane contact (Schulze, 2007) where the asperity was simulated by a hemisphere of radius r. As shown in the Figure 2.10, the distance between the wall

and tip of the roughness was kept constant, however, the distance between the wall and the spherical particle increases with the hemisphere radius, r. The van der Walls force decreases with an increase in the radius of the hemisphere, as long as radius is sufficiently small. However, for the larger values of the hemisphere radius, the calculated van der Walls force increases with r. In the former case the adhesive force between the hemisphere and the wall becomes dominant relative to the adhesive force between the spherical particle and the wall.

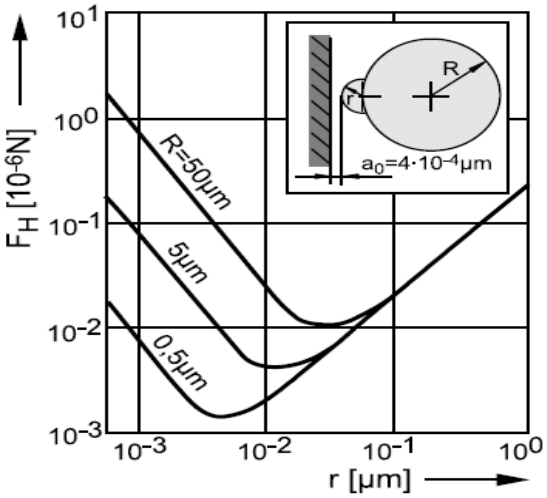

Figure 2.10 Influence of size of asperity on van der Waals force (After Schulze, 2007)

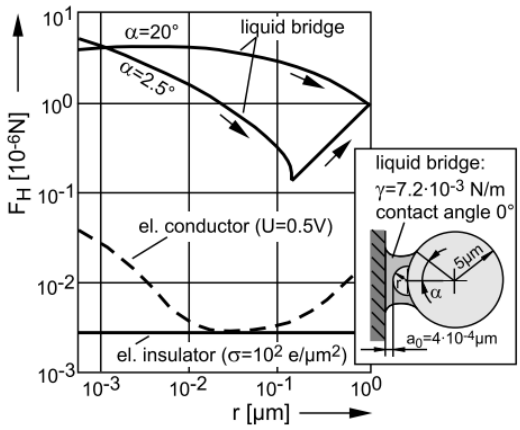

Figure 2.11 Effect of asperity on liquid bridge and electrostatic force (After Schulze, 2007)

Figure 2.11 shows the influence of particle asperity on liquid bridge force for two different liquid bridge angles. The particle asperity also affects the liquid bridge force, but the effect is rather small. The electrostatic force due to insulator is independent of size of asperity; however, the force due to conductor first decreases with increasing asperity and then increase with increasing asperity in similar fashion to van der Waals force.

For particles of the order of ten microns, produced by attrition, the typical size (diameter) of the asperities in the order of 0.2 µm is reported (Beach et al., 2002;

Massimilla and Donsi, 1976). The effect of attrition on the surface roughness of the particle is also demonstrated by limestone powder produced by attrition as shown in Figure 2.12. The surface irregularities can be also seen in detergent powders manufactured by a spray drying process (Figure 2.13).

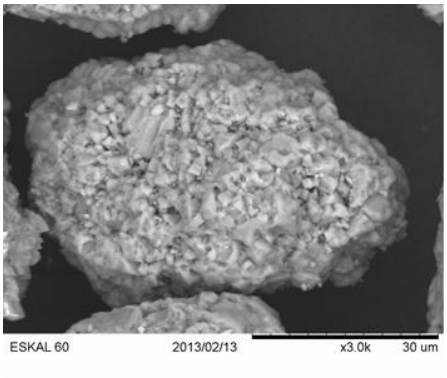

Figure 2.12 SEM image of 60 micron limestone powder showing asperities

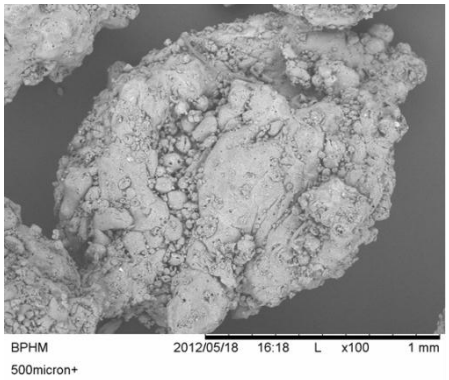

Figure 2.13 SEM image of detergent powder showing asperities

2.6.8 Measurement of adhesion

Inter-particle adhesive force can be measured using highly sophisticated techniques such as Atomic Force Microscopy (AFM) (Ando, 2000; Barrow and Williams, 2009; Butt et al., 2005; Carpick and Salmeron, 1997; Jones, 2003a; Jones et al., 2004). Figure 2.14 shows typical force-separation curve obtained using AFM. An AFM can measure the pull-off (adhesive) force required to separate two particles (agglomerates). Additionally it can provide information on force displacement relationship that can be used for contact modelling. Whilst many studies have been reported on these measurements using microscopic measurement techniques such as AFM, Nano-indentation the measurements tend to be on either highly idealised particle (such as specially manufactured perfect sphere) or suffer from enormous scatter and uncertainty with regard to the accuracy of the measurement (Heim et al., 2005; Tykhoniuk et al., 2007).

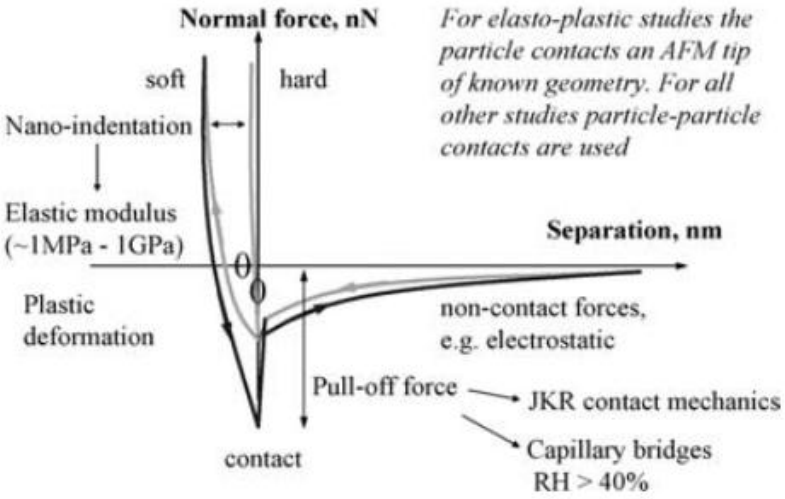

Figure 2.14 Schematic illustration of normal force-separation curve obtained in Air by AFM (Jones, 2003a)

Particle adhesion can also be measured indirectly by measuring bulk cohesion. The relationship between particle adhesion and bulk cohesion is reviewed in the following section.

2.7 *Particle adhesion to bulk cohesion*

Rumpf (1958) and (Kendall, 1988) proposed the two most widely accepted models which relate particle adhesion to bulk cohesion. Rumpf (1958) was first to propose a relationship between microscopic adhesion (inter-particle bond strength) and macroscopic tensile strength and made the following assumptions:

- Particles are hard, spherical and of equal size.
- Particles are randomly packed, and the packing structure is isotropic.
- The contact areas between particles are small compared to the surface area of the particles, such that the contact areas can be assumed to be contact points.
- The distribution of stress is homogenous and isotropic.

- Agglomerate fails by simultaneous rupture of all the bonds along a fracture plane.

Based on the above assumptions Rumpf derived the following relationship between the tensile strength (σ_t), and the inter-particle bond strength (f):

$$\sigma_t = \frac{f\ (1-\eta)Z}{\pi\, d^2} \tag{2.41}$$

where d is particle diameter, Z is coordination number and η is porosity.

Helle et al.(1985) reached at the same relationship using principals of virtual work.

The Rumpf equation was derived for isotropic and homogeneous stress, the effect of anisotropic distribution of contacts was studied by Emeriault and Chang (1997). Following the work from Emeriault and Chang, Quintanilla et al. (2001) derived a relationship for anisotropic contact angular distribution resulting from a uniaxial compression of the powder. The relationship between inter-particle contact force and applied stress is given as:

$$\sigma_t = \frac{f(1-\eta)Z}{\pi\, d^2}\left(1+\frac{2}{\sqrt{5}}\zeta\right) \tag{2.42}$$

ζ is a multiplicative factor taking into account anisotropy of the contact angular distribution. Radjai et al.(1998) estimated ζ~0.1 for a 2D system indicating 10% decrease in contact force. This correction is expected not to be much higher for a 3D system (Quintanilla et al., 2001). The effect of polydispersity has also been studied. Employing the principle of virtual work, Tsoungui et al. (1998) derived the mean normal force f on a contact as a function of applied stress σ_t for 3D poly-disperse system as:

$$\sigma_t = \frac{f(1-\eta)Z}{\pi\, d^2 \beta} \tag{2.43}$$

Where β is a parameter which is function of the variation of the density of the packing with the mean volume, the maximum value of β =1.5 for a bimodal distribution in a 3D system for a small particle fraction close to 0.2. It shows weak

dependence on particle size ratio. When β=1 for a mono-disperse packing, the equation gets back to the Rumpf equation.

Quintanilla et al. (2001) ignored polydispersity, and anistropic effect, and calculated average contact compressive normal force and average tensile normal force from bulk stresses based on Rumpf equation and found a good correlation between the estimated values of the adhesion force from bulk stresses and those measured from AFM. The result showed that average adhesion force is correlated to the estimated contact forces from macroscopic measurements. The adhesion force was found to increase with load force in both theoretical and experimental results. Both sets of data were in the same order of magnitude, and estimated force from the bulk stresses was about one-half of the average value measured from AFM. The reason for discrepancy between experimental and calculated result was explained by the application of consolidation stress to the granular system causing stress chaining; only a fraction of contacts carries most of the applied external load while the rest of contacts do not feel any load. Therefore, averaging the external bulk stress over all contacts, like in the Rumpf equation may lead to an underestimation of adhesion force at contact for a given load force.

Castellanos (2005) emphasized the drawback of the Rumpf equation is that it does not consider the force chain in the powder. While the existence of force chains in coarse granular materials is well established, the existence of force chains in fine, soft, highly compressible, and plastically deforming powders are not clear. For simplicity, and to establish a semi-quantitative relationship, Castellanos (2005) assumed a Gaussian distribution of contact force (based on (Erikson et al., 2002)) and argued that it is meaningful to define average force per contact.

Rumpf also assumed that an agglomerate fails by simultaneous rupture of all the bonds along a fracture plane. This assumption is contested by Kendall (1988) who

argued that simultaneous failures do not usually occur in practise and that the real failure mode is by cracking due to contacting particles in the agglomerate separating sequentially. The agglomerate would fail at a much lower stress than the stress needed to cause simultaneous failure because of imperfections and the Rumpf equation would overestimate strength of the agglomerate. Kendall proposed a new theory based on fracture mechanics analysis of smooth adhesive elastic spheres:

$$\sigma_t = 15.6(1-\eta)^4 \gamma^{1/6} \gamma_c^{\ 5/6} (dc)^{-1/2} \qquad \textbf{(2.44)}$$

where γ is surface energy (required to separate unit area of plane), γ_c is the fracture energy, c is the length of pre-existing crack. Equation (2.44 can also be rearranged as (Bika et al., 2001):

$$\sigma_t = 3.7(1-\eta)^4 \frac{f}{d\sqrt{dc}} \qquad \textbf{(2.45)}$$

While comparing equations (2.43) and (2.45), it can be seen that Kendall's equation shows strong dependence on porosity and a weaker dependence on the particle diameter than Rumpf's equation. Experimental data reported in literature displays consistency with either or both models (Moreno-Atanasio and Ghadiri, 2006). Ghadiri et al. (2007) proposed that Kendall's model can be suitable for brittle to semi-brittle solids, however Rumpf's model can be more suitable to describe failure of a ductile (plastically deformable) material. However, there is no detailed analysis available on dependency of the applicability of Rumpf and Kendall's model in literature. Additionally Subero (2001) evaluated models of Rumpf and Kendall's theories for dependency of agglomerate strength on porosity and showed that within the range of practical porosities, the model of Rumpf and the model of Kendall produced close values of agglomerate strength.

For modelling real material, it is extremely difficult to quantify bulk cohesion arising from different sources. For many systems measuring bulk cohesion can provide satisfactory results. In this study bulk measurement is a driver for model

development. Different method of measuring bulk cohesion is reviewed in the following section.

2.8 *Measurement of cohesive behaviour of bulk solids*

The cohesive behaviour of bulk solids is greatly affected by different sources of adhesion as explained in previous section. The cohesivity of the bulk solids affect the materials ability to flow (knows as flowability). There can be a number of ways to evaluate flowability of bulk solids. Here the testers used in industrial and academic practise are briefly described. For a detailed review on the testers please refer to the papers (Bell, 2001; Levy, 2001; Schulze, 2007; Schwedes, 2003; Stanley-wood, 2008).

Several empirical methods have been used to evaluate powder flowability; timed funnel flow, Hausner ratio, Carr's index and angle of repose. In the timed funnel flow test, the time taken for the powder to discharge through a funnel is measured. The larger time relates to a greater cohesive strength. There are a number of factors that may affect the flow time; for example particle size, shape, size distribution, density, particle to particle friction, particle to wall friction, and permeability of the powder (Bell, 2001). Many powder technologists object to the timed flow test method since the interaction among these parameters is unknown and the test method does not consider solid stress due to self-weight of the material. However it can be a good indicator of flow behaviour that resembles a test, i.e., flow from small bins (Bell, 2001).

The angle of repose method is often used to describe the flowability. Angle of repose is defined as the maximum angle at which a pile of unconsolidated material can remain stable. There are two different kind of angle of repose test: static and dynamic angle of repose. Static angle of repose can be measured by many different methods

and the angle depends on the method used. The most common way of measuring static angle of repose is to form a conical pile by gentle pouring. The static angle of repose test can be highly influenced by the test conditions, for example height of fall during pouring. The dynamic angle of repose is the angle at which a powder surface can remain stable in a drum rotating at certain speed. The rotating drum test is discussed in detail in the section 2.9.3.

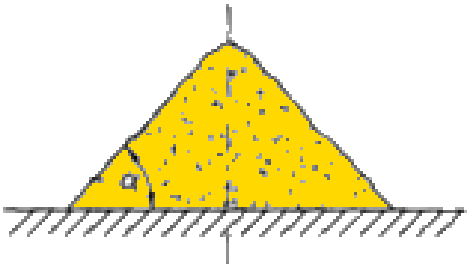

Figure 2.15 Static angle of repose

The Hausner ratio is the ratio of tapped bulk density to the loose bulk density and it relates to gain in cohesive strength after the compaction of granular material. Material with little gain in bulk density is considered to be non-cohesive (Hausner ratio less than 1.25), while an increasing value indicates increase in cohesion. The test measures a form of compressibility (on vibration) which does not always correlate with cohesive strength. Another limitation of the Hausner ratio is that it does not consider the bulk density of the material. For example, materials with the same Hausner ratio but different bulk densities will flow differently. Additionally, the value of the force required to achieve the tapped density is not known. Finally, the Hausner ratio does not link the cohesive strength to the application of the external stress. Another similar flowability measurement parameter is Carr's index. Carr's index is the ratio of increase in bulk density due to tapping. Carr's index of 5-15 indicates excellent, 12-16 good, 18-21 fair and > 23 poor flow. While both the Hausner ratio and Carr's index can give a quick and rough measure of powder cohesion in certain circumstances, these measures are criticized in academia for not having a strong theoretical basis.

Flowability can also be measured by using shear testers which are backed by well-established physical theory. Shear testers can be distinguished between direct and indirect shear testers. In direct shear testers, the material is forced to fail along a predefined failure zone whereas with indirect shear testers, the material fails along the weakest plane. The direction of principal stress rotates during the test in a direct shear tester, however, the direction of principal stress remains same during the test for indirect shear testers. Figure 2.16 shows the different kind of shear testers used. Some of the most used shear testers including Jenike, Peschl, and Schluze shear tests are described briefly in the next section.

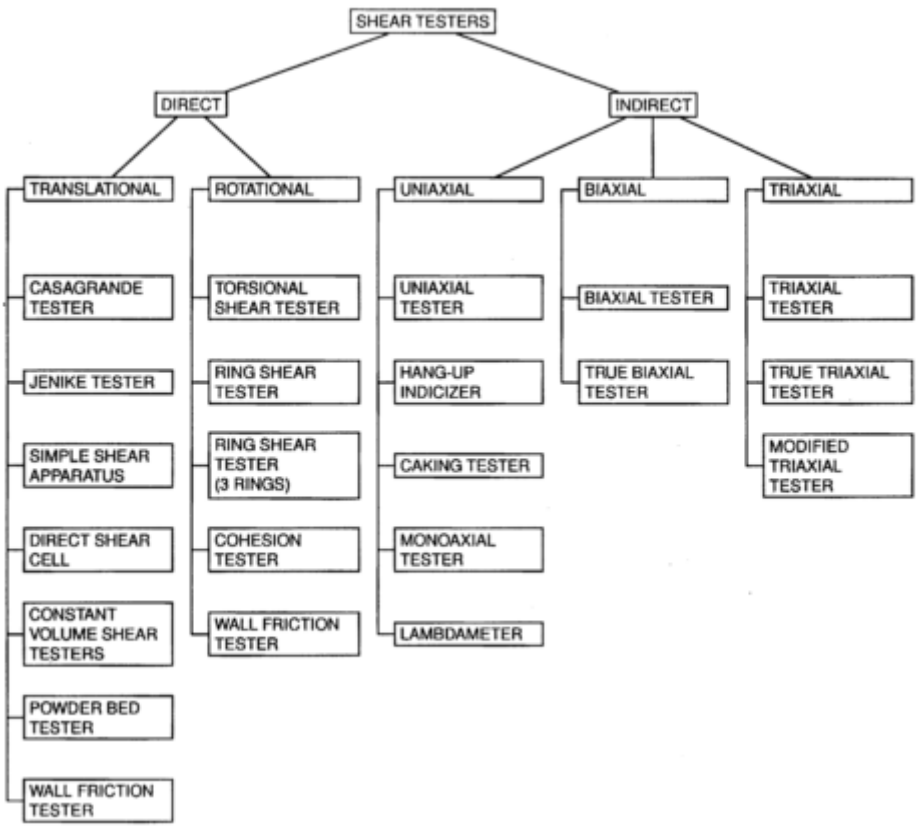

Figure 2.16 Shear testers (Schwedes, 2003)

2.8.1 Direct shear testers

Direct shear testers can measure flow properties of powders including internal and effective friction angle, wall friction angle, yield loci, and flow function. Flow

function is one of the major flow properties. Flow function is not measured directly, but extrapolated from direct shear tests data by construction of Mohr circles (Figure 2.17). The test involves pre-shearing of the sample first. For pre-shearing, the bulk solid is loaded in a vertical direction by a normal stress, then the sample is sheared at constant normal stress, constant shear stress, and constant bulk density. Such kind of state is known as steady state and the consolidated sample is known as critically consolidated with respect to pre-consolidation stress. After the bulk solid sample is consolidated by pre-shearing, the shear deformation is reversed until the shear stress is zero. This is followed by the application of a normal stress smaller than the pre-shear stress, and the sample is sheared to failure. This process is repeated for several normal stresses. The pre-shear and failure data are used to plot Mohr circles which define the state of stress of the powder on the normal stress and shear stress planes. The unconfined strength can be determined from Mohr circle. The plot of unconfined yield strength for different preconsolidation stresses provides flow function.

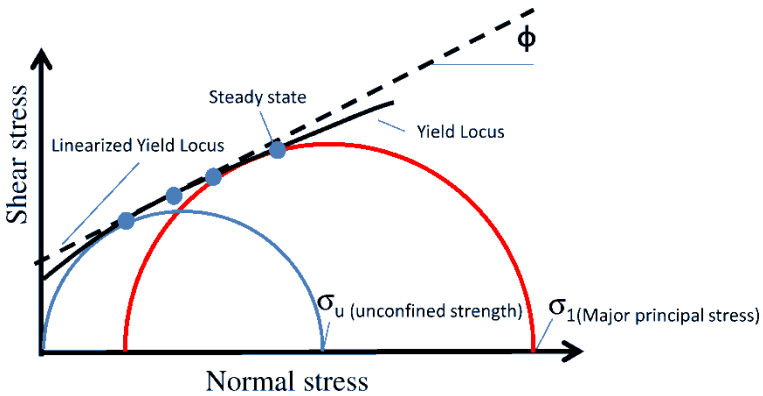

Figure 2.17 Measurement of unconfined yield strength

Direct shear testers can be translational or rotational. The Jenike shear tester (Figure 2.18) is arguably one of the most widely used translational shear testers in silo design. In a translational shear tester, shear is applied by translation motion. This limits the amount of shear displacement that can be applied for shearing action.

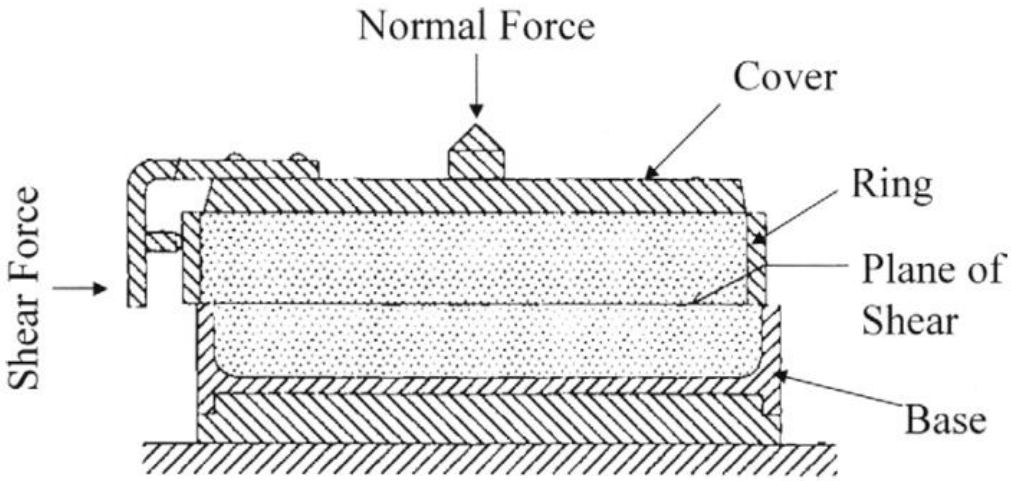

Figure 2.18 Jenike shear tester (Bell, 2001)

This limitation was overcome by a torsional shear tester by Peschl (Figure 2.19). The Peschl shear tester rotates the bottom half of a cylindrical specimen against stationary top half. However, one of the problems with torsional shear test is that the amount of the shear travel varies across the radius of the shear cell. Particles at the centre of the cell do not experience any motion whereas the particles towards the outside edge of the cell have increasing amount of shear travel. This will introduce stress inhomogeneity along the radius of the cell. While comparing unconfined strength at comparable values of major principal stress, the Peschl shear tester produced slightly lower value than the Jenike tester (Bell et al., 1994).

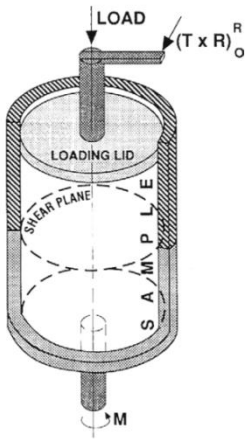

Figure 2.19 Peschl torsional shear tester (Bell, 2001)

The issue of non-uniform shear displacement in rotational tester can be minimized if the shear cell has an annular ring shape instead of a cylindrical one. This concept was first developed by Hvorslev (1937). The tester was heavy since it was designed for soil mechanics where stresses are high. Therefore the tester was not suitable for bulk handling. The first ring shear developed for bulk handling was by Carr and Walker (1968). The tester based on this model was mechanically robust but difficult to operate. A similar concept with a number of engineering improvement was developed by (Schulze, 1994). The test procedure used in the ring shear test is similar to that in Jenike shear test, and this test produced similar values of unconfined strength to the Jenike shear test at given value of principal stresses (Schulze, 2007).

.

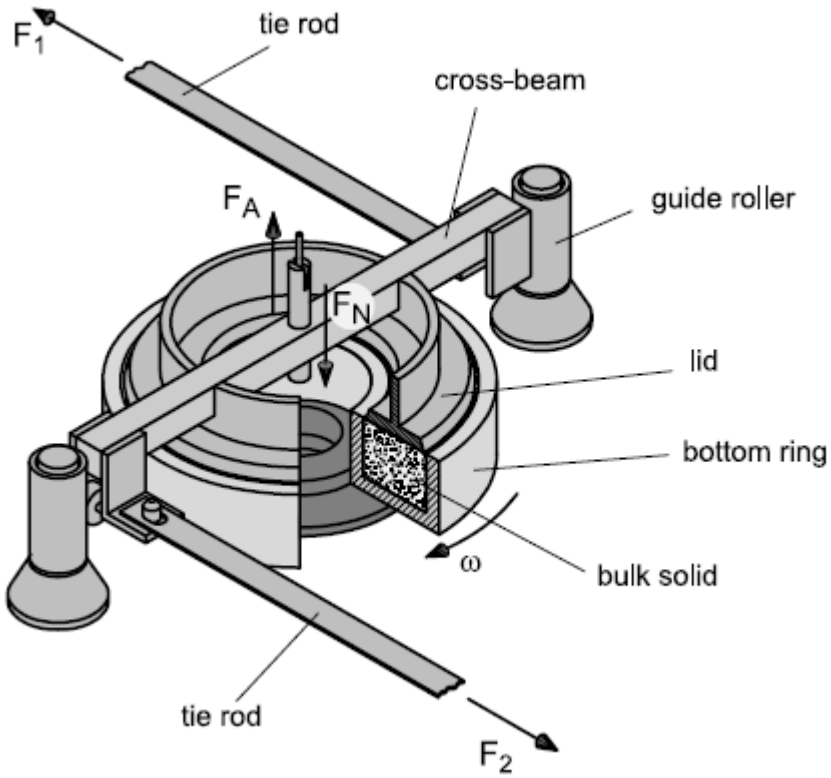

Figure 2.20 Schluze ring shear tester (Schulze, 2007)

Shear testers are very useful for designing bulk handling equipment including silos and hoppers. However, multiple test experiments are required to measure the unconfined yield strength.

For the careful measurement of mechanical behaviour of cohesive powder, true triaxial and biaxial tester can be used. However, these experiments are time consuming and expensive to conduct and are almost never used in industrial practise.

2.9 *Choosing a tester*

The testing of bulk solid is not always done to design a silo or other handling operations. Very often the testing is required for quality control, product development, and product screening purposes. Use of Jenike shear tester for this

purpose can be time consuming, and requires certain level of skill, so that it is often too difficult or costly to use for routine quality control proposes. Schulze (1994) annular ring shear tester is advantageous over the Jenike tester in terms of ease of use and time taken to conduct a flow function test. The major objections to these testers is their associated cost, delicacy, time needed to run a test and that their requirement that the powder specimen be of a certain volume, with larger particles excluded (Bell et al., 2007). Also, the flow function is not directly measured in these testers but is rather derived from yield loci and Mohr's circle construction. The derivation is often based on linearized yield loci which might be erroneous (Figure 2.17).

2.9.1 Uniaxial tester

Indirect uniaxial shear tests are often used to evaluate the flowability for a cohesive material (Bell et al., 2007; Enstad and Ose, 2003; Freeman and Fu, 2011; Parrella et al., 2008; Röck et al., 2006; Williams et al., 1971; Zhong et al., 2005). A uniaxial test involves three main steps (Figure 2.21):

- Confined compression: Application of vertical consolidation load for certain length of time (Figure 2.21 a),
- Unloading : removal of load and confinement (Figure 2.21 b), and
- Unconfined compression: finally application of vertical load until the sample fails (Figure 2.21 c).

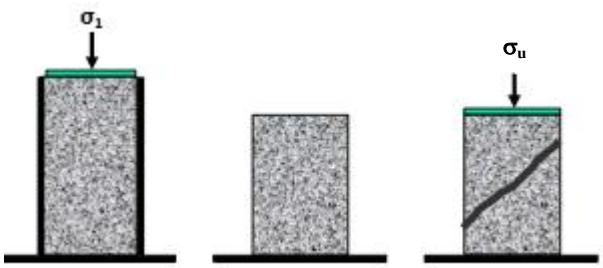

Figure 2.21 Stages in uniaxial test: a) Confined consolidation b) removal of load and confinement c) unconfined shearing

The application of vertical consolidation load and vertical loading to failure is appealing in simplicity from a mechanical perspective and it is physically similar to stress path associated with arching and the unconfined strength. In this study Edinburgh powder tester (EPT), an extended uniaxial tester is used. The results from the EPT are also compared with other commercial tester including the FT4 rheometer, and rotating drum tests.

The details of the tests are outlined in chapter 3.

Figure 2.22 Edinburgh Powder Tester

2.9.2 FT4 rheometer

The FT4 rheometer is a torsional shear cell (similar to Peschl). Briefly, in this test, the powder is first conditioned and presheared. The conditioning involves homogenisation of sample in a cylindrical vessel by rotating a blade through the powder sample in a defined motion. The vessel is then split and loaded to a specified normal stress using a vented piston. Subsequently, the vented piston was replaced with a shearing piston and the sample is presheared at a specified rate under the same

normal stress until a constant shear stress was reached. Once the sample reached the critical state characterised by constant deformation at constant volume and constant stress, the powder sample is loaded to a normal stress lower than normal stress used during preshearing and sheared at a specified rate again. The shear stress measured in this step defines a point on the yield locus of the compressed powder. The additional points on the yield locus are obtained by preshearing the sample again and shearing at progressively lower normal forces. This defines the yield locus at different preshear stresses. Further data analysis was required to derive the flow function and effective angle of internal friction. The data analysis in FT4 is automated; it applies a linear fit to the points on the yield loci. The unconfined strength and major principle stresses are then obtained by drawing Mohr circles.

Figure 2.23 FT4 Rheometer

2.9.3 Rotating drum test

The rotating drum test has been used for decades to understand the dynamic and shear behaviour of powder materials (Brewster et al., 2009; Dury and Ristow, 1999; Kaye et al., 1995; Mellmann, 2001). The test is mainly used to measure: dynamic angle of repose and time interval between events. The dynamic angle of repose is the angle made by the inclined surface of powder material while powder is rotated in a drum. The time interval between two avalanches relates to cohesion of the powder. For cohesionless materials during rotation, the most evident observable property is

the angle of the surface. This continuous "angle" in a rotating drum can depend strongly on the side wall which makes it more complicated to characterise such angles (Taberlet et al., 2006). For cohesionless materials reproducible results can be achieved, however cohesive materials may form multiple angle of repose in a single test. While experimental research to understand the dynamic behaviour of various non-cohesive samples has been successful, many challenges still remain for characterisation of cohesive powders (Wolf, 1981).

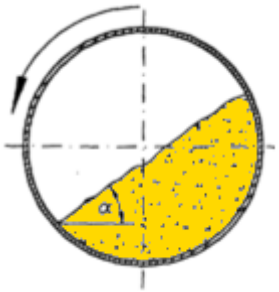

Equation 2.46 Dynamic angle of repose

2.10 *Summary*

The literature related to this study has been reviewed in this chapter. The literature includes: introduction of DEM, issues related to DEM, adhesive contact models in DEM, forces causing adhesion, relationship between adhesion and bulk cohesion, and measurement of cohesion and flow properties using laboratory experiments.

Although several contact models to model cohesive powder exists, there is a need for a meso-scale contact model that can capture the key elements of the frictional-adhesive contact mechanics and reproduce stress history dependent and other behaviour exhibited by cohesive powders. Whilst many studies have been reported on the measurement of contact model parameters using microscopic measurement techniques such as AFM, Nano-indentation and others, the measurements tend to be on either highly idealised particle (such as specially manufactured perfect sphere) or suffer from enormous scatter and uncertainty with regard to the accuracy of the

measurement. An alternative approach can be calibration of DEM model using bulk experiments. The calibration of a mesoscopic DEM contact model requires experimental measurements characterising the mechanical behaviour of powders. The mechanical behaviour of cohesive powders can be carefully measured using element tests such as biaxial test, true triaxial and hollow cylinder tests. However in practice these tests are expensive and slow to conduct and are almost never performed for many industrial applications requiring material characterisation. A simpler technique that could be used for filling this important gap with the focus of providing test data for model calibration and simulation validation is needed. Furthermore, in order to simulate large scale simulations, the scaling laws necessary to produce scale independent predictions for cohesionless and cohesive solids needs to be investigated.

Chapter 3

Characterisation of test solids[1]

3.1 *Introduction*

In the previous chapter literature relating to different experimental methods to measure flow properties was described and the reason for the choice of the testers was given. In this chapter, the objective is to evaluate the capability of Edinburgh Powder Tester (EPT) to measure flow properties of bulk solids and its potential of use for DEM model calibration purposes. Six different industrial solids are chosen and several physical measurements including particle size, size distribution, bulk density, and moisture content are made. The flow properties from EPT include measurement of compressibility, flow function, and unconfined stress strain. The effect of powder specimen aspect ratio (Height/Diameter) on powder compressibility is presented. Other tests including FT4 rheometer and rotating drum test are also conducted. The repeatability of measurements from FT4, EPT, and rotary drum is addressed for 4.7µm limestone powder which is the PARDEM reference powder. The relative flowability of powders in FT4, rotating drum, and EPT are compared. The relationships between flow properties of powders in FT4, rotating drum and EPT are also analysed and compared.

- [1] Based on Thakur, S.C., Ooi, J.Y., Imole, O.I., Wojtkowski, M.B., Magnanimo, V., Ahmadian, H., Montes, E.C., and Ramiaoli, M., (2013). *Characterisation of cohesive powders for bulk handling and DEM modelling*, in: Bischoff, M., Onate, Owen, D.R.J., Ramm, E. and Wriggers, P. (Ed.), III International Conference on Particle-Based Methods-Fundamentals and Applications. Stuttgart, Germany

3.2 *Materials and methods*

3.2.1 Physical characterisation of test solids

Three sample pairs were chosen. Each pair of samples had different levels of cohesion. The powders tested were: 4.7μm mean size Limestone A (commercial name ESKAL 500) and 31.3μm mean size Limestone B (commercial name ESKAL 30) supplied by KSL Staubtechnik, Germany; two spray dried detergent powders (Detergent A and Detergent B) with different formulations supplied by Newcastle Innovation Centre, Procter and Gamble, Newcastle, UK; and two cocoa powders with 10-12% fat (Cocoa-A) and 20-22% fat content (Cocoa-B) supplied by Nestle Product Technology Centre, Orbe, Switzerland. Please note that Limestone A is the PARDEM reference solid that have been extensively used in a collaborative European PARDEM project (www.pardem.eu).

Hitachi TM 1000 Scanning Electron Microscopy (SEM) was used in this study to acquire images for visual inspection regarding shape and surface roughness of particles. The SEM images of 6 industrial solids are shown in Figure 3.1. Larger size Limestone B seems rougher but rounder compared to Limestone A and similar trend can be found for Cocoa B and Cocoa A. No significant difference between shape and texture of two detergent powders can be seen from the SEM images.

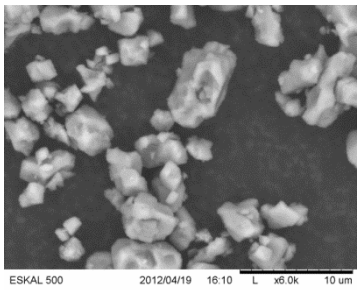

(a) Limestone A ($D_{50=}$ 4.7 μm)

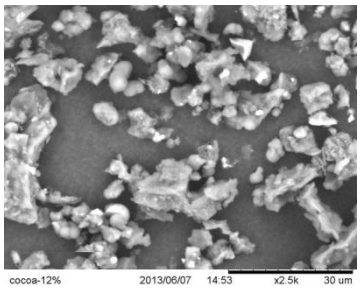

(b) Cocoa A ($D_{50=}$ 8.7 μm)

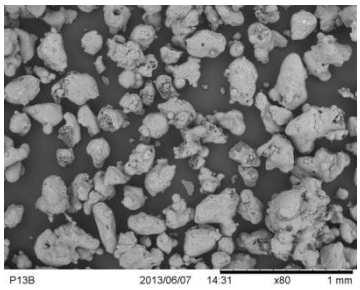

(c) Detergent A($D_{50=}$ 334 μm)

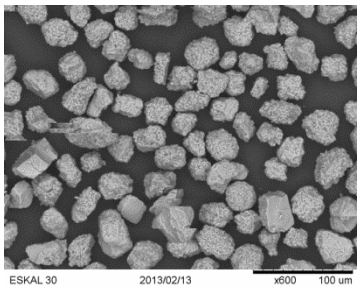

(b) Limestone B($D_{50=}$ 31.3 μm)

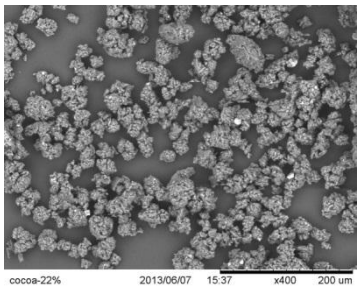

(b) Cocoa B($D_{50=}$ 24.2 μm)

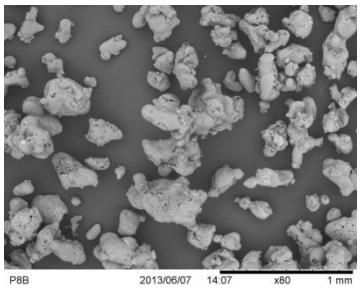

(c) Detergent B($D_{50=}$ 311 μm)

Figure 3.1 SEM images of industrial solids

(Note: Please note the different scales in the figure)

Particle skeletal density was measured using gas pycnometer (Accupyc 1340, Micromeritics, USA). The particle size distribution (PSD) of the limestone powder was supplied by manufacturer. The PSD of spray dried detergent powder was measured using mechanical sieve. The PSD of cocoa powders was measured by dry dispersion method using Malvern Mastersizer (provided by Nestle). Moisture content was measured by weighing 5 gms of a sample before and after drying in an oven at 100°C for 24 hrs. Each test was carried in duplicates. Bulk density of powder was determined by measuring the mass of the sample poured into known volume of EPT mould. The physical properties of the powders are summarised in Table 3.1. These powders are different in physical properties. The limestone powders are insensitive to humidity. However, detergent powders and cocoa powders are relatively

hygroscopic. These samples were sealed in air tight bags and experiments were conducted in a laboratory humidity (28-45%) and temperature (18-22°C) condition.

Table 3.1 Physical properties of powders

Material description	Solid density (kg/m^3)	Fill bulk density (kg/m^3)	Mean particle size (μm)			Span= $[\frac{D_{90}-D_{10}}{D_{50}}]$	Moisture content (%)
			D_{10}	D_{50}	D_{90}		
Limestone A	2745	754	1.42	4.7	7.39	1.27	0.25
Limestone B	2745	1320	21.1	31.3	45.83	0.79	0.25
Detergent:A	1892	401	167	334	1009	2.52	3.38
Detergent: B	2111	472	158	311	798	2.06	3.06
Cocoa A	1436	373	3.12	8.68	22.5	2.23	5.68
Cocoa B	1509	516	12.78	24.23	47.57	1.44	6.14

3.3 *Flow properties measurement*

3.3.1 Edinburgh Powder Tester

In an EPT test, the sample is poured into the consolidation cylinder of diameter 40 mm and height 80 mm. The sample is loaded by a weight and the force is recorded by a load cell attached to the consolidation plunger, this process of loading is referred as confined compression. After the sample is loaded for a selected consolidation time, the consolidation plunger is automatically retracted and the mould is manually slid down the pedestal, exposing a free standing column of consolidated powder sample. The unconfined sample is loaded to failure by a motor driven test piston at a speed of 0.4 mm/s, which is so chosen to conduct the test rapidly without affecting the measured unconfined yield strength. Watanabe and Groves (Watanabe and Groves, 1964) found that the unconfined strength of detergent samples was unaffected when the piston speed varied from 0.084 to 0.43 mm/s. The unconfined strength is automatically recorded, as well as the whole load-displacement curve.

The results from EPT covering the entire spectrum of loading regime from confined compression to unconfined shearing is presented below. The compression of bulk solids can be studied by plotting stress strain and/or corresponding stress-density and stress-porosity relationships. Figure 3.2 shows the change in strain as a function of applied stress, and Figure 3.3 and Figure 3.4 show the corresponding variation in bulk density (ρ_b) and porosity ($1-\rho_b/\rho_s$) as a function of consolidation stress. The powder compression process can be divided into two stages. In the first stage, the powder compression is mostly due to particle rearrangement while the second stage is related to particle rearrangement and elasto-plastic deformation of contacts. It can be seen that on the onset of consolidation strain and corresponding porosity and bulk density decreases rapidly until 16 kPa of stress (stage I). As the consolidation progressed further, strain and corresponding bulk density and porosity varied linearly with a flatter slope (stage II).

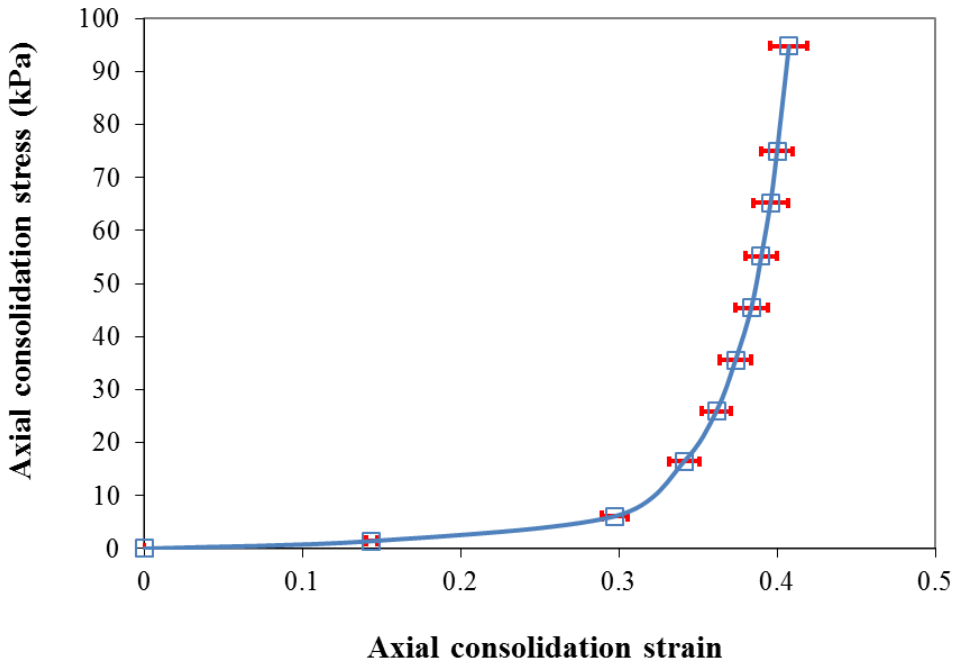

Figure 3.2 Stress strain response during confined compression- Limestone A

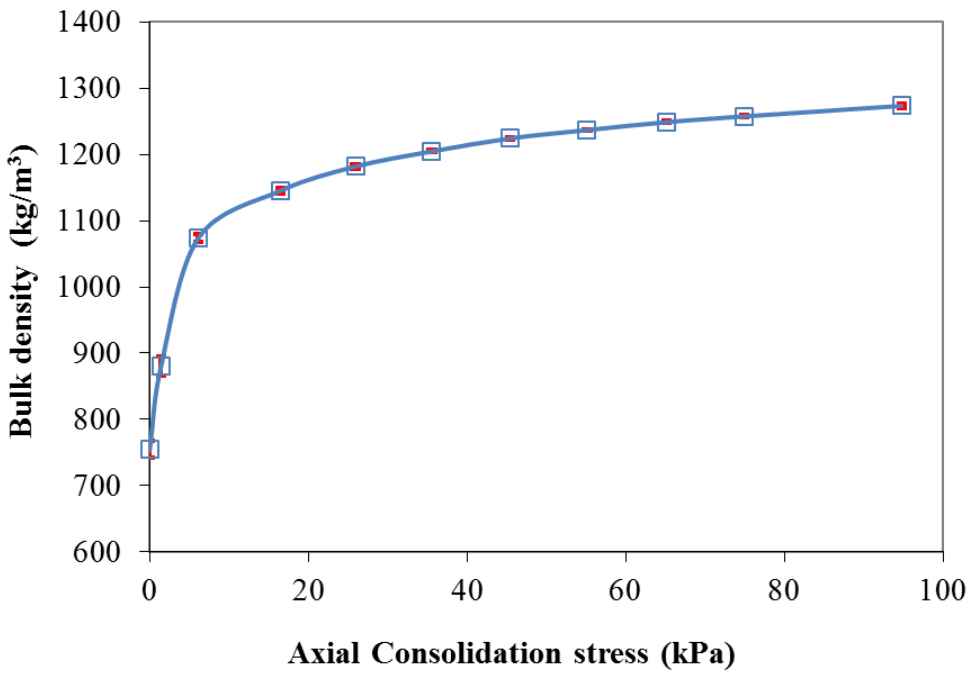

Figure 3.3 Bulk density and stress response during confined compression -Limestone A

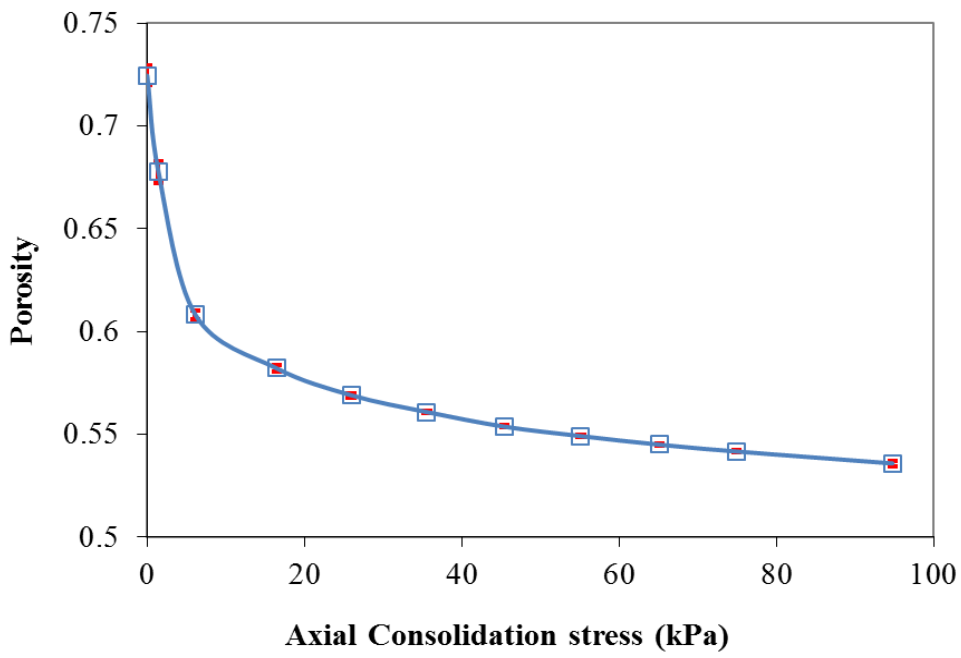

Figure 3.4 Porosity and stress response during confined compression- Limestone A

Figure 3.5 shows the loading response after removal of load and confinement for three consolidation stresses. It can be seen that as the consolidation stress (σ_1) increases the maximum value of stress (unconfined strength) and strain also increases showing stress history dependence.

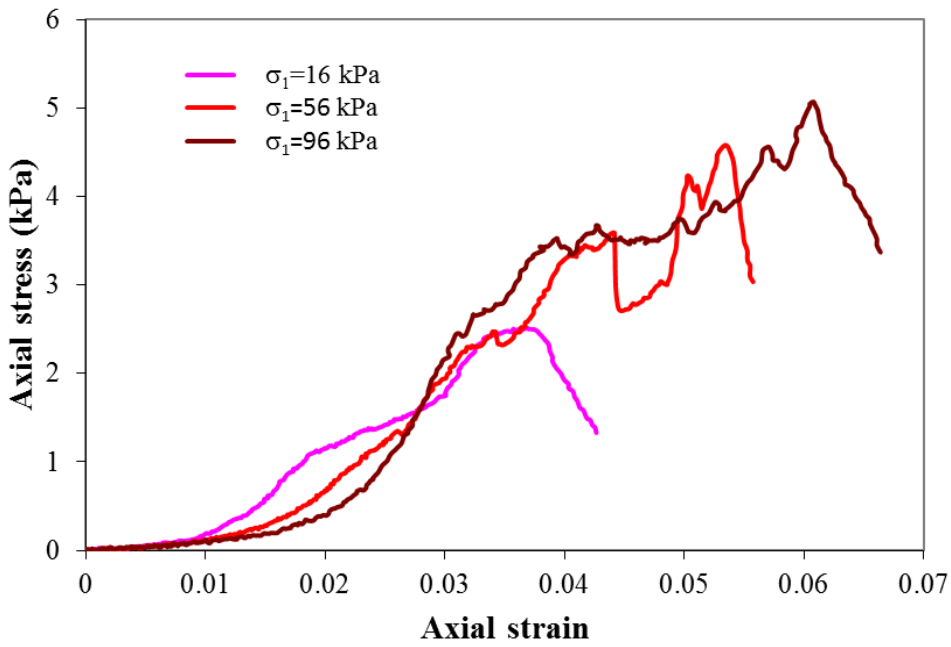

Figure 3.5 Unconfined stress strain response at different consolidation stress-Limestone A

The unconfined strength as a function of consolidation stress is plotted in Figure 3.6. All the experiments are conducted on three replicates and error bars are also shown in the corresponding figures. The maximums Coefficient of Variation (COV) for Limestone A at different consolidation stress is reported as; 2.8% for strain, 1.7% for bulk density, 0.78% for porosity, and 7.4% for unconfined yield strength measurements.

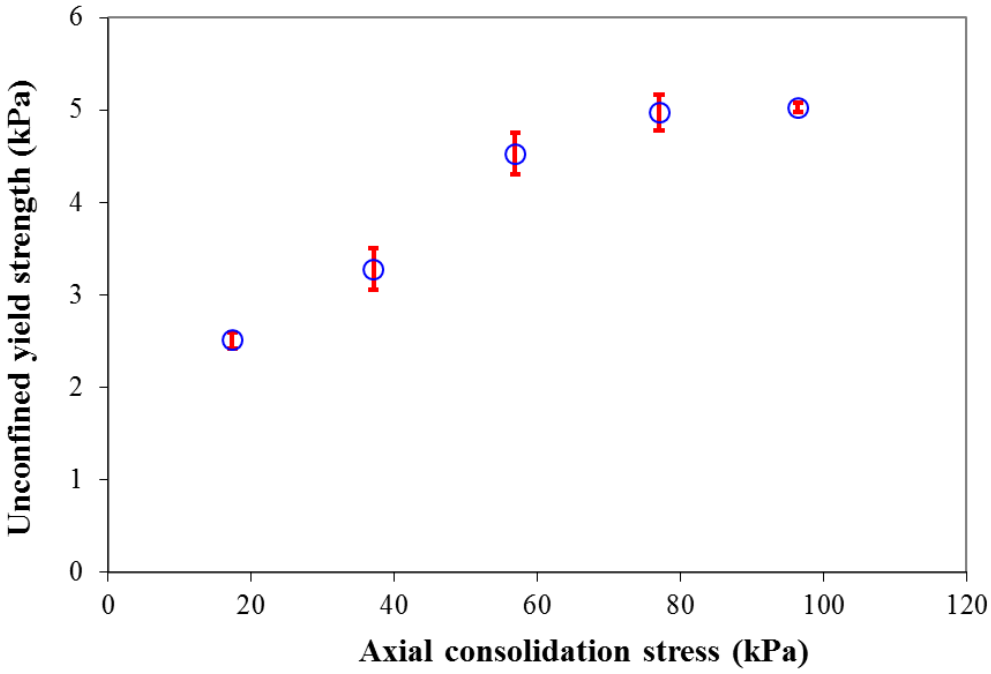

Figure 3.6 Flow function- Limestone A

It is further proposed that these bulk measurements can be used for DEM model calibration. These are the (vertical) stress-strain and the stress-porosity response during confined compression as well as the (vertical) stress-strain response during unconfined compression including the peak unconfined strength.

3.3.1.1 Effect of filling method

Fill method is known to affect the bulk mechanical behaviour of cohesionless solid however, the effect of fill method on behaviour of cohesive solids is not known very well. In this section we have investigated the effect of two fill methods on bulk compression. In the first method the EPT cylinder is filled by pouring the powder sample directly to the cylinder (Figure 3.7), and in the second method a sieve of 1.8 mm aperture is placed on the top of cylinder and powder is passed through the sieve and allowed to fall into the cylinder (Figure 3.8). The height of fall was kept similar in each method. Three tests are conducted for each fill method.

Figure 3.7 Direct filling by spoon

Figure 3.8 Filling by passing the powder through sieve

Figure 3.9 shows the effect of fill method on porosity stress relationship. The fill porosity by direct spoon filling method is slightly (approx. 2%) lower than that from filling through the sieve method. Passing the powder through sieves breaks the larger agglomerates into small ones and gives rise to formation of air pockets between smaller agglomerates during deposition. This may lead to higher initial porosity for the filling through sieve method. However as the consolidation stress is applied the porosity-stress line from both method almost converged. This could be due to expulsion of air voids on the application of stress. Filling through sieve method exhibited slightly larger scatter and requires an additional step for filling, therefore direct spoon filling method was used in this thesis. The filling method may have impact for some materials.

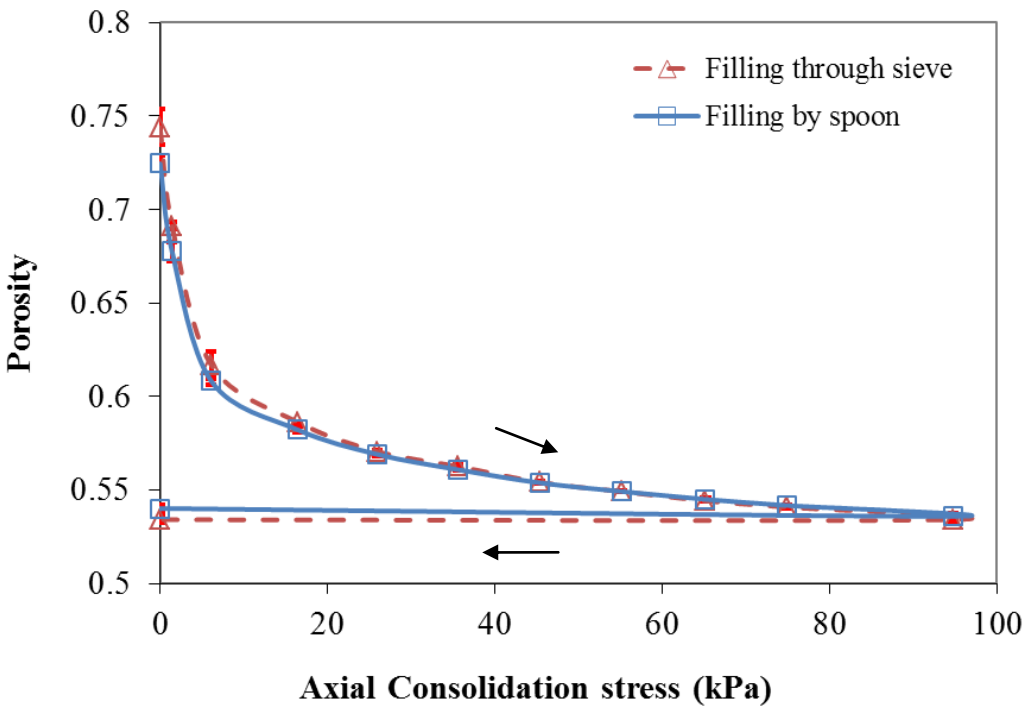

Figure 3.9 Effect of fill method on compressibility- Limestone A

3.3.1.2 Effect of powder sample aspect ratio

Friction between particle and wall is known to play an important role during confined compression of powder (Enstad and Ose, 2003). The volumetric compression of the powder is reduced when the aspect ratio (Height to diameter ratio) of the sample is increased. Here we have investigated the effect of aspect ratio on the compressibility of bulk powder using EPT.

The EPT compression assembly consists of an inner steel cylinder, perspex sleeve, locking pin, and loading piston (Figure 3.10). The locking pin is placed in the hole in the inner steel cylinder and the sleeve rests on the pin. After filling the powder sample into the prespex, the sample is then loaded to initial stress of 7 kPa and the pin is removed. The application of initial stress generates sufficient friction between particles and wall and holds the sleeve unsupported (Figure 3.10 b). The sample is then loaded to higher loads. We propose that this action allows for two directional compression of the sample and reduces the variability in bulk density across the height of the sample.

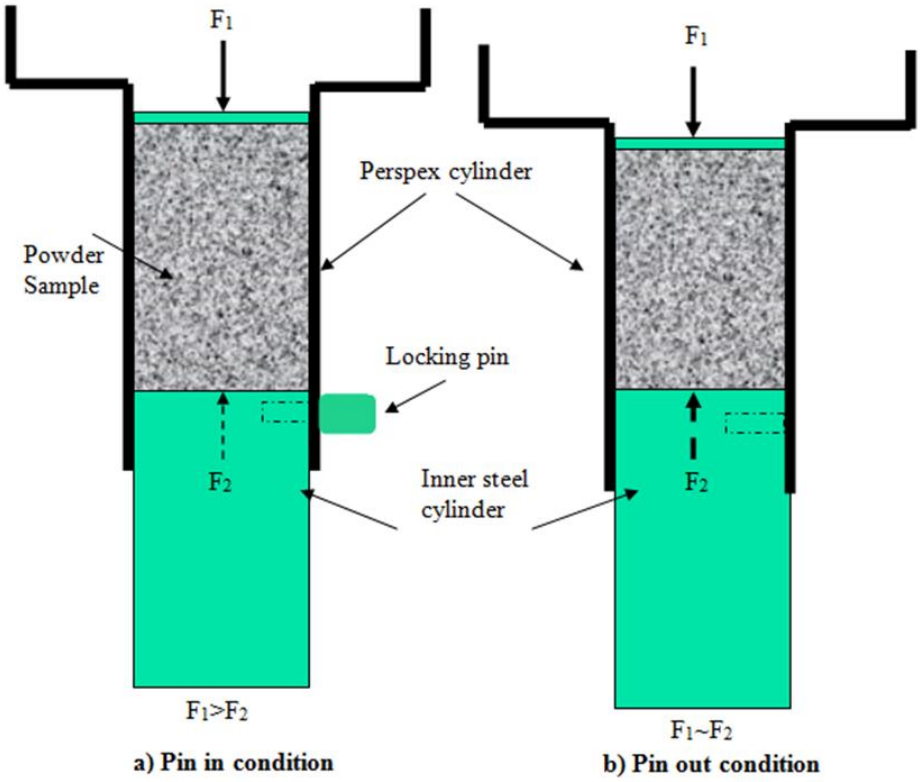

Figure 3.10 Schematic of pin in and pin out conditions in EPT

Figure 3.11-Figure 3.16 show the effect of aspect ratio on bulk compressibility at 4 normal stresses (20, 40, 60, and 100 kPa) for 6 industrial solids. The sample fill aspect ratio was varied in a range of 1-2. It was found that the sample bulk density increases slightly with decreasing aspect ratio. The increase was small but significant, especially for Limestone A and Cocoa A. For Cocoa A the bulk density increased only by 2.36% (COV=0.75%) when the aspect ratio was decreased from 2 to 1. The effect of aspect ratio on compressibility of the other powders was not so obvious. This could be due to slightly higher COV in measurement of density (3.5% for Detergent A). It is important to note that the two directional compressions in EPT is an improvement over one way punching in other uniaxial tester, and it seems to allow reduction in the density variation even at high aspect ratio.

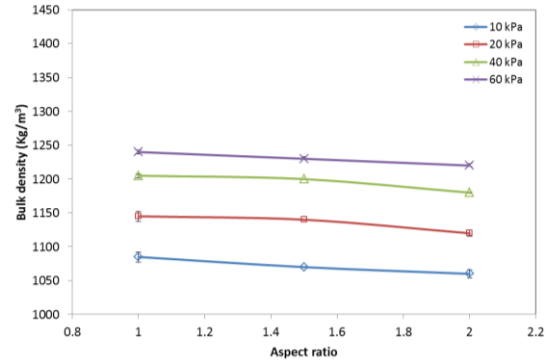

Figure 3.11 Limestone A (d_{50}=4.7 μm)

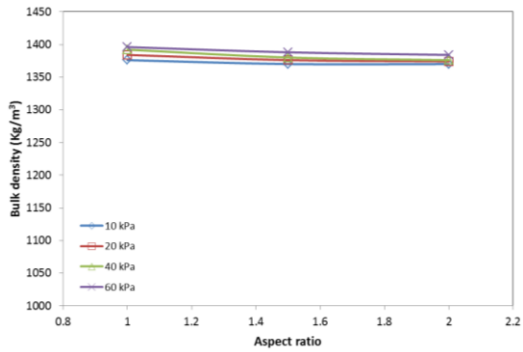

Figure 3.12 Limestone B (d_{50}=31.3 μm)

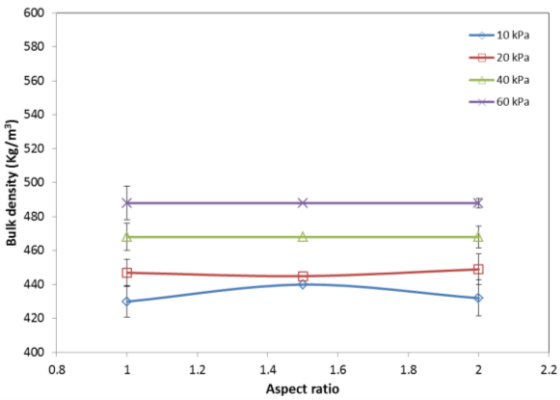

Figure 3.13 Detergent A (d_{50}=334 μm)

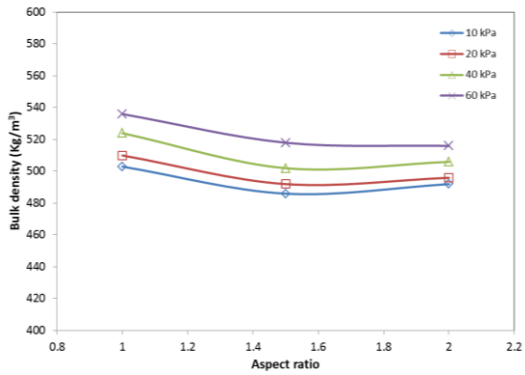

Figure 3.14 Detergent B (d_{50}=311 μm)

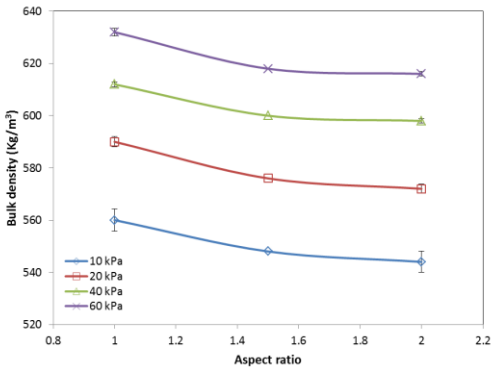

Figure 3.15 Cocoa A (d_{50}= 8.7 μm)

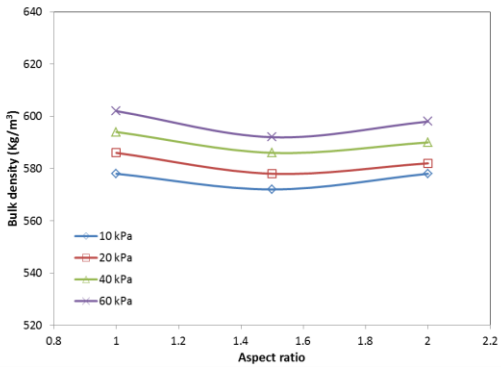

Figure 3.16 Cocoa B (d_{50}= 24.3 μm)

3.4 *FT4 rheometer*

The FT4 powder rheometer (Freeman Technology Ltd., Castlemorton Common, Worcestershire, UK) was used for the flow function and effective angle of internal friction measurement in a consolidated state. The FT4 apparatus is described elsewhere in literature (Freeman and Technology, 2005; Freeman et al., 2009). The procedure used to measure the flow properties is that recommended by the standard shear technique by FT4 rheometer. Briefly, in this test, the powder was first conditioned and presheared. The conditioning involves homogenisation of sample in a 50 mm diameter cylindrical vessel by rotating a blade through the powder sample in a defined motion for 1 cycle. The vessel was then split to a volume at 85mL and loaded to a specified normal stress using a vented piston. Subsequently, the vented piston was replaced with a shearing piston and the sample was presheared at a rate of 18°/minute under the same normal stress until a constant shear stress was reached. Once the sample reached the critical state characterised by constant deformation at constant volume and constant stress, the powder sample was loaded to a normal stress lower than normal stress used during preshearing and sheared at a rate of 18°/minute again. The shear stress measured in this step defines a point on the yield locus of the compressed powder. The additional points on the yield locus are obtained by preshearing the sample again and shearing at progressively lower normal forces. The preshearing process was repeated for 4 normal stresses (3kPa, 6kPa, 9kPa, and 15 kPa) and the samples were sheared at lower normal stresses. This defined the yield locus at different preshear stresses. Further data analysis was required to derive the flow function and effective angle of internal friction. The data analysis in FT4 is automated; it applies linear fit to the points on the yield loci. The unconfined strength and major principle stresses are then obtained by drawing Mohr circles. The effective angle of internal friction is the slope of the line passing through the origin of normal and shear stress plot and tangent to the Mohr circle passing through the preshearing point. The flow function is a measure of stress needed to make an arch collapse and make the material flow and effective angle of internal friction is a measure of the friction between particles.

3.5 ***Rotating drum test***

The AeroFlow tester (TSI Incorporated, USA) was used to investigate flowability of powder in dynamic regime. The tester rotates a shallow cylindrical glass drum (125 mm diameter, 25 mm depth), containing the sample, around its horizontal axis, at a constant rate (angular velocity w =0.3 rpm in this study) as shown in Figure 3.17. When the inclination angle of the material (e.g. powder) surface becomes too great for its granular structure to support it, the powder collapses. The angle at which powder collapses is referred to as an "event". Due to the cohesive nature of the sample, an etched metal collar insert was placed around the drum's circumferential inner wall to increase the roughness and to obtain more regular, periodic events.

The time interval between events and their (relative) amplitudes are detected and recorded by a light fixture and photo-voltaic cells assembly positioned vertically in front and behind the drum, respectively. While the original, commercial set-up with a light sensor is capable of detecting big changes, it is impossible to distinguish events. Therefore, to obtain the profiles of the powder surface, an external camera (Logitech HD Pro, Logitech Intl SA) was mounted in front of the rotating drum and images were taken in regular intervals of t_i = 0:25 seconds. Measurement of the time between the events is analysed using two methods. In method I, to calculate the time between events, one needs to know when an event is deemed to have taken place. An event is said to have taken place when two criteria are fulfilled. The first criterion is difference between the angles of surface recorded for successive time-steps should be greater than 5 degrees. However due to noise and too small events we introduce an additional criteria namely that the angle of surface recorded the next 5 time-steps must be lower than the angle of surface for immediate past the event recorded. In the method II, time between consecutive events is measured by applying Fourier transformation to the raw data. The method I measures the time between consecutive events independently of the size of avalanche, while the second method measure it only for major events.

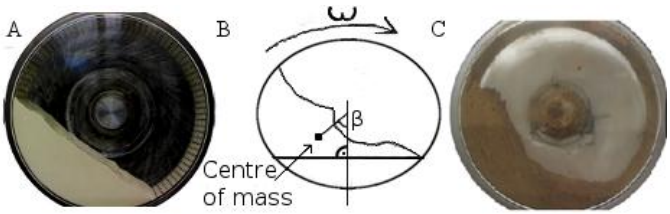

Figure 3.17 Angle of surface and angle of stability

For most cohesionless samples the angle of surface is well defined (see Figure 3.17 A). However, due to the irregular surface profile of cohesive samples (see Figure 3.17 C), a global quantity that captures the position of the bulk sample relative to a fixed reference frame is desirable. First, to obtain the (global) surface angle, the centre of mass is needed. Every pixel in the snapshots of the drum (pixel size 6.25cm/360) is analysed along both vertical and horizontal directions. Using the pixels enables us to calculate the horizontal and vertical positions – x and y, respectively – of the centre of mass. Note that for this analysis, the powder layer sticking on the cylinder wall away from the bulk is not taken into account. From this (at least for low filling height), the angle of surface is defined as $\beta = atan\ (x_c/y_c)$, where x_c and y_c are the average values of pixels on which a powder was detected, (see Figure 3.17 B). The (surface) angle for a powder in a rotating drum is thus defined as the angle between vertical and the line going through the centre of material mass and the centre point of the drum. From this, the average angle (of the surface profile) can then be computed as function of time, while the maximum angle, typically measured before the events, is referred to as "angle of stability".

3.6 *Results and discussions*

3.6.1 Repeatability

In order to understand the uncertainties associated with the different measurement techniques repeat tests on PARDEM reference solid (Limestone A) were conducted using EPT, FT4, and rotary drum. Table 3.2 shows flow properties measured by FT4 and Table 3.3 shows the unconfined yield strength measurement from EPT. The

maximum COV in unconfined yield strength and effective angle of internal friction (ϕ_e) measurement by FT4 was reported as 8.4% and 1.9% respectively. A COV of 7.4% was reported in unconfined yield strength measurement by EPT. With respect to time needed to run a flow function test with 4 preconsolidation stresses; it takes approximately 20 minutes in EPT, and 60-80 minutes in FT4 when standard testing procedure is followed.

Table 3.2 Powder flow properties produced by FT4 for Limestone A (μ±Sn)

σ_p, kPa	UYS, kPa	ϕ_e, °
3	1.92(±0.03)	41.85(±0.25)
6	2.52(±0.21)	39.16(±0.73)
9	3.75(±0.23)	38.02(±0.24)
15	3.97(±0.20)	37.46(±0.25)
Maximum COV (%)	8.4	1.9

Table 3.3 Powder flow properties produced by EPT for Limestone A (μ±Sn)

σ_p, kPa	UYS, kPa
17.3	2.50(±0.09)
37.1	3.27(±0.22)
56.9	4.70(±0.27)
77	4.97(±0.37)
96.4	5.03(±0.05)
Maximum COV (%)	7.4

Where, σ_p = preconsolidation stress, UYS=unconfined yield strength, μ=sample mean, S_n=standard deviation of sample, Coefficient of variation (COV)=S_n/ μ

For rotary drum measurements, the average time between events and angle of stability for the PARDEM reference solid was found to be 8.3 sec and 53° with COV of 50.2 and 9.6%, respectively.

3.6.2 Flow function from FT4 and EPT

The comparison of flow function from uniaxial test and shear cell test requires careful interpretation. The unconfined strength of a sample depends on the applied mean stress. Assuming axisymmetry and ignoring boundary friction, the three dimensional mean stress (σ_m) in the EPT uniaxial test can be evaluated as:

$$\sigma_m = \frac{\sigma_v + 2\sigma_r}{3} \tag{3.1}$$

where σ_v is the vertical stress, and σ_r is the radial stress. Within the bulk solid the radial stress (σ_r) is a result of applied vertical stress, which may be written as:

$$\sigma_r = k.\sigma_v \tag{3.2}$$

where k is lateral earth pressure ratio. Whilst the mean stress can be estimated in the EPT uniaxial test, the state of the three dimensional mean stress is not easy to evaluate in a direct shear test such as the FT4. The stress paths to failure of the samples are also different in the uniaxial and the direct shear tests. Additionally, in a direct shear test the powder is forced to fail along a predefined plane/zone whilst in a uniaxial test the sample fails along the weakest plane. Furthermore in a direct shear test, the sample supposedly reaches steady state before failure; however in EPT the sample does not reach steady state due to no pre-shearing action. Because of the aforementioned reasons it is impossible to make one to one comparison between the EPT results and the FT4 results. The measured flow function of the six industrial solids employing FT4 and EPT are shown in Figure 3.18 and Figure 3.19 respectively.

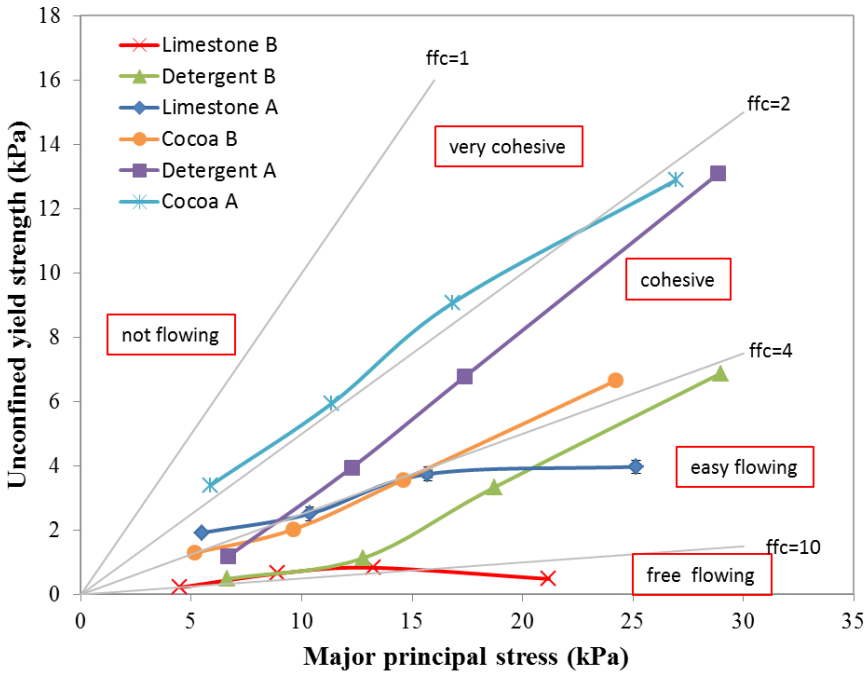

Figure 3.18 Flow function obtained by FT4

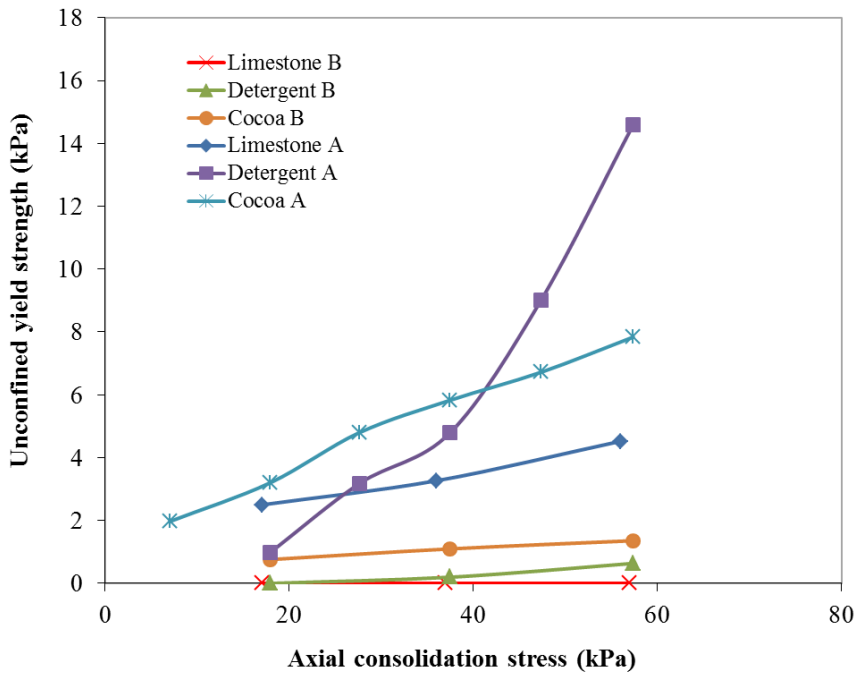

Figure 3.19 Flow function obtained by EPT

Powder flowability, as characterised by Jenike flow index (ffc=major principal stress/UYS) varied from very cohesive (Cocoa A) to free flowing (Limestone B) (see Figure 3.18). The larger the ffc better is the powder flowability. The powder flowability was found to be stress dependent. For Cocoa A, and Limestone A powder flowability generally increased with increasing consolidation stress. Most of the bulk materials exhibit such kind of behaviour and indicates elasto-plastic nature of the powders. Conversely for detergent powders, powder flowability decreased continually with increasing consolidation stress. The decrease in powder flowability with increasing stress possibly arises from plastic deformation of the soft detergent powders. For Cocoa B powder flowability first increased with increasing consolidation stress and then decreased. No trend in powder flowability with increasing stress was found for Limestone B. This could be probably due to larger scatter in UYS measurement especially at smaller strengths. No significant relationship between physical properties of the powders presented in Table 3.1 and flow index was found.

3.4 shows the ranking of the flowability of the test solids using FT4 and EPT. The samples are ranked by values of the unconfined yield strength at the given consolidation stress. The powders were ranked equal when the strength was within ±COV (measured for Limestone A). The EPT and FT4 produced similar ranking with some discrepancies. For the FT4 measurement at the major principal stress of 20 kPa, the UYS of Limestone A ranks lower than Cocoa B. In contrast, the UYS measured by EPT for Limestone A ranks consistently higher than Cocoa B. Further investigation is required to understand the reason for this discrepancy. Additionally in EPT, UYS of Detergent A at a higher stress (67kPa) is found to be higher than Cocoa A. This could be attributed to breakage and plastic deformation of detergent particles at high stress and may not be comparable to the strength at lower stresses in the FT4.

Table 3.4 Ranking of powders flowability using FT4 and EPT

FT4, Major Principle Stress (kPa)						EPT, Axial Stress (kPa)					
10		15		20		17		37		57	
Rank	Material	Rank	Material	Rank	Material	Rank	Material	Rank	Material	Rank	Material
=1	Limestone B	1	Limestone B	1	Limestone B	=1	Limestone B	1	Limestone B	1	Limestone B
=1	Detergent B	2	Detergent B	=2	Detergent B	=1	Detergent B	2	Detergent B	2	Detergent B
=3	Cocoa B	=3	Cocoa B	=2	Limestone A	3	Cocoa B	3	Cocoa B	3	Cocoa B
=3	Detergent A	=3	Limestone A	4	Cocoa B	4	Detergent A	4	Limestone A	4	Limestone A
=3	Limestone A	5	Detergent A	5	Detergent A	5	Limestone A	5	Detergent A	5	Cocoa A
6	Cocoa A	6	Cocoa A	6	Cocoa A	6	Cocoa A	6	Cocoa A	6	Detergent A

3.6.3 Angle of surface and angle of stability from rotary drum test

In this section, we summarise the flow measurements in dynamic stage using the rotating drum device. Figure 3.20 shows time between events and Figure 3.21 shows angle of stability measurement using method I as described in section 3.5. Each point on the graph is an average value for two repeat experiments on the same sample. It can be seen that the time between events and stability angle increases as the material cohesion indicated by UYS measurement from FT4 and EPT test increases. Additionally, the scatter of the results increased with increasing cohesion. Short and reproducible time for less cohesive powders and long and irregular time for more cohesive powder has also been reported by Kaye et al. (1995) and Thalberg et al. (2004). The time between events and stability angle could not be determined for Limestone B and Cocoa B. Unlike, the other samples; we do not observe the sharp drop in the angle of surface during the experiments with Limestone B. This is due the continuous movement of the powder sample. For Cocoa B, the material stuck to the side wall of the drum which made it impossible to perform reliable measurements.

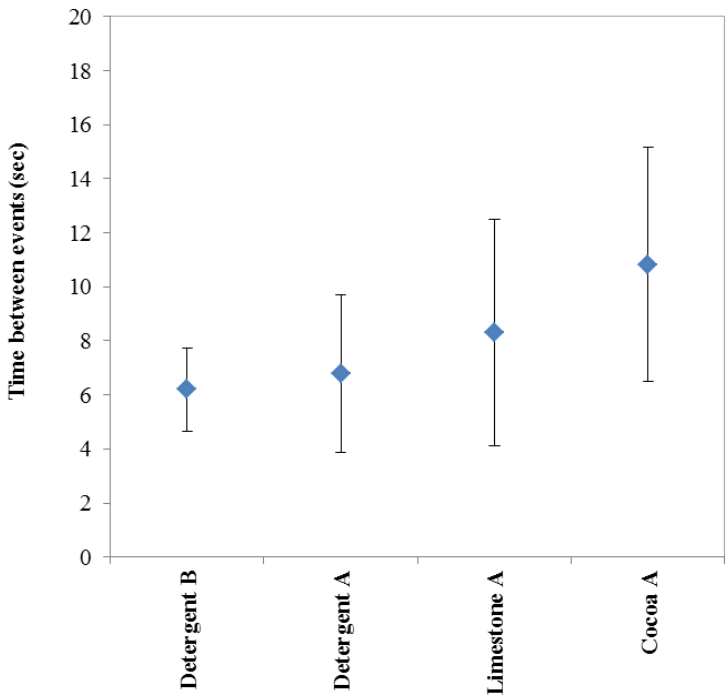

Figure 3.20 Time between events using rotating drum experiments

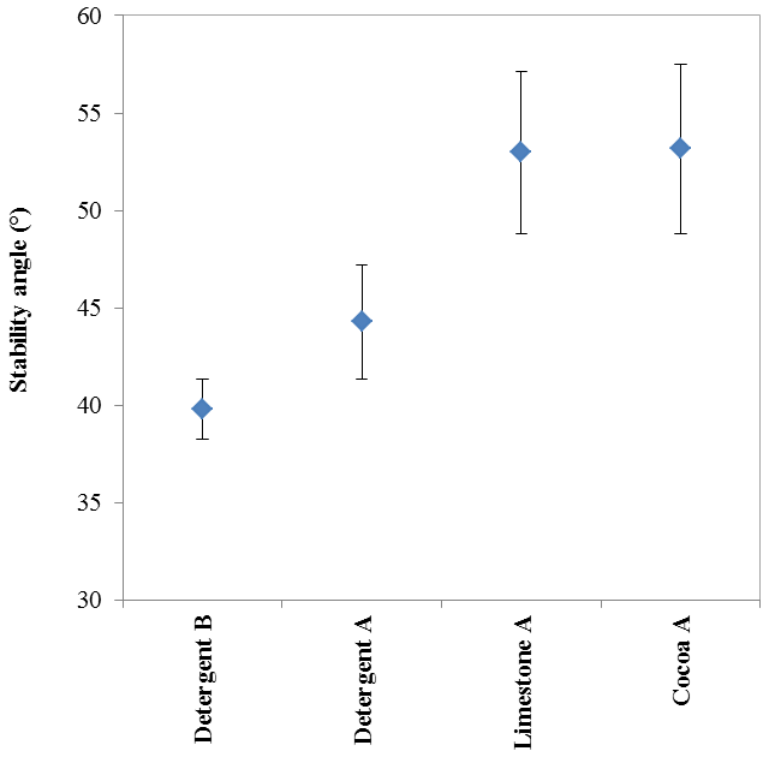

Figure 3.21 Angle of stability measurements using rotating drum test

The larger scatter in flow properties measurement from rotating drum makes it difficult to discriminate between flowability of different powders. The larger scatter very much reflect the characteristics of these materials at very low stress and flowing regimes where the adhesive forces lead to random formation of weak chain and agglomerate giving different structures. However, considering the mean value of measurements the powders are ranked and comparison is made with flow properties measurement from FT4 and EPT. Table 3.5 shows the flow properties measurement and corresponding ranking from rotary drum, FT4, and EPT.

Table 3.5 Measurement of flow properties using rotary drum, FT4 and EPT experiments

Materials	Rotating drum measurement			FT4 measurement		EPT measurement
	Time between events (Method I)- (sec)	Time between events (Method II)- (sec)	Stability angle (°)	ϕ_c at 3kPa preconsolidation stress (°)	UYS at 3kPa preconsolidation stress (kPa)	UYS at 17 kPa preconsolidation stress (kPa)
Detergent B	8.4 (1)	6.2 (1)	39.8(1)	42.9(2)	0.2 (1)	0 (1)
Detergent A	12.3 (2)	6.8(2)	44.3(2)	44.5(3)	1.2(2)	0.98 (2)
Limestone A	21(3)	8.3(3)	53(3)	41.9(1)	1.3(3)	2.5(3)
Cocoa A	25.6(4)	10.8(4)	53.2(4)	51.5(4)	3.4(4)	3.2(4)

Note: The numbers in parenthesis is the rank of powders by corresponding measured value

The time between events estimated by both methods (method I and method II) produced the same ranking, although method II (Fourier analysis) produced larger time between events. This is obvious since method I measures the time between consecutive events independently of the size of avalanche, while method II measures this only for major events. Samples with higher cohesivity are expected to have longer time between events. The time between events ranks similar to the UYS measurement from FT4 and EPT at low preconsolidation stress. However, at higher stresses, the ranking based on UYS measurement from EPT (see Table 3.5) is different which reflects the stress dependency of the flowability of powders.

Samples with higher friction and cohesivity are expected to have a higher angle of stability. In this study the stability angle was found to increase with increasing cohesivity, but this does not correlate well with ϕ_e alone. For example Limestone A has the lowest ϕ_e and conversely the second highest angle of stability. This indicates that cohesion affects the angle of stability more than ϕ_e for this specific case.

3.7 *Summary*

In this chapter, Edinburgh Powder Tester (EPT) has been evaluated for characterisation of flow properties of 6 industrial cohesive powders and the results are compared with commercial test method including FT4 rheometer and Rotating drum. The flow properties from EPT included (vertical) stress-strain and the stress-porosity/density response during confined compression as well as the (vertical) stress-strain response during unconfined compression including the peak unconfined strength. The results were highly repeatable and EPT can be an excellent candidate for DEM model calibration. The key results from this chapter are summarized below:

The bulk compressibility of PARDEM reference solid in EPT was independent of the chosen fill methods. It was found that the sample bulk density increases slightly with decreasing aspect ratio. The increase was small but significant, especially for Limestone A and Cocoa A. The effect of aspect ratio on compressibility of the other powders was not so obvious. This could be due to slightly higher COV in measurement of density (3.5% for Detergent A). The two directional compressions in EPT is expected to be an improvement over one way punching in other uniaxial testers; it allows reduction in the density variation across the height of the sample and increases the repeatability in unconfined yield strength measurement.

While comparing the results from EPT to the results from FT4, both EPT and FT4 produced repeatability measurement on PARDEM reference solid and can adequately discriminate between flowability of different industrial solids. The maximum coefficient of variation (COV) for unconfined yield strength measurement on EPT and FT4 was found to be 7.4% and 8.4% respectively. However, rotating drum exhibited a bigger scatter; time between events and angle of stability measurements on rotating drum had a COV of 50.2 and 9.6% respectively.

Powder flowability, as characterised by Jenike flow index, varied from very cohesive (Cocoa A) to free flowing (Limestone B). For Cocoa A, and Limestone A powder flowability generally increased with increasing consolidation stress indicating elasto-plastic nature of powders. In contrast for detergent powders, powder flowability decreased continually with increasing consolidation stress. The decrease in powder flowability with increasing stress possibly arises from plastic deformation of the soft detergent powders. For Cocoa B powder flowability first increased with increasing consolidation stress and then decreased. No trend in powder flowability with increasing stress was found for Limestone B. This could be possibly due to larger scatter in UYS measurement especially at smaller strengths. Regarding the ranking of powder by EPT and FT4, both experiments produced very similar ranking with some discrepancies when the samples were ranked by values of the unconfined yield strength at the given consolidation.

The larger scatter in flow properties measurement from rotating drum makes it difficult to discriminate between flowability of different powders. The larger scatter very much reflect the characteristics of these materials at very low stress and flowing regimes where the adhesive forces lead to random formation of weak chain and agglomerate giving different structures. When considering the mean values, the time between events and the angle of stability from rotating drum were found to increase with increasing unconfined yield strength measurement at the low stresses. This suggests that the time between events is an indicator of cohesion; short and reproducible time indicating less cohesion and long and irregular time indicating larger cohesion.

The experimental results have provided the test data for DEM model calibration and simulation validation in line with the goals of the European Commission funded PARDEM Marie Curie ITN Project.

Chapter 4

Micromechanical study of cohesive granular material[2]

4.1 *Introduction*

The flow function of a cohesive solid is an important material property for appropriate, efficient, and economic design of bulk handling equipment. Apart from the more traditional direct shear tests indirect uniaxial shear tests are often used to evaluate the flowability for a cohesive material. The flow function of a cohesive solid shows the manifestation of the unconfined yield strength that arises from the historical consolidation stress and therefore the cohesive strength is stress-history dependent. Such stress-history dependent cohesive behaviour must be captured if a numerical model is to successfully simulate the cohesive powder flow. A number of commonly used contact models including JKR, DMT, Maugis, and Matuttis and Schinner, which are elastic contact models, may not be able to capture the stress history dependent behaviour shown in experiments of cohesive powders.

Amongst other things, this chapter describes the development of a phenomenological discrete element method (DEM) model coupled with a calibration methodology for quantitative prediction of such powder flow behaviour. The details of the model and computational methodology, modelling strategy, and the DEM implementation to simulate confined and unconfined uniaxial loading to failure is described. The DEM predictions are compared with the experimental results before the effects of various

[2] Thakur, S.C., Morrissey, J.P., Sun, J., Chen, J-F., Ooi, J.Y. (2013). Micromechanical analysis of cohesive granular materials using discrete element model with an adhesive elastoplastic contact model. *Accepted in Granular matter*

parameters on filled porosity, compressibility, and unconfined strength are explored. The causes of the stress history dependency of the unconfined strength of cohesive solids are then investigated. Finally, the effect of limiting frictional criteria on the unconfined strength is explored. The results provide new insights and propose a micromechanical based measure for characterising the strength and flowability of cohesive granular materials.

4.2 *DEM modelling of uniaxial test*

A number of DEM studies have been conducted to investigate the behaviour of cohesive solids using the above mentioned contact models. Moreno-Atanasio *et al.* (2005) conducted DEM simulations of a uniaxial test using JKR elastic adhesive contact model to investigate the effect of cohesion on the flowability of a polydisperse particulate system. The mechanical properties of glass beads were used as DEM input parameters. They argued that for consolidation stresses in the range of 0-10 kPa the model produced unconfined yield strengths that could be classified as highly cohesive according to Jenike's classification. The unconfined strength increased with increasing consolidation stress showing stress history dependence. It may be argued that the stress history dependence is because the cohesive powder forms a loose initial structure which collapses on the application of load resulting in particle re-arrangement into a denser packing so that the deformation does not recover significantly on the removal of load, especially at low stress levels. The use of an elastic contact model may be suitable for simulating some materials such as elastic glass beads at low stresses where deformation is mainly due to particle re-arrangement. However, for many industrial processes, the stress can be much higher and the materials are evidently not elastic. In the case of cohesive solids, an adhesive elastic contact model may not be able to represent the realistic behaviour, where the permanent plastic deformation gives rise to stress history dependent behaviour.

Hassanpour and Ghadiri (2007) conducted both experimental and DEM studies on the flowability of powders using indentation and uniaxial compression tests on a small assembly of powders compacted at low pressures. They adopted a contact model based on the Hertzian analysis for the elastic regime, Thornton and Ning's (1998) model for the plastic deformation and the JKR theory (Johnson et al., 1971) for the adhesion force. DEM simulations based on single particle mechanical properties showed that the unconfined yield strength varies linearly with the consolidation stress, which is similar to the experiment, but there is a poor quantitative agreement between experiment and simulation, with a discrepancy up to 160%. The discrepancy was attributed to rough estimation of the adhesion parameter and the adoption of spherical particle shape in the DEM simulation.

The great majority of DEM studies in the literature were conducted using either 2D disks or 3D spheres. A number of numerical and experimental studies (Aoki and Suzuki, 1971; Chong et al., 1979; Li et al., 2004; Roberts and Beddow, 1968) have shown that particle shape affects the flowability of the powder. While spherical particles with higher rolling friction are introduced to simulate particle shape by many researchers (e.g.Wensrich and Katterfeld, 2012), it has been reported that spherical particles cannot represent the "real" solids regardless of the angle of inter-particle friction (Cleary, 2010). The spherical particles fails to capture interlocking related dilation, voidage distribution, and material shear strength arising from interlocking (Cleary, 2010). Therefore, it is important to introduce an appropriate degree of non-sphericity in particle shape to capture the behaviour of real solids which are very rarely spherical. This study deploys 3D non-spherical particle using multi-sphere technique as described in (Favier et al., 1999) which is also being used by many others (Chung and Ooi, 2006; Härtl and Ooi, 2008; Kodam et al., 2009; Kruggel-Emden et al., 2008; Thakur et al., 2013).

4.3 *Proposed contact model*

While JKR and DMT contact models are widely accepted contact models for an elastic sphere with adhesion, a number of elastic contact models including JKR (Johnson et al., 1971), DMT ((Derjaguin et al., 1975), Maugis (1992), and Matuttis and Schinner (2001) may not be able to capture the stress history dependent behaviour shown in experiments of cohesive powders (Bell et al., 2007; Enstad and Ose, 2003; Freeman and Fu, 2011; Parrella et al., 2008; Röck et al., 2006; Williams et al., 1971). Since the contact area between two fine particles is very small, even moderate forces (in the order of 1 nN) can cause plastic deformation at the contact (Tomas, 2007) which can give rise to a stress history dependent behaviour. Therefore, it is proposed that contact plasticity has an important role in correctly simulating the stress history dependency. While the elasto plastic contact models proposed by Thornton and Ning (1998) and Tomas (2001) are the most realistic, they have complicated formulations and can be computationally intensive to implement. The elastoplastic and adhesive contact model proposed by (Luding, 2008) and Walton and Johnson (2009) may not capture all the minute details at the particle contact, however these contact models are easy to implement, less computationally intensive and more suitable for simulating bulk system. The proposed contact model is conceptually similar to Luding's and Walton and Johnshon's model but has the additional capability of non-linearity for the loading and unloading paths. Atomic Force Microscopy (AFM) measurements of the contact force displacement curve of very fine particles of fumed silica and titania have shown smooth non-linear behaviour during both loading and unloading (Jones, 2003b). The non-linear behaviour after plastic yielding has also been reported by Vu-Quoc and Zhang (1999). In order to model both linear and nonlinear Normal Force Displacement behaviour of real solids, a power law is proposed for both loading and unloading paths in the contact model. The model comprises a nonlinear hysteretic spring model to account for the elastic-plastic contact deformation and an adhesive force component that is a function of the plastic contact deformation.

The DEM contact model proposed here is based on the physical phenomena observed in adhesive contact between micron sized particles (see Figure 2.14) or small agglomerates (Jones, 2003a). When two particles or agglomerates are pressed together, they undergo elastic and plastic deformations. It is assumed that the pull-off (adhesive) strength increases with an increase of the plastic contact area. A non-linear contact model that accounts for both the elastic-plastic contact deformation and the contact-area dependent adhesion is proposed. The schematic diagrams of particle contact and normal force-overlap (f_n– δ) curve for this model are shown in Figure 4.1.

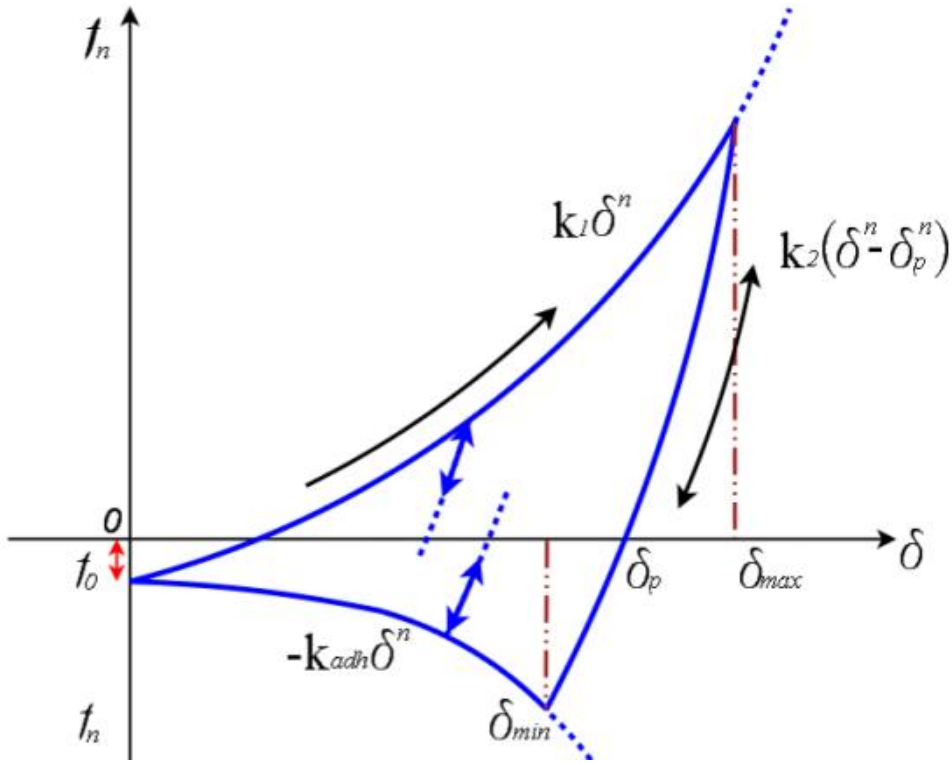

Figure 4.1 Normal contact force-displacement function for the nonlinear contact model

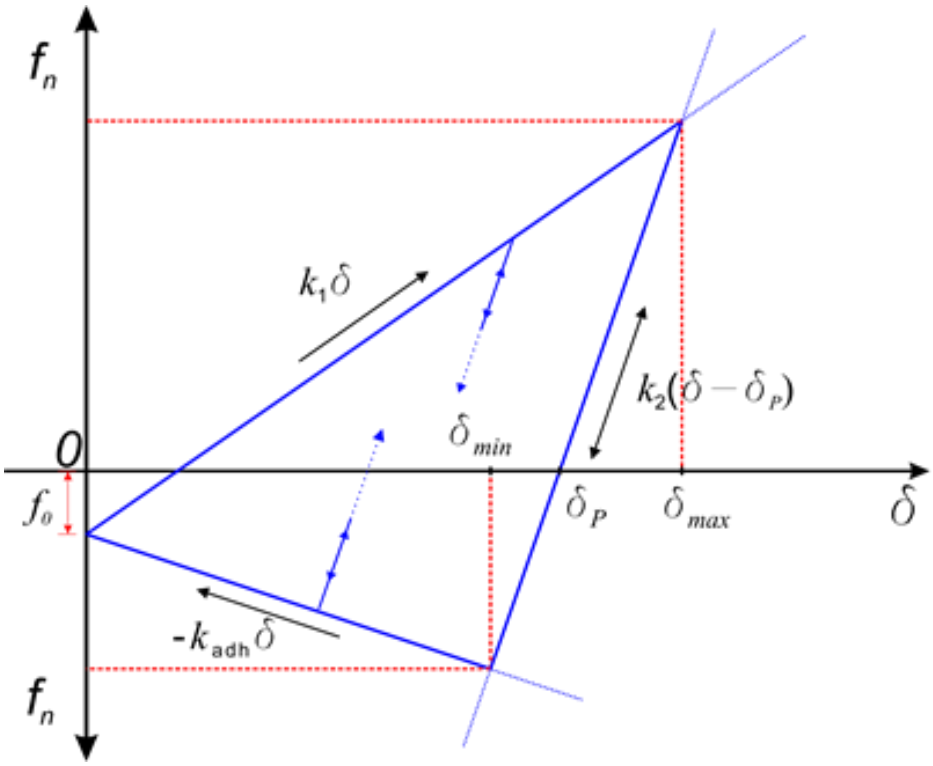

Figure 4.2 Normal contact force-displacement function for the linear contact model

The loading, unloading, re-loading, and adhesive branches are characterised by five parameters: the virgin loading stiffness parameter k_1, the unloading and reloading stiffness parameter k_2, the constant adhesive strength f_o, the adhesive stiffness parameter k_{adh} and the stiffness exponent n. During the initial loading, the contact model follows the virgin loading path, k_1, upon unloading of the contact; the contact will switch from the virgin loading path to the unloading/reloading path, k_2. During reloading, the contact force initially follows along the reloading k_2 path but switches to the virgin loading k_1 path when the previous maximum loading force is reached. Unloading along the k_2 path below the plastic overlap δ_p results in the development of an adhesive force until the maximum adhesive force is reached at $-k_{adh}\,\delta_{min}^{\,n}+f_0$. Further unloading past this point results in a reduction in both the normal overlap and the adhesive force until separation occurs ($\delta=0$). If reloading of the contact occurs while on the adhesion branch, the contact will reload along a k_2 path (there is an infinite number of k_2 paths depending on the point of first unloading), until the virgin loading k_1 path is reached, and will continue loading along k_1 path on further increase

of load. The contact information is lost when the particles are separated. This model does not consider hysteretic behaviour during reloading/unloading of the contact below δ_{min} as in Tomas's model. If k_1 is set equal to k_2 the model is reduced to an elastic contact model.

The unloading/reloading stiffness k_2 is not load dependant as in Luding's model (Luding, 2008). The model has been implemented with a power law exponent parameter n to describe the shape of all the three loading-unloading branches – they all become linear when $n=1$ (Figure 4.2). Both linear and nonlinear trends for normal force displacement relationship have been reported in experiments (Jones, 2003b) and numerical studies (Vu-Quoc and Zhang, 1999). In this first study of the model, the focus is on studying the influence of the contact plasticity and adhesion parameters (k_2, k_{adh} *and* f_o) without invoking the nonlinearity by setting $n=1$ which reverts the contact model to a linear version that is similar to several existing models (Luding, 2008a; Walton and Johnson, 2009). The simulations conducted using the non-linear model can be found in (Morrissey, 2013). The contact model has been implemented through the API in EDEM® v2.4 (and subsequent versions), a commercial DEM code developed by DEM Solutions Ltd (DEM Solutions, 2010). All the simulations conducted in this thesis were performed using EDEM.

The total contact normal force, $\boldsymbol{f_n}$, is the sum of the hysteretic spring force, f_{hys}, and the normal damping force, f_{nd}:

$$\boldsymbol{f_n} = (f_{hys} + f_{nd})\boldsymbol{u}, \tag{4.1}$$

where, $\boldsymbol{u}$ is the unit normal vector pointing from the contact point to the particle centre. The force-overlap relationship for normal contact, $f_{hys,}$ is mathematically expressed by equation 4.2.

$$f_{hys} = \begin{cases} f_0 + k_1\delta^n & \text{if } k_2(\delta^n - \delta_p^n) \geq k_1\delta^n \\ f_0 + k_2(\delta^n - \delta_p^n) & \text{if } k_1\delta^n > k_2(\delta^n - \delta_p^n) > -k_{adh}\delta^n \\ f_0 - k_{adh}\delta^n & \text{if } -k_{adh}\delta^n \geq k_2(\delta^n - \delta_p^n) \end{cases} \tag{4.2}$$

The normal damping force, $f_{nd,}$ is given by:

$$f_{nd} = -\beta_n \boldsymbol{v}_{relative,n} \tag{4.3}$$

where $v_{relative,n}$ is the magnitude of the relative normal velocity, and β_n is the normal dashpot coefficient expressed as:

$$\beta_n = \sqrt{\frac{4m^* k_1}{1+\left(\frac{\pi}{\ln e}\right)^2}} \tag{4.4}$$

with the equivalent mass of the particles m^* defined as $(m_i m_j / m_i + m_j)$, where m is the mass of the respective particles, and the coefficient of restitution e defined in the simulation as an input parameter.

The contact tangential force, $\boldsymbol{f_t}$, is given by the sum of tangential spring force, $\boldsymbol{f_{ts}}$, and tangential damping force, $\boldsymbol{f_{td}}$., as given by:

$$\boldsymbol{f_t} = (\boldsymbol{f_{ts}} + \boldsymbol{f_{td}}). \tag{4.5}$$

The tangential spring force is expressed in incremental terms:

$$\boldsymbol{f_{ts}} = \boldsymbol{f_{ts(n-1)}} + \boldsymbol{\Delta f_{ts}}, \tag{4.6}$$

where $\boldsymbol{f_{ts(n-1)}}$is the tangential spring force at the previous time step, and $\boldsymbol{\Delta f_{ts}}$ is the increment of the tangential force and is given by:

$$\boldsymbol{\Delta f_{ts}} = -k_t \boldsymbol{\delta_t}, \tag{4.7}$$

where k_t is the tangential stiffness, and $\boldsymbol{\delta_t}$ is the increment of the tangential displacement. While varying values for the tangential stiffness have been used in the literature, in this study it is set as $2/7k_1$ (O.R. Walton and Braun, 1986).The tangential damping force is product of tangential dashpot coefficient, β_t, and the relative tangential velocity, $\boldsymbol{v_{relative,t}}$ as given by Eq.4.8:

$$f_{td} = -\beta_t \boldsymbol{v}_{relative,t} \tag{4.8}$$

The dashpot coefficient β_t is given by:

$$\beta_t = \sqrt{\frac{4m^* k_t}{1+\left(\frac{\pi}{\ln e}\right)^2}} \tag{4.9}$$

The limiting tangential friction force is calculated using the Coulombic friction criterion with an additive term f_o *and* k_{adh}, so that the observed friction is given by:

$$f_{ct} \leqslant \mu \, |f_{hys} + k_{adh}\delta^n - f_o| \tag{4.10}$$

where f_{ct} is the limiting tangential force, f_n is contact normal spring force and μ is the friction coefficient. The default EDEM rolling friction model is adopted in this study. The total applied torque, $\boldsymbol{\tau_i}$, is given by:

$$\boldsymbol{\tau_i} = -\mu_r \mid f_{hys} \mid R_i \, \boldsymbol{\omega_i}, \tag{4.11}$$

where μ_r is the coefficient of rolling friction, R_i is the distance from the contact point to the particle centre of mass and $\boldsymbol{\omega_i}$ is the unit angular velocity of the object at the contact point.

There is some limited evidence in support of Eq. (4.10) in the experimental results from Skinner and Gane (1972), who conducted micro-friction experiments between soft metal stylus and a hard smooth surface of graphite or diamond in a scanning electron microscope and found that the attractive force can be considered as an additive term to the normal force in calculation of limiting friction. Savkoor and Briggs (1977), and Thornton and Yin (1991) derived similar equation based on contact mechanics theory. The limiting friction criteria is consistent with the criteria set in other existing tangential force models (Luding, 2008a; Thornton and Yin, 1991; Tomas, 2003; Walton and Johnson, 2009).

The relationship between limiting friction and normal force is described in section 2.5.2. Both linear and nonlinear relationship between normal force and friction force is found in literature. Although both linear and nonlinear relationships have been found between normal load and friction in microscopic friction experiments, a linear relationship in this study is assumed for two main reasons. Firstly, real materials generally have multi asperity contacts and the literature suggests linear relationship for multi asperity or plastic contacts (Jones et al., 2004). Secondly, elasto-plastic behaviour for fine adhesive particles can be expected in most cases of industrial processing and handling where averaged macroscopic stresses are above 1kPa (Tomas, 2007), and the nonlinear behaviour observed at low stresses in Friction Force Microscopy (FFM) can be ignored.

4.4 *Modelling strategy*

The above contact model in its full generic form captures the key elements of the frictional-adhesive contact mechanics in that: f_0 provides the van der Waals type pull-off strength; k_1 and k_2 provide the elastic-plastic contact; k_{adh} provides the adhesion unloading stiffness; the exponent n provides the nonlinearity and the resulting contact plasticity defines the total contact adhesion (see Figure 4.1). The model is thus expected to be capable of modelling truly micron sized particles to study phenomena such as fine agglomeration, attrition and flow.

To apply the model at the single particle level requires the model parameters to be determined at the true particle-particle interaction level. This would require one to consider the enormous complexity of interfacial interaction including the influence of surface topology and chemistry and properties of the interstitial media etc. Whilst many studies have been reported on these measurements using microscopic measurement techniques such as AFM, Nano-indentation and others, the measurements tend to be on either highly idealised particle (such as specially manufactured perfect sphere) or suffer from enormous scatter and uncertainty with

regard to the accuracy of the measurement (Heim et al., 2005; Tykhoniuk et al., 2007). Additionally, it is prohibitive to model each and every individual particle and cohesion arising from several different phenomena including van der Waals, capillary bridge and electrostatic forces separately, even in a very small system of fine powders. For example, a uniaxial test simulation of a cylindrical sample of 40 mm diameter and 80 mm in height with 4.7 μm sized limestone powder containing $>10^{12}$ particles may take in the order of 60 years if this was to be simulated with a 4 core, 64-bit computer.

This study focuses on an intermediate scale between the micro- and macro-scales, aiming to produce a phenomenological contact model that can reproduce the bulk cohesive strength, stress history dependency, and other behaviour evidenced in experiments. This study deploys 3D non-spherical particles in conjunction with a calibration strategy recognising the differences between the model and the real solids at the particle level to reproduce the bulk granular friction of a particulate system. The calibration of a mesoscopic DEM contact model requires experimental measurements characterising the mechanical behaviour of powders. The mechanical behaviour of cohesive powders can be carefully measured using element tests such as biaxial test, true triaxial and hollow cylinder tests. However in practice these tests are expensive and slow to conduct and are almost never performed for many industrial applications requiring material characterisation. Here a simpler technique that could be used for filling this important gap with the focus of providing test data for model calibration and simulation validation is investigated.

In this study, the Edinburgh Powder Tester, EPT (Bell et al., 2007) is employed. The EPT is a semi-automated uniaxial tester, providing rapid measurements of various bulk mechanical properties of powders, including the stress–strain and the stress–porosity response during confined compression as well as the stress–strain response during unconfined compression including the peak unconfined strength. The

reproducibility of results has been assessed for various materials with a coefficient of variation of typically less than 7% (Morrissey, 2013; Thakur et al., 2013).

In an EPT test, the sample is poured into the consolidation cylinder of diameter 40 mm and height 80 mm. The sample is loaded by a weight and the force is recorded by a load cell attached to the consolidation plunger. To minimise the effect of the friction between the particles and boundaries (Enstad and Ose, 2003), the sample is allowed to compress from both the top and bottom in the EPT. After the sample is loaded for a selected consolidation time, the consolidation plunger is automatically retracted and the mould is manually slid down the pedestal, exposing a free standing column of consolidated powder sample. The unconfined sample is loaded to failure by a motor driven test piston at a speed of 0.4 mm/s, which was so chosen to conduct the test rapidly without affecting the measured unconfined yield strength. Watanabe and Groves (1964) found that the unconfined strength of detergent samples was unaffected when the piston speed varied from 0.084 to 0.43 mm/s. The unconfined strength is automatically recorded, as well as the whole load-displacement curve. Consolidation stresses in the range of 16-96 kPa were applied in this study with 1 minute consolidation time. ESKAL 500® (*KSL Staubtechnik GmbH*), a limestone powder with particles of 4.7 μm mean diameter was tested in this study (Figure 4.3).

4.5 *Numerical simulation set-up*

The DEM was used to simulate a series of uniaxial test experiments in a cylindrical mould. The proposed contact model was only applied to particle-particle interactions. Particle-geometry interactions were modelled using the Hertz-Mindlin (no-slip) contact model and hence no particle-geometry adhesion was allowed. Non-spherical particles were used, each consisting of two overlapping (paired) spheres of 1 mm diameter (*d*) giving a particle aspect ratio of 1.5 (Figure 4.4). This relatively simple two-sphere shape was chosen based on the findings from two studies. The first study (Chung, 2006) showed that accurate representation is not necessary to produce

satisfactory predictions as long as there is sufficient shape interlocking to generate the bulk friction. The second study showed that for purely spherical system, the maximum bulk friction under direct shear testing saturates at ~0.8 even for sliding friction of up to 2.0, whereas for two overlapping sphere with aspect ratio of 1.5, a full spectrum of bulk friction up to ~1.9 can be predicted (Härtl and Ooi, 2011). Thus, by choosing the two-sphere model, it can be expected that the DEM model to be able to capture a wide range of bulk frictional characteristics for any real complex shape particles.

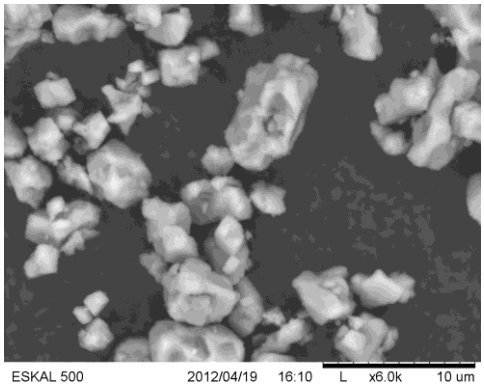

Figure 4.3 Scanning electron microscopic (SEM) image of ESKAL 500

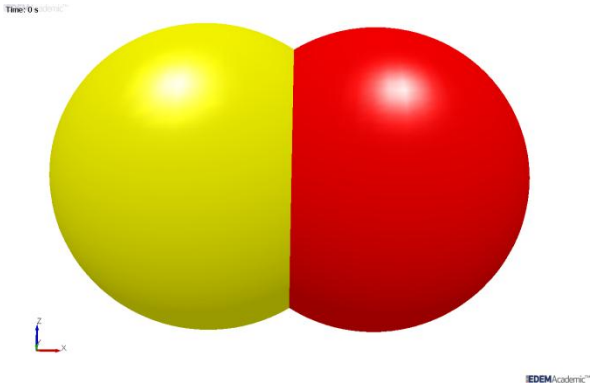

Figure 4.4 Paired particle of aspect ratio of 1.5 used in DEM

The parameters used in the simulations are listed in Table 4.1. The loading stiffness k_1 was chosen so that it is sufficiently stiff to avoid excessive particle overlap but not too stiff to avoid significant computational cost, and yet provide a close match to the experimental loading response. In order to reduce the computational time further, density scaling (Sheng et al., 2004) was used as simulations are in quasi-static regime. The inertial number is often used to measure the significance of the dynamic effects in granular material. Inertial number is the ratio of measure of inertial forces of particles to imposed force:

$$I = \frac{\dot{\gamma} d_{avg}}{\sqrt{P/\rho}} \tag{4.12}$$

where $\dot{\gamma}$ = shear rate, davg=average particle diameter, P=pressure, and ρ= particle density.

An inertial number of less than $1x10^{-4}$ was observed for all simulation parameters and confirms that the simulations are in the quasi-static regime (Midi, 2004). The simulation time step was chosen to be equal to $0.1\sqrt{m/k_2}$: no noticeable difference in results was found between simulations with time step of $0.03\sqrt{m/k_2}$ and $0.1\sqrt{m/k_2}$. The ratio of k_2/k_1 was varied from 1 to 100 by increasing k_2. Since the constant adhesive strength f_0 and the load-dependent adhesion represent different origins leading to cohesion, they are studied separately in section 6 for the former and 7 for the latter.

Table 4.1 Simulation parameters

Number of Particles	2200
Particle aspect ratio	1.5
Particle Density, ρ *(kg/m^3)*	10000
Coefficient of restitution, e (particle to particle and particle to wall)	0.4
Loading Spring Stiffness, k_1 *(kN/m)*	1
Unloading Spring Stiffness, k_2 *(kN/m)*	1, 1.25, 2, 5, 10, 100
Adhesive strength at first contact or constant adhesive strength, f_0, *(N)*	-0.002~-0.05
Adhesive Parameter Stiffness, k_{adh} *(kN/m)*	0.1 ~ 100
Particle Static Friction, μ_{sf}	0.5
Particle Rolling Friction, μ_{rf}	0.001
Wall Friction, μ_{wf}	0
Top and Bottom Platen Friction, μ_{Pf}	0.1
Platen speed, (s^{-1})	0.1-0.2
Simulation Time-step (s)	8×10^{-7} ~ 2×10^{-6}

DEM simulations using the proposed contact model were conducted for a series of uniaxial compression tests in a cylindrical mould of 15 mm diameter with top and bottom platens. This represents a scale of approximately 1/3 of the original experimental set-up, to reduce the computational cost. The initial filling height varied with DEM input parameters. However, the consolidated aspect ratio of the sample

for the DEM simulations was kept in a narrow range of 1.2 to 1.4 which was used in the experiment. Each simulation consists of three stages – filling the cylindrical mould to form the initial packing used for all stress levels; confined consolidation to the required stress level and subsequent unloading; and finally unconfined compression of the sample to failure after the removal of the mould. The process is visualised in Figure 4.5.

Figure 4.5 DEM simulation of uniaxial test: a) loading, b) unloading, and c) unconfined compression

The random rainfall method was adopted to form a random packing. To ensure that the system reached a quasi-static state, loading only commenced when the kinetic to potential energy ratio was less than 10^{-5} with a constant coordination number. The potential energy in the system is calculated based on a datum level of z_d = 0mm, which in this study relates the bottom of the mould. The confined consolidation process was conducted by moving the top platen downwards at a constant speed of 5mm/s (strain rate ≈ $0.2s^{-1}$) to apply a vertical compression. After consolidating the sample to the desired stress, the load on the assembly was released by moving the top platen upwards at the same constant speed. The lateral confining walls were then removed and the unconfined sample was allowed to relax for 0.1 seconds. This allowed the kinetic energy generated from the removal of the confining wall and

upward retreat of the top platen to dissipate. The sample was then crushed to failure by moving the top platen downwards again, at a constant rate of 2 mm/s (strain rate ≈ 0.1 s^{-1}). To investigate the effect of applied strain rate, simulations were conducted with varying strain rate in a range of 0.02 to 60 s^{-1}, for elastic ($k_2=k_1$) and elasto-plastic ($k_2=100k_1$) case. For both cases, it was found that confined and unconfined stress-strain behaviour does not change significantly with strain rate below 0.5s^{-1}. Therefore, a strain rate smaller than 0.5s^{-1} was chosen in this study. The effect of strain rate on confined and unconfined compression is studied in detail in Chapter 6. The failure of the sample was characterised by a drop in stress accompanied by a drop in the coordination number (Z) (see Figure 4.16). The bottom platen remained stationary in all stages.

4.6 *Numerical repeatability and prediction of flowability*

Three numerical samples (samples 1, 2 and 3 below) with the same model parameters were created using the random particle generator implemented within the particle factory in the commercial code. These samples were then consolidated to 100 kPa prior to an unconfined compression test to failure to assess the variability in the results related to the generation of different particle packings in the assemblies. The scatter of these numerical samples was evaluated. Figure 4.6 and Figure 4.7 present the axial stress-strain response during confined and unconfined compression, respectively. For confined compression, some variations in the stress-strain behaviour are noted. For unconfined compression, the average unconfined strength was found to be 6.6 kPa with a coefficient of variation (COV) = 3.4 %. The small COV indicates that randomly generated particle assembly has minor effect on the bulk response. While three data points would not usually be considered sufficient for rigorous statistical analysis, the very low COV indicates that the numerical scatter introduced by the random initial packing is small. The presence of numerical scatter should always be checked and used in the interpretation of the numerical results.

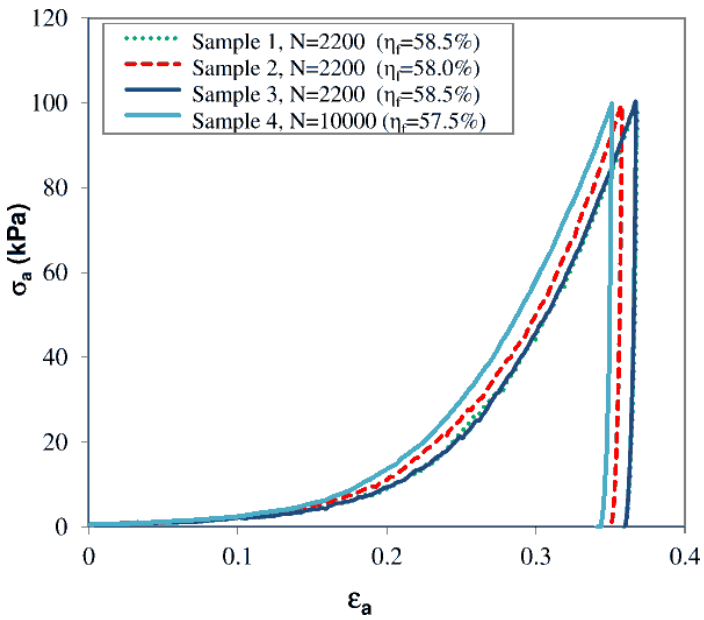

Figure 4.6 Confined compression - axial stress (σ_a) vs axial strain (ε_a) for three random simulations and a large size simulation

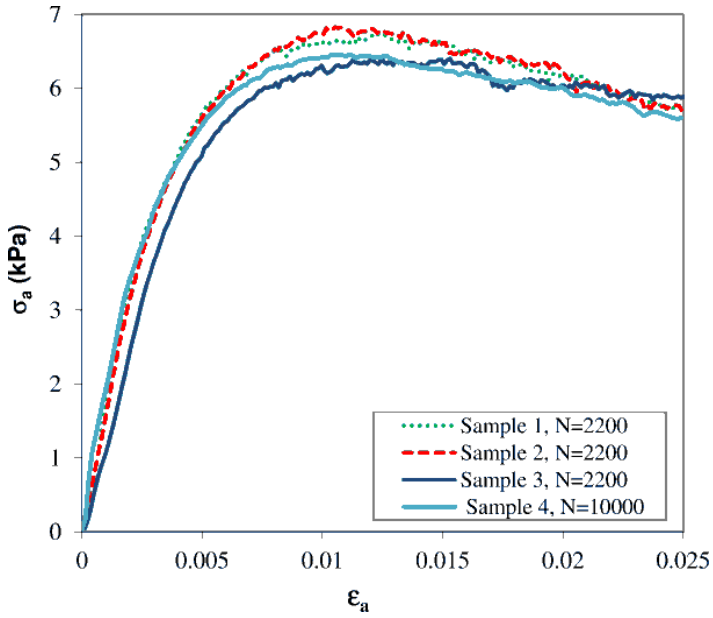

Figure 4.7 Unconfined compression- axial stress (σ_a) vs axial strain (ε_a) for three random simulations and a large size simulation

(Contact model parameters used are: f_0 = -0.002N, k_2 =100 and k_{adh} =0 kN/m (Note: N=number of particles, η_f=porosity corresponding to 0.5kPa stress)

To investigate the influence of numerical sample size, an additional simulation (sample 4) with 10,000 paired-sphere particles was performed and the results are included in Figure 4.6 and Figure 4.7. The comparison shows that the sample size does not have a significant effect on the prediction. For confined compression, the 10,000 particle system predicted ~1.5% smaller compression at the peak compared to the average peak strain of the samples with 2,200 particles. This can be attributed to a lower filled porosity for the 10,000 particle system because of a smaller boundary effect. For unconfined compression to failure, the unconfined peak strength is also within the scatter of the measurement for 2,200 particles. A more rigorous assessment of sample size would require more repeat random simulations to establish the statistical scatter which is beyond the scope of this study.

The capability of the model is explored for predicting the unconfined yield strength of Limestone A (ESKL 500-a PARDEM reference solid) under different consolidation stresses. Figure 4.8 shows the predicted axial stress-strain responses during unconfined uniaxial compression of samples which have been consolidated at five stress levels: 16, 36, 56, 76, and 96 kPa. The initial loading stiffness increases as the consolidation stress increases. This has arisen from the change in the packing structure with decreasing porosity as consolidation stress increases. The maximum stress during unconfined compression (i.e. the unconfined strength σ_u) is plotted against the consolidation stress (see Figure 4.9). For the parameters chosen, the model predicted a flow function that is in good quantitative agreement (within ~12%) with the experimental results. The simulation results show a strong dependence on the consolidation stress history as measured in the experiments. The reason for this stress-history dependency is related to the contact plasticity: the micromechanical aspects will be elucidated in the following section.

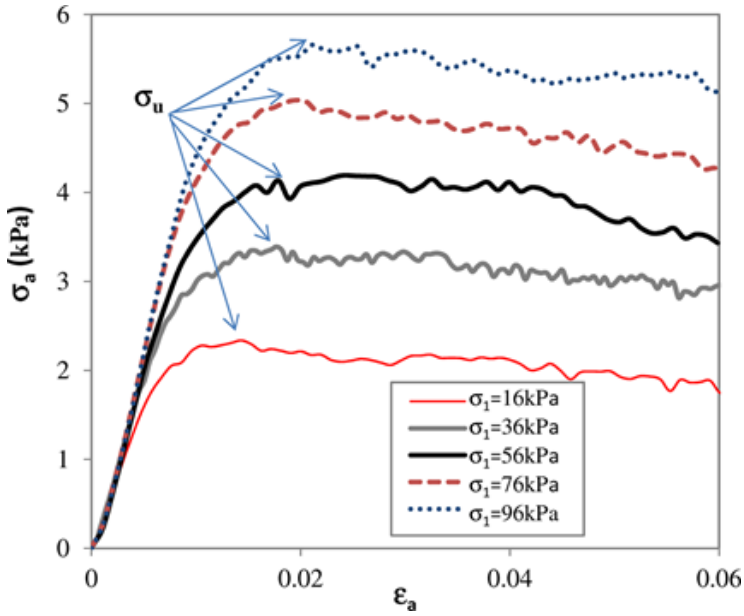

Figure 4.8 Predicted unconfined axial stress (σ_a)-strain (ε_a) relationship.

Contact model parameters used are: f0=-0.003 N, k2=3.5 and kadh=0 kN/m

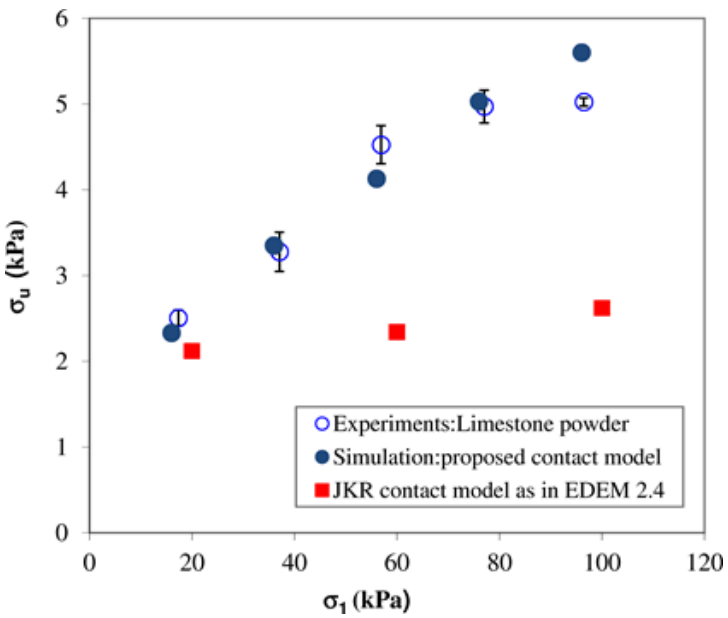

Figure 4.9 Predicted vs. test flow function for a limestone powder.

Contact model parameters used are: f0=-0.003 N, k2=3.5 and kadh=0 kN/m

Figure 4.9 also shows the simulation results using the modified JKR cohesive model with an elastic Hertzian contact in the EDEM code version 2.4 (DEM Solutions Ltd., 2011) which show only a slight increase in unconfined strength as consolidation stress increases, giving an increasingly large discrepancy with the experimental observations with increasing consolidation stress. The results shown in Figure 4.8 and Figure 4.9 indicate that the implemented model is capable of capturing the salient features of a real cohesive powder.

4.7 *Micromechanical analyses of porosity, plasticity and cohesion*

The origin of the stress history dependent cohesion strength predicted by the model is explored here from a micromechanical point of view. The relationships between bulk material properties; namely the unconfined strength, the bulk plasticity and the porosity; and the microstructural properties are explored. Simulations of confined followed by unconfined compression, as described in Section 3, were performed for particle stiffness k_2 varying from 1 to 100 kN/m as listed in Table 4.1, and consolidation stress levels from 20 to 100 kPa. The level of contact plasticity was changed prior to the generation of the particles and was maintained for both the confined consolidation and unconfined compression to failure. The adhesion stiffness parameter k_{adh} was set to zero in the first instance so that the influence of the constant pull-off force f_0 can be explored (see Figure 4.10a).

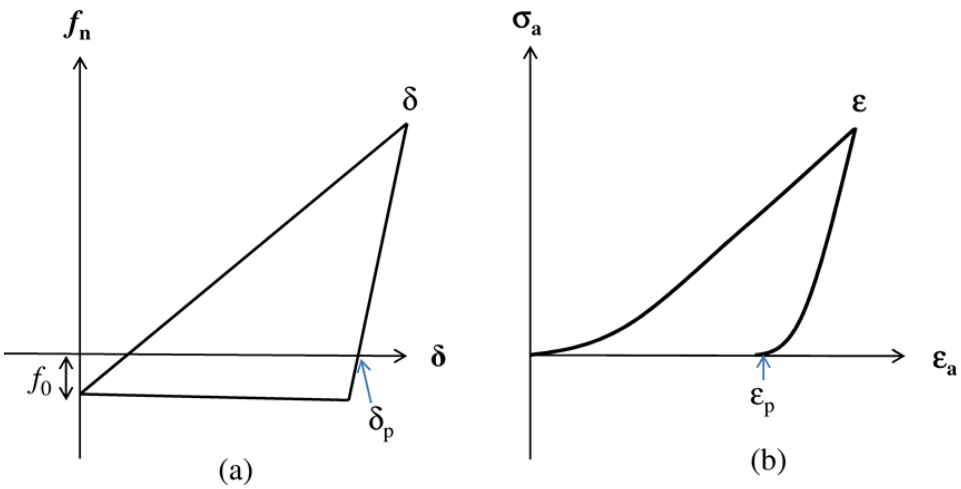

Figure 4.10 (a) Linear elasto-plastic contact model with constant contact adhesion (b) Typical bulk stress strain response during confined compression

In an elasto-plastic contact, the contact plasticity λ_p may be defined as the ratio of the maximum plastic deformation δ_p to the total deformation δ at the contact. For the linear version of the contact model (n=1, see Figure 4.10a), λ_p becomes a simple function of the loading k_1 and unloading k_2 stiffnesses:

$$\lambda_p = \frac{\delta_p}{\delta} = 1 - \frac{k_1}{k_2} \qquad \textbf{(4.13)}$$

Similarly the bulk plasticity can be defined as the ratio of the bulk plastic deformation ε_p to the total deformation ε, as shown in Figure 4.10b.

$$\lambda_b = \frac{\varepsilon_p}{\varepsilon} \qquad \textbf{(4.14)}$$

Figure 4.11 shows the predicted flow functions for a range of contact plasticity (induced by varying the stiffness ratio k_1/k_2). The slope of the flow function is an indication of the level of cohesion for a given set of parameters. The level of cohesion can increase from two sources: increasing coordination number and flattening of the contact under loading. It is evident that the flow function is strongly dependent on the contact plasticity: a cohesive material with a constant particle-level adhesion force f_0 can change from being only slightly cohesive to moderately cohesive when the contact plasticity λ_p increases from 0 (elastic - no residual inter-particle contact deformation after unloading) to nearly 1 (no recovery of elastic deformation after unloading). When the contacts are elastic, the stress-history dependency largely disappears. Increasing the level of contact plasticity, which reduces elastic rebound, allows the consolidated assembly to maintain a lower consolidated porosity following unloading of the sample. The lower consolidated porosity in-turn leads to a higher number of inter-particle contacts, which generates a higher unconfined strength when the assembly is failed. Since load dependent adhesion was intentionally set as zero ($k_{adh}=0$: see Figure 4.10a), the increasing level of cohesion with increasing contact plasticity relates solely to the increasing contacts between particles.

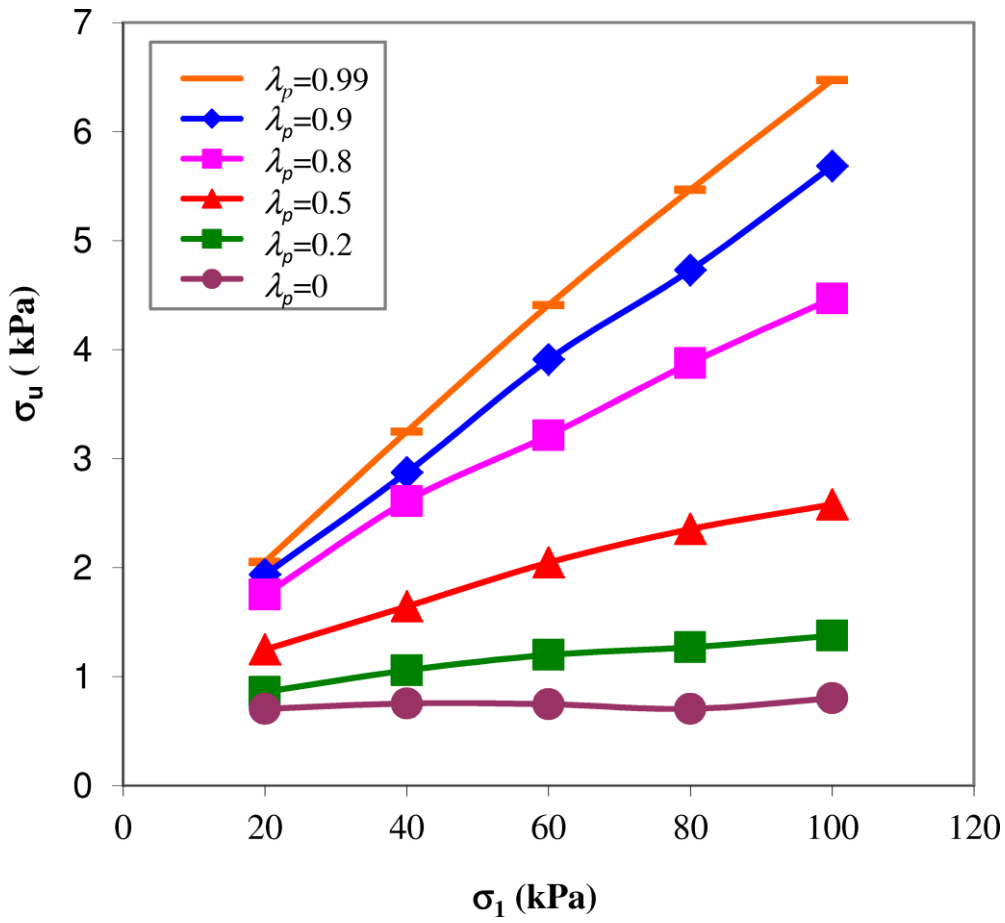

Figure 4.11 Effect of particle contact plasticity on flow function (f_0=-0.002 N, K_{adh}=0 kN/m)

The loss of stress-history dependent unconfined strength when contacts are elastic explains why adhesive models with elastic contact such as JKR and DMT models have difficulties in adequately capturing the stress history effect of cohesive solids. Most fine cohesive powders exhibit plasticity even at relatively low consolidation stress where a modest amount of force may lead to plastic yielding and irreversible deformation at the tiny particle-particle contact (Luding and Alonso-Marroquin, 2011). As shown by Hietsland (1997), a modest amount of plastic deformation at particle contact may cause a dramatic increase in the strength of consolidated powders, which is in line with the simulation results in this study. From the mesoscopic perspective where a DEM particle represents a local assembly of primary particles, it is easy to see the presence of contact plasticity. An appropriate level of plasticity in the contact model should be included when modelling cohesive powders.

Figure 4.12 shows the effect of particle contact plasticity λ_p on bulk plasticity. It is seen that the bulk plasticity increases with increasing λ_p. When λ_p is small, the bulk plasticity arises predominantly from particle rearrangement which is greater during initial compression from the loose filled state; this give rise to a larger bulk plasticity $\varepsilon_p/\varepsilon$ for a smaller consolidation stress. As λ_p increases and contributes to overall deformation, the bulk plasticity $\varepsilon_p/\varepsilon$ increases as expected, but this must approach unity as the contact plasticity λ_p approaches unity. On its own, bulk plasticity cannot fully explain the stress history effect of a material because particles with elastic contacts can have very different bulk plasticity (see Figure 4.12) but very little stress history effect (see Figure 4.11), whilst particles with elastic-plastic contacts can have similar bulk plasticity but very strong stress history dependence.

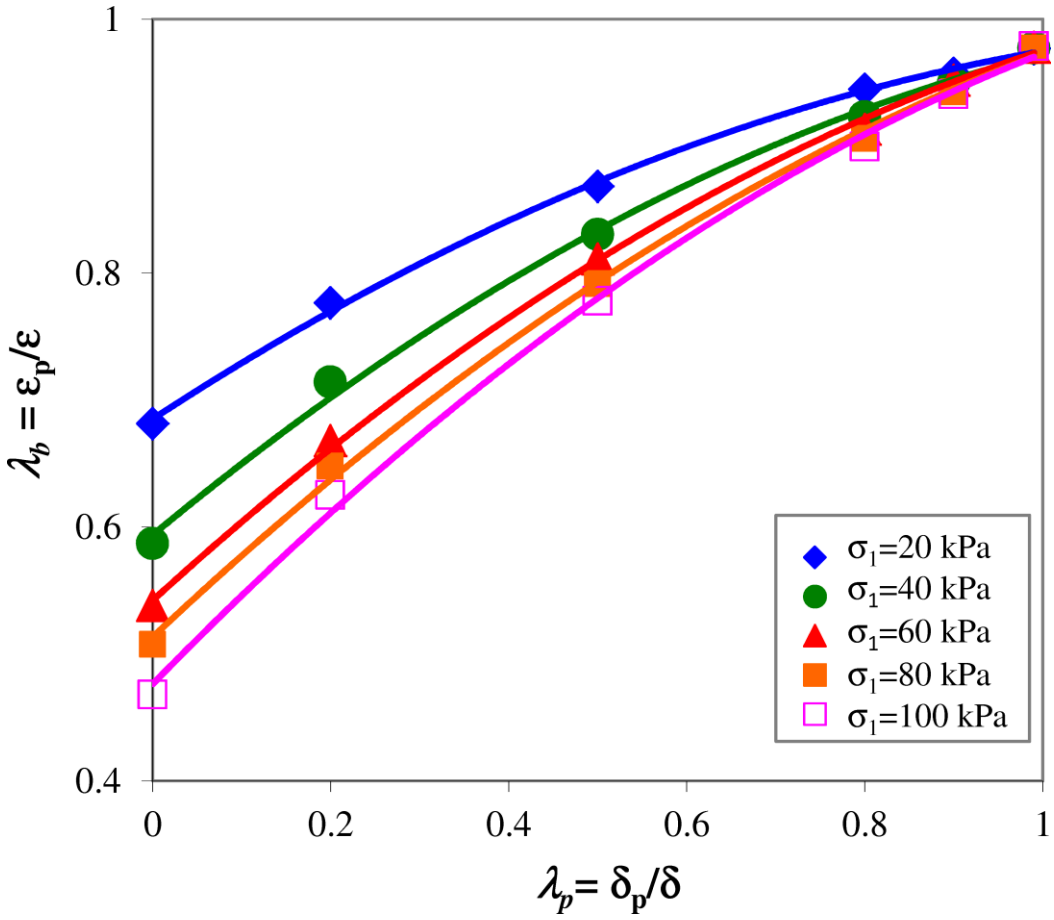

Figure 4.12 Bulk plasticity ($\varepsilon_p/\varepsilon$) as a function of particle plasticity

Figure 4.13 shows the effect of contact plasticity λ_p on the loading-unloading response under confined compression. Three cases are shown: elastic contact (λ_p =0), almost rigid plastic contact (λ_p =0.99) and an intermediate value of plasticity (λ_p =0.5). Even for elastic contact, significant bulk plastic deformation can arise from particle rearrangement. As contact plasticity increases, plastic contact deformation increases under loading resulting in a stiffer response on unloading. The softer loading responses with increasing λ_p appears surprising at first since the loading parameter k_1 was set to be constant for all three cases. The answer lies in the larger initial sample porosity when λ_p is larger. A closer look at the DEM results show that a larger contact plasticity λ_p gives rise to a greater degree of clustering during the filling process which resulted in larger voids between the clusters: this gives rise to a greater initial porosity and hence a softer response during compression. This is further highlighted in Figure 4.14, where the variation in sample porosity with consolidation stress is plotted. At low consolidation stresses there is a significant difference in the observed porosities which converge onto a single loading curve at greater consolidation stresses (say 5 kPa). For the unloading path, particle contact plasticity significantly affects the bulk unloading stiffness as expected. As the contact plasticity decreases the assembly rebounds to a higher consolidated porosity.

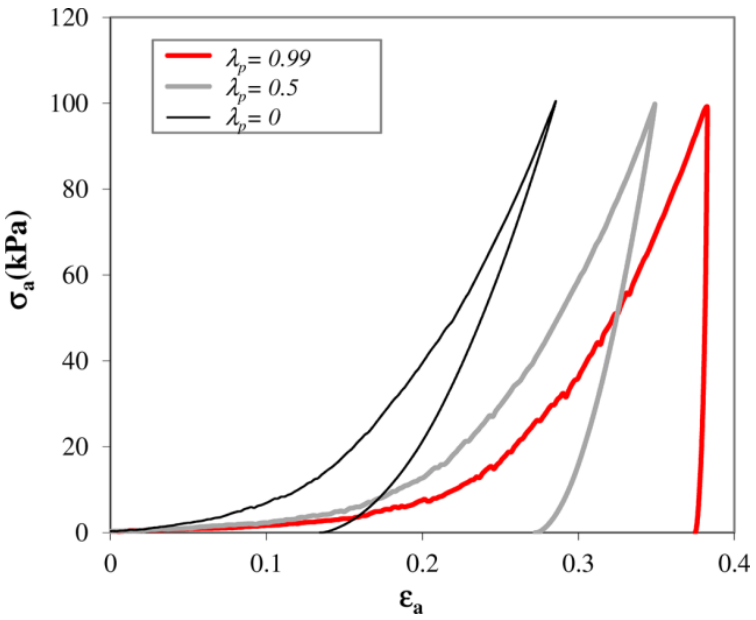

Figure 4.13 Confined compression- axial stress (σ_a) vs. axial strain (ε_a) with λ_p = 0

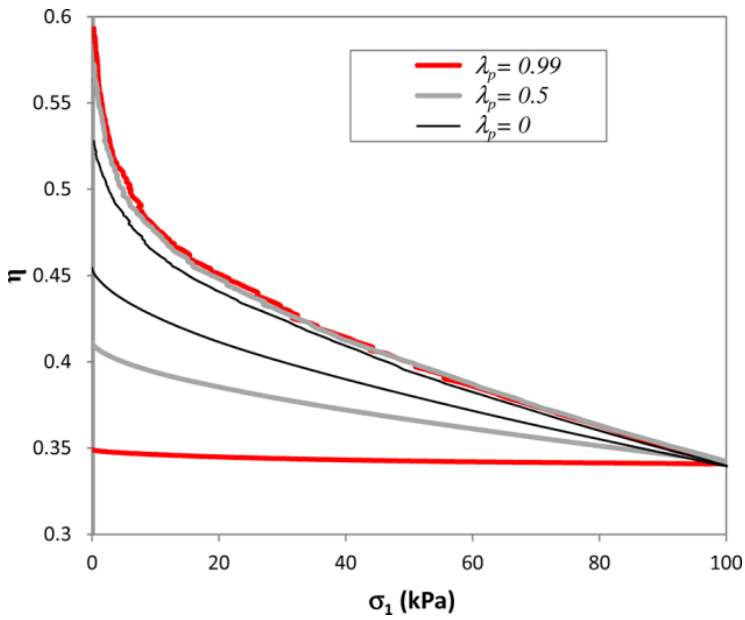

Figure 4.14 Confined compression- porosity (η) vs. axial strain (ε_a) with λ_p = 0.99

Next the relationship between porosity and unconfined yield strength is explored. Figure 4.15 plots the unconfined yield strength (σ_u) against the consolidated porosity after unloading (η_c) for different contact plasticity λ_p. For each λ_p, σ_1 varies from 20 kPa to 100 kPa, with the porosity at 20 kPa being the highest in all cases. As the consolidation stress increases, the unconfined yield strength increases whilst the porosity decreases, similar to the findings from conventional soil/powder consolidation experiments (Schofield and Wroth, 1968). The dependence on contact plasticity is evident where increasing λ_p has resulted in an increasing range of consolidated porosity η_c which gives rise to an increasing range of unconfined strength. However the lines are unique below a plasticity of 0.8, so the bulk porosity alone is not sufficient to account for the history-dependent strength across materials with different contact plasticity. Above a plasticity of 0.8 the results seem to converge. This is because as the level of contact plasticity tends above 0.8, the coordination number reaches a limiting value for a certain consolidated porosity (only true when f_o=constant and k_{adh}=0).

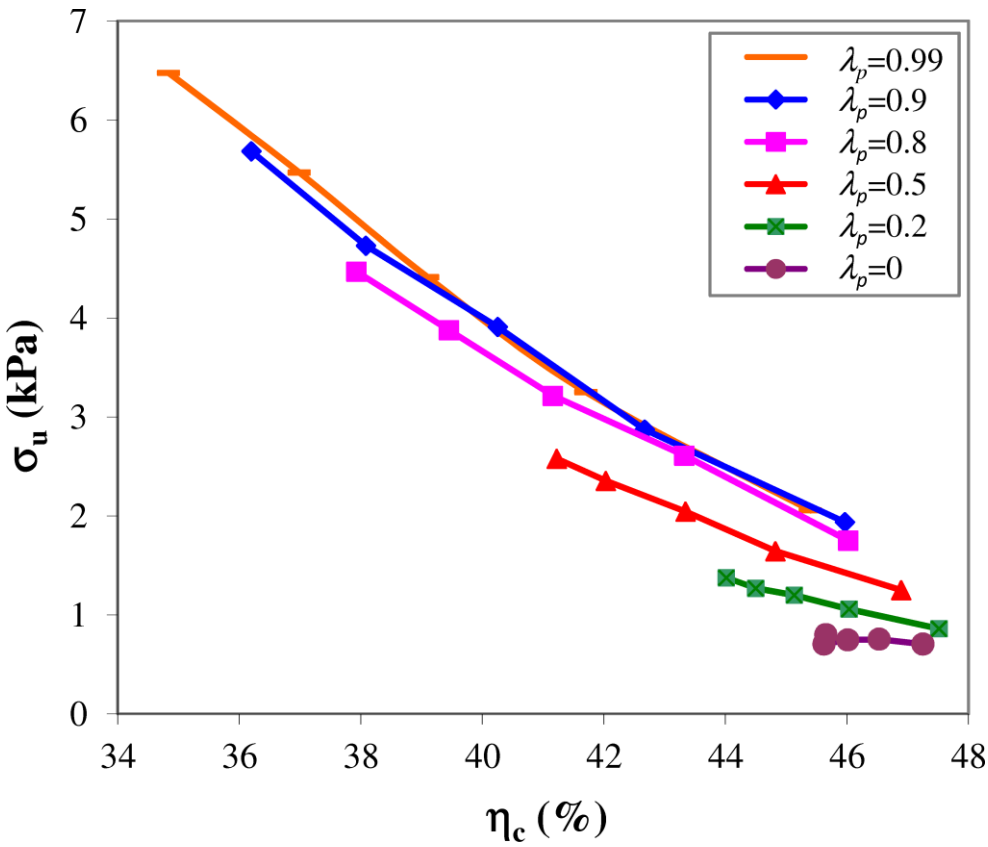

Figure 4.15 Unconfined strength (σ_u) as a function of consolidated porosity (η_c) at different contact plasticity

Figure 4.11 above has shown how the unconfined strength increases with increasing consolidation stresses at different levels of contact plasticity. To explore the mechanism for this stress-history dependence, the stress-strain loading paths to failure for several simulations are re-plotted in terms of the normalised axial stress and the instantaneous coordination number (Z_i) in Figure 4.16. The axial stress (σ_a) is normalised with f_0/d^2 which relates to particle adhesive strength. The arrows indicate the direction of loading, from the start of unconfined loading to post-peak. As loading progresses, the axial stress increases strongly with only a very small decrease in the coordination number before reaching the peak (unconfined strength). Further loading of the sample following the peak leads to a significant drop in the observed coordination number which is associated with increasing dilation (increasing volume) and decreasing post peak strength (Jenike, 1964; Schofield and Wroth, 1968). This trend is consistent for all simulations in this study.

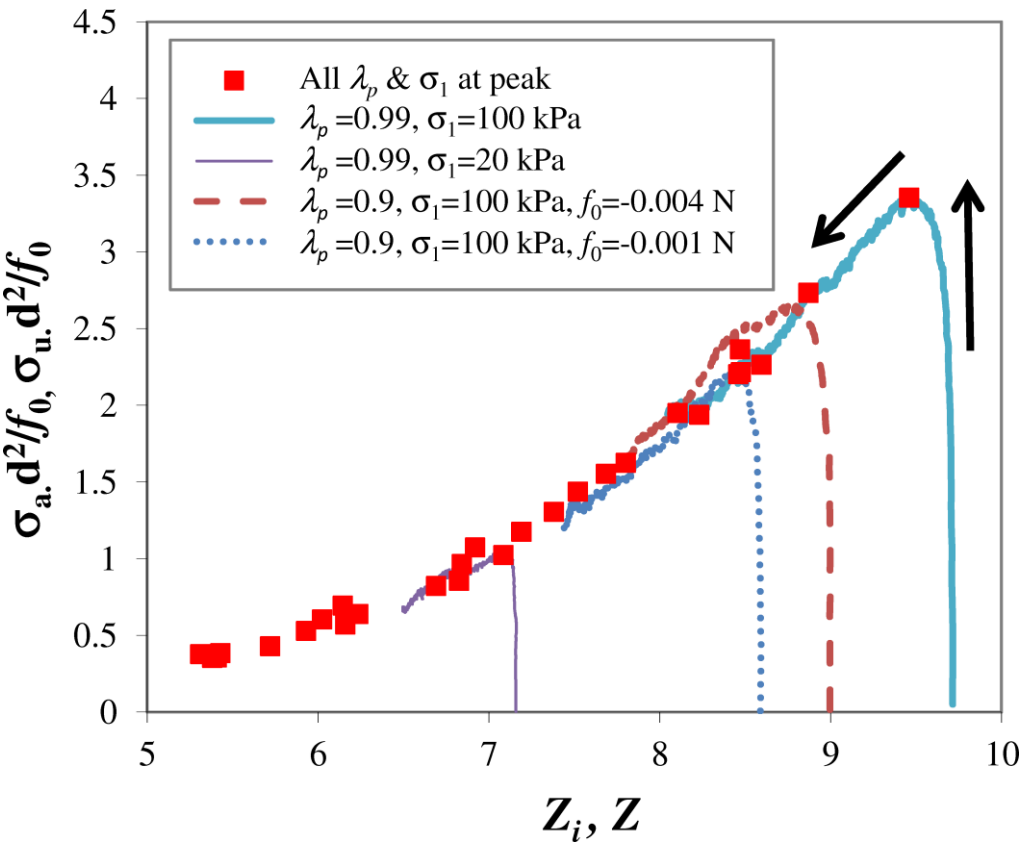

Figure 4.16 Normalised unconfined strength ($\sigma_a d^2/f_0$, $\sigma_u d^2/f_0$) versus coordination number (Z_i, Z): f_0=-0.002N unless stated explicitly

Superimposed on Figure 4.16 are the normalised unconfined strength $\sigma_u d^2/f_0$ and the coordination number Z at the peak for all simulations with $k_{adh}=0$ (denoted by ■). All data points collapse into a single 'critical curve' for the full range of contact plasticity and consolidation stresses in Figure 4.11. This critical line is analogous to the concept of critical state in soil mechanics (Wood, 1990). It indicates that with a constant contact adhesion f_o (k_{adh}=0), the microscopic mechanism for the increasing bulk cohesion under increasing stress (stress-history effect) is due to the increasing number of contacts as a result of both the consolidation stress and contact plasticity.

4.8 *Interaction between adhesion parameters*

Cohesion in bulk materials may arise from different sources of adhesion at particle level and these are represented by two parameters in the contact model: f_0 and k_{adh}. In

the section above, the bulk cohesion arising only from a constant adhesive strength f_0 coupled with contact plasticity is explored. In this section the interaction between the two is studied. Simulations with constant adhesion only, load-dependent adhesion (f_0=0, k_{adh} ≠0) only, and with both f_0 and k_{adh} not equal to zero were performed. The effect of these parameters on fill porosity, compressibility, and flow function are investigated below.

The effect of contact adhesion on fill porosity (η_f) which is defined as the sample porosity at a very low nominal consolidation stress of 0.3 kPa after filling, is first explored. The fill porosity depends on the method of filling which is described in Section 4. While comparing the effect of k_{adh} and f_o on the filled porosity it is important to note that f_o is an adhesive strength (N) whilst k_{adh} is adhesive stiffness (N/m). It is therefore difficult to compare the effect of these parameters on the filled porosity directly.

Figure 4.17 shows the fill porosity arising from two different scenarios: varying f_0 with k_{adh}=0 and varying k_{adh} with f_0=0. For the system with zero adhesion (k_{adh}=0, f_0=0), the porosity is 41% (shown as dashed line in the figure) which is consistent with the findings for cohesionless paired non-spherical particle with aspect ratio of 1.5 (Härtl and Ooi, 2008). This can be compared with the porosity of 36% for random packed mono-disperse and frictionless spheres, showing the effect of non-sphericity on porosity. As the contact adhesion increases either by increasing k_{adh} or f_0, the filled porosity also increases. Contact adhesion causes the particles to stick together during the filling process and form local clusters leading to chain like structure and thus higher porosity. The adhesive forces provide a higher resistance to counteract the effect of gravity force and provide mechanical stability. These forces restrict the relative movement between particles and significantly reduce the densification due to rolling and sliding between particles (Yang et al., 2000).

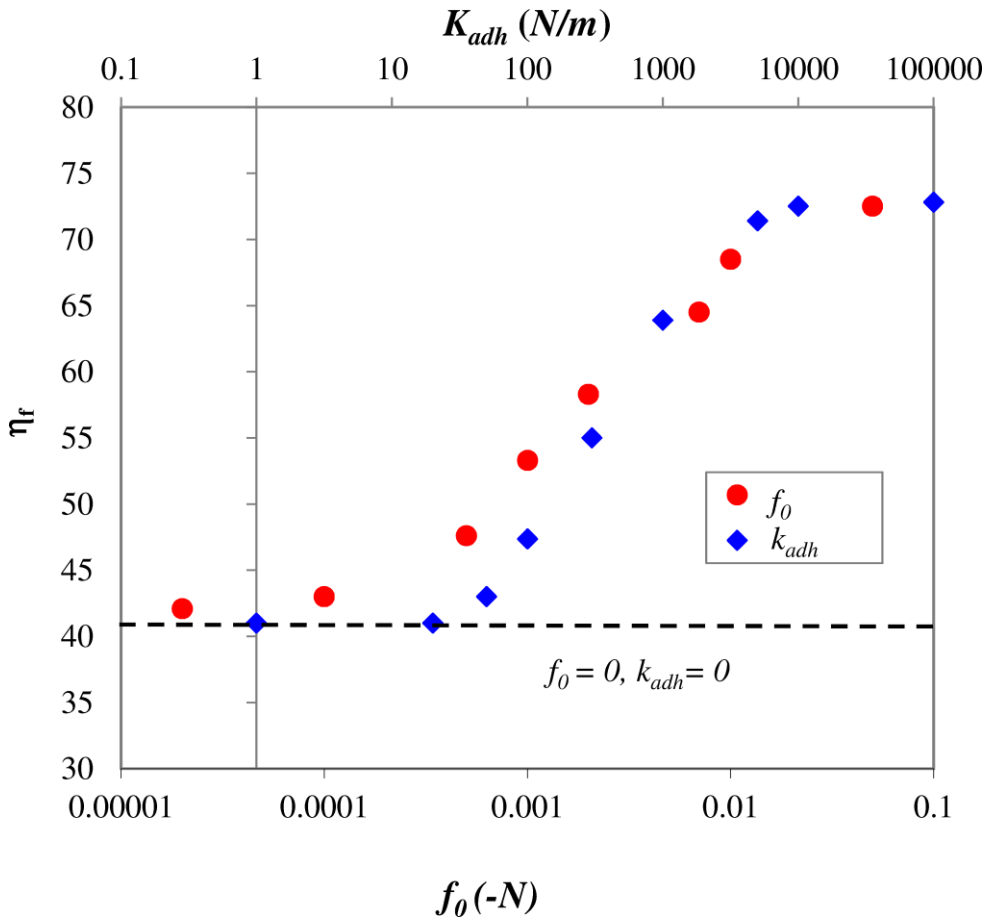

Figure 4.17 - Variation of porosity (η_f) at end of filling with k_{adh} and f_0: k_1 = 1 and k_2 = 10 kN/m

The porosity initially increases slowly with increasing adhesion parameters, before it increases rapidly after reaching the inflection point and finally reaches a plateau. It should be noted that the adhesion strength at contact is not fully mobilised during the filling process. For a fair comparison of the effect of adhesion parameters on the porosity would require calculation of average mobilised adhesive (tensile) force in each system. The average tensile force is defined as the ratio of total tensile force to the number of tensile contacts in the system. The Figure 4.18 shows the result in Figure 4.17 re-plotted in terms of average tensile force (f_{at}) normalised by gravitational force (f_g). It is notable to find that for both adhesion parameters, the inter-particle force ratio (f_{at} / f_g) vs porosity relationship converges to a single line. This suggests that porosity relates strongly to mobilised adhesive (tensile) force regardless of constant adhesion or load dependent adhesion.

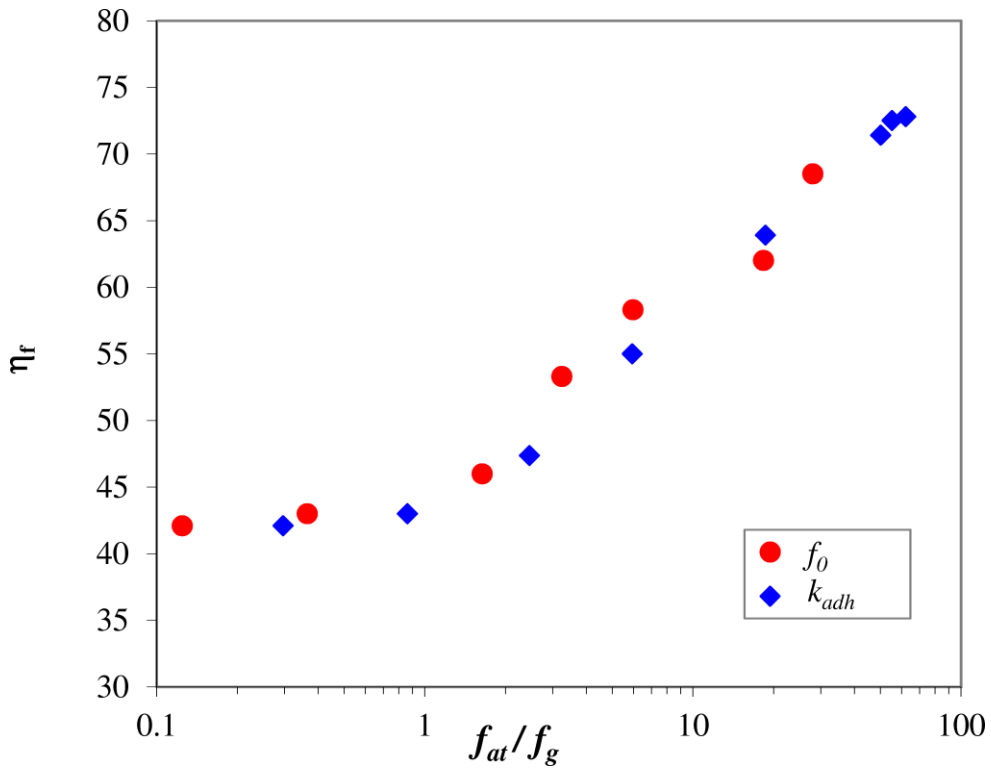

Figure 4.18 Inter-particle force ratio vs fill porosity

Next the effect of adhesion on bulk compressibility is explored. The consolidated bulk porosity (η_c) of the sample was calculated from the height of the consolidated sample after unloading. Figure 4.19 shows the consolidated porosity as a function of the consolidation stress for different adhesion parameters. As the consolidation stress increases, the consolidated bulk porosity reduces for all adhesion parameters investigated. The porosity of the sample increases as the level of adhesion (coming from f_o and k_{adh}) increases for the same consolidation stress. It is noted that the rate of decrease in porosity for k_{adh} is noticeably slower than those with a nonzero f_0 because the adhesive force is proportional to k_{adh} and is thus higher at a higher stress level, making the sample more difficult to compact. Additionally, for constant adhesion, porosity decreases more rapidly on the first application of stress and then slows down as the stress increases further. The rapid decrease in porosity at lower stress can be attributed to higher particle rearrangement resulting from the looser packing formed.

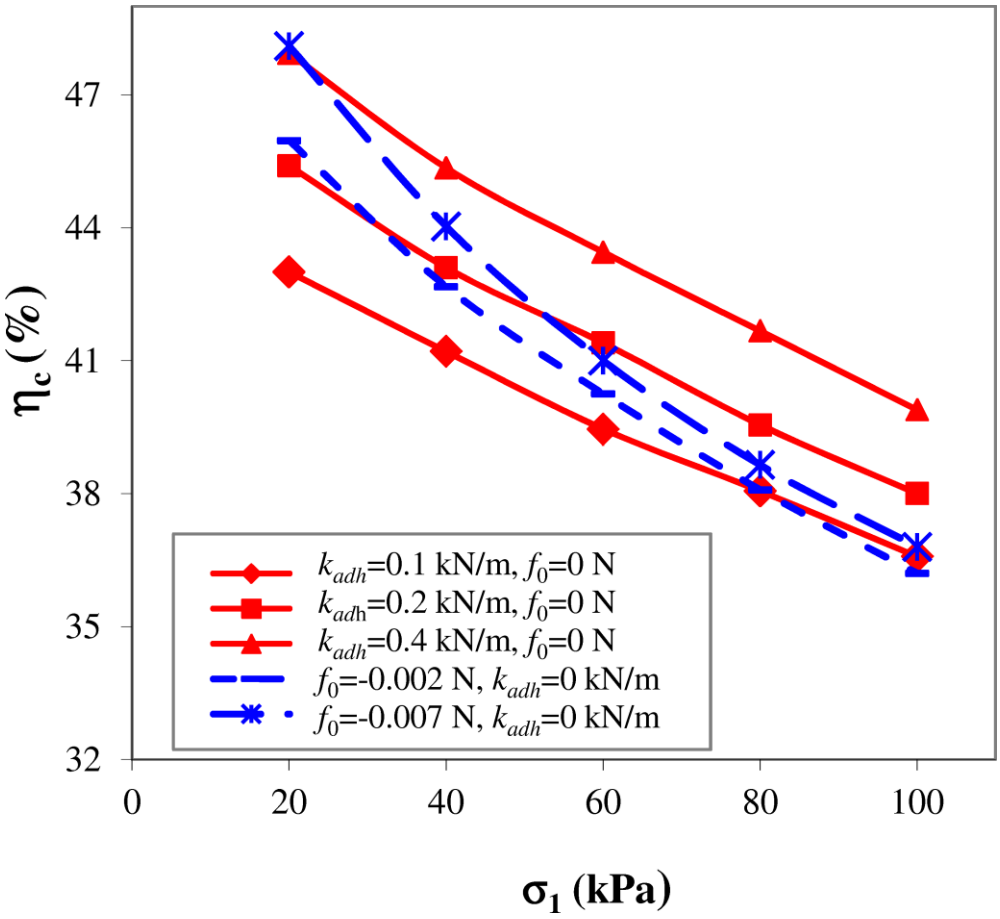

Figure 4.19 Consolidated porosity (η_c) as a function of consolidation stress (σ_1): k_1 = 1 and k_2 = 10 kN/m

Finally, the effect of adhesion on the computed flow function is investigated. Figure 4.20 shows that the unconfined compressive strength increases with the consolidation stress for all the adhesion parameters, showing the stress history dependency phenomenon. Within the range of the consolidation stress studied, the predicted unconfined strength for cases with both non-zero k_{adh} and f_0 is found to be approximately the sum of the contributions from k_{adh} and f_0 separately when all the other DEM input parameters are kept constant. In this example, the slope of the flow function for the case with k_{adh}=*0.1* kN/m and f_0=0 N is greater compared to that with k_{adh}=0 kN/m and f_0=-0.002 N. In the former case, the unconfined strength increases because both the coordination number *Z* and the load-dependent adhesion increases

with loading whilst in the latter case, the strength only increased as a function of increasing *Z*.

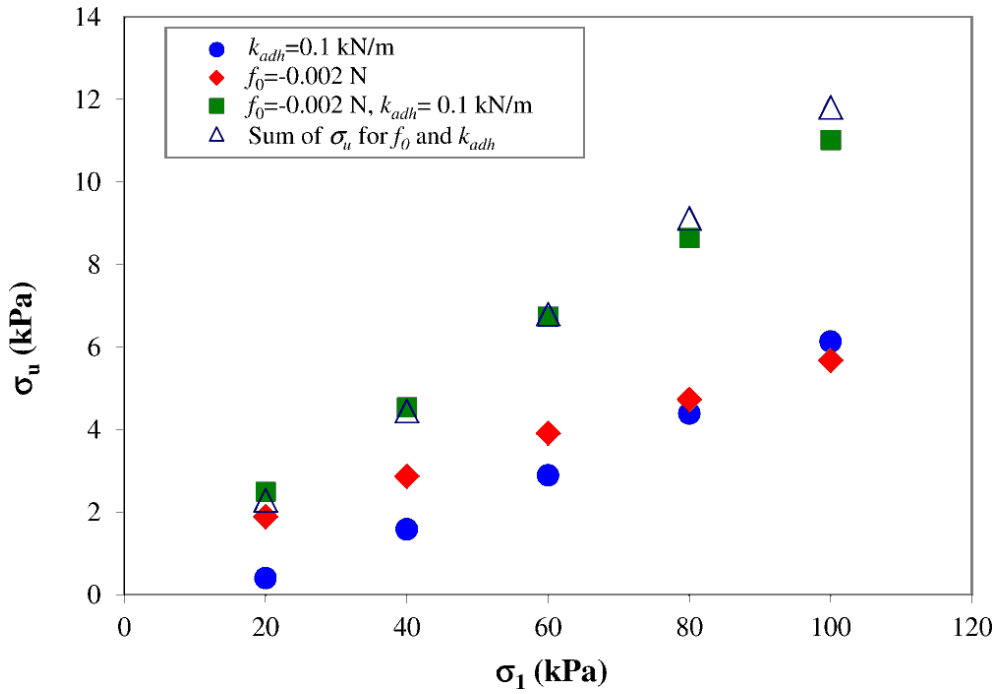

Figure 4.20 Predicted flow function for different k_{adh} and f_0 with k_1 = 1 and k_2 = 10 kN/m

It is evident from the above discussion that the consolidated porosity (η_c) and coordination number *(Z)* play a pivotal role in characterising the bulk cohesion. Here how the mesoscopic contact parameters relate to microscopic cohesion is explored. Rumpf (1962) was the first to propose a simple model relating tensile strength (σ_t) to average adhesive strength (F_{at}) at the particle level for a system of hard mono-disperse spheres with a random isotropic packing as follows:

$$\sigma_t = \frac{F_{at}(1-\eta)Z}{\pi d^2} \tag{4.15}$$

where d is the diameter of particle, η is the porosity, and Z is the coordination number. It should be noted that this equation was developed for an ideal packing of hard spheres with isotropic and homogenous distribution of stresses. However, our experimental setup of uniaxial compaction is anisotropic in nature. The effect of

anisotropy has been investigated by Quintanilla et al. (2001) and they reported that the anisotropy does not affect the relationship significantly.

Rumpf (1962) derived the equation for tensile strength of agglomerates, whilst in this study, our focus is on the bulk compressive strength. The relationship between tensile strength and unconfined compressive strength can be derived from the construction of Mohr Circle (Figure 4.21) by assuming a linear cohesive-frictional material. The unconfined compressive strength σ_u is thus related to the unconfined tensile strength σ_t by the simple expression:

$$\sigma_u = \frac{1+\sin\phi}{1-\sin\phi}\sigma_t \tag{4.16}$$

where, ϕ is the linearised angle of internal friction.

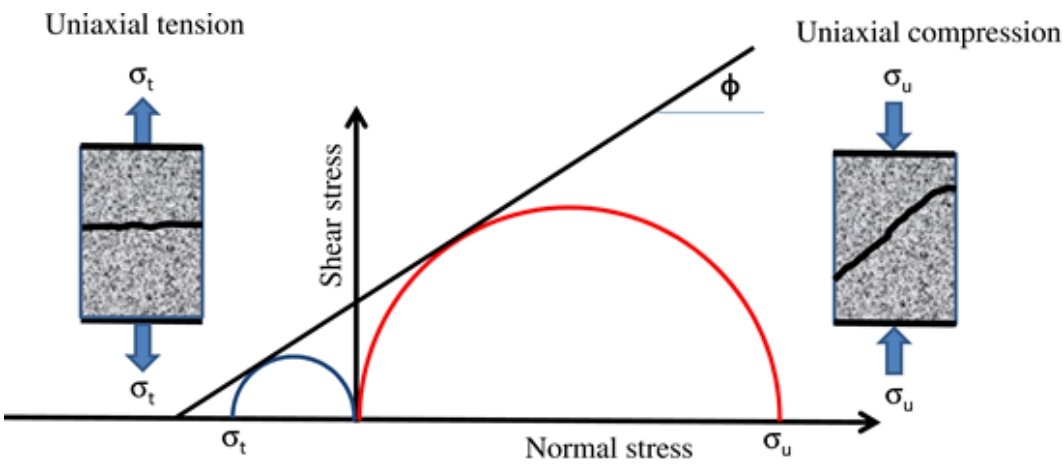

Figure 4.21 Mohr circle for uniaxial tension and compression

It is thus proposed that the unconfined compressive strength would have the same micromechanical origins as the tensile strength. From equations (4.15 and (4.16, the normalised unconfined strength can be defined as:

$$\frac{\sigma_u}{(f_{atp}/d^2)} \propto (1-\eta_c)z \tag{4.17}$$

where f_{atp} is the average tensile contact force evaluated for the whole particle system at the unconfined strength (σ_u) state. The relationship between the normalised unconfined strength and the product of Z and solid volume fraction (1-η_c) for the full range of adhesion parameters is shown in Figure 4.22. A unique linear relationship exists between the two quantities, which is similar to the finding from Rumpf Rumpf (1962). This proposes that the bulk unconfined strength for the same size particle is governed by the contact tensile force at failure, the coordination number and the solid fraction. This relationship reveals an important microstructural mechanism for bulk cohesion and can be used to facilitate unifying the characterisation and modelling of cohesive granular materials with different adhesion parameters.

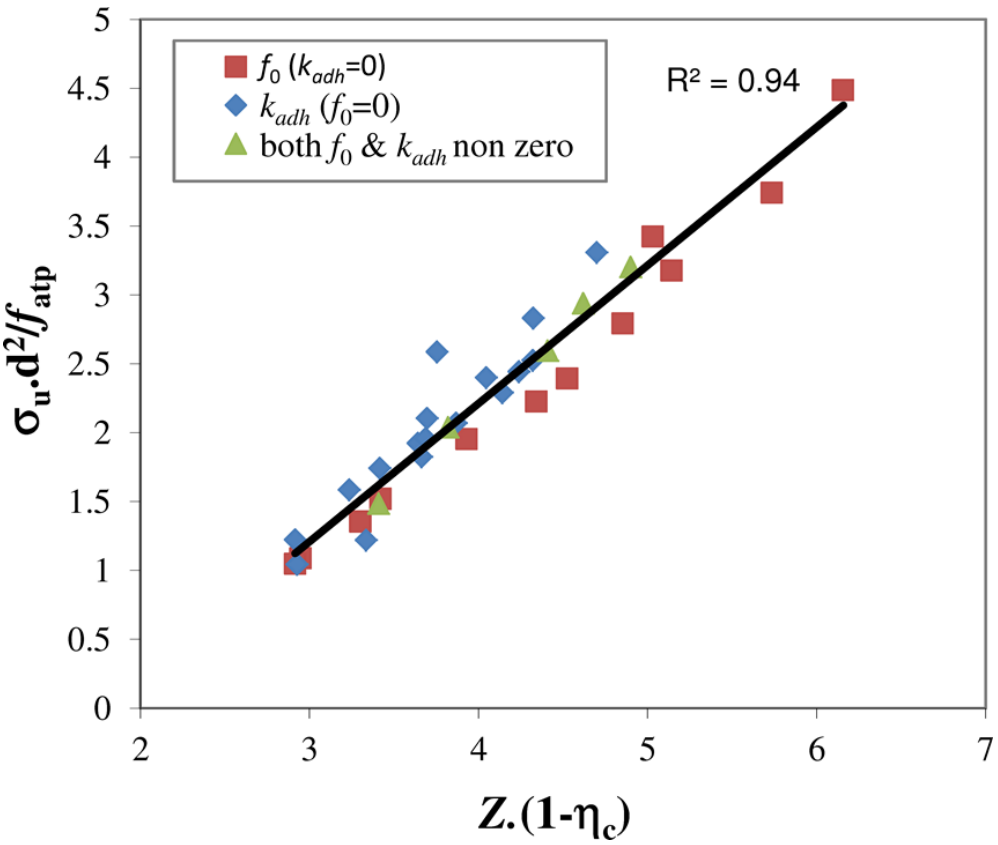

Figure 4.22 Normalised unconfined compressive force ($\sigma_u d^2/f_{atp}$) as a function of coordination number (Z) and consolidated porosity (η_c)

It may first seem counter-intuitive why the unconfined compressive strength should relate to the tensile contact force. The effect of the tensile contact force can be elucidated by the example simulations shown in Figure 4.23. The figure shows the

stress strain result during unconfined compression. Two pair of simulations with the same simulation parameters but different limiting friction criteria $f_{ct} \leq \mu |F_n|$ and $f_{ct} \leq \mu |(f_n + k_{adh}\delta^n - f_o)|$: the former has been explored elsewhere (Gilabert et al., 2007) and the latter is adopted in the present model (see Equation 8). It can be seen that there is a huge reduction in the computed unconfined strength as well as initial stiffness if the limiting tangential force does not include the tensile strength component. This can be seen for both cases: combination of constant adhesion and load dependent adhesion (f_o & k_{adh} - case I) and constant adhesion (f_0 - case II). When friction limit does not include tensile (adhesive) component, the tensile force remains similar but the unconfined strength reduces significantly due to reduced shearing resistance. This confirms that the major contribution of the tensile force to the compressive strength is from adhesive force contributing to limiting tangential force and not directly from the tensile force itself. This is also in line with the observation that under uniaxial unconfined compression, the mode of failure is predominantly shear failure rather than tensile failure (Schofield and Wroth, 1968; Wood, 1990).

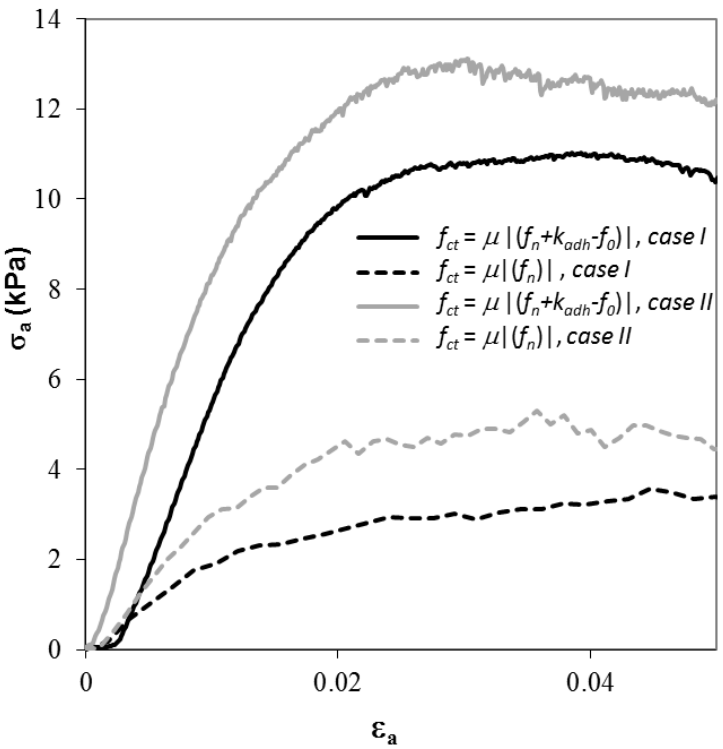

Figure 4.23 Unconfined stress strain behaviour as a function of limiting friction (case I: f_0=-0.002 N, k_2=10 and K_{adh}=0.1 kN/m, case II: f_0=-0.007 N, k_2=10 and k_{adh} =0 kN/m)

4.9 *Summary*

The DEM simulations and micromechanical analysis of cohesive powders using an adhesive elasto-plastic contact model have been presented. The results have shown that the model is capable of capturing the important stress-history dependency of powders' unconfined cohesive strength, as observed in experiments. This suggests that the elasto-plastic adhesive model may be used to simulate cohesive solids subjected to different flow and stress regimes.

The particle contact plasticity has been found to be essential for capturing the stress history dependence and to produce a realistic flow function. Micromechanical analysis revealed that increased particle contact plasticity increases the bulk plasticity. The contact plasticity prevents excessive elastic rebound at the contact level which leads to a lower porosity on the application of stress. For constant adhesive strength, the unconfined strength has been shown to correlate with the instantaneous coordination number at the peak state. This provides a microscopic explanation for the unconfined strength variation and also indicates that the coordination number can be used as a state variable to avoid invoking the history effect. In some sense, this correlation is a new microscopic (or meso-scale) flow function.

When the contact adhesive strength increases, the filled porosity also increases. Higher adhesive forces allow the particles to stick together during the filling process, leading to stronger chain like structure and ultimately higher filled porosity. The adhesive forces provide a high resistance to counteract the effect of gravity force and provide some mechanical stability which restricts the relative movement between particles. For both load dependent k_{adh} and constant adhesive strength f_0, a unique relationship between porosity and mobilised adhesive force was found. On the application of confined compression, the load-dependent adhesion provides a greater resistance to volumetric compression because the adhesive strength is proportional to

k_{adh} and is thus higher at higher stress levels, making the sample more difficult to compact.

While comparing the effect of adhesion parameters on unconfined strength within a range of consolidation stresses, it has been found that the predicted unconfined strength for cases with both non-zero k_{adh} and f_0 is approximately the sum of the contributions from k_{adh} and f_0 separately; when all the other DEM input parameters are kept constant. A linear relationship has been established between the normalised unconfined strength and the product of coordination number and solid volume fraction. This gives a general microscopic (or meso-scale) flow function for different materials with distinct cohesion strength origins.

Significantly, it has been found that contribution of adhesive force to the limiting friction has a significant effect on bulk unconfined strength. Failure to include the adhesive contribution in the calculation of the frictional resistance may lead to under-prediction of unconfined strength and incorrect failure mode.

Chapter 5

Numerical upscaling in uniaxial test simulation[3]

5.1 *Introduction*

One of the major shortcomings of DEM is the computational cost required when the number of particles is huge, especially for fine powders. In the previous chapter, modelling of powder at meso level is proposed. Meso level is an intermediate length scale between micro and macro level. This chapter explores the possibility that mesoscopic particle DEM model exhibit bulk mechanical loading response in uniaxial test that is similar to a material comprised of much smaller particles. The chapter investigates comprehensive 3D powder modelling in uniaxial test simulation describing more than one loading regimes namely compression and shear. The target is for the DEM model with scaled up particle to exhibit the compression and shearing bulk behaviour in a uniaxial test exhibited by a cohesive powder. An attempt is made to investigate the scaling of contact stiffness (normal and tangential) and adhesive force in the cohesive contact model that would permit a mesoscopic representation of a cohesive powder using much larger DEM particles

This chapter begins with discussing scaling approach employed in this study and exploring theoretical and empirical relationship between particle contact parameters and particle size. The description of simulation set up to evaluate the scaling rules is provided next. Finally, DEM simulations with different size of particles and scaling

---

- [3] Based on Thakur, S.C., Ooi, J.Y., Ahmadian, H. (2013). Scaling of discrete element model parameter in uniaxial test simulation. *Submitted to Chemical Engineering Science.*

rules are performed and scaling relationships are provided for cohesionless and cohesive system. This is a first step towards a mesoscopic representation of a cohesive powder that is phenomenological based to produce the key bulk characteristics of a granular solid and the results indicate that it has potential to gain considerable computational advantage for large scale DEM simulations.

5.2 *Scaling approach*

Several approaches are used for scaling in granular system as described in section 2.3.3. One of the approaches is to maintain geometric, mechanical, and dynamic similarity under which the scaled model can exactly reproduce the mechanical behaviour of physical model. However maintaining all the similarity principle may result into computationally equivalent to the modelling of physical system with no scaling at all (Feng et al.(2007)). One possible solution is to use larger size elements (particles) to reduce the number of particles whilst keeping the original system size the same, however, this would violate geometric similarity and may introduce some error in the bulk response Feng et al.(2007). The major issue in this kind of approach is to adjust DEM model parameters such that DEM simulation result exhibits the same dynamic and static properties as the experimental granular material. This approach is sometimes referred to as coarse graining approach (CGA) or similar particle assembly (SPA) and has been used by a few researchers in the field of cavity filling (Bierwisch et al., 2009), pneumatic conveying (Sakai and Koshizuka, 2009), fluidized bed (Mokhtar et al., 2012; Sakai et al., 2012) and rotating drum (Walton and Johnson, 2010).

5.2.1 Scaling relations for cohesionless system

To maintain the mechanical and dynamic similarity, the contact model should be scale invariant. However, in linear spring contact model in 3D, the force displacement relationship is dependent on the size of the particle and is not scale invariant (Feng et al., 2007). Therefore contact stiffness needs to be scaled with

radius of the particle. For the oblique impact of elastic spheres, Maw et al., (1976) provided a solution that relates contact normal stiffness to the radius of the particles as:

$$k_n = \frac{16}{15} R^{*\frac{1}{2}} E^* \left(\frac{15 m^* V^2}{16 E^* R^{*\frac{1}{2}}} \right)^{\frac{1}{5}} \quad \textbf{(5.1)}$$

where m^* is the equivalent mass, R* is the equivalent radius, E* is the equivalent Young's modulus, and V is a typical impact velocity. In the equation above if mass is expressed in terms of radius, the equation can be expressed as:

$$k_n = C R^* \rho^{*1/5} E^{*4/5} \quad \textbf{(5.2)}$$

where C is a constant. The equation 5.3 suggests contact normal stiffness should scale linearly with particle radius. In another study, Potyondy and Cundall (2004) assumed a linear relationship between particle size and Young's modulus as (5.4):

$$k_n = 2 E^* R^* \quad \textbf{(5.4)}$$

The commercial code EDEM developed by DEM Solutions uses solution provided by Maw et al. (1976) and another commercial code PFC3D developed by Itasca uses the solution provided by Potyondy and Cundall (2004).

Obermayr et al. (2011) assumed stiffness calculated from deformation of an elastic rod as (5.5):

$$k_n = \frac{\pi R_{avg} E}{2} \quad \textbf{(5.5)}$$

where R_{avg} is the average radius of contacting particles and E is the Young's modulus.

Regardless of different scaling relationship purposed by researchers, it is clear that normal contact stiffness scales linearly with radius of the particle in linear spring contact model. However, the stiffness in Hertz-Mindlin contact model is scale invariant for 3D (Feng et al., 2007). No literature can be found for scaling of unloading stiffness for the case of elasto-plastic contact model.

The scaling relationships for other DEM parameters including tangential stiffness, damping constant, density, sliding friction, and rolling friction is discussed herein. According to Mindlin and Deresiewicz (1953), the ratio of normal to tangential stiffness is a material property and independent of size of the particles. This would require tangential stiffness to scale linearly with the radius of the particle. The damping constant may have effect in dynamic cases, however, for quasi-static simulation (Midi, 2004) such as ours the effect of damping will not be significant (Obermayr et al., 2011). Moreover, it was proved by Kruggel-Emden et al. (2010) that while compressing the sample at relatively lower rate, dynamic effects are of a smaller importance. In dynamic cases damping constant can be scaled linearly with radius of the particle as suggested by Bierwisch et al., (2009). For the scaled system to reproduce same mechanical behaviour, the density of gravitational potential energy should be same as in the original system. The density of gravitational potential energy is independent of particle radius if porosity of the system is constant. This requires particle density in the original system and scaled system to be the same. Sliding friction is invariant with respect to scaling (Pöschel et al., 2001). Rotational motion (rolling friction) is not scaled.

5.2.2 Scaling relations for cohesive system

Van der Waals force is a major source of adhesion in fine size particles. Theoretical adhesive elastic force models such as JKR and DMT (Derjaguin et al., 1975; Johnson et al., 1971) relates adhesive force due to van der Walls attraction to the radius of the particles as (5.6) and (5.7):

$$f_{0DMT} = -4\pi\gamma R^* \quad \textbf{(5.6)}$$

$$f_{0JKR} = -3\pi\gamma R^* \quad \textbf{(5.7)}$$

where γ=surface energy per unit contact area (J/m^2). For plastic contacts (Thornton and Ning, 1998), the plastic deformation at the contact causes increase in pull off force approximately by a factor of 2 compared to JKR model with elastic contacts and pull-off force is given by (5.8):

$$f_{0plastic} \approx -6\pi\gamma R^* \quad \textbf{(5.8)}$$

In addition, the pull-off force (Israelachvili, 1992) between two approaching spheres of equal diameter is given by (5.9):

$$f_0 = \frac{AR^*}{6s^2} \quad \textbf{(5.9)}$$

where A=Hamaker's constant and s=separation between the particles. Hamaker's constant (A) can be expressed as (5.10):

$$A = \pi^2 C_f \rho_a^{\ 2} \quad \textbf{(5.10)}$$

where C_f is a constant and ρ_a is number of atoms per unit volume of contacting bodies and is a material property. The above deductions suggest that the adhesive force is linearly proportional to the radius of the particle.

According to early work of Rumpf (1962), the relationship between tensile strength (σ_t), and the inter-particle contact force (f_0) for a system of hard mono-disperse sphere with a random isotropic packing is given by the following equation (5.11):

$$f_0 = \frac{4\pi R^2}{\phi Z}\sigma_t \quad \textbf{(5.11)}$$

where ϕ = packing fraction, and Z = co-ordination number.

This suggests that inter-particle contact force should scale up with square of the radius of the particle. In addition, as the particle size (of spherical particle) decreases,

contact surface area per unit volume of the particle increases. Since adhesive forces are related to the surface area of a particle and since the surface area is proportional to the square of the radius of the particle**,** this suggests that adhesion force is quadratically proportional to the radius of the particle.

Some researcher suggests keeping the bond number (f_0 / f_g) same in original and scaled system, where f_g is the gravitational force that is equal to the weight of the particle and is expressed as (5.12):

$$f_g = \frac{4}{3}\pi R^3 \rho \qquad \textbf{(5.12)}$$

where ρ= density of the particle. Therefore, $\frac{f_0}{f_g} \propto R^3$. This suggests f_0 should be scaled cubically with the radius of the particle.

Equations (5.6-(5.12 approaches suggest that adhesive force may scale linearly, quadratically, and cubically with the particle radius.

5.3 ***Simulation set-up***

The computer simulations reported here consider a series of uniaxial compression tests in a rectangular cuboid of 50 mm thickness (>6*diameter of the largest particle), 150 mm width, and 300 mm height (see Figure 5.1). Periodic boundaries were used along X and Y direction to avoid the wall effect. The cuboid contains a top and a bottom plate. Each simulation consisted of several stages of loading: a) filling the cuboid; b) confined consolidation to a 40kPa stress level and subsequent unloading, c) and finally unconfined compression of the sample to failure after the removal of the confining mould. The random rainfall method was adopted to provide a random packing of particles. For cohesionless case, similar porosity for different size particles were achieved by vibrating the system with frequency of 60 Hz and amplitude of 1.5mm for simulation time of 2 seconds. To ensure that the system reached a quasi-static state, loading only commenced when the kinetic to potential

energy ratio was less than 10^{-5} with a constant coordination number. For cohesive system, it was difficult to get reproducible porosity in fill stage, therefore, the porosity corresponding to an initial vertical stress of 5 kPa is considered as initial packing for subsequent loading.

Compression was achieved by moving the top plate at a constant speed until a desired bulk vertical stress was attained. Subsequently, unloading was performed by an upward retreat of the upper plate. The confining periodic boundaries were then removed and the unconfined samples were allowed to reach the new equilibrium, and finally the top platen was lowered to fail the sample. The loading and unloading were performed at an axial speed of 10 mm/s (strain rate<$0.1s^{-1}$) throughout to ensure quasi-static loading. The quasi-static loading was confirmed by inertia number being less than $1x10^{-4}$ (Midi, 2004) in all simulations. The lower plate remains stationary in all stages.

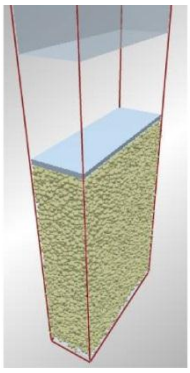

Figure 5.1 Simulation set-up

Three special cases of the contact model proposed in previous chapter are explored here. The scaling law was first applied for the cohesionless case (case I), and for the constant adhesion case (case II), and finally for the load dependent adhesion case (case III) as shown in Figure 5.2.

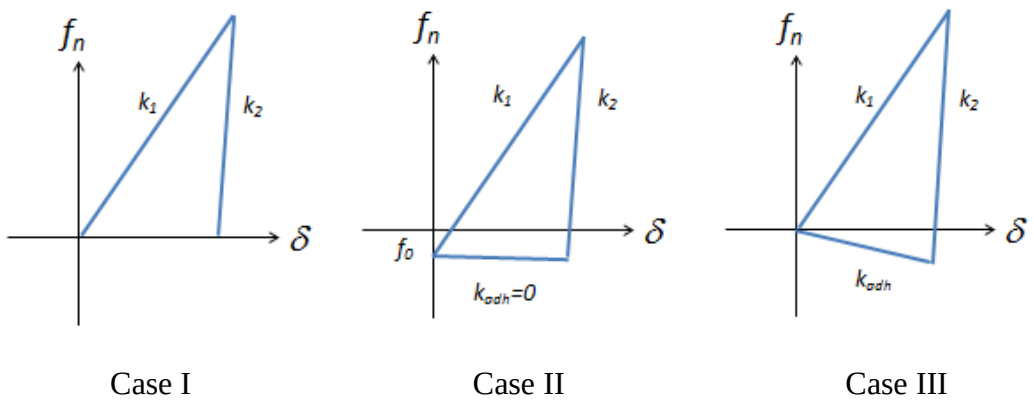

Figure 5.2 Different cases of simulated contact model

The parameters used in the simulations are listed in Table 5.1. For simplicity, the particle shape used in this study was chosen as spherical and uniform size. The cohesive contact model was only applied to particle-particle interactions. The particle-geometry interactions were modelled using the Hertz-Mindlin (no-slip) contact model and hence no particle-geometry adhesion was included.

Table 5.1 DEM input parameters

Particle density, ρ (kg/m^3)	2000
Loading spring stiffness, K_1 (N/m)	5x10^3 to 1x10^4
Unloading spring stiffness, K_2 (N/m)	2.5x10^4 to 5x10^4
Load dependent stiffness, K_{adh} (N/m)	5x10^3 to 7.5x10^3
Adhesion force, f_0 (N)	0 to -1.6
Tangential stiffness, K_t (N/m)	2/7 K_1
Particle static friction, μ_{sf}	0.5
Particle rolling friction, μ_{rf}	0.001
Particle radius (R), mm	2.5 to 5
Top and bottom platen friction, μ_{Pf}	0.3
Simulation time step (s)	1x10^{-5}

5.4 *Simulation results*

5.4.1 Cohesionless system

To isolate the effect of adhesion on bulk response, the scaling law was first explored for cohesionless system (case I). The DEM contact model with elastic plastic deformation but no adhesion is used in this case. Figure 5.3 and Figure 5.4 show the axial stress vs axial strain and the corresponding stress-porosity response during the confined loading and unloading simulation respectively. The simulation with R=2.5 mm particle is taken as the reference case. The particle density and sample porosity were kept similar throughout to keep the density of gravitational potential energy the same in both the large particle and the small particle systems. For the first case (unscaled), the particle size was increased to 3.75mm without scaling the stiffness (all model parameters unchanged). It can be clearly seen that increasing the particle size without scaling the stiffness produces a softer bulk response compared to the reference case, for the similar initial porosity (Figure 5.4). However, when stiffness was scaled linearly with the particle radius, the stress-strain response and the corresponding porosity-stress response for the 3.75mm particle almost converged to that for the reference case of 2.5mm particle. The variation of porosity across the height of the sample was also investigated (see Figure 5.5). It can be seen that porosity was very similar for reference case and scaled case, however, porosity for unscaled case was consistently smaller across the height of the sample. It can be concluded that very similar bulk loading and unloading stiffnesses are predicted for the simulations with scaled contact normal and tangential stiffness. However, there was a discrepancy when particle size was increased without scaling the stiffnesses.

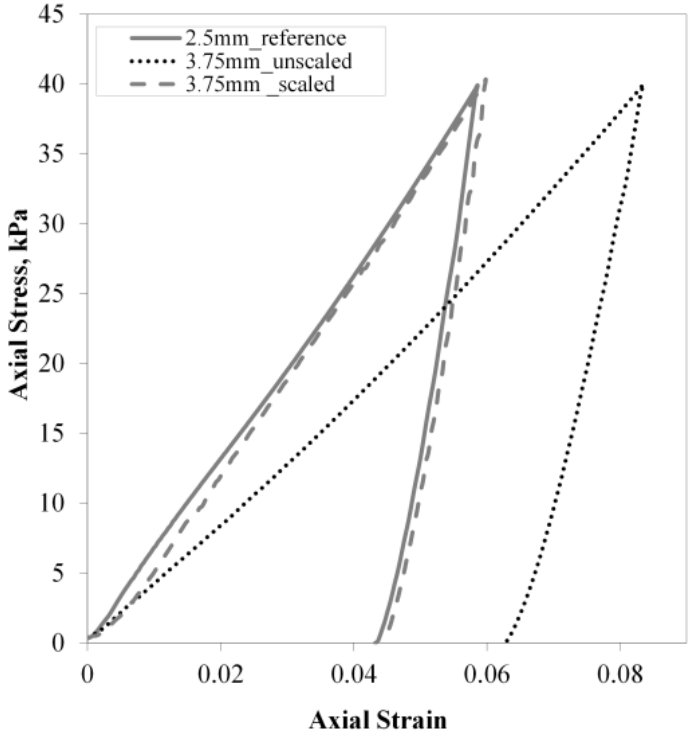

Figure 5.3 Confined compression: Axial strain vs axial stress

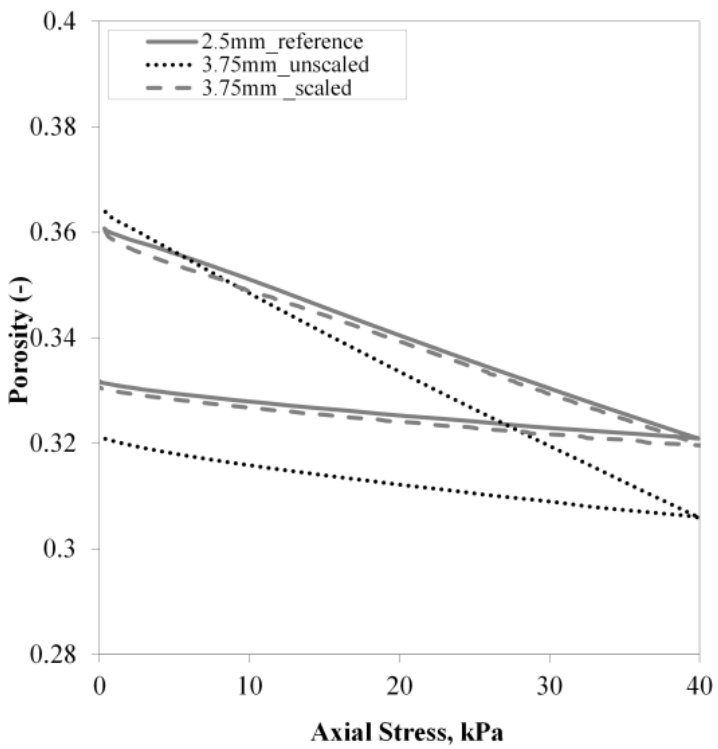

Figure 5.4 Confined compression: Axial stress vs. porosity

Furthermore, an investigation of the coordination number (CN) in the systems is shown in Figure 5.6. This shows that the CN during the loading and unloading also evolved in the same fashion for the reference case and the scaled simulation, however, the CN for the unscaled case increased at a higher rate compared to the reference case.

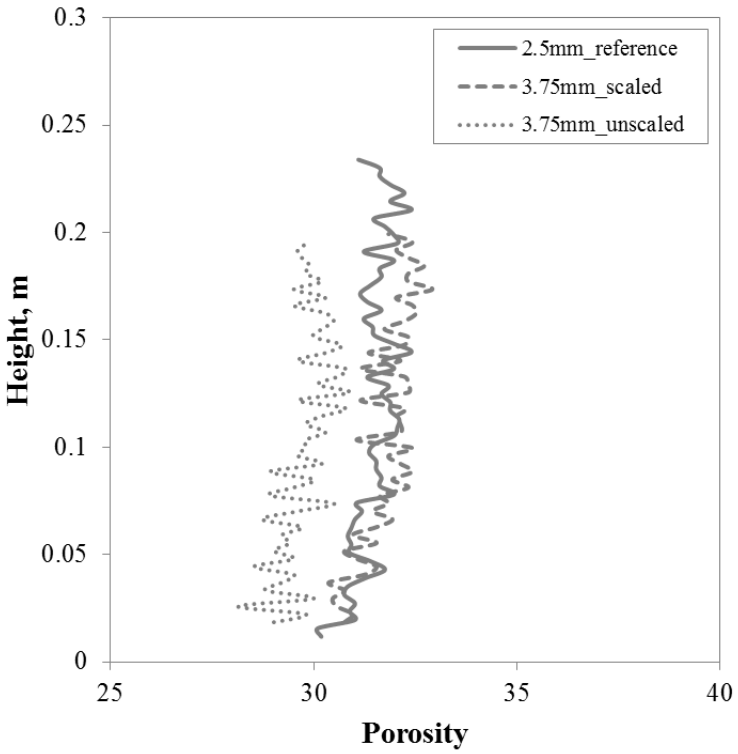

Figure 5.5 Porosity variation plotted against the height

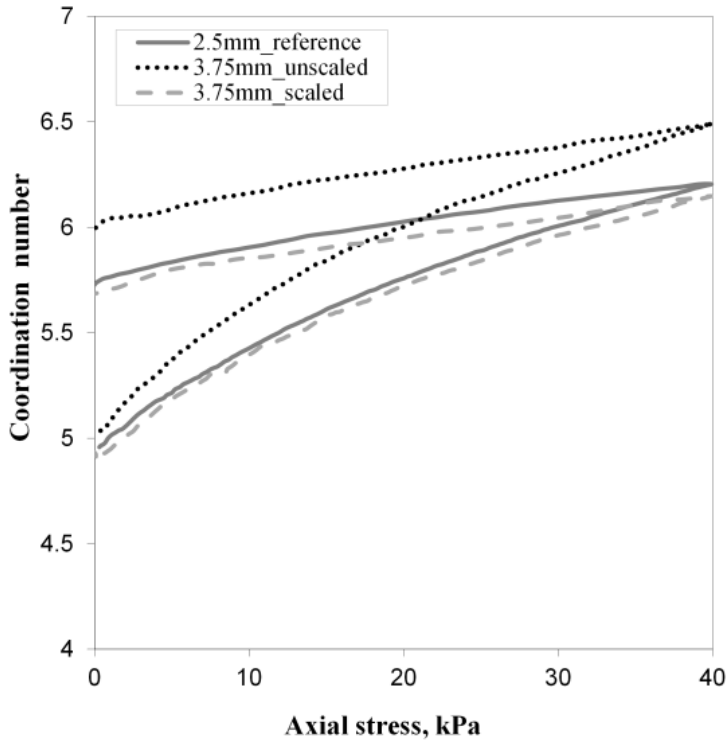

Figure 5.6 Evolution of coordination number

5.4.2 Cohesive system

5.4.2.1 Constant adhesion

For the cohesive system, simulation of confined loading leading to unconfined compression (shearing) was conducted. The normal and tangential stiffness (both loading and unloading) were scaled linearly as in the cohesionless system. Additionally, linear, quadratic, and cubic scaling of the adhesive force parameter f_o with particle radius was explored. The load dependent adhesion (k_{adh}) was set to zero (case II). Figure 5.7 and Figure 5.8 show the axial stress vs strain and the corresponding porosity-stress response for different particle sizes with different scaling approaches for the adhesive force. When the adhesive force was scaled linearly with particle size, the initial porosity at 5kPa stress level (Figure 5.8) was found to be lower when compared to the quadratic and cubic scaling. The linear scaling produced less compression under loading than the quadratic and cubic scaling

as shown in stress-strain curve (Figure 5.7). Conversely the cubic scaling of adhesive force with particle size produced a higher initial porosity and the sample compressed the most during loading. However, the quadratic scaling of adhesive force with particle size produced very similar stress-porosity and stress-strain response for particle size in a range of 2 to 3.75 mm.

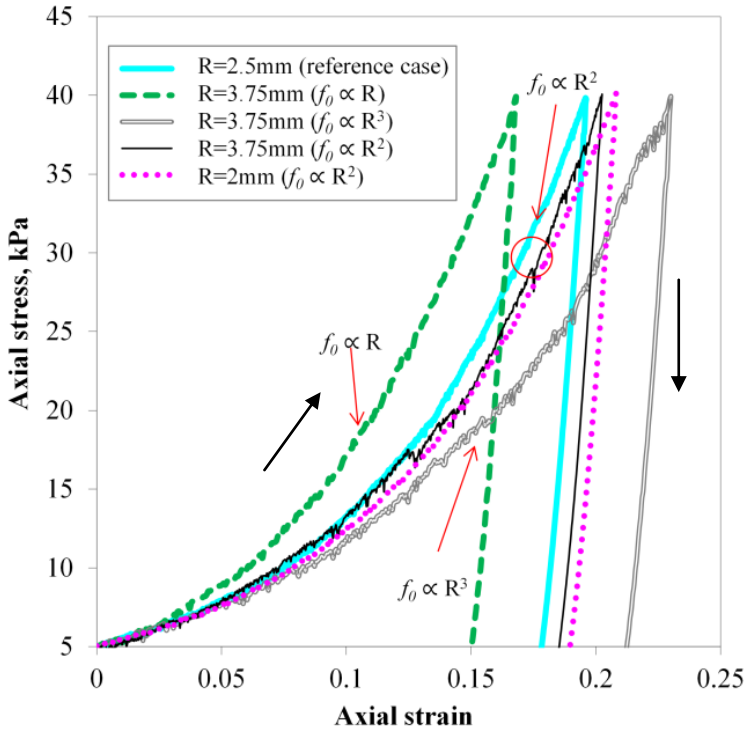

Figure 5.7 Confined compression: Axial stress vs strain

Note: The black arrows shows loading/unloading path

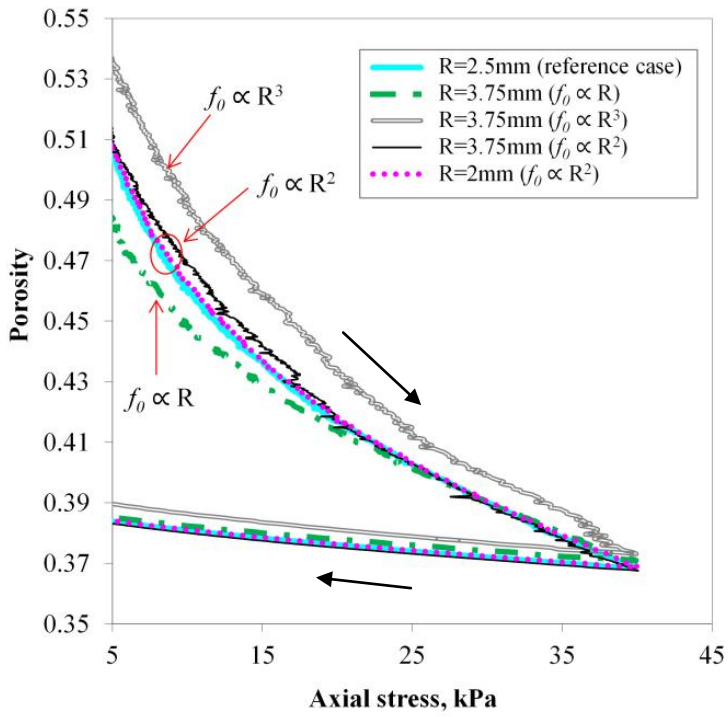

Figure 5.8 Confined compression: Porosity vs axial stress

The scaling of the adhesive force was further examined by looking into the unconfined compression behaviour. Figure 5.9 shows that the linear scaling with particle size underestimated the unconfined strength and cubic scaling overestimated the strength. This also suggests that scaling cohesive force by keeping the bond number constant (i.e cubic scaling) is not the right strategy. However, when adhesive force was scaled quadratically for different size particles of 2-3.75 mm, a very good agreement between reference case and scaled case can be found.

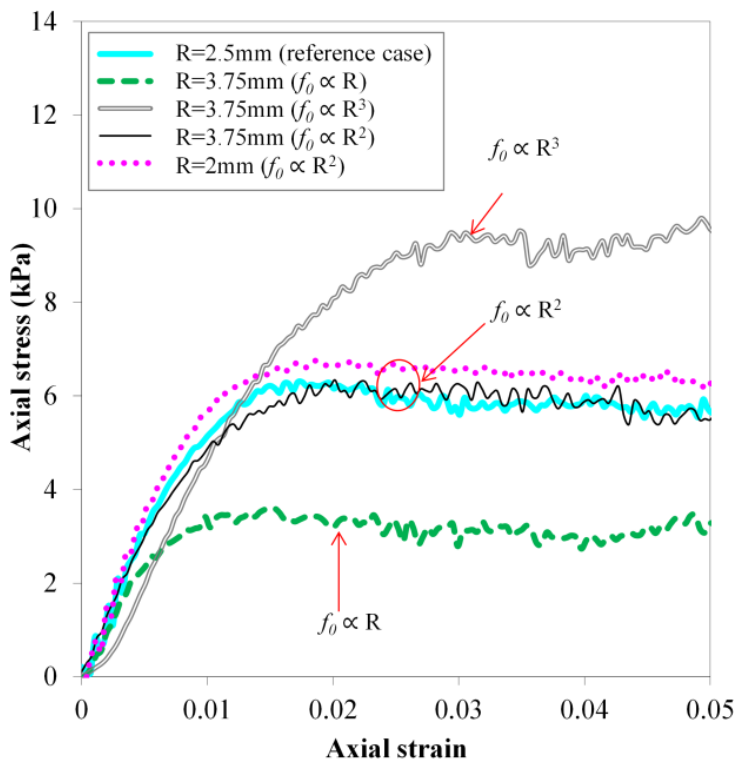

Figure 5.9 Unconfined compression: Axial stress vs strain

The above analysis has clearly shown that that adhesive force scales quadratically with the particle radius. This is consistent with results from Walton and Johnson (2009a) on the DEM simulations of rotary drum flows using their previously implemented DEM code (Walton and Johnson, 2009). They found that the scaling of the pull-off force with the square of the particle size produced flows that were qualitatively in agreement. Bierwisch et al. (2009) also found in simulations of rapid granular flow from a moving container and angle of repose formation that the adhesive force scales with the square of the radius of the particles. According to our study the combined linear scaling of the spring contact stiffness and quadratic scaling of the adhesive force parameter appear to be a robust strategy for the upscaling of particle size.

Figure 5.10 shows reduction in simulation time with decreasing size of particles. More than seven fold decrease in computational time was observed if particle size is

scaled from 2 mm to 3.75 mm for the simulation of uniaxial compression using 12 core processors in this study. With the increase in particle size, the stiffness is increased however the number of particles decreases significantly (34500 to 5100) and causes significant reduction in computational time. The scaling laws allow the use of larger particle sizes whilst reproducing similar mechanical response of a particulate assembly with smaller particles and help to reduce the computational time significantly.

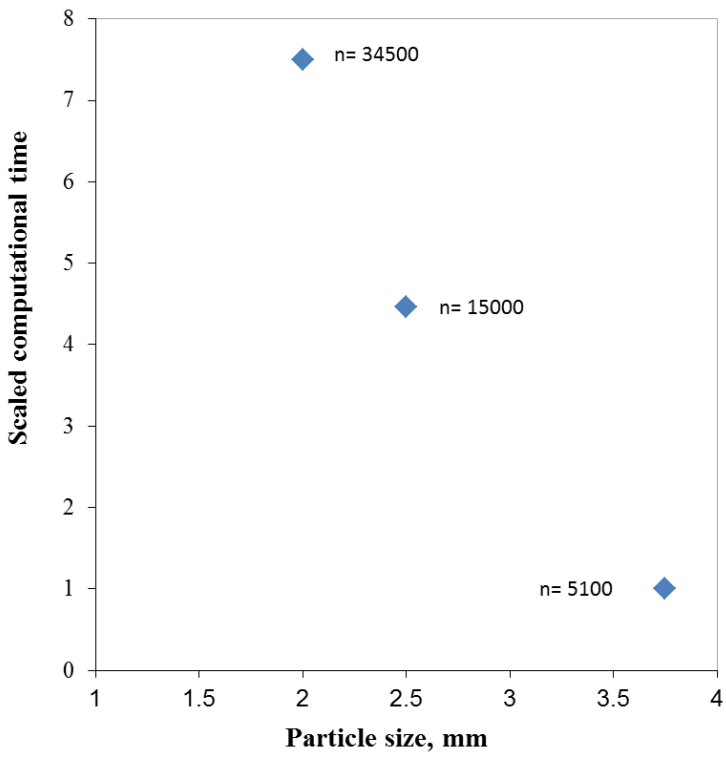

Figure 5.10 Reduction in computational time with scaling

Note: n= number of particles corresponding to the particle sizes.

5.4.2.2 Load dependent adhesion

In this section the scaling of load dependent stiffness (k_{adh}) with zero f_o (case III) is explored. The normal loading and unloading stiffness and tangential stiffness are scaled linearly as established in previous section. Additionally, the k_{adh} is scaled linearly with the radius of the particle. Figure 5.11 and Figure 5.12 shows stress

strain and corresponding porosity stress behaviour during confined compression, respectively. Similar stress strain response with small discrepancy in peak strain can be observed for scaled and reference case. The slightly lower peak strain for the scaled case can be attributed to slightly lower initial porosity arising from random generation of particles. Although a small difference in initial porosity for scaled and reference sample can be seen, both curves converge at higher stress (Figure 5.12).

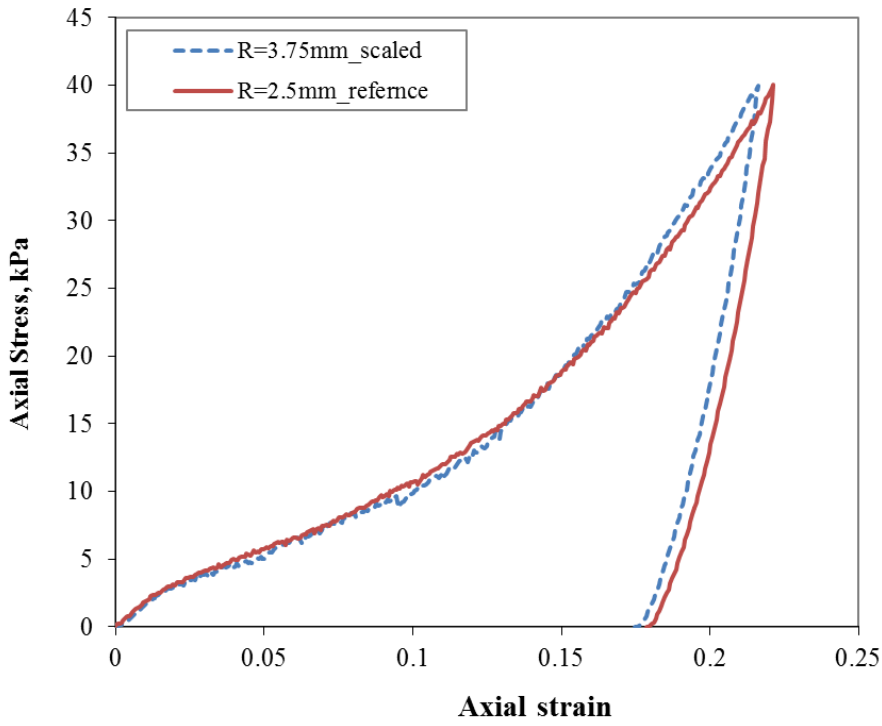

Figure 5.11 Confined compression: Axial stress vs strain

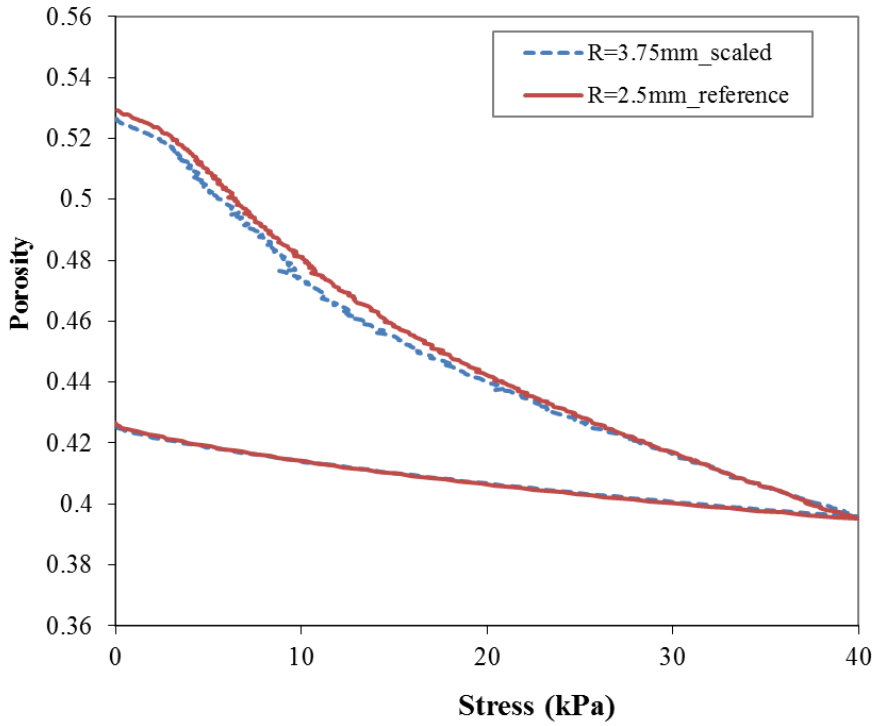

Figure 5.12 Confined compression: Porosity vs axial stress

Figure 5.13 shows stress strain response during unconfined compression. The initial stiffness during unconfined compression are almost identical for the both cases, however, the maximum strength for scaled case was 9.5% lower than that for reference case. The low strength associated with scaled case was found to be related with lower CN. After the end of consolidation when confinement is removed, CN drops. The drop in CN was higher for the scaled case, although the CN at the end of consolidation was the same in both cases.

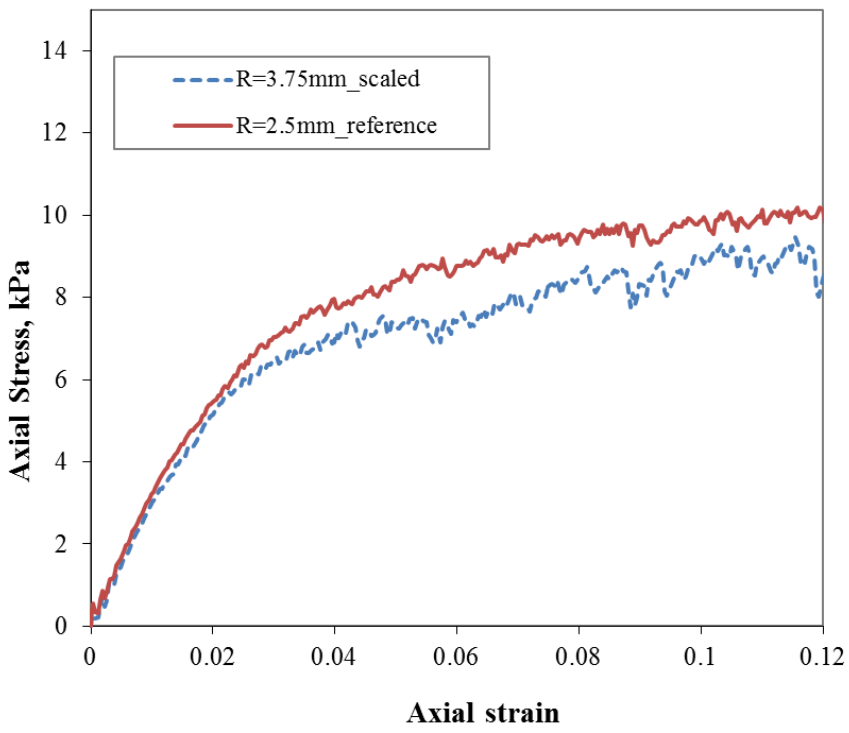

Figure 5.13 Unconfined compression: Axial stress vs axial strain

5.5 *Summary*

A study of the scaling laws to produce scale independent computations of confined compression and unconfined loading has been presented. In the linear spring model with elasto-plastic deformation and no cohesion, the contact loading and unloading stiffness (normal and tangential) was found to scale linearly with particle size. A very good agreement in the macroscopic (stress-strain and stress-porosity relations) and the microscopic (stress-coordination number relation) behaviour was found for different particle sizes when the contact stiffness was scaled linearly. For the simulation with a constant adhesion, the scaling of the adhesion force parameter with the square of the particle radius (2~3.75mm) produced confined stress-strain and stress-porosity behaviour, and unconfined stress-strain behaviour that remained remarkably similar as the size of the particles were increased. Furthermore, linear scaling of load dependent stiffness with the radius of particle produced very similar confined stress-strain and corresponding stress-porosity relation. Also almost identical stiffness during unconfined compression was found. However, the

unconfined strength for scaled system was within 10% of that for the reference system. Thus, by scaling the stiffness linearly and adhesive force quadratically, a DEM model using larger particle size can exhibit similar bulk properties as the system with small particle size. This scaling may have limitations when length scale of the particle size becomes comparable to the length scale of system. Nevertheless, such scaling laws are particularly useful for studying very large scale particulate systems with considerably less computational time.

Chapter 6

Influence of DEM input parameters and model implementation[4]

6.1 *Introduction*

In Chapter 3 the Edinburgh Powder Tester, an extended uniaxial tester, has been highlighted as a tester capable of measuring the mechanical characteristics of a powder for DEM model calibration. This chapter describes an investigation of the influence of the key DEM input parameters, as well as the model implementation considerations in the DEM modelling of uniaxial tests. Amongst other things, the influence of the particle contact normal loading stiffness, tangential stiffness, particle contact friction coefficient, numerical time step, strain rate and boundary conditions on the whole spectrum of testing scenarios: from filling, confined compression, to unconfined loading during an uniaxial test simulation is explored. The full sequence of the uniaxial test provides a full spectrum of loading scenarios likely to be encountered in material handling operations, ranging from filling porosity, confined compression under placement or shearing under flow regimes. The results give a sound indication of the relative importance of the input parameters and the model implementation to produce satisfactory predictions.

- [4] Based on Thakur, S.C., Ooi, J.Y., Ahmadian, H.. Influence of DEM model parameters in uniaxial test simulation. *In Preparation 2014*

It should be noted that the effect of the adhesion parameters (f_0, k_{adh}) and contact plasticity (ε_p) has been presented in Chapter 4. The effect of particle size has been investigated in Chapter 5. The model set-up and DEM parameters used for uniaxial test simulations in this chapter are the same as stated in Chapter 5, except where explicitly mentioned.

6.2 *Experimental behaviour of cohesive powder under compression and shear*

Powder filling, compression, and shearing is relevant to many industrial processes. As discussed in Chapter 3 the Edinburgh Powder Tester can make a number of pertinent bulk measurements. These are the vertical stress-strain (Figure 6.1) and the stress-porosity (Figure 6.2) response during confined compression. The powder compression process can be divided into two main stages. Stage I is dominated by particle rearrangement while stage II is dominated by the elasto-plastic particle contact deformation.

The EPT can also provide the (vertical) stress-strain (Figure 6.3) response during unconfined compression. The initial linear slope of unconfined stress strain plot is termed the initial loading stiffness. The peak stress at which the sample fails is known as the unconfined strength. Figure 6.4 is a plot of unconfined strength as a function of consolidation stress.

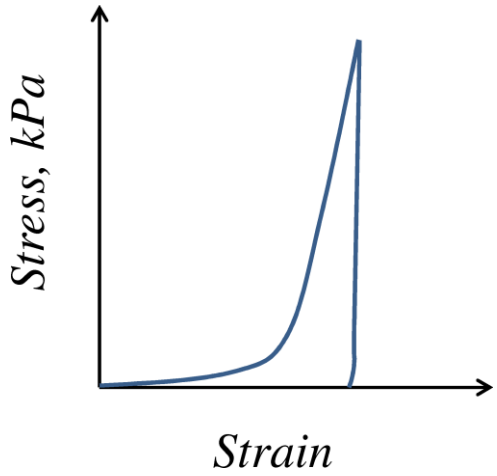

Figure 6.1 Typical stress–strain behaviour during confined loading-unloading, obtained from EPT

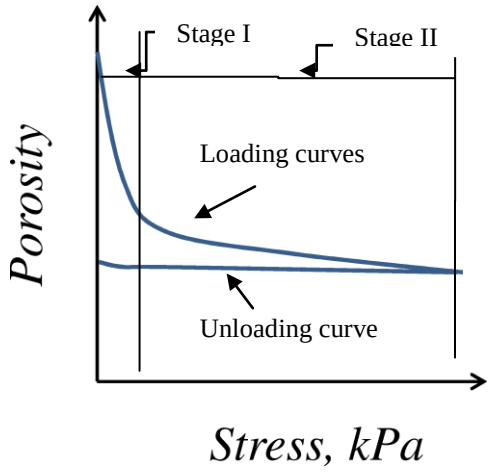

Figure 6.2 Typical porosity–stress behaviour during confined loading-unloading, obtained from EPT

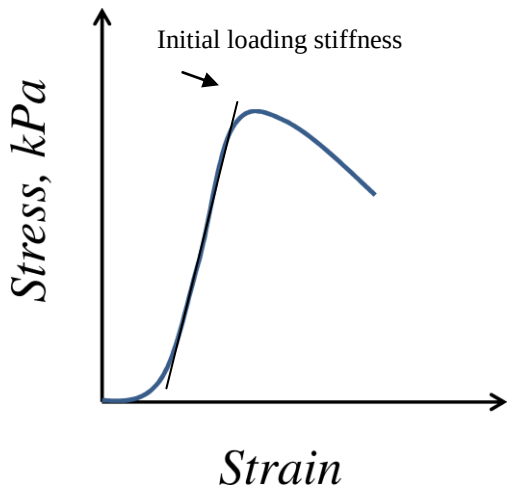

Figure 6.3 Typical stress-strain behaviour during unconfined compression to failure obtained from EPT

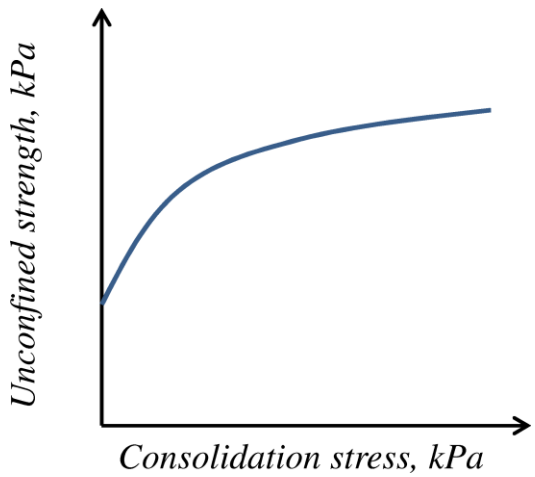

Figure 6.4 Typical flow function obtained from EPT

The confined compression behaviour is relevant to die compression and tableting used in several industries. The unconfined stress strain behaviour including peak strength gives a measure of flowability and relevant to many different industrial

processes when the material is required to undergo plastic flow with sometimes very large deformation.

6.3 *DEM input parameters*

The effect of DEM input parameters including particle contact loading stiffness, particle tangential stiffness and inter-particle friction coefficient is explored next.

6.3.1 Particle contact loading (plastic) stiffness

Particle stiffness is often reduced in DEM simulations to reduce computational time, since the critical time step is inversely proportional to $\sqrt{k_{max}}$ (see Eqn. **(2.7)**. For some classes of problems, particle stiffness may not have significant effect on the prediction and reducing it may therefore reduce the computational cost. In this study, the particle contact normal loading stiffness (k_1) was varied in a range of 0.5 - 5 kN/m to explore the effect on bulk response. The other parameters are kept constant.

Figure 6.5 shows the effect of the normal loading stiffness k_1 on the porosity-stress responses during confined compression. It is shown that the fill porosity does not change significantly when k_1 is increased for the range of stiffness investigated, as long as the particle overlap is kept less than 5%.

The powder compression process can be broadly divided into two stages; stage I and stage II. Stage I relates predominantly to particle rearrangement at low consolidation stresses while stage II relates to compression at particle contacts with particle rearrangement to a smaller extent. From Figure 6.5, it can be observed that the porosity decreases sharply and nonlinearly during the initial stage I, this is consistent with experimental results of fine powders under initial compression. Furthermore, it is very interesting to find that the drop in porosity is very similar for all magnitudes of loading stiffness k_1, indicating that particle rearrangement is independent of particle contact loading stiffness. As the consolidation progressed (stage II), the

porosity varied linearly with a flatter slope compared to stage I, again confirming the observed experimental behaviour for limestone powders. The sample with lower k_1 exhibits a steeper slope in stage II, showing larger compressibility than the sample with higher k_1. This is expected as the contact loading stiffness is expected to affect the bulk loading stiffness. Upon unloading, the samples exhibit almost parallel unloading curves indicating that contact loading stiffness k_1 does not affect the bulk unloading stiffness.

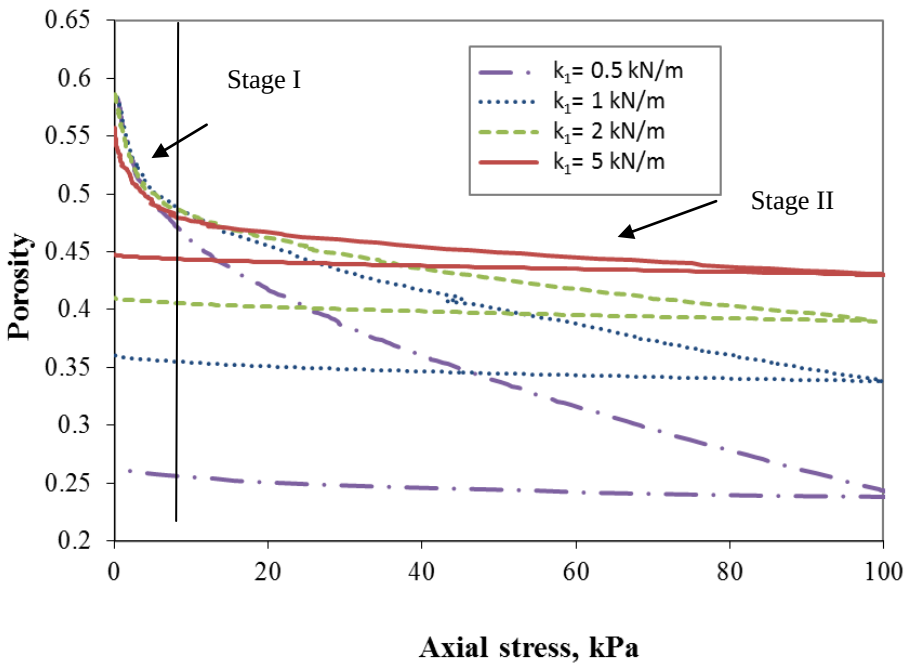

Figure 6.5 Effect of contact loading stiffness (k_1) on porosity stress behaviour during confined compression

After unloading the confinement is removed and the sample is failed by displacement driven load. Figure 6.6 shows the effect of contact loading stiffness on the unconfined stress strain behaviour. As the contact loading stiffness is decreased, the unconfined strength is increased. Additionally, the softening response after reaching a peak becomes more prominent with decreasing stiffness showing over-consolidated behaviour.

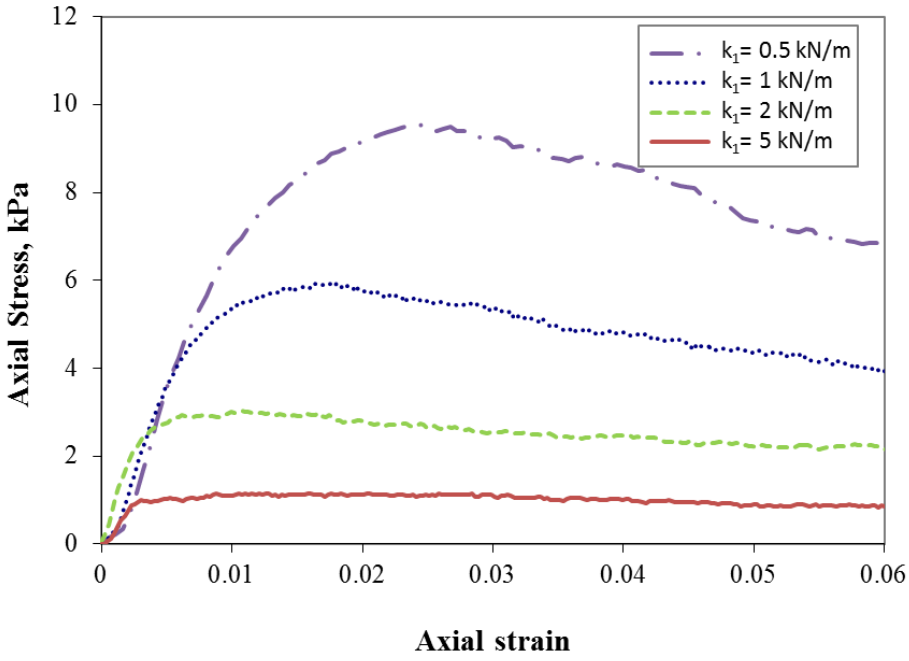

Figure 6.6 Effect of loading stiffness on unconfined stress strain behaviour

The increase in strength due to decreasing stiffness can be related to the consolidated porosity becoming smaller. The plot between consolidated porosity and unconfined strength for varying stiffness is shown in Figure 6.7. The decrease in the porosity gives rise to increase in the CN with the corresponding increase in the unconfined strength (as also explained in section 4.7).

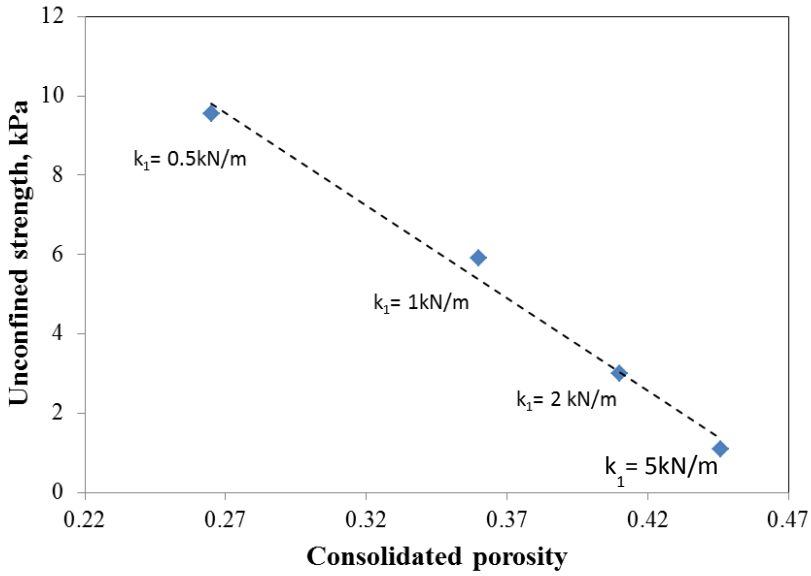

Figure 6.7 Effect of consolidated porosity (@100kPa) on unconfined strength for varying contact loading stiffnesses

6.3.2 Particle tangential stiffness

Tangential stiffness may play a significant role in the compressive and shearing behaviour of powders and this has not been explored extensively in literature yet. The ratio of tangential stiffness to normal stiffness (k_t/k_n) is varied by only varying tangential stiffness whilst the normal stiffness is kept constant. The tangential stiffness is varied in the range of 1-1/10. Figure 6.8 shows the effect of tangential stiffness on porosity-stress response during confined compression. It can be observed from the figure that the tangential stiffness does not affect the initial fill porosity. On the first application of stress (up to 5 kPa) the porosity decreases in similar non-linear fashion for all stiffness. As the consolidation stress progresses further, the porosity varies linearly. The sample with the lowest tangential stiffness (k_t/k_n =1/10) exhibits a steeper slope compared to that with a higher tangential stiffness (k_t/k_n =1), indicating a larger compressibility. For lower tangential stiffness slip sets in earlier and allows for larger inter-particle relative displacement and ultimately leading to larger compressibility.

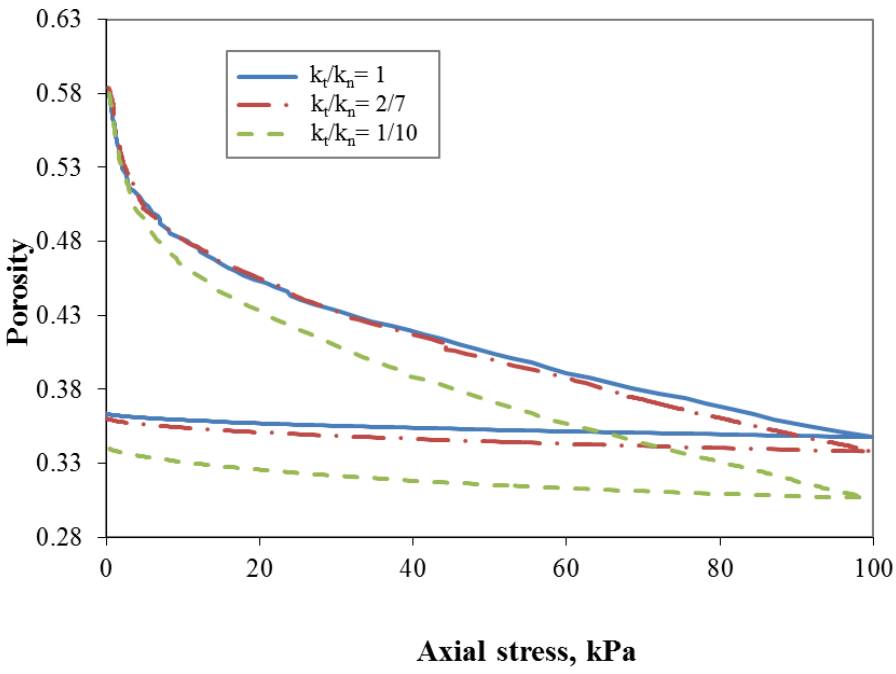

Figure 6.8 Effect of tangential stiffness on porosity stress behaviour

Figure 6.9 shows the effect of tangential stiffness on unconfined stress strain response. As the tangential stiffness increases, the initial loading stiffness also increases. This is in contrast to the relatively unchanged initial loading stiffness with increasing contact normal stiffness. The unconfined strength remains more or less similar (within 7% approx.). The peak strain increases with decreasing stiffness. It should be noted that unconfined stress-strain simulations shown in Figure 6.9 were conducted after unloading the samples and the porosities at the start of unconfined compression were different. The effect of tangential stiffness alone on unconfined stress strain is obscured by the differences in the porosity at the beginning of unconfined compression.

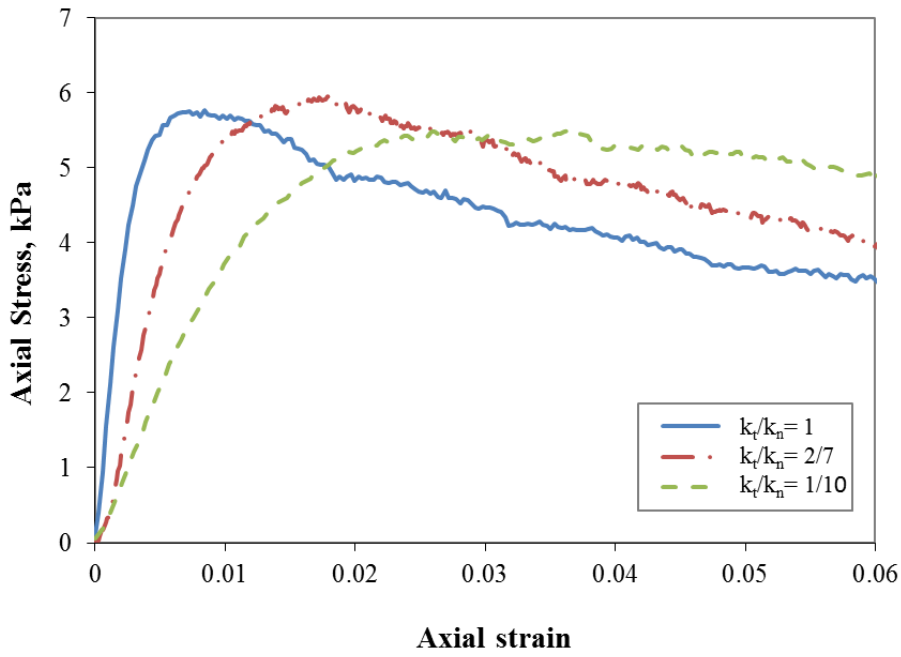

Figure 6.9 Effect of tangential stiffness on unconfined stress strain

To isolate the effect of porosity and tangential stiffness on unconfined stress strain behaviour, another set of simulations with the same consolidated porosity but different tangential stiffness were conducted as shown in Figure 6.10. The consolidated sample with $k_t/k_n=1$ is taken as reference sample for other k_t/k_n ratio. It can be observed that increasing tangential stiffness increases the initial loading stiffness, peak strain, and unconfined strength. The stress strain response almost converges after strain of 3.5%. For lower tangential stiffness, relative shear

displacements are larger, resulting in a greater sample deformation before failure sets in.

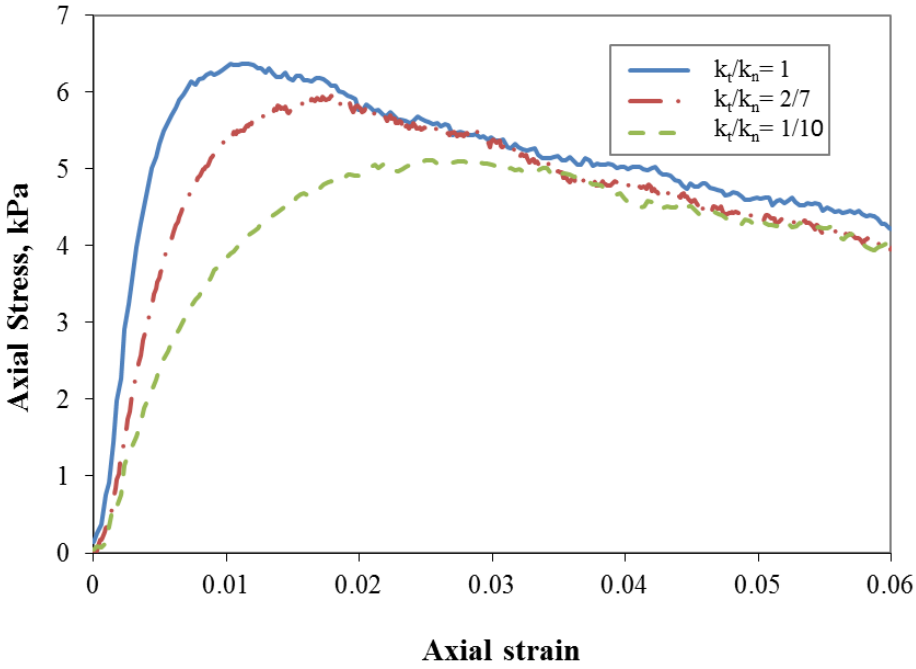

Figure 6.10 Effect of tangential stiffness on unconfined stress strain (same porosity)

The higher unconfined strength for higher tangential stiffness can be explained by Figure 6.11. The figure is a plot of stress vs coordination number of the assemblies with varying tangential stiffnesses. All the samples have very similar porosity and coordination number (Z) at the beginning of unconfined compression. As loading progresses, the axial stress increases strongly with only a very small decrease in the coordination number before reaching the peak (unconfined strength). Further loading of the sample following the peak leads to a significant drop in the observed coordination number which is associated with increasing dilation (increasing volume) (Jenike, 1964; Schofield and Wroth, 1968) and decreasing post peak strength. The sample with higher tangential stiffness achieves a higher coordination number Z which gives rise to a higher unconfined strength. The sample with higher stiffness compresses more during unconfined compression compared to the sample with lower stiffness due to delay in slip setting in. This could be the reason for higher coordination number for a higher tangential stiffness.

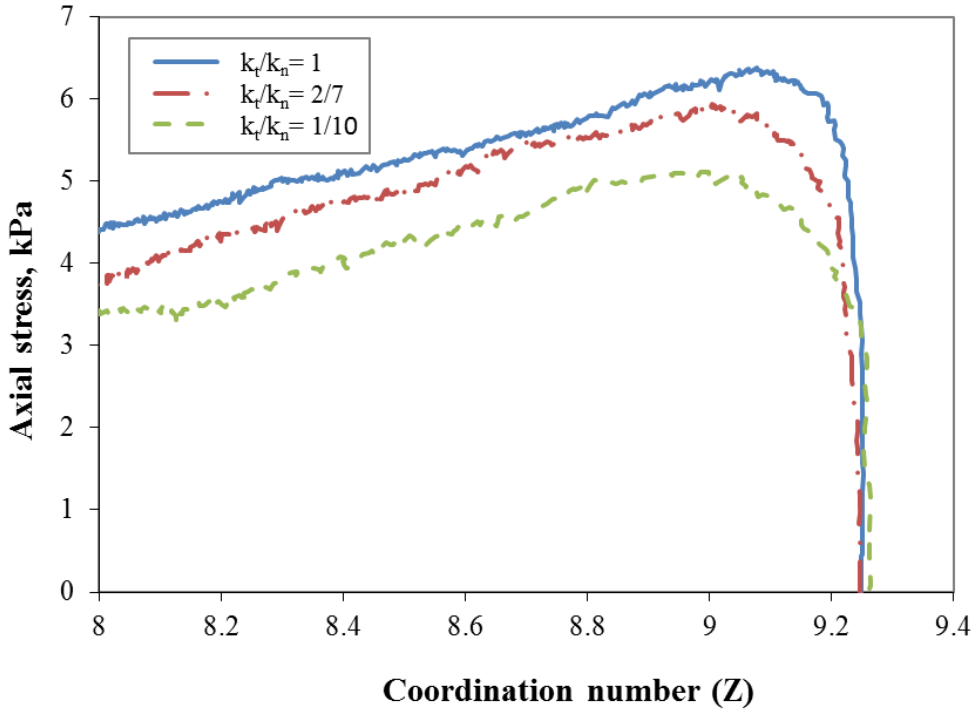

Figure 6.11 Effect of tangential stiffness on evolution of coordination number during unconfined compression

6.3.3 Inter-particle friction coefficient

The effect of the inter-particle friction coefficient on packing, compression, and shear behaviour in uniaxial test simulations is explored next. The value of μ_{sf} is varied in a range of 0-1.0.

Figure 6.12 shows the influence of particle to particle friction on porosity-stress response during confined compression. With an increasing inter-particle friction coefficient, the fill porosity also increases in a nonlinear fashion (also see Figure 6.13). A porosity of 41.5% was observed for the frictionless case and 58.5% for the μ_{sf} =1 case. As coefficient of friction increases from 0 to 0.5, there is significant increase in porosity; however, further increase in friction leads to a very small increase in fill porosity. On the application of a consolidation stress the porosity decreases sharply. As the consolidation stress increases further, the porosity decreases at a constant slope. The slopes are almost parallel for different coefficients

of friction indicating that friction does not affect the slope of the loading curves (or bulk loading stiffness). The consolidated porosity increases with increasing μ_{sf} (see Figure 6.13). A higher coefficient of friction provides a larger resistance to inter-particle sliding and ultimately gives rise to a higher consolidated porosity. For unloading, the slope of the unloading line seems to be more or less parallel with an increasing μ_{sf}.

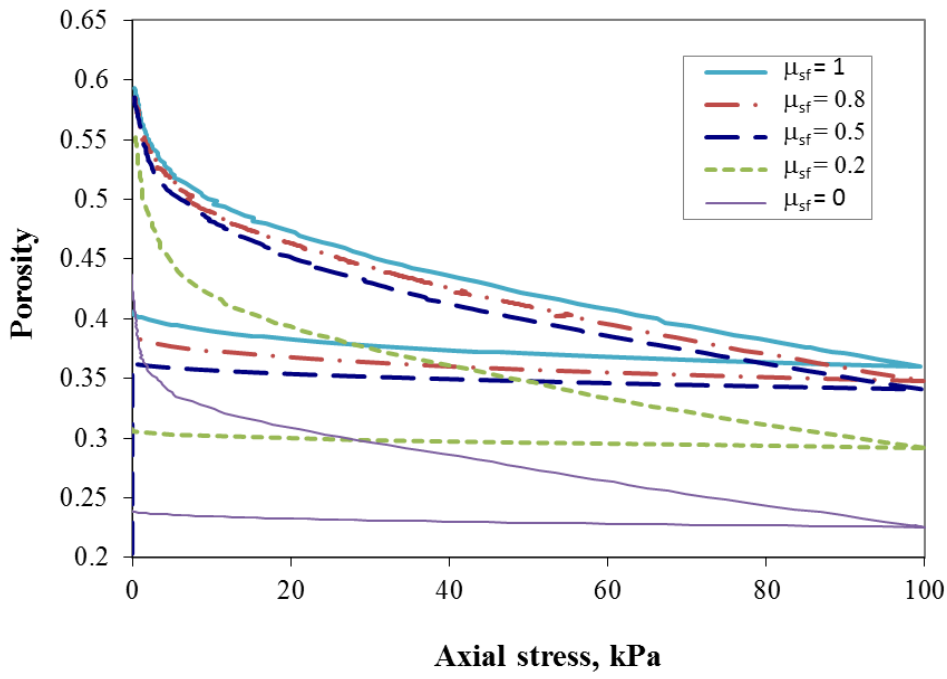

Figure 6.12 Effect of inter-particle friction coefficient on stress porosity relationship

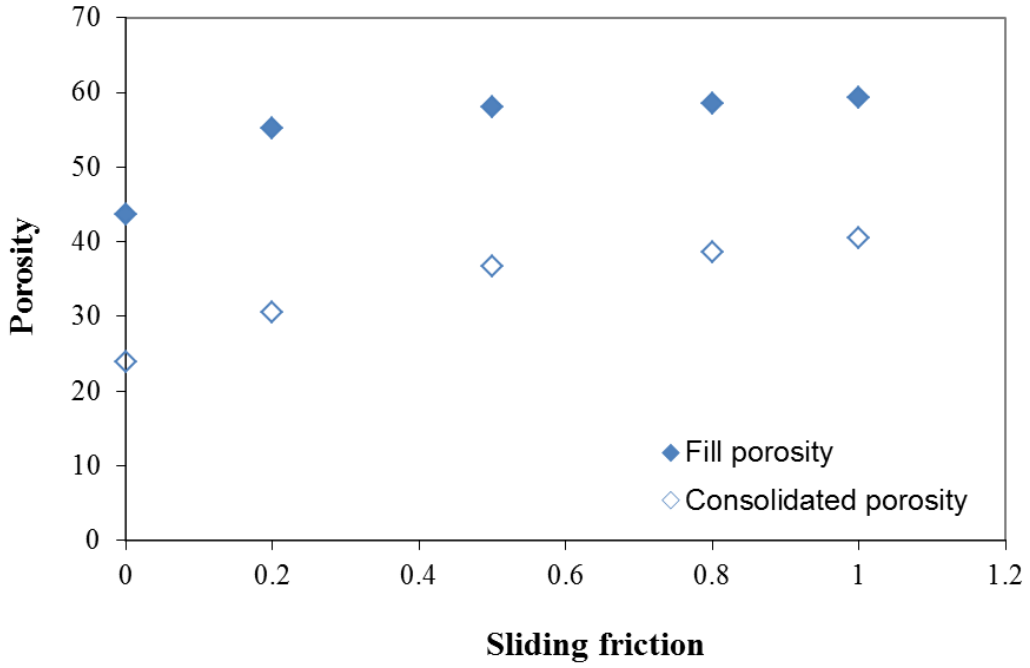

Figure 6.13 Effect of inter-particle friction coefficient on fill and consolidated porosity

Figure 6.14 shows the effect of μ_{sf} on the unconfined strength response. It is important to observe that even the sample with zero particle sliding friction has a significant unconfined strength. This could be due to particle adhesion and friction due to interlocking of non-spherical particles. As the μ_{sf} increases to 0.2 the unconfined strength increases significantly, although the consolidated porosity corresponding to μ_{sf} = 0.2 is higher compared to the porosity at μ_{sf} = 0 (Figure 6.13). The increase in unconfined strength is attributed to the increased in shearing resistance due to increasing μ_{sf}. Upon further increases of μ_{sf}, the unconfined strength decreases. The decrease in unconfined strength with increasing μ_{sf} is counterintuitive; it is believed that increase in friction leads to higher unconfined strength due to frictional resistance. However, it is important to note that with increasing friction compressibility decreases and sample compresses to a higher porosity which ultimately gives rise to a lower co-ordination number and lower strength. Increasing μ_{sf} to a value greater than 0.8 lead to only a minor decrease in unconfined strength.

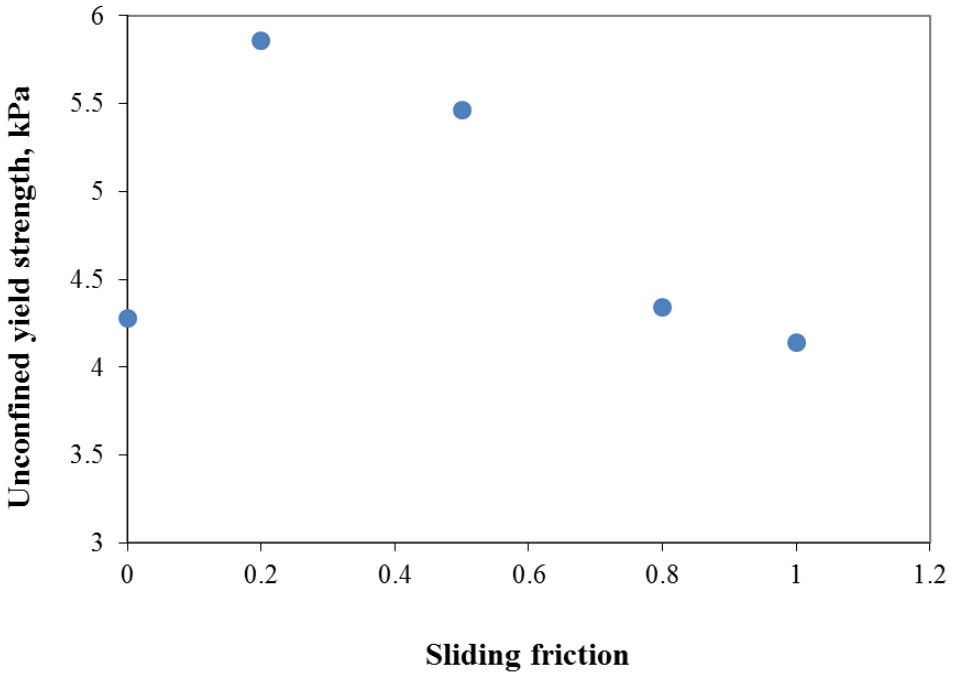

Figure 6.14 Effect of inter-particle friction coefficient on unconfined yield strength

Figure 6.15 shows the effect of μ_{sf} on unconfined stress strain behaviour. It is observed that initial stiffness decreases with increasing particle friction due to a reduction in consolidated porosity with increasing friction (see Figure 6.12). Additionally, a greater softening of the post peak strength can be observed for lower μ_{sf} which is associated with a larger dilation.

.

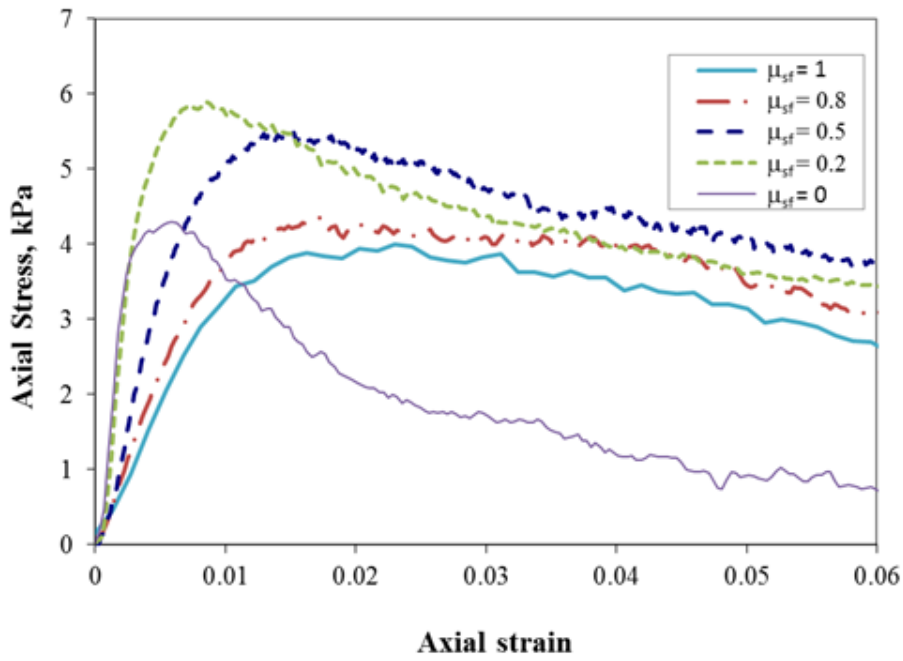

Figure 6.15 Effect of inter-particle friction coefficient on unconfined stress strain behaviour

In order to shed light on the effect of packing, three simulations with the same initial packing but different μ_{sf} (0.2-0.8) were performed (see Figure 6.16). The figure shows that both peak stress (unconfined strength) and peak strain increase significantly with increasing μ_{sf}. Additionally, it is interesting to note that friction does not affect initial loading stiffness which confirms that the decreasing initial loading stiffness with increasing μ_{sf} seen in the previous Fig. 6.15 is due to the resulting greater consolidated porosity with greater friction. The softening in the post peak regime also increases with increasing friction due to the increased dilation with increasing friction.

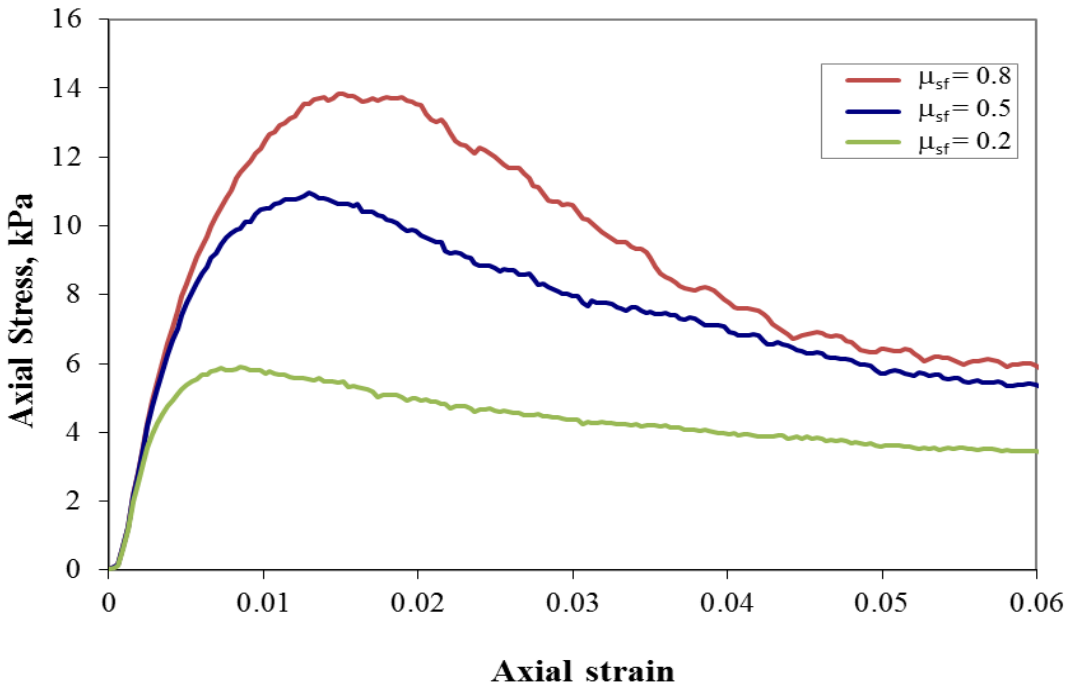

Figure 6.16 Effect of inter-particle friction coefficient on unconfined stress strain (same porosity)

6.4 *DEM model implementation*

The effect of DEM model implementation including numerical time-step, strain rate, and boundary friction is explored next.

6.4.1 Numerical time-step

Choosing an appropriate time step is very critical in DEM simulation. If a very small time step is chosen, the simulation will take a very long time to complete. However, if the time step is too large, considerable particle overlap can occur which can result in erratic bulk response and computational instability. In order to investigate the effect of time step on numerical bulk response, simulations were performed with fixed time steps of 3, 10, 20, 30, 50, and 70% of T_c (as in equation **(2.7)**. For all simulations the uniaxial cylinder was filled anew, as a result a different packing will be formed which may result into slightly different bulk response. The simulations were filled a new since time step may have effect on filling. To assess the variability due to different packing three simulations with a time step of 10% were conducted. Figure 6.17 shows the axial porosity-stress response during confined compression for

all time steps except 70% of Tc. For time step up to 50% of Tc, the simulation results are within the scatter of the results for 10% of Tc. Small differences in axial porosity-stress relation can be noticed for time step larger than 30% of Tc but this could be a result of different packing. When time step is increased to 70% of Tc, the initial porosity decreased to 47.6% from a porosity of ~60% at smaller time steps. The simulation with 70% of Tc was not pursued further.

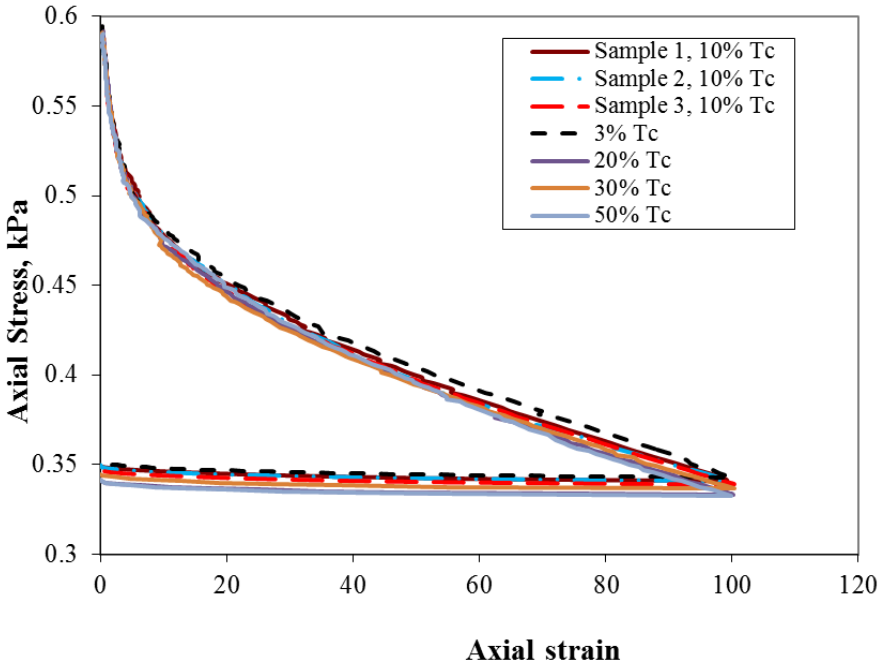

Figure 6.17 Effect of time step on confined stress strain behaviour

Figure 6.18 shows the effect of time step on unconfined stress strain behaviour. No significant deviation in the unconfined stress strain behaviour was found with increasing time step to 50 % of T_c.

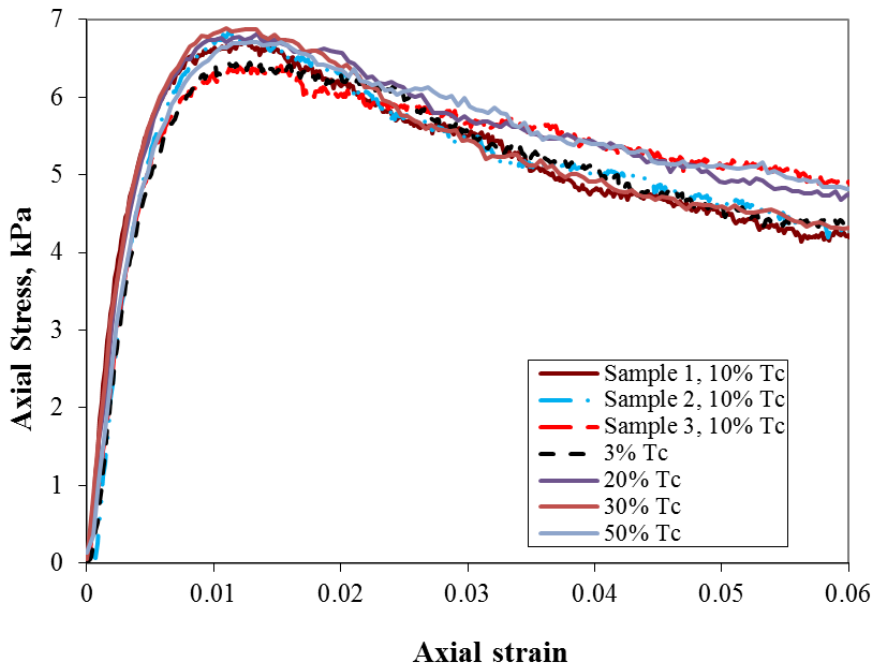

Figure 6.18 Effect of time step on unconfined stress strain behaviour

This limited study on computational timestep suggests that the time step can be increased up to 50% of Tc to get satisfactory predictions. In this study time step of less than 10% of Tc was used for all simulations.

6.4.2 Strain rate

Particulate solids may display a range of stress regimes in different bulk handling applications. The stress regime may include quasi-static, intermediate, and dynamic regime (Tardos, 2003). In quasi-static regime the stresses inside the material are supported by frictional interaction between particles, and the velocity between the particles are nearly zero or very small. In this regime stresses are independent of velocity or strain rate. In the dynamic regime the stresses inside the material are supported by collision between the particles, and the velocity between the particles are large but much smaller than the velocity of interstitial fluid between the particles. In this regime stresses are dependent on the velocity of the particles. Between the quasi-static and inertial regime is the intermediate regime, where both frictional and collisional interactions must be considered. In this study, the effect of strain rate in

the quasi-static and intermediate regime (Tardos, 2003) in uniaxial test simulations is investigated.

Figure 6.19 shows the effect of strain rate on the confined stress porosity response. The strain rate was varied in a range of 0.02 s^{-1} to 5 s^{-1}. It can be seen that the loading response is largely unaffected by the strain rate in this range. The unloading curves are almost identical for strain rates up to 0.5 s^{-1}, and no fluctuations in stress can be seen.

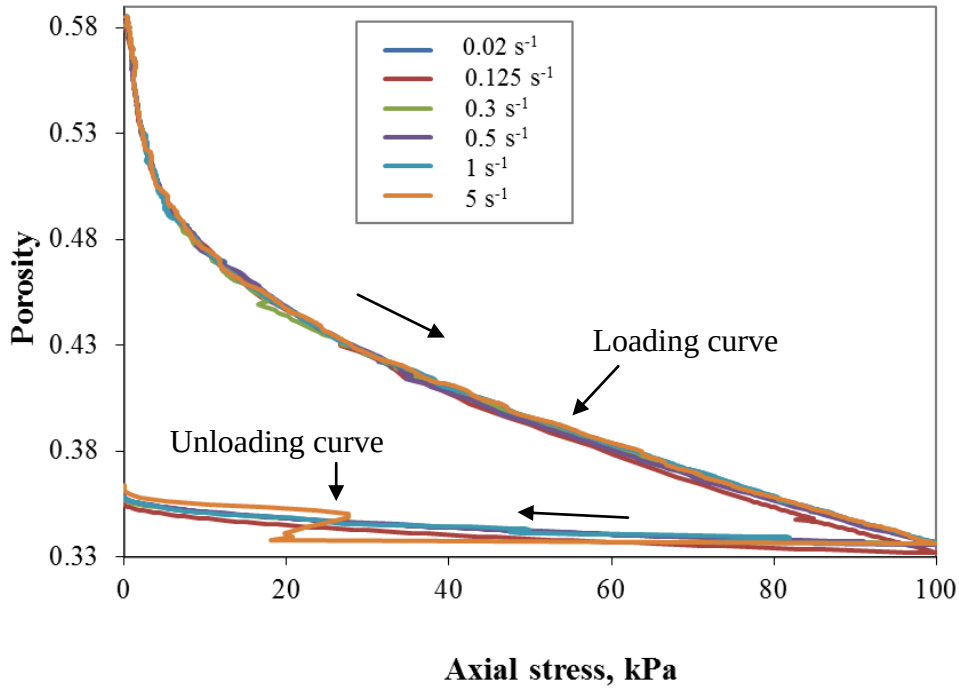

Figure 6.19 Effect of strain rate on porosity stress behaviour during confined compression

Some fluctuation in stress can be observed at higher strain rates during unloading. Figure 6.20 shows the stress fluctuation seen at higher strain rates (>0.5s^{-1}) during unloading. The stress fluctuation at higher strain rates is a characteristic of intermediate regime (Tardos, 2003). Studying the visualisation of the DEM results show that the stress fluctuation is due to stick-bounce behaviour which arise from the unloading at higher strain rate. For loading, the particles are confined and collisions between particle-particle and particle-wall are prohibited, therefore, loading behaviour is unaffected by strain rate. However, for unloading as the top unloading

plate retreats, particles bounce back due to the empty space created by upward retreat of the top platen.

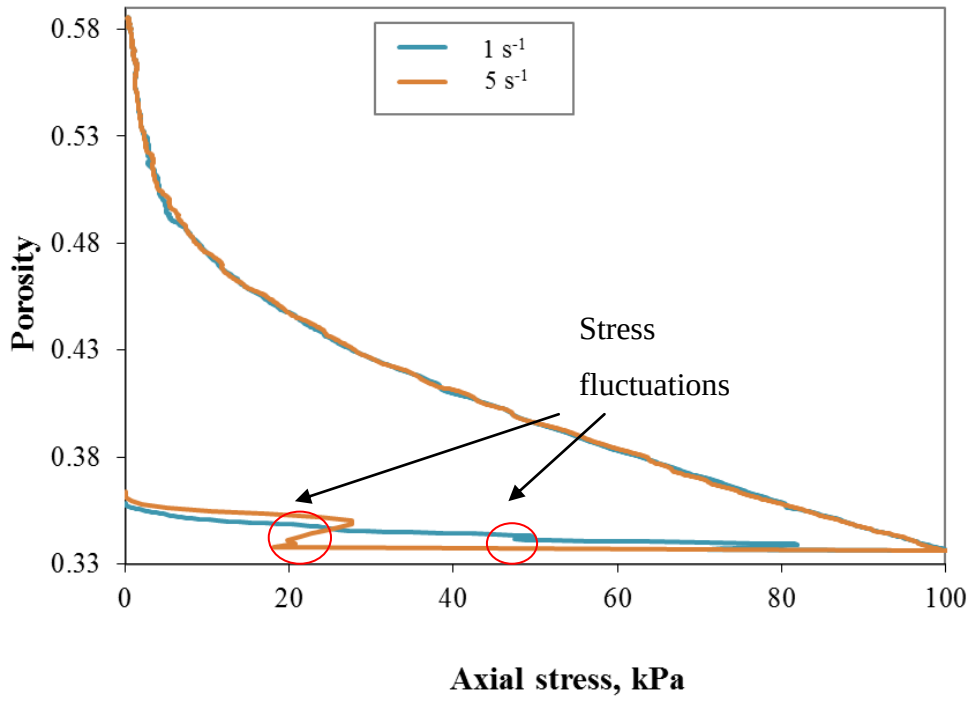

Figure 6.20 Effect of strain rate (1 s^{-1} - 5 s^{-1}) on porosity stress behaviour during confined compression

The effect of strain rate on unconfined compression behaviour is also explored. Figure 6.21 shows the effect of strain rate on unconfined strength for consolidation stresses of 20 kPa and 100 kPa. The unconfined strength is almost independent for values of strain rate lower than 1 s^{-1} for both consolidation stresses. For the strain rate higher than 3 s^{-1}, a sudden increase in unconfined strength can be observed. By fitting a power law (shown by dotted line) to the data for the value of strain rate above 3s^{-1}, an index of less than 2 can be found. A power index of less than 2 indicates the behaviour typical for dense systems and corresponds to an intermediate regime between quasi-static and rapid granular flow (Moreno-Atanasio et al., 2005; Tardos, 2003). The strain rate dependency in intermediate regime (slope of the fitted line) increases with decreasing consolidation stress. Such behaviour was also found in a uniaxial test simulation using JKR contact model (Moreno-atanasio et al.

(2005)). Simulations at higher strain rate were also repeated using smaller time steps and it was found that the increase in UYS with time is not an artefact of time step.

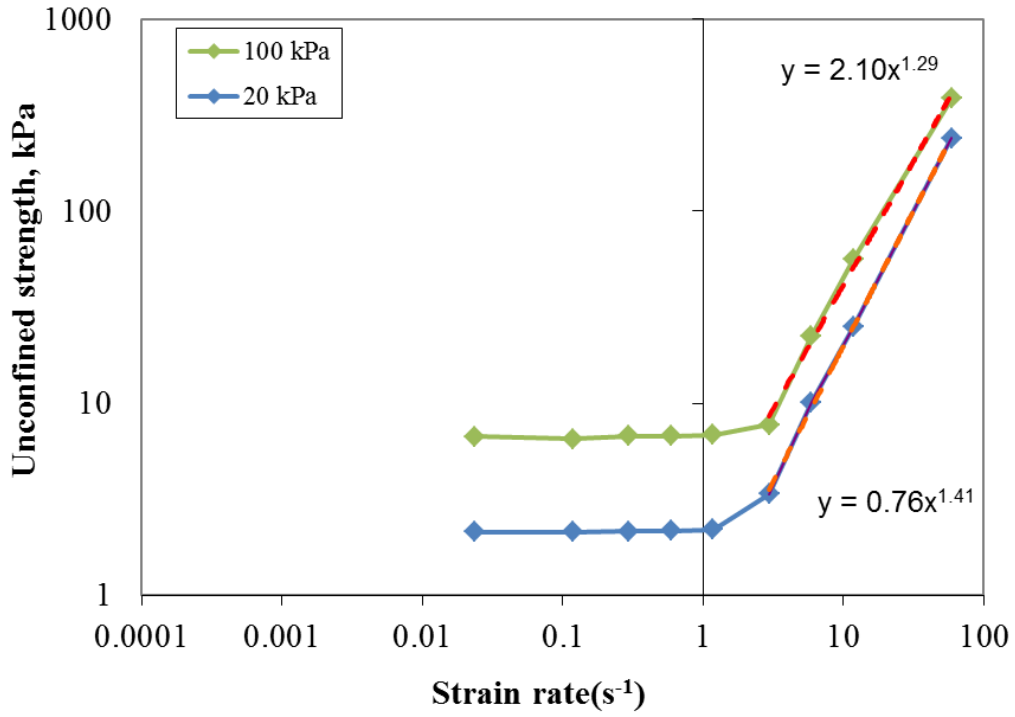

Figure 6.21 Effect of strain rate on unconfined strength at two consolidation stresses ($k_2=10^5$ N/m, $k_{adh}=0$ N/m)

Figure 6.22 shows the effect of strain rate on contact plasticity, for contact plasticity of λp=0 (elastic) and 0.99 (relatively plastic). The unconfined strength is independent of strain rate for strain rate smaller than 1 s^{-1} and index number of less than 2 is found which is similar to the behaviour observed in Figure 6.21 where λ_p=0.99. The slope of the fitted (dotted) line seems to increase with increasing plasticity.

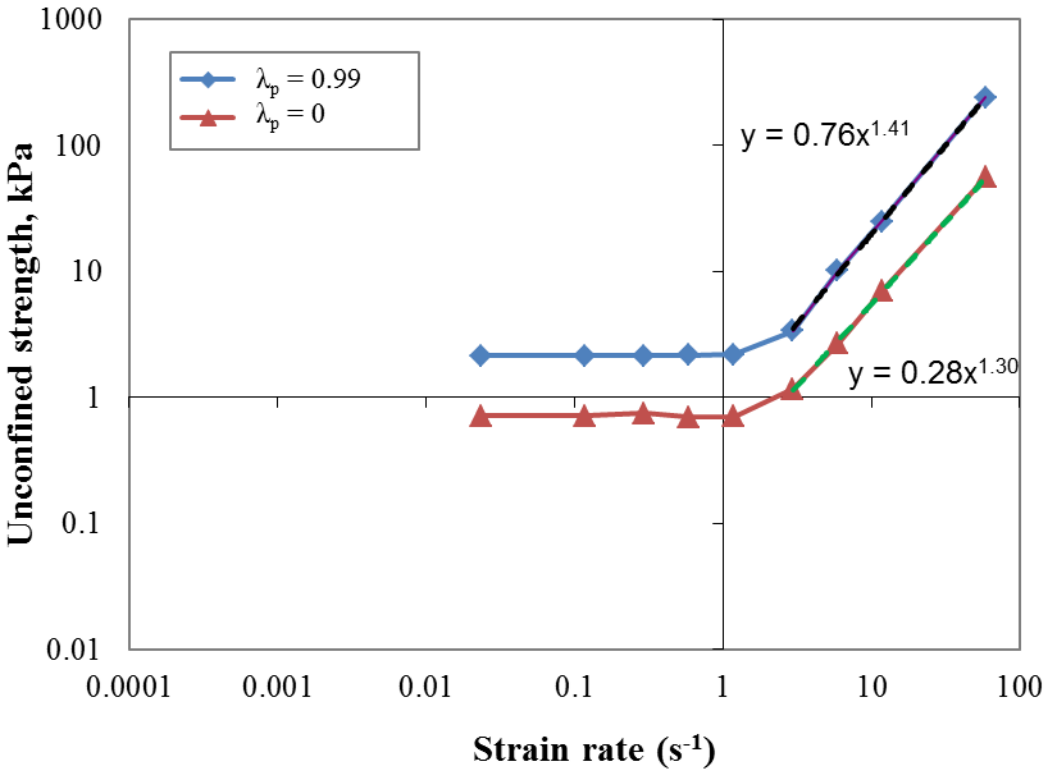

Figure 6.22 Effect of strain rate on unconfined strength at two levels of contact plasticity

The effect of strain rate on unconfined stress strain is also investigated. The unconfined stress-strain behaviour is almost identical for the strain rates of less than 0.6 s^{-1}, however from strain rate of 0.6 s^{-1} upwards, the unconfined stress strain behaviour starts deviating from the other results. Therefore in this study the strain rate smaller than 0.6 s^{-1} is used. The strain rate corresponds to quasi-static regime with inertia number of less than $1*10^{-3}$; Inertia number being the ratio of measure of inertial forces of particles to imposed force and is often used to measure the significance of dynamic effects in granular material. For quasi-static regime, Midi (2004)defines an inertia number less than 10^{-2} for dense granular system.

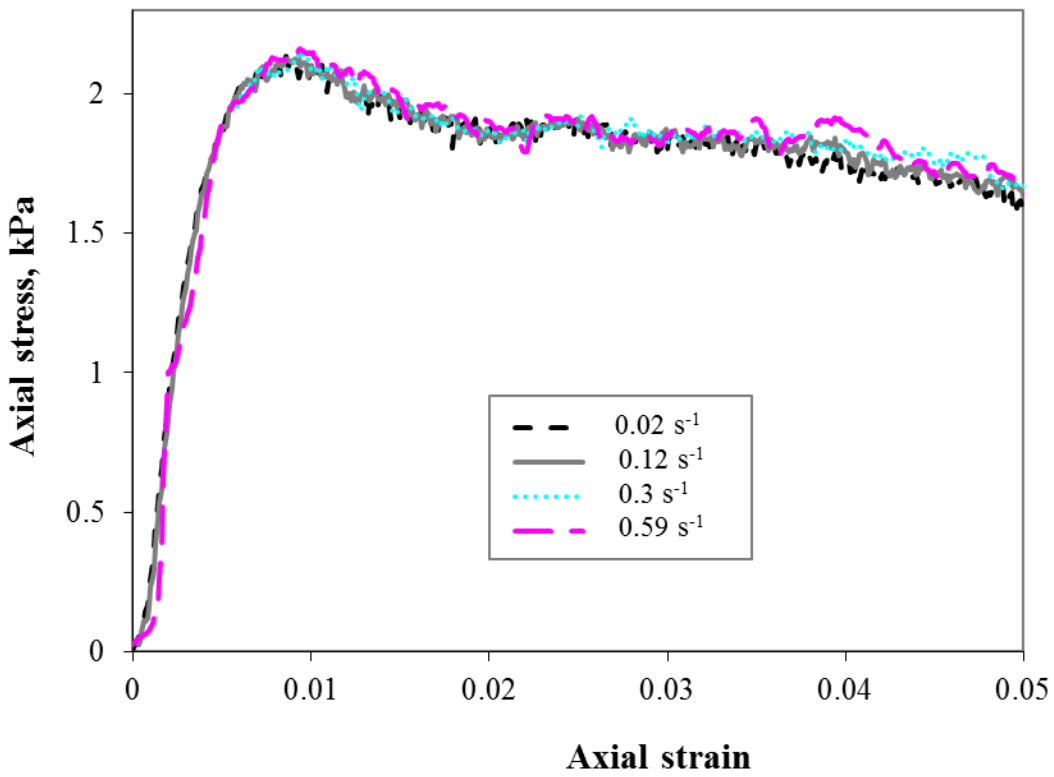

Figure 6.23 Effect of strain rate on unconfined stress strain behaviour (Maximum inertial number range ($2.3*10^{-5}$-$7.1*10^{-4}$))

6.4.3 Boundary friction

6.4.3.1 Particle to cylinder wall friction

In uniaxial testers, the stress is normally applied through loading platen at the top (Figure 6.24). The applied stress (σ_a) at the top is transmitted to the powder and to the die wall. The stress transmitted (σ_t) to the base platen is less than σ_a due to friction between the powder and the cylinder wall. The friction between particle and cylinder wall (μ_{wf}) is expected to play a key role in packing, confined, and unconfined compression response of powders. To evaluate the effect of cylinder wall friction on bulk response, uniaxial simulations with varying value of (μ_{wf} = 0-0.8) are performed.

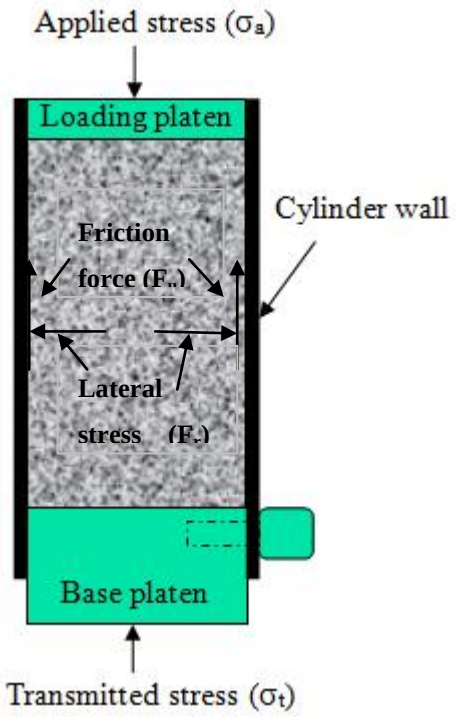

Figure 6.24 The geometry and loading in uniaxial test with various parameters defined

The coefficients of inter-particle friction and the particle to platen (both loading and base platen) friction were both kept constant at 0.5 throughout the simulations. Figure 6.25 shows the effect of μ_{wf} on porosity-stress response during confined compression. A very small increase in fill porosity with increasing μ_{wf} can be observed, with the fill porosity increasing from 58.7% at $\mu_{wf} = 0$ to 60% at $\mu_{wf} = 0.8$. The effect of particle to wall friction on fill porosity is thus much smaller compared to the effect of particle to particle friction on fill porosity. On the application of stress (stage I), porosity decreases more sharply for lower μ_{wf} showing a larger particle rearrangement. As the consolidation progresses (stage II), the sample with lower μ_{wf} continues to compress more and exhibits a steeper slope in porosity-stress curve. With increasing μ_{wf}, the amount of force transmitted into cylinder wall also increases and thus reduces the compression of the powder. It should be noted that with wall friction effect mean stress in the system also decreases (Figure 6.26).

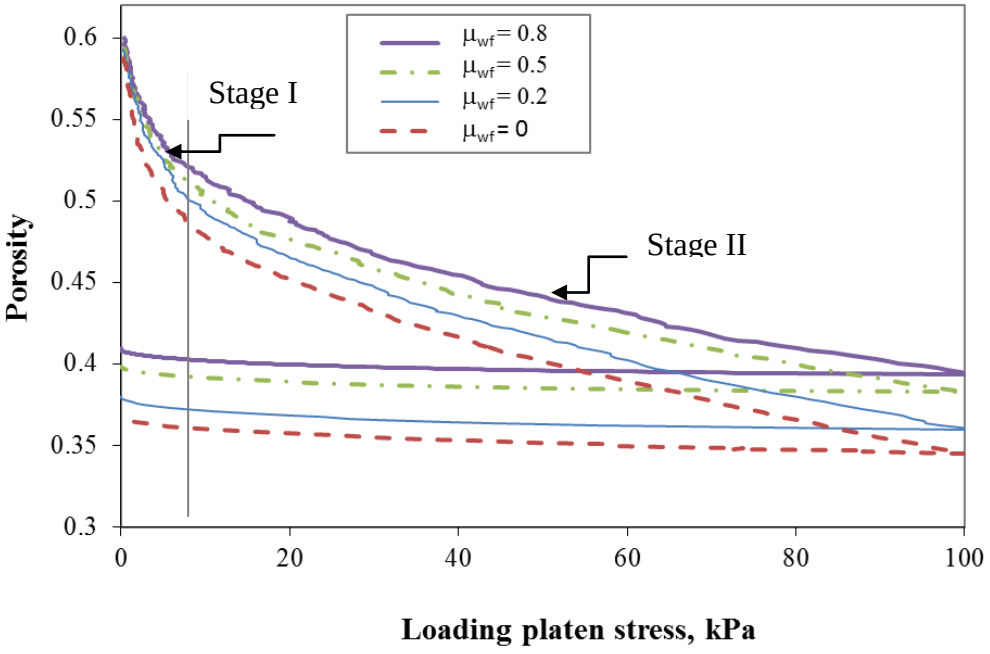

Figure 6.25 Effect of particle to cylinder wall friction on stress porosity relationship

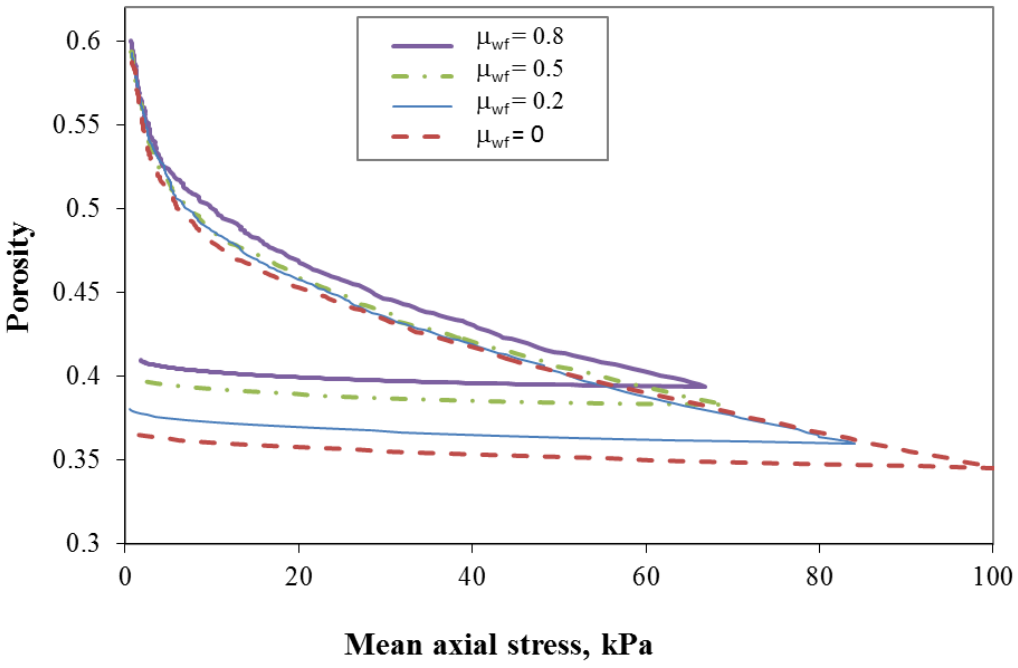

Figure 6.26 Effect of particle to cylinder wall friction on stress porosity relationship

The reduction in mean axial stress leads to reduction in consolidated porosity which ultimately affects unconfined yield strength. Figure 6.27 shows the effect of particle to cylinder wall friction on unconfined strength. It can be observed that the unconfined strength decreases in a nonlinear fashion with increasing $\mu_{wf.}$ When μ_{wf} is increased from 0 to 0.2, the unconfined strength decreases strongly (approx. by 25%). The rate of decrease in unconfined strength decreases with increasing $\mu_{wf.}$ When μ_{wf} is increased from 0.5 to 0.8, the unconfined strength only decreases by approximately 2.5%. The decrease in unconfined strength with increasing μ_{wf} can be related to consolidated porosity.

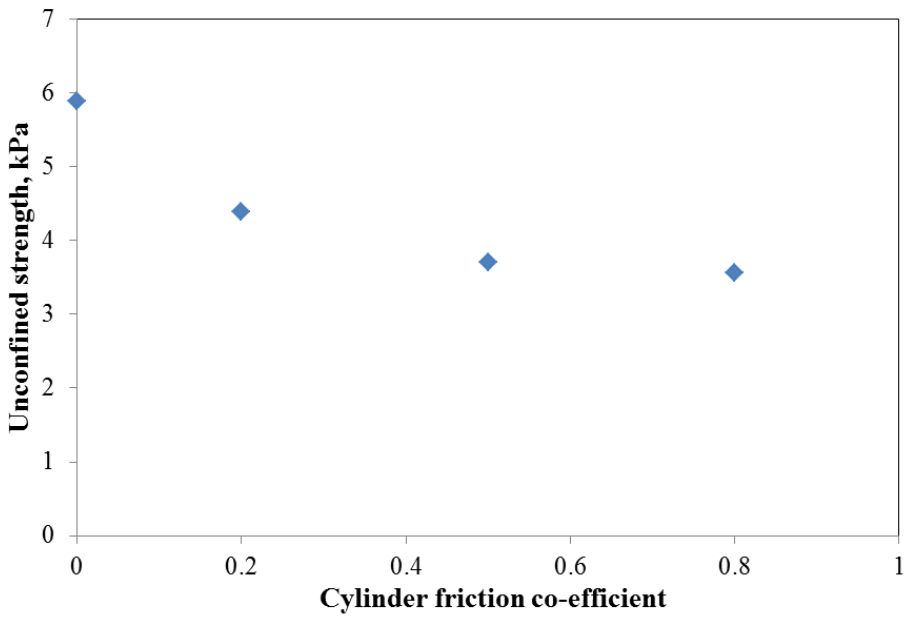

Figure 6.27 Effect of particle to wall friction on unconfined strength

6.4.3.2 Particle to platen friction

In a uniaxial test with frictionless walls and platen, the major principal stress is aligned with the direction of the vertical applied load. However, for frictional walls or platens, the direction of major principal stress deviates from the direction of

applied stress. Here the effect of particle to platen (both loading and base) friction on the confined compression behaviour is investigated, both for frictionless cylinder walls (Figure 6.28) and cylinder walls with friction (Figure 6.29). The same initial packing was used for all simulations. The particle to platen friction was varied in a range of 0-0.8. It can be observed that particle to platen friction does not have a significant effect on the porosity stress response. Whilst the sample with frictionless platen (μ_{plf} =0) compresses the most, further increase of $\mu_{plf,}$ produces negligible change in the stress porosity behaviour.

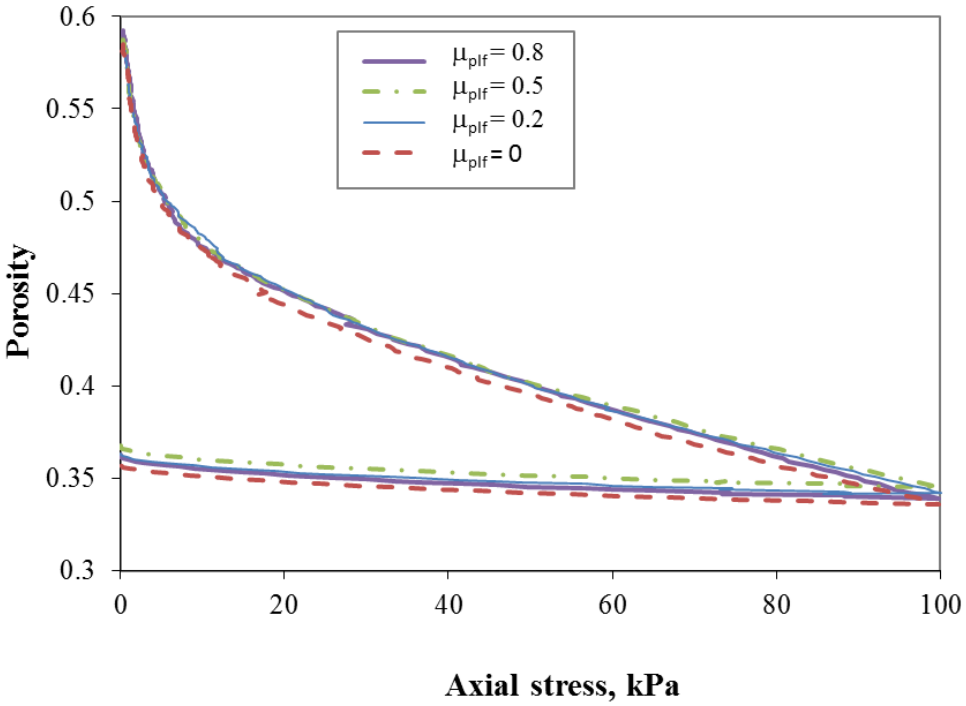

Figure 6.28 Effect of end platen friction on porosity stress relationship (frictionless cylinder walls)

A cylinder with a frictionless wall is a hypothetical situation. Next the effect of end platen friction on the samples with frictional walls (μ_{wf} =0.5) is explored (Figure 6.29). As μ_{plf} is increased no significant change in porosity-stress relationship can be noticed similar trend to the results for 0 wall friction but slightly higher consolidated porosity due to wall friction effect.

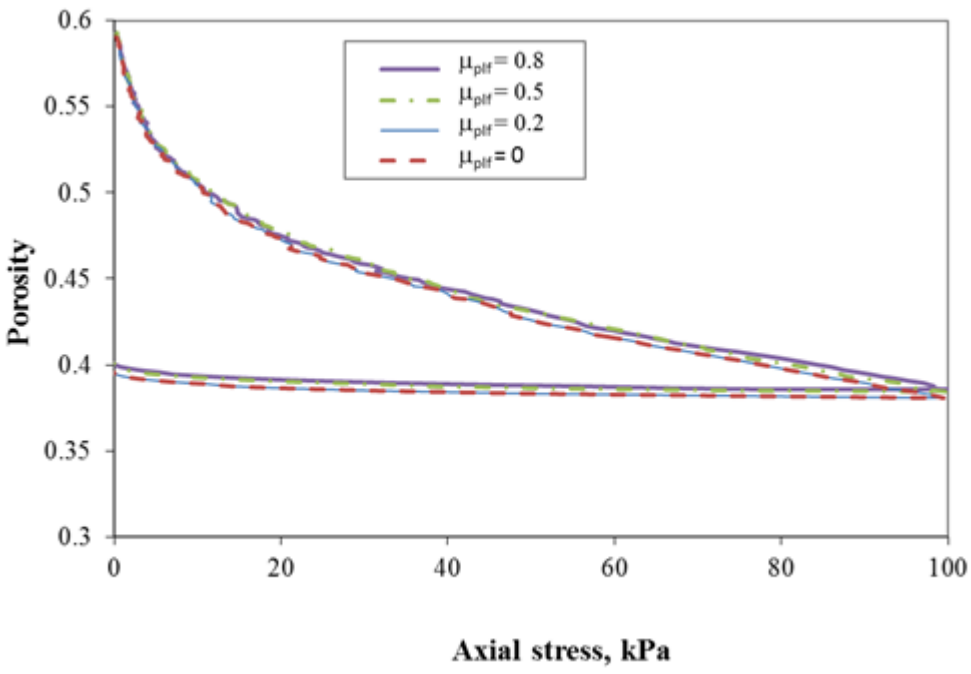

Figure 6.29 Effect of end platen friction on porosity stress relationship (cylinder wall friction=0.5)

The effect of end platen (loading and base) friction on the unconfined stress strain response is explored next. Unconfined compression simulations were performed on the sample with same packing and consolidated porosity. End platen friction was varied in a range of 0.1 to 0.8. The simulation with zero end platen friction was not possible since the sample keep slipping away from the end platen. Figure 6.30 shows the effect of end platen friction on unconfined stress strain behaviour. It can be observed that unconfined strength increases with increasing end platen friction. Unconfined strength increases significantly (13% approx.) when end platen friction is increased from 0.1 to 0.5 and the strength plateaus on further increase of end platen friction. Increasing end platen friction causes an increase in lateral restraint effect and therefore causes an increase in apparent strength. Such a behaviour was also noted by Bishop, A.W., Green (1965) in triaxial tests of cohesionless soil, especially for samples with a shorter aspect ratio.

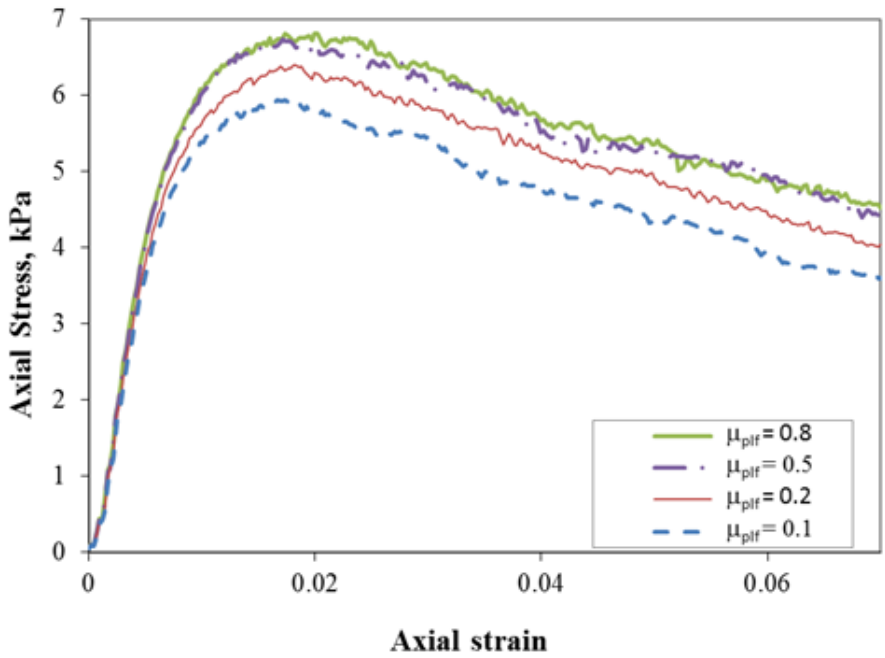

Figure 6.30 Effect of end platen friction on unconfined strength

The effect of lateral restraint due to end platen friction can also be seen in Figure 6.31. It is observed that as the platen friction increases the sample bulges more towards the centre of the sample than near the bottom of the sample.

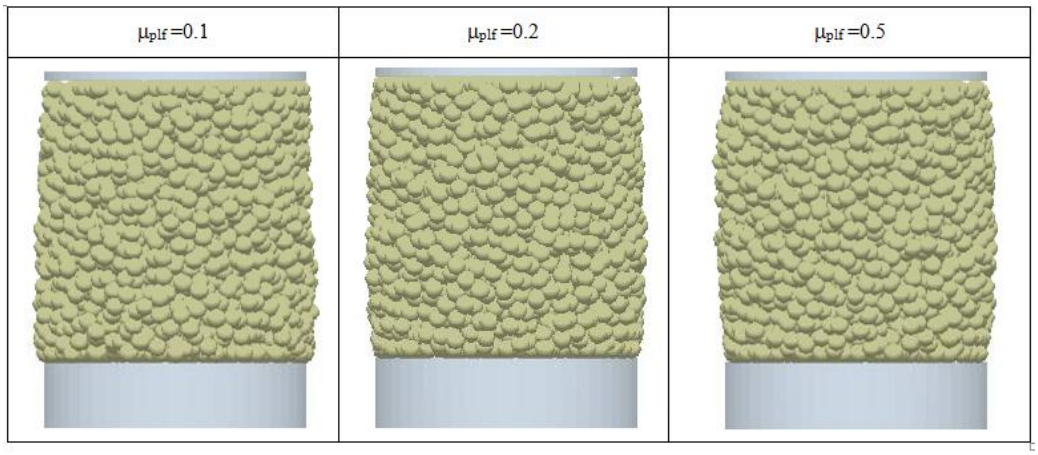

Figure 6.31 Effect of lateral constraint due to end platen friction

6.5 *Summary*

The influence of DEM input parameters and model implementation have been explored to study the effect on the bulk behaviour in uniaxial test simulations. The full sequence of the uniaxial test provides a full spectrum of loading scenarios likely to be encountered in material handling operations, ranging from filling porosity, confined compression under placement or shearing under flow regimes. The contact model parameters explored include particle contact normal loading stiffness, tangential stiffness, and contact friction coefficient. The DEM model implementation parameters included numerical time step, strain rate, and boundary condition. Many useful observations have been made with significant implications for the relative importance of the DEM input parameters. The major conclusions are:

- Particle contact normal stiffness has significant effect on the confined compression of a bulk sample, and therefore, should not be reduced to gain computational speed-up. Whilst particle contact loading stiffness does not affect particle rearrangement during the initial application of stress in confined compression simulation, the particle stiffness directly influences the bulk stiffness. The sample with lower stiffness compresses more and provides a higher unconfined strength compared to the sample with higher stiffness.
- Whilst the tangential stiffness does not affect fill porosity and initial rearrangement significantly, it is shown to influence the overall confined and unconfined compression response of a particle assembly. Reducing the tangential stiffness increases the overall compressibility and reduces the initial stiffness during unconfined compression, but does not affect the unconfined strength. However, for a sample with the same consolidated porosity, increasing the tangential stiffness increases both the initial loading stiffness and unconfined strength.
- Inter-particle friction coefficients affect the packing, compression, and unconfined strength of the sample assembly. Increasing the inter-particle friction coefficient increases fill porosity, and reduces the sample

compression. The effect of friction on unconfined strength is governed by the interplay of consolidated porosity (related to the coordination number) and shearing resistance due to increase friction coefficient. The sample unconfined strength first increases and then decreases with increasing inter-particle friction. For the unconfined simulations with the same consolidated porosity, the unconfined strength was increased and overconsolidation behaviour was enhanced with increasing inter-particle friction coefficient.

- Varying the fixed time step between 3 to 50% of Tc has no significant effect on packing, confined and unconfined compression of the sample. Increasing the time step above 50% of Tc causes a huge reduction in porosity resulting from larger particle overlap and leads to computational instability.
- For the range of strain rates (0.02 s^{-1} to 5 s^{-1}) investigated, the strain rate does not affect loading response during confined compression of the sample. However, stress fluctuations are observed during sample unloading for strain rates above 0.5 s^{-1}. For unconfined compression, the sample unconfined strength is not significantly affected for strain rate below 1 s^{-1}. But for strain rate of 0.59 s^{-1}, the sample unconfined stress strain response starts showing some deviations from the results of lower strain rates.
- Cylinder wall friction coefficient has a small influence on fill porosity. However, an increase in cylinder wall friction coefficient causes significant reduction in sample compression and unconfined strength. This is due to reduction in the stress experienced by the solid leading to reduction in unconfined strength.
- End platen friction coefficient does not have a significant effect on the compression of sample with and without frictionless walls.

Chapter 7

Example application to detergent powders[5]

7.1 *Introduction*

The major objective of this chapter is to study packing, compression, and caking behaviour of spray dried detergent powders using the EPT, and to model the full spectrum of the loading regimes from compression to shear failure using DEM. The EPT is used to measure the mechanical properties including the stress-strain response and the corresponding porosity change as a function of consolidation stress in a confined cylinder. In addition, the stress strain response during unconfined shearing and the cake strength as a function of consolidation stress is evaluated. The physical properties of the powders, which may affect the mechanical properties, are also measured. These include moisture content, particle size, size distribution, shape, inter- (between particles) and intra (inside particles)-porosity. DEM modelling is then used to simulate the packing, compression and shear behaviour, which is compared with the experiments for one example detergent powder. The simulations utilised a recently developed contact model that uses hysteretic non-linear loading and unloading paths to model the elasto-plastic permanent contact deformation and an adhesion parameter which is a function of the maximum contact overlap.

[5] Based on Thakur, S.C., Ahmadian, H., Sun, J., Ooi, J.Y. (2013). An experimental and numerical study on packing, compression, and shear behaviour of detergent powders. *Accepted in Particuology*

7.2 *Materials*

In this study, spray dried detergent (SDD) powders were investigated, which constitute 60%–70% of the commercially available detergent washing powders and are the most common detergent powders sold worldwide with billions of dollars sales. Two SDD powders produced with low moisture content (Sample A) and high moisture content (Sample B) were selected, covering a range of unconfined yield (cake) strength. The chemical composition and moisture content of spray dried powders vary across different size fractions. Therefore, the spray dried powders were separated into three different size fractions, <250 µm (small size), 250–500 µm (medium size), and >500 µm (large size). Tests were conducted on bulk samples covering all particle size range as well as different size fractions.

7.3 *Measurement of powder physical properties*

Before any measurement on the specimen is made, it is vital that a representative sample is obtained. In this study the samples obtained from a spray dried tower was first mixed in a rotary mixer to get a homogenous sample and also to reduce the bulk powder down to a 5 kg batch. The powder is then further sampled down to the 1 kg size using a split sampler. Finally, the powder is sampled down to required sizes using a Pascal turntable sample divider, a spinning sample divider. The rotation speed and vibration levels in a Pascal turntable sample divider were chosen to provide a uniform flow of powder. Since spray dried powders are sensitive to moisture and humidity, the powders were packed and sealed in air tight containers for further testing.

The powder moisture content, particle size and size distribution, inter- plus intra-particle pore, and shape were characterised, using moisture balance, mechanical sieve analysis, gas pycnometry, mercury porosimetry, and scanning electron microscope (SEM). Moisture content by weight was measured using an oven-drying method. A temperature of 105 °C and heating time of 24 h was used. The moisture content and its distribution across different size fractions are shown in Table 7.1

Distribution of moisture content (%) across different size fractions (n=3). The moisture contents of Sample B were higher than those of Sample A for all size fractions. Additionally for both samples, the larger size fractions had higher moisture contents than the smaller size fractions. This could be due to the agglomeration of primary particles into larger sizes with higher internal moisture. It should be noted that the moisture content is not free and mobile surface moisture; but rather moisture after the powders have gone through drying process in a spray drying tower.

Table 7.1 Distribution of moisture content (%) across different size fractions (n=3)

Size fractions	Sample A		Sample B	
	M	RSD (%)	M	RSD (%)
Bulk	2.29	2.39	4.74	2.70
>500μm	2.55	4.99	4.96	4.24
500-250μm	2.30	3.30	4.43	2.50
<250μm	2.12	4.30	4.17	4.80

Notes: n=number of samples, M=Mean, RSD=Relative Standard Deviation=standard deviation/mean

The size distributions of the SDD powders were measured using vibrating mechanical sieves following the ASTM D6913 procedure. The amplitude and frequency of vibration were set to minimise breakage of agglomerates and to ensure thorough sieving of the sample. The full size distributions of particle size on weight basis are shown in Figure 7.1. The median particle sizes D_{50} of Sample A and Sample B were approximately 480 and 390 µm respectively. Both powders have a similar coefficient of uniformity, C_u, (D_{60}/D_{10}) of 3.6.

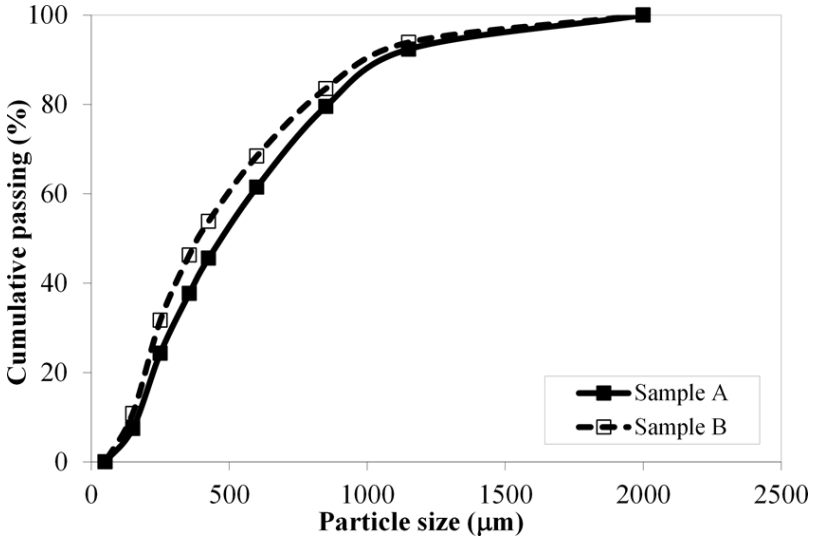

Figure 7.1 Particle size distribution of the spray dried detergent powders

Inter- and intra-particle porosity was characterised using measurements from gas pycnometry and mercury porosimetry. A gas pycnometer, Accupyc II 1340 (Micromeritics, USA), was used to measure skeletal density (solid density), based on a gas displacement method to measure volume accurately. Helium gas is used as it obeys the ideal gas law and is able to penetrate small pores (ASTM D5550, 2006) due to its small atomic number. However Helium does not permeate any closed pores. The average values of skeletal density from five runs are 1919 and 1910 kg/m^3 for Sample A and Sample B respectively. There was no significant difference between skeletal density measurements across different size fractions.

Pore size charactersation of the spray dried samples was conducted using mercury porosimetry (AutoPore IV, Micromeritics, USA). The instrument provides a wide range of information, e.g. the pore size distribution, the total pore volume (inter- and intra-particle pores) or porosity, the skeletal and envelope density. The instrument characterises a material's porosity by applying various levels of pressure to a sample immersed in mercury. The pressure required to intrude mercury into the sample's pores is inversely proportional to the size of pores and given by the Washburn's equation (Washburn, 1921).

A Hitachi TM 1000 SEM was used in this study for visual inspection of particles. The SEM photographs of three different size fractions of Sample A and Sample B are shown in Fig. 2 and Fig. 3 respectively. A significant amount of pore openings can be seen on the surface of the particles. No discernible difference in shape and texture of respective size fractions of Sample A and Sample B was found. It can be seen from Figure 7.2 and Figure 7.3 that the larger particles are not individual but agglomerates of primary particles.

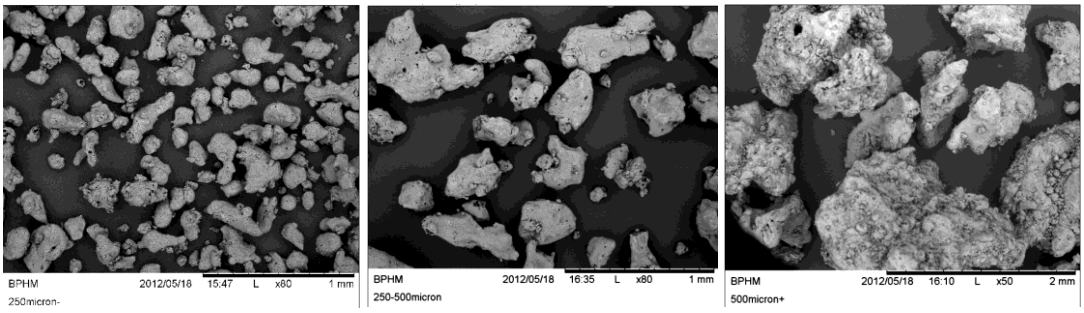

Figure 7.2 SEM photographs of different size Sample A: (a) passing through 250 µm, (b) between 250–500 µm, and (c) retained on 500 µm

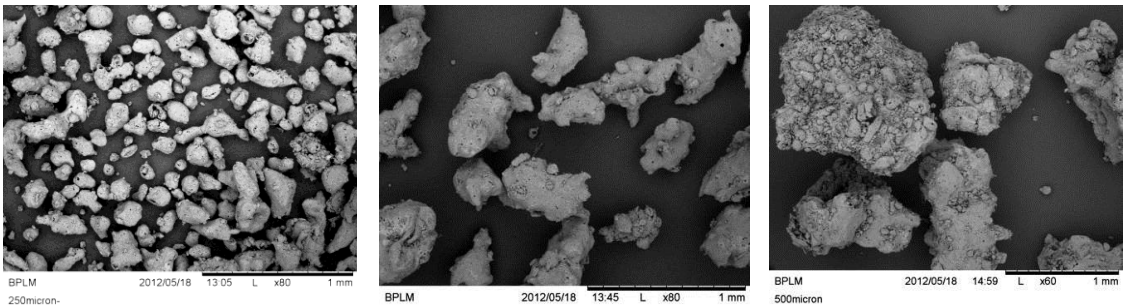

Figure 7.3 SEM photographs of different size Sample B: (a) passing through 250 µm, (b) between 250–500 µm, and (c) retained on 500 µm

7.4 *Measurement of powder mechanical properties*

The EPT was employed to measure the packing, compression, and shear behaviour of the SDD powders. The main differences between EPT and some previous uniaxial tester lies in the attention to mechanical details, the level of care directed to the consolidation as well as failure load application, and the strategic

intent (Bell et al., 2007). The height of the specimen is measured continually with a built-in linear variable voltage transformer (LVDT) displacement transducer of an accuracy of 0.1 mm attached to the loading piston. The powder compressibility can then be evaluated from the measurement.

The photographic illustration of the EPT test procedure is shown in Figure 7.4. In the EPT, the powder sample is poured into the consolidation cylinder. The sample is loaded by applying a constant weight to the consolidation cell and the force is recorded by the load cell attached to the consolidation plunger. After the sample is loaded for 1 min, the consolidation plunger is automatically lifted off leaving the consolidated sample. The mould is then manually slid down the pedestal, exposing a free standing column of consolidated powder sample. The sample is then failed by a motor driven test piston and the stress-strain response during the unconfined axial loading to failure can be recorded. The loading piston travels with a speed of 0.4 mm/s. The speed of the piston is so chosen that the test can be conducted rapidly, and at the same time unconfined yield strength is not compromised. Watanabe and Groves (1964), who used another uniaxial tester found that unconfined strength of detergent samples was unaffected if the piston speed was varied in a range of 0.084 to 0.43 mm/s.

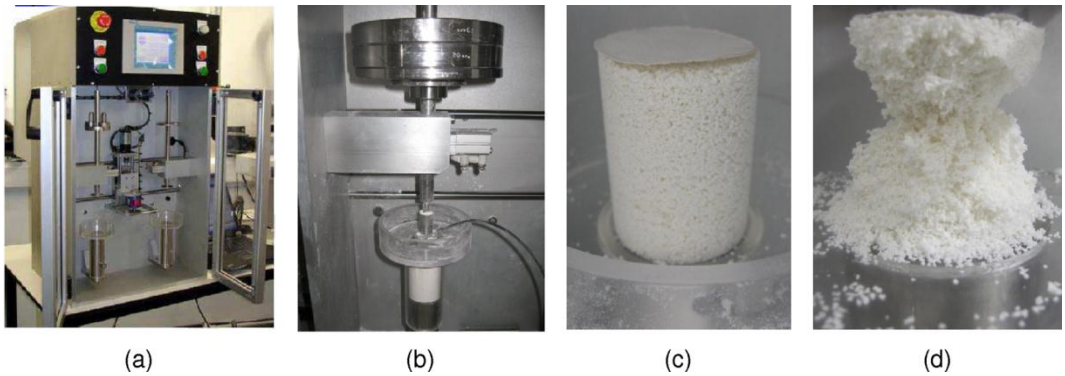

Figure 7.4 (a) Edinburgh Powder Tester, (b) compression, (c) unconfined sample, and (d) crushed sample.

The friction between the particles and boundary may affect the compressibility of the powders in uniaxial tests (Enstad and Ose, 2003). In the EPT, boundary effect is reduced by allowing the powder sample to compress from both the top and bottom. Further to minimize any effect of boundary friction, the sample aspect ratio (sample height at 1 kPa stress to diameter ratio) during confined compression is kept in a narrow range of 1.3–1.4. During unconfined compression, the sample aspect ratio is kept between 1.2–1.4 which was found to give very good test reproducibility in unconfined strength measurement. Previous studies have proposed an aspect ratio of tan (45°+Φ/2) or larger, where Φ = angle of shearing resistance of the powder, to minimise the effect of end plate friction (Bishop & Green, 1965; Rock & Schwedes, 2005; Williams et al., 1971). Williams et al. (1971) argued that for lower values of aspect ratio, the failure of the sample can take place only when part of the specimen slips along one of the end platens, which would require extra work to be done causing an increase in unconfined yield strength. However, the present study found that even with aspect ratio between 1.2–1.4 which is much smaller than tan (45°+Φ/2), the failed sample did not intersect the end platen (see Figure 7.4(d) for a typical failure). A higher aspect ratio would also increase the effect of wall friction and cause a greater density variation across the height of the specimen which can compromise measurement reproducibility.

It is further proposed that these highly repeatable bulk measurements can be used for DEM model calibration. These are the (vertical) stress-strain and the stress-porosity response during confined compression as well as the (vertical) stress-strain response during unconfined compression including the peak unconfined strength.

7.5 *Results and discussion*

7.5.1 Experimental results

7.5.1.1 Packing

The EPT was used to measure the bulk porosity of the powder under compression. The initial bulk porosity was measured corresponding to a small applied initial stress

of 1 kPa (approx). This helps to reduce the variability of the fill porosity measurement and give a stable measurement of the initial height of the specimen with a level surface. The height and weight of the specimen were used to calculate the average value of the bulk density (ρ_b). The sample bulk porosity (η) can then be calculated using ρ_b, moisture content (w), and the particle density (ρ_s) as follows:

$$\eta = 1 - \frac{\rho_b}{\rho_s (1+w)}. \tag{7.1}$$

However, in this study the particle density was measured for the powder with moisture, therefore the moisture was not considered in porosity calculation, and porosity was simply calculated as:

$$\eta = 1 - \frac{\rho_b}{\rho_s}. \tag{7.2}$$

The porosity comprises of the inter-particle pores as well as the open and closed intra-particle pores. However, the skeletal density measurement of the SDD samples before and after milling was found to be similar, indicating insignificant closed pores in the samples. The average bulk porosity of Sample A and Sample B for full size fraction and different sieve cut fractions are shown in Table 7.2. The bulk porosities of the larger sieve cut fractions for both samples were higher compared to those of the smaller sieve cut fractions. It can be seen from the SEM images that the larger fractions are agglomerates of the primary particles. In addition to the intra and inter-particle porosity, the inter-agglomerate porosity also contributes to the total porosity leading to a higher porosity for the larger fractions.

Table 7.2 Initial sample porosity (%) measurements for Sample A and Sample B powders

Size fractions	Sample A		Sample B	
	M	RSD (%)	M	RSD (%)
All fractions (*n*=3)	72.5	0.36	69.6	0.35
>500 µm (*n*=1)	77.7	–	75.2	–
500–250 µm (*n*=1)	75.4	–	72.8	–
<250 µm (*n*=1)	72.2	–	69.8	–

NB: *n* = number of measurements; initial porosity taken at a consolidation stress of 1 kPa.

The bulk porosity of the full size fraction of Sample A was found to be higher than that of Sample B (see Table 7.2). Indeed the bulk porosities of different size fractions of Sample A were consistently higher than the corresponding fractions of Sample B. This was deemed counterintuitive considering that both samples have similar shape, morphology and gradation, except higher moisture content for Sample B. One might speculate that a higher moisture content (Sample B) could lead to a more-open structure and a higher porosity resulting from higher adhesive forces at the particle contacts (assuming that moisture is at the contacts). It should be noted that the microstructure of spray dried powder comprises porous primary particles and agglomerates of these primary particles. Such a microstructure cannot be easily defined by a single value of bulk porosity. Therefore, a combination of measurements using mercury porosimetry and gas pycnometry was used to estimate porosity between the particles (inter-porosity) and porosity inside the particles (intra-particle porosity). Inter-particle porosity was calculated as:

$$\eta_{\text{inter}} = 1 - \frac{\rho_{\text{b}}}{\rho_{\text{s}}(1-\eta_{\text{p}})}, \qquad \textbf{(7.3)}$$

where η_{inter} is the inter-particle porosity, and η_{p} is the particle porosity which was calculated as:

$$\eta_{\mathrm{p}} = \frac{v_{\mathrm{pores}}}{(v_{\mathrm{pores}} + \frac{1}{\rho_{\mathrm{s}}})}, \tag{7.4}$$

where, v_{pores} = specific volume (mL/g) of mercury penetrating the particle pores.

The fraction of total void space in a sample contributed by particle porosity is termed as intra-particle porosity and expressed as:

$$\eta_{\mathrm{intra}} = \eta_{\mathrm{p}}(1-\eta). \tag{7.5}$$

Because of difficulty in separating inter- and intra-particles for full size fraction samples, inter- and intra-porosity was estimated for the 250–500 µm narrow size fractions assuming that the intra-porosity measurement will be valid for other size fractions and full size fraction. The assumption is reasonable since intra-particle porosity relates to primary particles and should be independent of size of agglomerates (i.e. different size fractions). Table 7.3 shows the breakdown of the total porosity for 250–500 µm for the SDD powders in terms of inter- and intra-particle porosity. The inter-particle porosity of Sample B was 2.6% higher than that of Sample A which is indeed consistent with the proposition of increasing inter-particle porosity with increasing moisture content. However, the intra-particle porosity for Sample A was 5.2% higher than that of Sample B which masked the higher inter-particle porosity in Sample B and led to a higher overall porosity for the Sample A. The higher amount of intra-particle porosity for Sample A can be attributed to the way the samples were processed in the spray drying tower. Sample A was exposed to slightly higher temperature in the spray drying tower causing puffing or shrinking and leading to more porous primary particles.

Table 7.3 Breakdown of bulk porosity (%) for the SDD powder sample (250–500 µm)

Types of porosity	Sample A		Sample B	
	M	RSD (%)	M	RSD (%)
Bulk porosity	75.4	–	72.8	–
Intra particle porosity	21.38	0.85	16.19	3.45
Inter particle porosity	54.02	–	56.61	–

7.5.2 Confined compression and decompression

The compression process was studied by plotting the axial stress-strain measurements and the porosity-stress measurements. Figure 7.5 shows the axial strain for three specimens of Sample A and Sample B as a function of the consolidation stress and Figure 7.6 shows the corresponding porosity variation as a function of consolidation stress. Sample B exhibited a higher overall compressibility than Sample A despite the fact that the initial (bulk) porosity of Sample B was lower. In Figure 7.6, the powder compression process can be divided into two stages; stage I relating to particle rearrangement (mostly compression of inter-porosity), and stage II when the elasto-plastic deformation causing squashing of both inter- and intra-particle porosity began to dominate. It can be seen that at the onset of consolidation the porosity decreased sharply (stage I). During stage II as the consolidation progressed, the porosity varied linearly with a flatter slope compared to stage I. The steeper slope of the porosity stress curve for Sample B indicates larger particle rearrangement during stage I, and larger elasto-plastic deformation for stage II. The larger particle rearrangement of Sample B can be resulting from higher (2.6% for 250–500 µm size) inter-particle porosity compared to Sample A (Table 7.3). The larger elasto-plastic deformation in stage II for sample B may be arising from higher moisture increasing the plasticity at contacts (Okasanen, & Zografi, 1990) and agglomerate breakage due to weakening of the solid bridges (Yan & Barbosa-Canovas, 1997; Yan & Barbosa-Canovas, 2001).

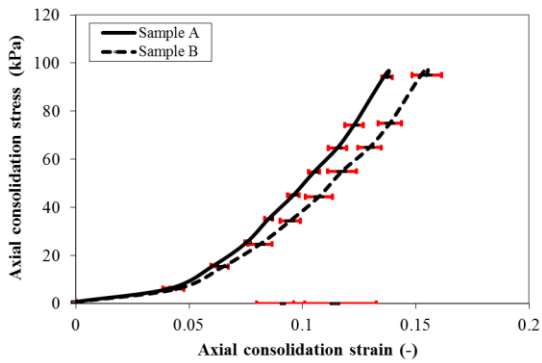

Figure 7.5 Confined stress strain behaviour for full size range Sample A and Sample B

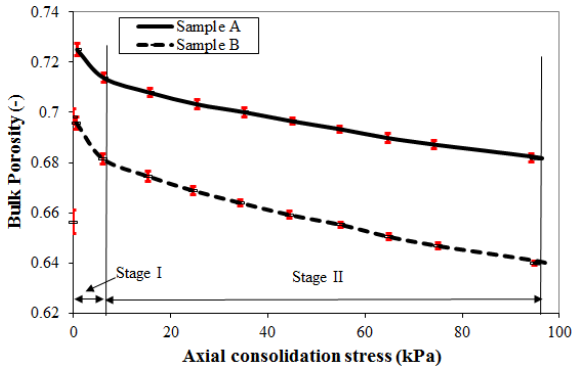

Figure 7.6 Confined porosity-stress behaviour of full size range Sample A and Sample B

Once the desired consolidation stress was reached, the sample was unloaded and the sample height was recorded to calculate the consolidated porosity (denoted by points on X-axis, see Figure 7.6. None of the powders returned to the initial porosity upon unloading indicating substantial plastic deformation arising from the particle rearrangement, breakage, and plastic deformation at the contacts. As can be seen from Figure 7.6 the maximum difference in porosity measurements for each of the powders at any specific applied stress was less than 0.5% (see error bars) indicating a high level of reproducibility.

Figure 7.7 shows axial stress-strain behaviour and Figure 7.8 shows corresponding porosity change as a function of consolidation stress for different sieve-cut fractions of Samples A and B. While comparing different size fractions of the sample, the larger sieve-cut fraction compresses more, which could be related with compression of larger inter-agglomerate pore, breakage of the large size agglomerates, and larger plastic deformation. It has been found in literature that as the size of the agglomerate (food powder) increased a higher volume reduction for large size agglomerates during compression in a cylindrical mould was found (Yan and Barbosa-Canovas, 1997). The particle size effect on breakage was explained by the larger particles having more edges or corners on their surface than the smaller ones, resulting in more abrasion and chipping. While comparing compression behaviour of

corresponding sieve-cut samples of two SDD powders, sample A compresses less showing a similar trend to the full size fraction.

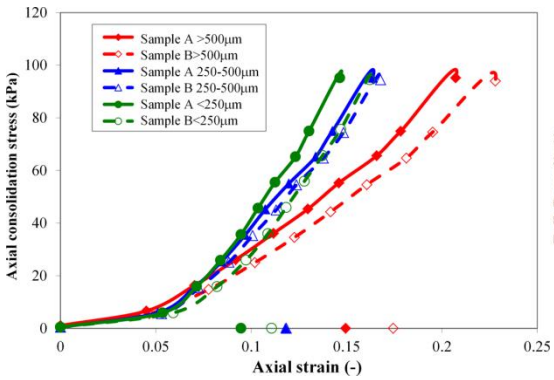

Figure 7.7 Confined stress-strain behaviour of different sieve cut fractions of Sample A and Sample B.

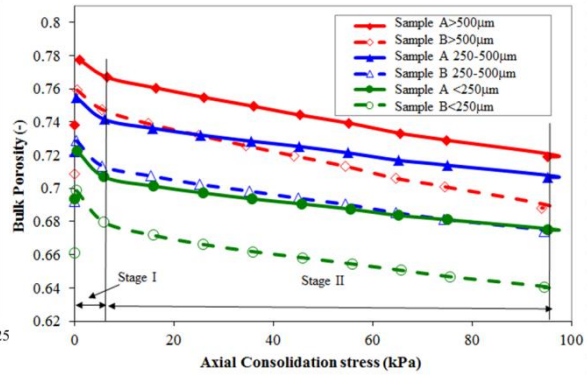

Figure 7.8 Confined porosity-stress behaviour of different sieve cut fractions of Sample A and Sample B.

In addition, a larger gradient in porosity-stress curve (for both stage I and stage II) is found for Sample B. For example, the decrease in bulk porosity for 250–500 µm sample B was 0.2% and 0.5% higher than the same size fraction sample A for stage I and stage II, respectively. This again indicates larger particle rearrangement in stage I and larger elasto-plastic deformation in stage II for sample B.

7.5.3 Unconfined compression and flow function

The unconfined stress-strain behaviour for all samples was obtained but the results are presented only for full size range SDD powders. Figure 7.9 and Figure 7.10 show typical stress-strain behaviour during unconfined compression for four different (20–80 kPa) consolidation stresses, for sample A and sample B respectively. The peak stress at which the sample fails (denoted by drop down in stress) is known as the unconfined yield strength. Very often in literature only the unconfined yield strength as a function of consolidation stress is reported. However, the area under the unconfined stress-strain curve is related to the energy required to fail the sample and needs to be captured in the DEM simulations. It can be seen that both the unconfined

strength and the area under the curve increase with increasing consolidation stress for both samples.

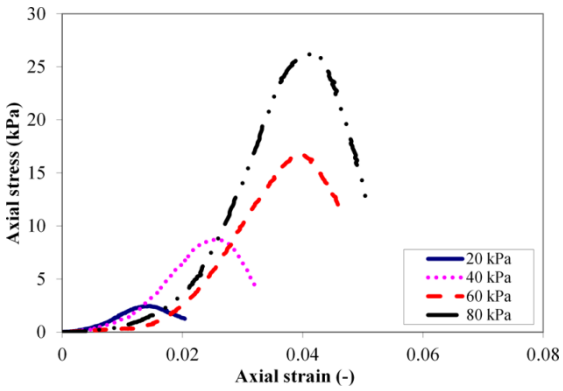

Figure 7.9 Unconfined stress strain of Sample A

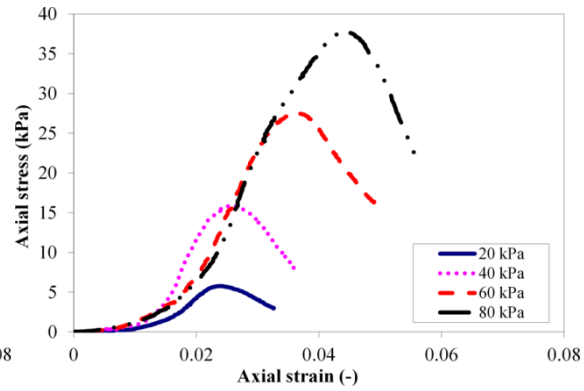

Figure 7.10 Unconfined stress-strain of Sample B

Figure 7.11 and Figure 7.12 show the relationship between unconfined strength and consolidation stress, otherwise known as flow function. The reproducibility of EPT was tested for full size range SDD bulk samples. The relative standard deviation (RSD) at 37 kPa of consolidation stress for Sample A and Sample B (3 tests each on fresh samples) were found to be 4.8% and 2.8%, respectively. Whilst three data points would not usually be considered sufficient for rigorous statistical analysis, the low RSD indicates that the reproducibility of EPT is very high.

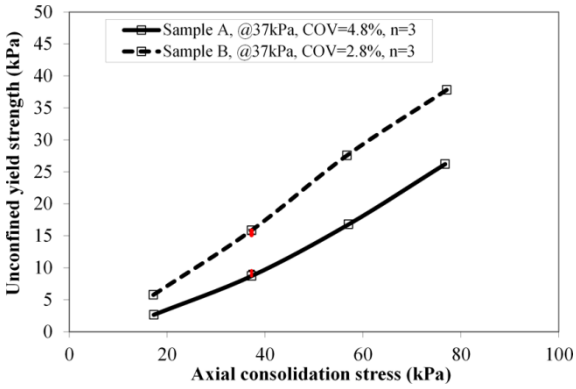

Figure 7.11 . Flow functions for uncut Sample B and Sample A

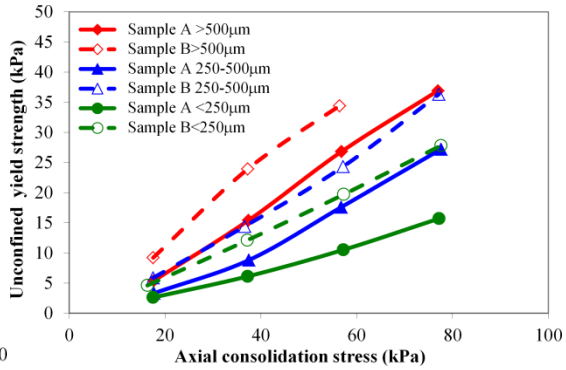

Figure 7.12 Flow functions for different size fractions of Sample B and Sample A.

The Sample B displayed higher unconfined strength at the same consolidation stress. The most plausible explanation is that moisture increases stickiness and plasticity of the contact leading to higher unconfined strength. Higher plastic deformation has been observed for Sample B during confined compression (see Figure 7.5Figure 7.6). For the different sieve-cut fractions of Sample B (Figure 7.12), larger sieve-cut fractions showed higher unconfined strength compared to small sieve cut fractions (for the larger than 500 µm fraction consolidated at 77 kPa, the unconfined strength exceeded the 45 kPa limit of the load cell). The plausible explanation for lower strength associated with finer particles is that the fine fractions contain a disproportionate amount of anticaking agents which reduces the adhesion between particles and that fine fractions have a slightly lower moisture content compared to the coarser fractions. In contrast, the coarser particles have higher moisture content and have shown previously to deform more plastically (see Figure 7.7) compared to small size particles, which may probably give rise to higher contact area and therefore higher adhesion. This is consistent with previous findings that small increase in moisture content (0.6%) produced significant increase in cake strength (64%) of SDD powders (Watanabe and Groves, 1964).

7.6 *DEM simulation*

7.6.1 Model implementation

There are several challenges in modelling cohesive powder at individual particle level. First, it is computationally prohibitive to model each and every individual particle and the cohesion arising from several different phenomena including van der Waals, capillary bridge, and electrostatic forces separately. Second, real particles are not spherical and can have surface asperities and contact occurs not at a single point but through multiple asperities. Finally, it is very difficult to measure input parameters including adhesive force, contact stiffness, coefficient of restitution etc. for cohesive powders. For example, enormous scatter in data has been reported in measurement of adhesive pull-off force using AFM measurement (Heim et al., 2005; Tykhoniuk et al., 2007). In our approach, the focus is on an intermediate scale between the micro- and macro-scales, aiming at a phenomenological contact model that can reproduce the bulk cohesive strength, stress history dependency, and other behaviour evidenced in bulk experiments.

As a first step towards calibration of DEM model parameters, a simplified linear version of the contact model, i.e., parameter n=1 (Luding, 2008a; Walton and Braun, 1986) is used. The cohesive contact model was only applied to particle-particle interactions. The particle-geometry interactions were modelled using the Hertz-Mindlin contact model and hence no particle-geometry adhesion was permitted. For this investigation, the DEM parameters were estimated to match primarily the compression and the unconfined strength of Sample B retained on 500 µm sieve. The DEM input parameters used are presented in Table 7.4.

Table 7.4 Simulation parameters

Size of overlapping spheres of aspect ratio of 1.5, (mm)	2
Number of particles (–)	3500
Loading spring stiffness, k_1 (N/m)	1×10^{6}
Unloading spring stiffness, k_2 (N/m)	4×10^{6}
Adhesive force, f_0 (N)	–0.004
Adhesive parameter stiffness, k_{adh} (N/m)	2×10^{6}
Particle static friction, μ_{sf} (–)	0.6
Particle rolling friction, μ_{rf} (–)	0.001
Wall friction, μ_{wf} (–)	0.4
Top and bottom platen Friction, μ_{Pf} (–)	0.4
Coefficient of restitution, e (–)	0.4
DEM time step, t_s (s)	4.6×10^{-6}

The geometric similarity between the experiments and simulations was maintained by using the same diameter mould. In order to predict the mechanical behaviour of real adhesive frictional material which is neither spherical nor smooth, it is important that non-spherical shape is considered to mimic the geometric interlocking that exists. In this simulation, the cylinder was filled with 3500 non-spherical particles, each consisting of two overlapping spheres of 2 mm diameter giving a particle aspect ratio of 1.5. It should be noted that the DEM particles in this study are mesoscopic representation of the detergent powders. A study on numerical scaling of DEM parameters in uniaxial test has shown that if the DEM input parameters are scaled properly, size independent bulk stress-strain results can be obtained (Thakur et al., 2013). Therefore, particle size larger than realistic size particles is used. The particle size distribution can have an effect on the bulk behaviour but is not considered in this simulation where a detergent powder with a narrow size range has been chosen for comparison.

Each simulation consists of three stages: (1) filling the cylindrical mould to form the initial packing used for all stress levels; (2) confined consolidation to the required stress level and subsequent unloading; and (3) unconfined compression of the sample to failure after the removal of the mould. The process is visualised in Figure 7.13. The random rainfall method was adopted to provide a random packing of particles. To ensure that the system reached a quasi-static state, loading only commenced when the kinetic to potential energy ratio was less than 10^{-5} with a constant coordination number. The confined consolidation process was conducted by moving the top platen downward at a constant speed of 10 mm/s (strain rate ≈ 0.14 s^{-1}) to apply a vertical compression. After consolidating the sample to the desired stress, the load on the assembly was released by moving the top platen upward at the same constant speed. The lateral confining walls were then removed and the unconfined sample was allowed to relax for a short period of time (0.1 s). This allowed the kinetic energy generated from the removal of the confining wall and upward retreat of the top platen to dissipate. The sample was then crushed to failure by moving the top platen downward again at a constant rate of 5 mm/s (strain rate ≈ 0.1 s^{-1}).

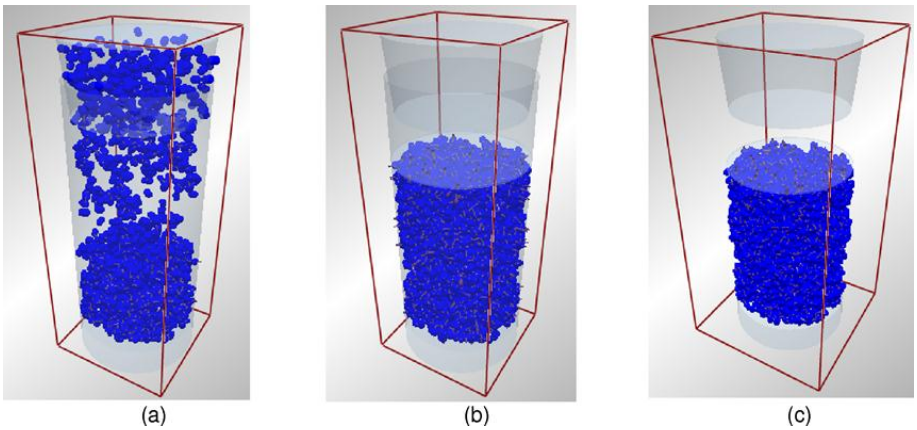

Figure 7.13 Snapshots of uniaxial test simulations: (1) filling, (2) confined consolidation, and (3) unconfined compression

7.6.2 Simulation results

Sample B with particle size range 500–2000 µm is chosen for DEM model calibration. The compression and decompression behaviour (stress-strain and change in porosity-stress) is shown in Figure 7.14and Figure 7.15. The predicted stress-strain response matches very well with the experimental stress-strain behaviour of Sample B with particle size range 500–2000 µm. However, there is a discrepancy in porosity-stress behaviour with the DEM predicting a lower initial porosity. This can be attributed to the highly irregular shape, intra-particle porosity, and surface asperities of Sample B as shown by the SEM photographs (Figure 7.3c), which have not been properly accounted for in the DEM model. This warrants further investigation into the interaction between inter- and intra-particle porosity on packing and compressibility behaviour of cohesive powder. However, when change in porosity is plotted against applied consolidation stress, the results show reasonable agreement between the simulation and the experiments (see Figure 7.15).

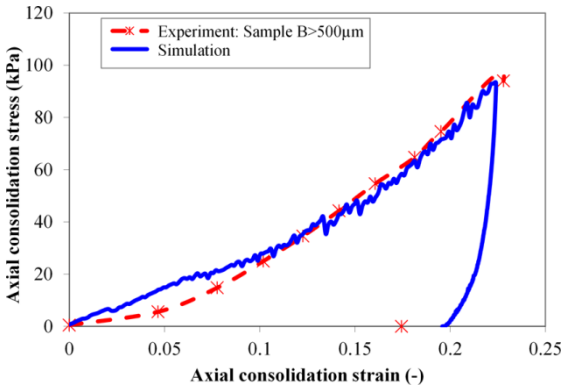

Figure 7.14 Confined stress-strain behaviour (simulation vs experiments)

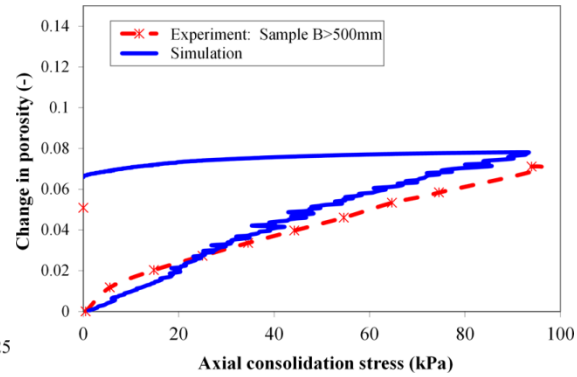

Figure 7.15 Change in porosity vs stress behaviour (simulation vs experiments)

Figure 7.16 and Figure 7.17 compare simulation and experimental results for the unconfined loading response (to failure) and the flow function, respectively. The computed peak unconfined strength compares reasonably well at 37 kPa consolidation stress. However, the initial stiffness in DEM simulation was steeper than the experiments. Furthermore, overconsolidation behaviour was not observed in the simulations. This could be due to the fragile nature of the SDD powders

undergoing breakage during shearing. From Figure 7.17, the flow function result from DEM simulations compares reasonably well to experimental results, especially at higher consolidation stresses (40–60 kPa).

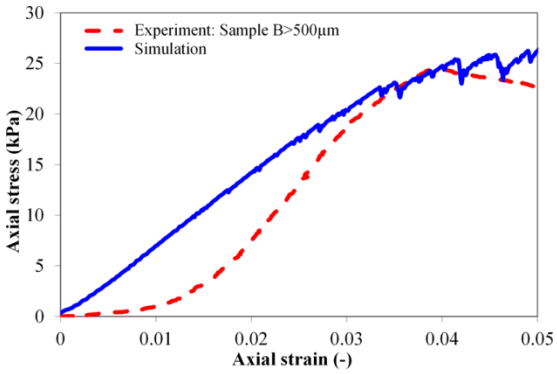

Figure 7.16 Unconfined stress-strain behaviour (simulation vs experiments)

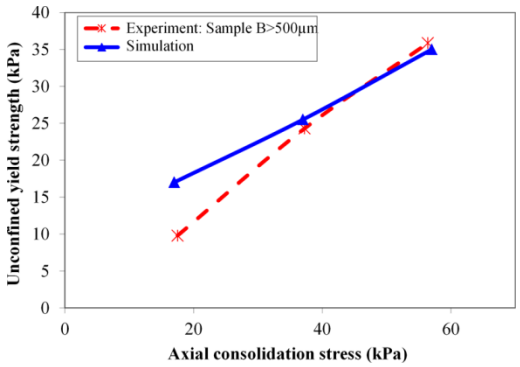

Figure 7.17 Flow function behaviour (simulation vs experiments)

7.7 *Summary*

The packing, compression and flowability behaviour of two spray-dried powders manufactured at two different moisture contents have been studied using the EPT uniaxial tester. The EPT provided highly reproducible measurements of the confined compression (giving the porosity-stress function) and the unconfined compression to failure (giving the flow function) of the powders: these can be very useful in describing the handling characteristics of these powdered products including screening new products, studying formulation changes and the effect of anticaking agent etc.

Comparing the two manufactured powders, the low moisture sample had higher intra-particle porosity and lower inter-particle porosity, resulting in a higher overall porosity. However the higher intra-particle porosity did not lead to a higher compressibility under load. For the high moisture sample, the higher moisture gave rise to higher inter-particle porosity and a higher plasticity at the contacts under load,

resulting in a higher overall compressibility. The higher plasticity at the contacts eventually led to a higher cake strength for the high moisture sample.

For different sieve-cut samples, it was found that moisture content was not uniformly distributed, with the larger size fractions having higher moisture contents, most probably due to the agglomeration of primary particles into larger sizes enclosing higher internal moisture. The larger size fractions showed higher total porosity compared to the smaller size fractions. It is noted that the larger fractions are agglomerates of the primary particles. Thus the inter-agglomerate porosity also contributed to the total porosity leading to a higher porosity for the larger fractions. Higher initial porosity, and high moisture associated with large size fractions explains why large size fractions always showed a higher compressibility than the smaller size fractions.

Additionally, the larger size fractions also showed higher cake strength than the full size range in each of the two powders. This has the practical implication that if the detergent powder segregates during the handling and transport operation, the coarser fraction may dominate the overall caking behaviour of the detergent powders. In addition, the powders with higher inherent moisture content can have a higher cohesivity and may therefore cause more flowability problems especially when subjected to significant consolidation stresses.

The filling and, confined compression/decompression, followed by the unconfined loading to failure, in an EPT test have been simulated with DEM using a recently developed elasto-plastic adhesive contact model. The simulation results are in reasonably good agreement with the experimental results for the flow function and compression behaviour but less so for other observed features. Further development of contact model is underway to improve the predictive capabilities.

This study is the first step towards using DEM to model cohesive powders for industrial scale applications. However, this first step demonstrated the model's capability to predict the pertinent macroscopic behaviour of a cohesive powder under

compression and shear and its potential for modelling complex industrial processes involving these loading regimes.

Chapter 8

Conclusions and recommendations for future research

The research in this thesis has been carried out to develop a mesoscopic phenomenological based DEM contact model for cohesive solids that can reproduce the bulk cohesive strength, stress history dependency, and other behaviour evidenced in experiments. The predictive capability of the proposed DEM contact model was evaluated by attempting to simulate the behaviour of a limestone and a spray dried detergent powder under quasi-static and slow shearing regimes. The effect of the key DEM model parameters on the full spectrum of cohesive behaviour from filling of a space (fill porosity) to loading under confined compression, and finally unconfined loading to failure was studied. The scaling of DEM model parameters for mesoscopic representation of cohesive powder to produce scale independent predictions under quasi-static and slow shearing regime was also investigated. This chapter summarizes the key conclusions in the thesis and make some recommendations for future research.

8.1 *Characterization of test solids*

Edinburgh Powder Tester (EPT) has been evaluated for the characterisation of the flow properties of 6 industrial cohesive powders and the results were compared with two commercial test methods including the FT4 rheometer and the rotating drum device. The bulk compressibility of PARDEM reference solid in EPT was found to be insensitive to the fill methods used. While comparing the results from EPT to the results from FT4, both EPT and FT4 produced highly repeatable measurements on the PARDEM reference solid and can adequately discriminate between flowability of different industrial solids. The maximum coefficient of variation (COV) for

unconfined yield strength measurement on EPT and FT4 was found to be 7.4% and 8.4% respectively. However, the rotating drum device exhibited a bigger scatter; time between events and angle of stability measurements on the rotating drum had a COV of 50.2% and 9.6% respectively. The results indicated that EPT can be an excellent candidate for DEM model calibration.

8.2 *Micromechanical study of cohesive powder*

The DEM simulations and micromechanical analysis of cohesive powders using an adhesive elasto-plastic contact model have been presented. The implemented contact model has been shown to be capable of predicting the experimental flow function (unconfined compressive strength versus the prior consolidation stress) for a limestone powder which has been selected as a reference solid in the Europe wide PARDEM research network. This suggests that the elasto-plastic adhesive model may be used to simulate cohesive solids subjected to different flow and stress regimes. Contact plasticity in the model is shown to affect the flowability significantly and is thus essential for producing satisfactory computations of the behaviour of a cohesive granular material. The model predicted a linear relationship between a normalized unconfined compressive strength and the product of coordination number and solid fraction. Importantly, it has been found that contribution of adhesive force to the limiting friction has a significant effect on bulk unconfined strength. Failure to include the adhesive contribution in the calculation of the frictional resistance may lead to under-prediction of unconfined strength and incorrect failure mode. The results provide new insights and propose a micromechanical based measure for characterising the strength and flowability of cohesive granular materials.

8.3 *Scaling of DEM model parameter*

Scaling of DEM input parameters in a 3D simulation of the loading regimes in a uniaxial test indicated that whilst both normal and tangential contact stiffness (loading, unloading, and load dependent) scales linearly with radius of the particle, the adhesive forces scales with the square of the radius of the particles. This is a first

step towards a mesoscopic representation of a cohesive powder that is phenomenological based to produce the key bulk characteristics of a granular solid and the results indicate that it has potential to gain considerable computational advantage for large scale DEM simulations.

8.4 *Parametric study*

The influence of DEM input parameters and the model implementation on the bulk response in uniaxial test simulation have resulted into many useful observations. Particle contact normal stiffness has significant effect on the confined compression of a bulk sample, and therefore, should not be reduced to gain computational speed-up. Whilst particle contact loading stiffness does not affect particle rearrangement during the initial application of stress in confined compression simulation, the particle stiffness directly influences the bulk stiffness. The sample with lower stiffness compresses more and provides a higher unconfined strength compared to the sample with higher stiffness. Whilst the tangential stiffness does not affect fill porosity and initial rearrangement significantly, it is shown to influence the overall confined and unconfined compression response of a particle assembly. Reducing the tangential stiffness increases the overall compressibility and reduces the initial stiffness during unconfined compression, but does not affect the unconfined strength. However, for a sample with the same consolidated porosity, increasing the tangential stiffness increases both the initial loading stiffness and unconfined strength.

Inter-particle friction coefficients affect the packing, compression, and unconfined strength of the sample assembly. Increasing the inter-particle friction coefficient increases fill porosity, and reduces the sample compression. The effect of friction on unconfined strength is governed by the interplay of consolidated porosity (related to the coordination number) and shearing resistance due to increase friction coefficient. The sample unconfined strength first increases and then decreases with increasing inter-particle friction. Cylinder wall friction coefficient has a small influence on fill porosity. However, an increase in cylinder wall friction coefficient causes significant

reduction in sample compression and unconfined strength. This is due to reduction in the stress experienced by the solid leading to reduction in unconfined strength. End platen friction coefficient does not have a significant effect on the compression of sample with and without frictionless walls.

For the range of strain rates (0.02 s^{-1} to 5 s^{-1}) investigated, the strain rate does not affect loading response during confined compression of the sample. However, stress fluctuations are observed during sample unloading for strain rates above 0.5 s^{-1}. For unconfined compression, the sample unconfined strength is not significantly affected for strain rate below 1 s^{-1}.

8.5 *Comparison of experiments and DEM simulation for detergent powder*

Finally the calibration procedure was applied to a spray dried detergent powder and the simulation results are compared to whole spectrum of loading regime in a uniaxial (EPT) experiment. The filling and, confined compression/decompression, followed by the unconfined loading to failure of a sample spray dried detergent powder in an EPT test was simulated with the elasto-plastic adhesive contact model. The simulation results are in reasonably good agreement with the experimental results for the flow function and compression behaviour but less so for other observed features. This represents a first step towards using DEM to model cohesive powders for industrial scale applications. It demonstrated the model's capability to predict the pertinent macroscopic behaviour of a cohesive powder under compression and shear and its potential for modelling complex industrial processes involving these loading regimes.

8.6 *Recommendation for future research*

Some potential areas of future research are outlined below:

- The two directional punching in EPT is expected to be an improvement over one way punching in other uniaxial testers; it allows a reduction in the density

variation across the height of the sample and increases the repeatability in unconfined yield strength measurement. To verify this, a load cell can be installed at the bottom of the EPT cylinder to find out the amount of stress transferred in the pin-out condition. Additionally suitable experiments can be carried out to investigate the density distribution across the height of the sample.

- The particle scaling was investigated only for quasi-static simulation and monodisperse spherical particles. Further investigation should be made for the validity of scaling laws for polydisperse particles and non-spherical shape. Additionally the scaling was only investigated for a size range between 2~3.75mm, this can be extended to smaller size. Furthermore, the validity of scaling rules should also be investigated for dynamic simulations.
- Many bulk material exhibit time dependent unconfined strength. The current DEM contact model does not account for the time dependent strength. Factors affecting time dependent strength should be studied and time dependent parameter can be incorporated in the DEM contact model.

- The study of influence of the selected DEM input parameters in this thesis has highlighted the relative importance of these parameters. Further studies are clearly warranted. For example the effect of coefficient of restitution and particle density is not explored in this thesis because it was deemed to be less important for quasi-static simulation. Additionally, natural particle size variation exists in real materials. The influence of particle size distribution on the bulk response should be investigated.
- An extensive parametric study should be carried out. To limit the number of simulations required, design of experiments method can be used. The data provided by DEM simulations can be used in the development of parametric optimization procedure.
- To increase the confidence in DEM model calibration procedure, the calibrated DEM model can be validated against some other independent experiment.

References

Ando, Y., 2000. The effect of relative humidity on friction and pull-off forces measured on submicron-size asperity arrays. Wear 238, 12–19. doi:10.1016/S0043-1648(99)00334-8

Aoki, R., Suzuki, M., 1971. Effect of particle shape on the flow and packing properties of non-cohesive granular materials. Powder Technol. 1–3.

ASTM D 5550, 2006. Standard Test Method for Specific Gravity of Soil Solids by Gas Pycnometer, Annual Book of ASTM Standards.

Barrow, M.S., Williams, P.R., 2009. Application of Atomic Force Microscopy for the Study of Tensile and Microrheological Properties of Fluids 245–274.

Beach, E.R., Tormoen, G.W., Drelich, J., Han, R., 2002. Pull-off force measurements between rough surfaces by atomic force microscopy. J. Colloid Interface Sci. 247, 84–99. doi:10.1006/jcis.2001.8126

Bell, T.A., 2001. Solids flowability measurement and interpretation in industry, in: Levy, A., Kalman, H. (Eds.), Handbook of Conveying and Handling of Particulate Solids. pp. 3–13.

Bell, T.A., Catalano, E.J., Zhong, Z., Ooi, J.Y., Rotter, J.M., 2007. Evaluation of the Edinburgh Powder Tester, in: Proceedings of PARTEC. pp. 2–6.

Bell, T.A., Ennis, B.J., Grygo, R.J., 1994. Practical Evaluation of the Johanson Hang-Up Indicizer. Bulk Solids Handl. 14, 117.

Bergstrm, L., 1997. Hamaker constants of inorganic materials 70, 125–169.

Berman, A., Drummond, C., Israelachvili, J., 1998. Amontons' law at the molecular level. Tribol. Lett. 4, 95–101.

Bierwisch, C., Kraft, T., Riedel, H., Moseler, M., 2009. Three-dimensional discrete element models for the granular statics and dynamics of powders in cavity filling. J. Mech. Phys. Solids 57, 10–31. doi:10.1016/j.jmps.2008.10.006

Bika, D.G., Gentzler, M., Michaels, J.N., 2001. Mechanical properties of agglomerates. Powder Technol. 117, 98–112.

Bishop, A.W., Green, G.E., 1965. The influence of end restraint on the compression strength of a cohesionless soil. Géotechnique 15, 243–266.

Brewster, R., Grest, G., Levine, A., 2009. Effects of cohesion on the surface angle and velocity profiles of granular material in a rotating drum. Phys. Rev. E 79, 011305. doi:10.1103/PhysRevE.79.011305

Brilliantov, N., Albers, N., Spahn, F., Pöschel, T., 2007. Collision dynamics of granular particles with adhesion. Phys. Rev. E 76, 051302. doi:10.1103/PhysRevE.76.051302

Briscoe, B., Kremnitzer, S.L., 1979. A study of the friction and adhesion of polyethylene-terephthalate monofilaments. J. Phys. D Appl. 505.

Bröckel, U., Kirsch, R., Wahl, M., Feise, H.J., 2007. Formation and Strength of Solid Bridges in Bulk Solids. Part. Sci. Technol. 26, 23–32. doi:10.1080/02726350701759084

Butt, H.-J., Cappella, B., Kappl, M., 2005. Force measurements with the atomic force microscope: Technique, interpretation and applications. Surf. Sci. Rep. 59, 1–152. doi:10.1016/j.surfrep.2005.08.003

Carpick, R.W., Salmeron, M., 1997. Scratching the Surface: Fundamental Investigations of Tribology with Atomic Force Microscopy. Chem. Rev. 97, 1163–1194.

Carr, J., Walker, D., 1968. An annular shear cell for granular materials. Powder Technol.

Castellanos, A., 2005. The relationship between attractive interparticle forces and bulk behaviour in dry and uncharged fine powders, Advances in Physics. doi:10.1080/17461390500402657

Chaudhuri, B., Mehrotra, A., Muzzio, F.J., Tomassone, M.S., 2006. Cohesive effects in powder mixing in a tumbling blender. Powder Technol. 165, 105–114. doi:10.1016/j.powtec.2006.04.001

Chong, Y.S., Ratkowsky, D.A., Epstein, N., 1979. Effect of particle shape on hindered settling in creeping flow. Powder Technol. 23, 55–66.

Chung, Y., 2006. Discrete element modelling and experimental validation of a granular solid subject to different loading conditions. Philosophy. The University of Edinburgh. PhD dissertation.

Chung, Y., Ooi, J., 2008. A study of influence of gravity on bulk behaviour of particulate solid. Particuology 6, 467–474.

Chung, Y.C., Ooi, J.Y., 2006. Confined Compression and Rod Penetration of a Dense Granular Medium : Discrete, in: Modern Trends in Geomechanics. pp. 223–239.

Cleary, P.W., 2010. Particuology DEM prediction of industrial and geophysical particle flows &. Particuology 8, 106–118. doi:10.1016/j.partic.2009.05.006

Cleary, P.W., Sawley, M.L., 2002. DEM modelling of industrial granular flows: 3D case studies and the effect of particle shape on hopper discharge. Appl. Math. Model. 26, 89–111.

Coetzee, C.J., Els, D.N.J., 2009. Calibration of granular material parameters for DEM modelling and numerical verification by blade–granular material interaction. J. Terramechanics 46, 15–26. doi:10.1016/j.jterra.2008.12.004

Cundall, P.A., 1988. Formulation of a three-dimensional distinct element model—Part I. A scheme to detect and represent contacts in a system composed of many polyhedral blocks. Int. J. Rock Mech. Min. Sci. Geomech. Abstr. 25, 107–116.

Cundall, P.A., Strack, D.L., 1979. A discrete numerical model for granular assemblies. Geotechnique 1, 47–65.

D'Addetta, G.A., 2004. Discrete Models for Cohesive Frictional Materials. Universitat Stuttgart.

Dahneke, B., 1972. The influence of flattening on the adhesion of particles. J. Colloid Interface Sci. 40.

DEM Solutions, 2010. EDEM 2.3 User Guide, ReVision. Edinburgh, Scotland, UK.

DEM Solutions Ltd., 2011. EDEM 2.4 Theory Reference Guide. Edinburgh, Scotland, UK.

Deng, X.L., Davé, R.N., 2013. Dynamic simulation of particle packing influenced by size, aspect ratio and surface energy. Granul. Matter 15, 401–415. doi:10.1007/s10035-013-0413-0

Derjaguin, B., Muller, V.M., Toporov, Y.P., 1975. Effect of contact deformations on the adhesion of particles. J. Colloid Interface Sci. 53, 314–326.

Di Renzo, A., Di Maio, F.P., 2005. An improved integral non-linear model for the contact of particles in distinct element simulations. Chem. Eng. Sci. 60, 1303–1312.

Dry, R.J., Christensen, I.N., Thomas, G.C., 1988. The effect of naturally-occurring interparticle forces on the fluidisation characteristics of fine iron oxide powders. Chem. Eng. Sci. 43, 1033–1038.

Dury, C.M., Ristow, G.H., 1999. Competition of mixing and segregation in rotating cylinders. Phys. Fluids 11, 1387. doi:10.1063/1.870003

Ecke, S., 2001. Friction between Individual Microcontacts. J. Colloid Interface Sci. 244, 432–435.

Emeriault, F., Chang, C., 1997. Interparticle forces and displacements in granular materials. Comput. Geotech. 20, 223–244.

Enstad, G., Ose, S., 2003. Uniaxial testing and the performance of a pallet press. Chem. Eng. Technol. 26, 171–176.

Erikson, J., Mueggenburg, N., Jaeger, H., Nagel, S., 2002. Force distributions in three-dimensional compressible granular packs. Phys. Rev. E 66, 040301. doi:10.1103/PhysRevE.66.040301

Favier, J., Fard, M., 1999. Shape representation of axi-symmetrical, non-spherical particles in discrete element simulation using multi-element model particles. Eng. Comput. 16, 467–480.

Favier, J.F., Abbaspour-Fard, M.H., Kremmer, M., Raji, A.O., 1999. Shape representation of axi-symmetrical, non-spherical particles in discrete element simulation using multi-element model particles. Eng. Comput. 16, 467–480. doi:10.1108/02644409910271894

Feng, Y., Han, K., Owen, D., Loughran, J., 2007. Upscaling of discrete element models for particle systems, in: Proceedings of the 4 Th Int. Conf. on Discrete Element Methods. pp. 27–29.

Finnie, G.J., Kruyt, N.P., Ye, M., Zeilstra, C., Kuipers, J.A.M., 2005. Longitudinal and transverse mixing in rotary kilns: a discrete element method approach. Chem. Eng. Sci.

Fitzpatrick, J.J., Hodnett, M., Twomey, M., Cerqueira, P.S.M., O'Flynn, J., Roos, Y.H., 2007. Glass transition and the flowability and caking of powders containing amorphous lactose. Powder Technol. 178, 119–128. doi:10.1016/j.powtec.2007.04.017

Forsyth, A.J., Rhodes, M.J., 2000. A Simple Model Incorporating the Effects of Deformation and Asperities into the van der Waals Force for Macroscopic Spherical Solid Particles. J. Colloid Interface Sci. 223, 133–138.

Foster, K.D., Bronlund, J.E., Paterson, a. H.J. (Tony), 2006. Glass transition related cohesion of amorphous sugar powders. J. Food Eng. 77, 997–1006. doi:10.1016/j.jfoodeng.2005.08.028

Freeman, R., Fu, X., 2011. The Development of a Compact Uniaxial Tester, in: Particulate Science Analysis. Edinburgh, UK, pp. 1–6.

Freeman, R., Technology, F., 2005. Measuring the flow properties of consolidated , conditioned and aerated powders – a comparative study using a powder rheometer and a rotational shear cell, in: Particulate Systems Analysis. pp. 1–12.

Freeman, R.E., Cooke, J.R., Schneider, L.C.R., 2009. Measuring shear properties and normal stresses generated within a rotational shear cell for consolidated and non-consolidated powders. Powder Technol. 190, 65–69. doi:10.1016/j.powtec.2008.04.084

Ghadiri, M., Moreno-Atanasio, R., Hassanpour, A., Antony, S.J., 2007. Analysis of Agglomerate Breakage, in: Salman, A.D., Ghadiri, M., Hounslow, M.J. (Eds.), Handbook of Powder Technology. pp. 837–872.

Gilabert, F.A., Roux, J.N., Castellanos, A., 2007. Computer simulation of model cohesive powders: influence of assembling procedure and contact laws on low consolidation states. Phys. Rev. E 75, 011303.

Hamaker, H.C., 1937. The London – van der Waals attraction between spherical particles_Hamaker. Physica IV.

Härtl, J., Ooi, J.Y., 2008. Experiments and simulations of direct shear tests: porosity, contact friction and bulk friction. Granul. Matter 10, 263–271. doi:10.1007/s10035-008-0085-3

Härtl, J., Ooi, J.Y., 2011. Numerical investigation of particle shape and particle friction on limiting bulk friction in direct shear tests and comparison with experiments. Powder Technol. 212, 231–239.

Hassanpour, A., Ghadiri, M., 2007. Characterisation of Flowability of Loosely Compacted Cohesive Powders by Indentation. Part. Part. Syst. Charact. 24, 117–123.

Heim, L., Farschi, M., Morgeneyer, M., Schwedes, J., Butt, H.J., Kappl, M., 2005. Adhesion of carbonyl iron powder particles studied by atomic force microscopy. J. Adhes. Sci. Technol. 19, 199–213.

Helle, A.S., Easterling, K.E., Ashby, M.F., 1985. Hot-isostatic pressing diagrams: New developments. Acta Metall. 33, 2163–2174.

Hertz, H., 1881. On the contact of elastic solids. J. reine angew. Math 92, 110.

Hiestand, E.N., 1997. Principles, tenets and notions of tablet bonding and measurements of strength. Eur. J. Pharm. 44.

Hogue, C., 1998. Shape representation and contact detection for discrete element simulations of arbitrary geometries. Eng. Comput. 15, 374–390. doi:10.1108/02644409810208525

Höhner, D., Wirtz, S., Scherer, V., 2011. Comparison of the multi-sphere and polyhedral approach to simulate non-spherical particles within the discrete element method : In fl uence on temporal force evolution for multiple contacts. Powder Technol. 208, 643–656. doi:10.1016/j.powtec.2011.01.003

Hvorslev, M.J., 1937. Über die Festigkeitseigenschaften gestörter bindiger Böden. Danmarks naturvidenskabelige samfund, i kommission has GEC Gad.

Israelachvili, J.N., 1992. Intermolecular and surface forces. San Diego Acad.

Itasca, 2003. PFC 3D user manual. Itasca consulting group Inc, Minneapolis.

Jenike, A.W., 1964. Storage and flow of solids. Bull. 123.

Jensen, R.P., Bosscher, P.J., Plesha, M.E., Edil, T.B., 1999. DEM simulation of granular media—structure interface: effects of surface roughness and particle shape. Int. J. Numer. Anal. Methods Geomech. 23, 531–547. doi:10.1002/(SICI)1096-9853(199905)23:6<531::AID-NAG980>3.0.CO;2-V

Johanson, K., 2009. Effect of particle shape on unconfined yield strength. Powder Technol. 194, 246–251.

Johnson, K.L., Kendall, K., Roberts, A.D., 1971. Surface energy and the contact of elastic solids. Proc. R. Soc. London. A. Math. Phys. Sci. 324, 301.

Jones, R., 2003a. From Single Particle AFM Studies of Adhesion and Friction to Bulk Flow: Forging the Links. Granul. Matter 4, 191–204.

Jones, R., 2003b. Inter-particle forces in cohesive powders studied by AFM: effects of relative humidity, particle size and wall adhesion. Powder Technol. 132, 196–210.

Jones, R., Pollock, H.M., Geldart, D., Verlinden-Luts, A., 2004. Frictional forces between cohesive powder particles studied by AFM. Ultramicroscopy 100, 59–78.

Kaerger, J.S., Edge, S., Price, R., 2004. Influence of particle size and shape on flowability and compactibility of binary mixtures of paracetamol and microcrystalline cellulose. Eur. J. Pharm. Sci. 22, 173–9. doi:10.1016/j.ejps.2004.03.005

Kaye, B.H., Gratton-Liimatainen, J., Faddis, N., 1995. Studying the Avalanching Behaviour of a Powder in a Rotating Disc. Part. Part. Syst. Charact. 12, 232–236. doi:10.1002/ppsc.19950120505

Kendall, K., 1988. Agglomerate strength. Powder Metall. 31, 28–31.

Ketterhagen, W.R., Curtis, J.S., Wassgren, C.R., Hancock, B.C., 2009. Predicting the flow mode from hoppers using the discrete element method. Powder Technol. 195, 1–10. doi:10.1016/j.powtec.2009.05.002

Kodam, M., Bharadwaj, R., Curtis, J., Hancock, B., Wassgren, C., 2009. Force model considerations for glued-sphere discrete element method simulations. Chem. Eng. Sci. 64, 3466–3475.

Kruggel-Emden, H., Rickelt, S., Wirtz, S., Scherer, V., 2008. A study on the validity of the multi-sphere Discrete Element Method. Powder Technol. 188, 153–165.

Kruggel-Emden, H., Stepanek, F., Munjiza, A., 2010. A study on adjusted contact force laws for accelerated large scale discrete element simulations. Particuology 8, 161–175. doi:10.1016/j.partic.2009.07.006

Kuhl, E., 2000. Numerical models of cohesive frictional materials. Stuttgart Univ. (Germany).

Latham, J.-P., Munjiza, A., 2004. The modelling of particle systems with real shapes. Philos. Trans. A. Math. Phys. Eng. Sci. 362, 1953–72. doi:10.1098/rsta.2004.1425

Levy, A., 2001. Handbook of conveying and handling of particulate solids, 2001st ed. Elsevier Science.

Li, J., Langston, P.A., Webb, C., Dyakowski, T., 2004. Flow of sphero-disc particles in rectangular hoppers—a DEM and experimental comparison in 3D. Chem. Eng. Sci. 59, 5917–5929.

Luding, S., 2008. Cohesive, frictional powders: contact models for tension. Granul. Matter 10, 235–246.

Luding, S., Alonso-Marroquin, F., 2011. The critical-state yield stress (termination locus) of adhesive powders from a single numerical experiment. Granul. Matter 13, 109–119.

Luding, S., Manetsberger, K., Mullers, J., 2005. A discrete model for long time sintering. J. Mech. Phys. Solids 53, 455–491.

Luding, S., Tykhoniuk, R., Tomas, J., 2003. Anisotropic Material Behavior in Dense, Cohesive-Frictional Powders. Chem. Eng. Technol. 26, 1229–1232. doi:10.1002/ceat.200303236

Markauskas, D., Kačianauskas, R., Džiugys, A., Navakas, R., 2009. Investigation of adequacy of multi-sphere approximation of elliptical particles for DEM simulations. Granul. Matter 12, 107–123. doi:10.1007/s10035-009-0158-y

Massimilla, L., Donsi, G., 1976. Cohesive forces between particles of fluid-bed catalysts. Powder Technol. 15, 253–260.

Matsusaka, S., Maruyama, H., Matsuyama, T., Ghadiri, M., 2010. Triboelectric charging of powders: A review. Chem. Eng. Sci. 65, 5781–5807.

Matuttis, H., Schinner, A., 2001. Particle simulation of cohesive granular materials. Int. J. Mod. Phys. C 12, 1011–1021.

Maugis, D., 1992. Adhesion of spheres: the JKR-DMT transition using a Dugdale model. J. Colloid Interface Sci. 150.

Maw, N., Barber, J., Fawcett, J., 1976. The oblique impact of elastic spheres. Wear.

Mellmann, J., 2001. The transverse motion of solids in rotating cylinders—forms of motion and transition behavior. Powder Technol. 118, 251–270. doi:10.1016/S0032-5910(00)00402-2

Midi, G.D.R., 2004. On dense granular flows. Eur. Phys. J. E. Soft Matter 14, 341–65. doi:10.1140/epje/i2003-10153-0

Mindlin, R.D., 1949. Compliance of elastic bodies in contact. Trans. ASME, J. Appl. Mech. 17, 259.

Mindlin, R.D., Deresiewicz, H., 1953. Elastic spheres in contact under varying oblique forces. J. Appl. Mech 20.

Mio, H., Akashi, M., Shimosaka, A., Shirakawa, Y., Hidaka, J., Matsuzaki, S., 2009. Speed-up of computing time for numerical analysis of particle charging process by using discrete element method. Chem. Eng. Sci. 64, 1019–1026. doi:10.1016/j.ces.2008.10.064

Mokhtar, M.A., Kuwagi, K., Takami, T., 2012. Validation of the Similar Particle Assembly (SPA) Model for the Fluidization of Geldart ’ s Group A and D Particles 58. doi:10.1002/aic

Molerus, O., 1975. Theory of yield of cohesive powders. Powder Technol. 12, 259–275.

Moreno-atanasio, R., Antony, S.J., Ghadiri, M., 2005. Analysis of flowability of cohesive powders using Distinct Element Method. Powder Technol. 158, 51–57.

Moreno-Atanasio, R., Antony, S.J., Ghadiri, M., 2005. Analysis of flowability of cohesive powders using Distinct Element Method. Powder Technol.

Moreno-Atanasio, R., Ghadiri, M., 2006. Mechanistic analysis and computer simulation of impact breakage of agglomerates: Effect of surface energy. Chem. Eng. Sci. 61, 2476–2481.

Morrissey, J.P., 2013. Discrete Element Modelling of Iron Ore Pellets to Include the Effects of Moisture and Fines. Doctoral dessertation, University of Edinburgh.

Munjiza, A., Owen, D.R.J., Bicanic, N., 1995. A combined finite-discrete element method in transient dynamics of fracturing solids. Eng. Comput. 12, 145–174. doi:10.1108/02644409510799532

Nedderman, R.M., 2005. Statics and kinematics of granular materials, Annals of Physics. Cambridge University Press, Cambridge.

Ng, T.-T., Lin, X., 1997. A three-dimensional discrete element model using arrays of ellipsoids. Géotechnique 47, 319–329. doi:10.1680/geot.1997.47.2.319

O'Sullivan, C., Bray, J.D., 2004. Selecting a suitable time step for discrete element simulations that use the central difference time integration scheme. Eng. Comput. 21, 278–303. doi:10.1108/02644400410519794

Obermayr, M., Dressler, K., Vrettos, C., Eberhard, P., 2011. Prediction of draft forces in cohesionless soil with the Discrete Element Method. J. Terramechanics 48, 347–358. doi:10.1016/j.jterra.2011.08.003

Okasanen, C.A. and Zografi, G., 1990. The relationship between the glass transition temperature and water vapor absorption by poly(vinylpyrrolidone). Pharm. Res. 7, 654–657.

Palzer, S., 2005. The effect of glass transition on the desired and undesired agglomeration of amorphous food powders. Chem. Eng. Sci. 60, 3959–3968. doi:10.1016/j.ces.2005.02.015

Parrella, L., Barletta, D., Boerefijn, R., Poletto, M., 2008. Comparison between a uniaxial compaction tester and a shear tester for the characterization of powder flowability. KONA Pow Par J 26, 178–189.

Pöschel, T., Salueña, C., Schwager, T., 2001. Scaling properties of granular materials. Phys. Rev. E 64, 1–4. doi:10.1103/PhysRevE.64.011308

Potyondy, D.O., Cundall, P. a., 2004. A bonded-particle model for rock. Int. J. Rock Mech. Min. Sci. 41, 1329–1364. doi:10.1016/j.ijrmms.2004.09.011

Quintanilla, M.A.S., Castellanos, A., Valverde, J., 2001. Correlation between bulk stresses and interparticle contact forces in fine powders. Phys. Rev. E 64, 1–9. doi:10.1103/PhysRevE.64.031301

Radjai, F., Wolf, D.E., Jean, M., Moreau, J.J., 1998. Bimodal character of stress transmission in granular packings. Phys. Rev. Lett. 80, 61–64.

Roberts, T.A., Beddow, J.K., 1968. Some effects of particle shape and size upon blinding during sieving. Powder Technol. 2, 121–124.

Röck, M., Ostendorf, M., Schwedes, J., 2006. Development of an Uniaxial Caking Tester. Chem. Eng. Technol. 29, 679–685.

Rock, M., Schwedes, J., 2005. Investigations on the caking behaviour of bulk solids—macroscale experiments. Powder Technol. 157, 121–127.

Rumpf, H., 1958. Grundlagen und Methoden des Granulierens. Chemie Ing. Tech. CIT 30, 144–158. doi:10.1002/cite.330300307

Rumpf, H., 1962. The strength of granules and agglomerate, in: Knepper, W. (Ed.), Agglomeration. Wiley Interscience, New York.

Ruths, M., Alcantar, N.A., Israelachvili, J.N., 2003. Boundary Friction of Aromatic Silane Self-Assembled Monolayers Measured with the Surface Forces Apparatus and Friction Force Microscopy. Society 11149–11157.

Sakai, M., Koshizuka, S., 2009. Large-scale discrete element modeling in pneumatic conveying. Chem. Eng. Sci. 64, 533–539. doi:10.1016/j.ces.2008.10.003

Sakai, M., Takahashi, H., Pain, C.C., Latham, J.-P., Xiang, J., 2012. Study on a large-scale discrete element model for fine particles in a fluidized bed. Adv. Powder Technol. 23, 673–681. doi:10.1016/j.apt.2011.08.006

Santner, E., Stegemann, B., n.d. Adhesion measurements by AFM – a gateway to the basics of friction. Mater. Res.

Savkoor, A., Briggs, G., 1977. The effect of tangential force on the contact of elastic solids in adhesion. Proc. R. Soc. London. A. Math. Phys. Sci. 356, 103–114.

Schofield, A., Wroth, P., 1968. Critical State Soil Mechanics. McGraw-Hill.

Schubert, H., 1984. Capillary forces - modeling and application in particulate technology. Powder Technol. 37, 105–116.

Schulze, D., 1994. A New Ring Shear Tester for Flowability and Time Consolidation Measurements, in: 1st International Particle Technology Forum. Denver, Colorado, USA, pp. 11–16.

Schulze, D., 2007. Powders and bulk solids: Behavior, characterization, storage and flow, Journal of Statistical Mechanics: Theory and Experiment. Springer Verlag.

Schwarz, U.D., Zwörner, O., Köster, P., Wiesendanger, R., 1997. Quantitative analysis of the frictional properties of solid materials at low loads. I. Carbon compounds. Phys. Rev. B 56, 6987.

Schwedes, J., 2003. Review on testers for measuring flow properties of bulk solids. Granul. Matter 5, 1–43.

Seville, J., Tüzün, U., Clift, R., 1997. Processing of Particulate Solids. Springer Netherlands, Dordrecht. doi:10.1007/978-94-009-1459-9

Sheng, Y., Lawrence, C.J., Briscoe, B.J., Thornton, C., 2004. Numerical studies of uniaxial powder compaction process by 3D DEM. Eng. Comput. 21, 304–317.

Skinner, J., Gane, N., 1972. Sliding friction under a negative load. J. Phys. D. Appl. Phys. 5, 2087.

Stanley-wood, N., 2008. Bulk solids handling: equipment selection and operation, Bulk Solids Handling.

Subero, J., 2001. Impact breakage of agglomerates. Surrey University.

Taberlet, N., Richard, P., John Hinch, E., 2006. S shape of a granular pile in a rotating drum. Phys. Rev. E 73, 050301. doi:10.1103/PhysRevE.73.050301

Tabor, D., 1977. Surface forces and surface interactions. J. Colloid Interface Sci. 58, 2–13.

Tardos, G., 2003. Slow and intermediate flow of a frictional bulk powder in the Couette geometry. Powder Technol. 131, 23–39. doi:10.1016/S0032-5910(02)00315-7

Tatemoto, Y., Mawatari, Y., Noda, K., 2005. Numerical simulation of cohesive particle motion in vibrated fluidized bed. Chem. Eng. Sci. 60, 5010–5021.

Thakur, S. C., Ahmadian, H., Sun, J., Ooi, J.Y., 2013. An experimental and numerical study of packing, compression, and caking behaviour of detergent powders. Particuology. doi:10.1016/j.partic.2013.06.009

Thakur, S.C., Ahmadian, H., Sun, J., Ooi, J.Y., 2013. Scaling of discrete element model parameters in uniaxial test simulation, in: Proceedings of DEM6 Conference. Golden, Clorado.

Thalberg, K., Lindholm, D., Axelsson, A., 2004. Comparison of different flowability tests for powders for inhalation. Powder Technol. 146, 206–213. doi:10.1016/j.powtec.2004.08.003

Thompson, D., 1972. Fertilizer caking and its prevention, in: Fertilizer Society. York.

Thornton, C., Ning, Z., 1998. A theoretical model for the stick/bounce behaviour of adhesive, elastic-plastic spheres. Powder Technol. 99, 154–162.

Thornton, C., Randall, C.W., 1988. Micromechanics of Granular Materials. Appl. Theor. Contact Mech. to Solid Part. Syst. Simul. 133.

Thornton, C., Yin, K., 1991. Impact of elastic spheres with and without adhesion. Powder Technol. 65, 153–166.

Ting, J.M., Meachum, L., Rowell, J.D., 1995. Effect of particle shape on the strength and deformation mechanisms of ellipse-shaped granular assemblages. Eng. Comput. 12, 99–108.

Tomas, J., 2000. Particle adhesion fundamentals and bulk powder consolidation. Kona.

Tomas, J., 2001. Assessment of Mechanical Properties of Cohesive Particulate Solids. Part 1: Particle Contact Constitutive Model. Part. Sci. Technol. 19, 95–110. doi:10.1080/02726350152772056

Tomas, J., 2003. Mechanics of nanoparticle adhesion–a continuum approach. Part. surfaces 8, 183–229.

Tomas, J., 2004. Mechanics of Particle Adhesion 1. Process Eng. 1–92.

Tomas, J., 2007. Adhesion of ultrafine particles—A micromechanical approach. Chem. Eng. Sci. 62, 1997–2010.

Tsoungui, O., Vallet, D., Charmet, J., 1998. "'Partial pressures'" supported by granulometric classes in polydisperse granular media ´. Phys. Rev. E 57, 4458–4465.

Tsuji, Y., Tanaka, T., Ishida, T., 1992. Lagrangian numerical simulation of plug flow of cohesionless particles in a horizontal pipe. Powder Technol. 71, 239–250.

Tykhoniuk, R., Tomas, J., Luding, S., Kappl, M., Heim, L., Butt, H.-J., 2007. Ultrafine cohesive powders: From interparticle contacts to continuum behaviour. Chem. Eng. Sci. 62, 2843–2864.

Vu-Quoc, L., Zhang, X., 1999. An elastoplastic contact force–displacement model in the normal direction: displacement–driven version. Proc. R. Soc. London. Ser. A Math. Phys. Eng. Sci. 455, 4013–4044.

Vu-Quoc, L., Zhang, X., Lesburg, L., 2001. Normal and tangential force–displacement relations for frictional elasto-plastic contact of spheres. Int. J. Solids Struct. 38, 6455–6489.

Vu-Quoc, L., Zhang, X., Walton, O.., 2000. A 3-D discrete-element method for dry granular flows of ellipsoidal particles. Comput. Methods Appl. Mech. Eng. 187, 483–528. doi:10.1016/S0045-7825(99)00337-0

Walton, O.R., Braun, R.L., 1986. Viscosity, granular-temperature, and stress calculations for shearing assemblies of inelastic, frictional disks. J. Rheol. (N. Y. N. Y). 30, 32.

Walton, Otis R, Braun, R.L., 1986. Calculations for Shearing Assemblies of Inelastic , Frictional Disks. J. Rheol. (N. Y. N. Y). 30, 949–980. doi:10.1122/1.549893

Walton, O.R., Johnson, S.M., 2009. Simulating the effects of interparticle cohesion in micron-scale powders, in: AIP Conference Proceedings. Golden, Colorado, pp. 897–900. doi:10.1063/1.3180075

Walton, O.R., Johnson, S.M., 2010. DEM Simulations of the effects of particleshape, interparticle cohesion, and gravity on rotating drum flows of lunar regolith, in: Earth and Space. Honolulu, Hawaii, pp. 1–6.

Washburn, E.W., 1921. The dynamics of capillary flow. Phys. Rev. 17, 273.

Watanabe, H., Groves, W.L., 1964. Caking test for dried detergents. J. Am. Oil Chem. Soc. 41, 311–315.

Wensrich, C.M., Katterfeld, A., 2012. Rolling friction as a technique for modelling particle shape in DEM. Powder Technol. 217, 409–417. doi:10.1016/j.powtec.2011.10.057

Williams, J.C., Birks, A.H., Bhattacharya, D., 1971. The Direct Measurement of the Failure of a Cohesive Powder. Powder Tech 4, 328–337.

Wolf, G., 1981. Chocolate, Cocoa and Confectionery; Science and Technology., Food / Nahrung. WILEY-VCH Verlag GmbH. doi:10.1002/food.19810250618

Wood, D.M., 1990. Soil behaviour and critical state soil mechanics. Cambridge University Press.

Wu, C.-Y., Cocks, A.C.F., 2006. Numerical and experimental investigations of the flow of powder into a confined space. Mech. Mater. 38, 304–324.

Xu, B., 1997. Numerical simulation of the gas-solid flow in a fluidized bed by combining discrete particle method with computational fluid dynamics. Chem. Eng. Sci. 52, 2785–2809. doi:10.1016/S0009-2509(97)00081-X

Yan, H., Barbosa-Canovas, G.V., 1997. Compression characteristics of agglomerated food powders: Effect of agglomerate size and water activity. Food Sci. Technol. Int. 3, 351–359.

Yan, H., Barbosa-Canovas, G.V., 2000. Attrition evaluation for selected agglomerated food powders: The effect of agglomerate size and water activity. J. Food Process Eng. 24, 37–49.

Yang, R.Y., Zou, R.P., Yu, A.B., 2000. Computer simulation of the packing of fine particles. Phys. Rev. E 62, 3900–3908.

Yang, S.-C., Hsiau, S.-S., 2001. The simulation and experimental study of granular materials discharged from a silo with the placement of inserts. Powder Technol. 120, 244–255.

Yen, K., Chaki, T., 1992. A dynamic simulation of particle rearrangement in powder packings with realistic interactions. J. Appl. Phys. 71, 3164–3173.

Zhang, X., Vu-Quoc, L., 2007. An accurate elasto-plastic frictional tangential force–displacement model for granular-flow simulations: Displacement-driven formulation. J. Comput. Phys. 225, 730–752.

Zhong, W., Xiong, Y., Yuan, Z., Zhang, M., 2006. DEM simulation of gas–solid flow behaviors in spout-fluid bed. Chem. Eng. Sci. 61, 1571–1584.

Zhong, Z., Ooi, J.Y., Rotter, J.M., 2005. Predicting the handlability of a coal blend from measurements on the source coals. Fuel 84, 2267–2274.

Zhou, C., Ooi, J.Y., 2009. Numerical investigation of progressive development of granular pile with spherical and non-spherical particles. Mech. Mater. 41, 707–714.

Zhu, H., Zhou, Z., Yang, R., Yu, A., 2008. Discrete particle simulation of particulate systems: A review of major applications and findings. Chem. Eng. Sci. 63, 5728–5770. doi:10.1016/j.ces.2008.08.006

Zou, R.P., Yu, A.B., 1996. Evaluation of the packing characteristics of mono-sized non-spherical particles. Powder Technol. 88, 71–79.